Magazine of Civil Engineering

120(4), 2023

ISSN 2712-8172

Magazine of Civil Engineering

ISSN 2712-8172

Online peer-reviewed open-access scientific journal in the field of Civil and Construction Engineering

Founder and Publisher: Peter the Great St. Petersburg Polytechnic University

This journal is registered by the Federal Service for Supervision of Communications, Information Technology, and Mass Media (ROSKOMNADZOR) in 2020. Certificate El No. FS77-77906 issued February 19, 2020.

Periodicity: 8 issues per year

Publication in the journal is open and free for all authors and readers.

Indexing: Scopus, Web of Sceince (ESCI, RSCI), DOAJ, Compendex, Google Academia, Index Copernicus, ProQuest, Ulrich's Serials Analysis System, CNKI

Corresponding address: 29 Polytechnicheskaya st., Saint Petersburg, 195251, Russia

Chief science editor: associate member of RAS, D.S. in Engineering, Vitaly V. Sergeev

Deputy chief science editors:
D.S. in Engineering, Galina L. Kozinetc

D.S. in Engineering, Sergey V. Korniyenko

Executive editor: Ekaterina A. Linnik

Translator, editor: Darya Yu. Alekseeva

DT publishing specialist:
Anastasiya A. Kononova

Contacts:
E-mail: mce@spbstu.ru
Web: http://www.engstroy.spbstu.ru

Date of issue: 03.07.2023

Contents

Magazine of Civil Engineering

ISSN 2712-8172

journal homepage: http://engstroy.spbstu.ru/

Research article

UDC 627.81:556.5

DOI: 10.34910/MCE.120.1

Engineering hydrology technologies to reduce threats from ice phenomena

D.V. Kozlov , ***N.T. Dzhumagulova***

Moscow State University of Civil Engineering (National Research University), Moscow, Russian Federation

dnazira@rambler.ru

Keywords: water safety, water body, river, dangerous hydrological phenomenon (process), iced phenomenon (process), ice regime, ice-clogging, modeling, monitoring

Abstract. Introduction. The floods caused by ice phenomena are among the "three leaders" of dangerous hydrological phenomena that damage the economy and the environment in Russia. Methods. The methodological basis of the study was: passive experiment, analysis and synthesis, generalizations, methods of mathematical modeling of hydrological and hydraulic processes, multivariate analysis and expert assessments. Results and Discussion. Generalization, analysis and systematization of knowledge about the processes of formation of ice difficulties were carried out. It is shown that under the conditions of climate change and ice regime of water bodies as a result of human economic activity, the methods of forecasting ice phenomena are being transformed, which are mainly based on statistical dependencies established according to the hydrometeorological observations. An updated zoning of the territory of Russia by the genesis of the ice phenomena and types of dangerous hydrological phenomena with recorded material damage is presented. The views on modern methods of monitoring dangerous ice phenomena and the use of its results for timely forecasting, adoption of rules for the use of water resources and preventive measures are expounded, while the consequences of the impact of these phenomena on water bodies are assessed. The modern trends in the development of mathematical modeling of the processes of formation of ice hanging dams and ice jams, the transporting ability of subglacial flows in combination with models of river flow formation and functioning of water management systems are revealed. The prospects for research aimed at developing measures to counter threats to water safety caused by dangerous ice phenomena are determined. Conclusion. The results of qualitative and quantitative analysis can be used to collect information on the consequences of exposure and monitoring of ice hazards. Trends in the development of mathematical modeling of the processes of congestion and anchor ice dam formation, transporting ability of subglacial flows in sections of rivers with engineering structures are associated with a combination of hydrodynamic models, models of river flow formation and the functioning of water management systems. The prospects for research aimed at developing measures to counter threats to water safety caused by dangerous ice phenomena were determined.

Funding: The article is based on the results of the scientific project "Development of composite modeling methods for exploratory design and feasibility study of hydraulic structures" (2023 NRU MGSU).

Citation: Kozlov, D.V., Dzhumagulova, N.T. Engineering hydrology technologies to reduce threats from ice phenomena. Magazine of Civil Engineering. 2023. 120(4). Article no. 12001. DOI: 10.34910/MCE.120.1

1. Introduction

Water safety is the most important challenge of our time. For the national safety of Russia, the water factor is associated, first of all, with such sources of risks as accidents at hydraulic structures and floods caused by dangerous hydrological phenomenon (DHP). DHP occur in the vast majority of countries of the world [1]. In Russia, the damage from all possible hydrometeorological phenomena is 80–90 % of the total damage of a natural environment. At the same time, floods caused by high water, ice jam or ice hanging dam are among the "three leaders" of the DHP, which have a "damaging effect on people, economic sectors and the environment" [1]. In 2020, The Russian Federal Service for Hydrometeorology and Environmental Monitoring (Roshydromet) recorded 1,000 dangerous hydrometeorological phenomena in Russia (97 phenomena more than in 2019), of which 372 phenomena caused significant damage to critical infrastructure [2]. Such DHPs in each of the subjects of Russia have their own characteristics and different repeatability. The role of each of the possible sources of an emergency accompanied by the occurrence of significant material damage is different and unique both in time and place of origin on the territory of the country [1, 3].

Over the past 25 years, more than 130 ice-clogging floods with recorded material damage have been registered in Russia. The scale of damage varies: from the maximum in the spring of 2001 on the Lena River to the insignificant – in sparsely populated river basins of the Far North. The studies of the processes of ice jam both in natural riverbeds and in regulated sections of rivers show that the development of ice jam and ice hanging dam, as a rule, leads to a decrease channel capacity of the channel and a significant rise in the water level in the river. The annual ice floods on the Sukhona River near Veliky Ustyug [3], the winter flooding on the Volga River in Yaroslavl in 2020 [4], and the formation of congestion in the alignment of the bridge gate across the river are a confirmation of that [5].

Despite the sufficient study of the ice regime of rivers and the processes of ice jams, there are still some urgent problems of the engineering hydrology concerning dangerous ice phenomena, which include:

- the study of the causes and features of their formation;
- the analysis of achievements in the development and application of methods for calculating and forecasting their quantitative characteristics;
- their physical and mathematical modeling;
- monitoring and consequences of their formation both in natural environment and on regulated sections of rivers, including in the presence of engineering structures, to reduce threats to water safety.

The technological complex of engineering hydrology includes monitoring of surface and groundwater, including the observations (with a system for collecting and transmitting information) and the measurements of physical and geographical characteristics; the water resources management technologies; the statistical analysis of hydrological data; the modeling of hydrological (and hydraulic) systems; the hydrological forecasts.

In this study, using the capabilities of the technological complex of engineering hydrology, the following tasks were solved:

1. The search for statistically significant trends in the historical timing of the ice formation and the ice break-up (based on a statistical analysis of the characteristics of the ice regime of the mouth section of the Northern Dvina River in the retrospective period).

2. The classification of the subjects of the Russian Federation by the spectrum of hazardous hydrological and ice phenomena (ice jams and ice hanging dams) with recorded material damage, statistical assessment of the long-term dynamics of these phenomena and the advanced nature of their forecasts in each of the regions.

3. The qualitative and quantitative assessment of the factors that influenced the occurrence of ice jam and the development of winter flooding in the regulated section of the river (based on the results of monitoring the hydrometeorological and hydrological situation in the Volga River basin below the Rybinsk hydroelectric complex).

4. The mathematical modeling of the river flow in the area of the bridge crossing in the conditions of ice jam formation (on a section of the Volga River to assess the flow velocities and slopes of the water surface) followed by an assessment of ice impacts on the temporary transport structure.

2. Materials and Methods

2.1. Area of research

2.1.1. The ice regime of rivers of the north of the European part of Russia

Due to intensive anthropogenesis and climate change, the ice regime of the rivers of Russia, as part of the hydrological regime of the river, underwent significant changes in the XX–XXI centuries. In order to assess the latest changes of the ice regime, it is necessary to retransform information about the ice regime of watercourses in the past.

The continuous data on the ice regime of Russian rivers are available since the first half of the XVIII century. For example, information about the timing of freezing and the complete clearance of the Northern Dvina River from ice has been known since 1734. For the first time, the analysis of long-term observations of the timing of the ice phenomena onset in the basin of this river was performed by K.S. Veselovsky in 1857. In 1868–1869 S.F. Ogorodnikov systematized this information, pointing to the factors affecting the height of water rises, linking the height of the spring flood of the river "... with the rapidity of snow melting, the thickness and strength of the ice, the strength or direction of the wind during the ice breakup of the lower part of the river" [1]. Today, these are generally accepted predictors in models for forecasting the height of ice jams rises in water levels [6]. In the same work, an assumption was made about the possibility of predicting the timing of freezing and ice breakup: "the ice breakup and freezing of rivers are inextricably linked with the air temperature". The research of S.F. Ogorodnikov was developed in the works of M.A. Rykachev (1886)[2] and P.N. Orlov (1915)[3].

The surface air temperature is one of the indicators characterizing the climate change at high latitudes. Compared with the variations in air temperature, the rate of warming in the Arctic in recent decades has exceeded the global and regional warming rates [7]. The increase in the average annual temperature in Arkhangelsk in the last decades of the twentieth century was 0.6 °C, the temperature increase at a rate of 1 °C per 100 years occurred mainly in the cold period of the year [3]. The variability of the near-surface air temperature in the Dvina River Bay of the White Sea was studied for 1915–2015 [8]. It was found that the increase in the average daily air temperature in the spring has shifted to an earlier date, and the decrease in autumn – to a later date; the average rate of change was 10 days in 100 years.

The consequence of the change in the temperature regime was a change in the ice regime of the Northern Dvina River. The dates of freezing have shifted to a later date and the dates of clearing from ice – to the earlier ones [3]. For the lower section of the river for 1880–2004, a statistically significant trend in the timing of the appearance of ice and ice breakup dates was obtained. The freezing came later by 4–5 days, and the ice breakup 2 days earlier. The general trend of shifts in the timing of the appearance of ice and the freezing was revealed throughout the observation period, starting from 1734.

The data on the ice regime of the Northern Dvina River for 1961–2016 were analyzed [9]. For the lower reaches of the river, the dates of freezing shifted by 5 days, the freezing started at higher water levels, which caused an increase in the frequency of ice jams. The timing of cleaning from ice shifted by 4–5 days.

The ice and temperature regimes of the Northern Dvina River according to the reports of the Solombala hydrological post and the Arkhangelsk meteorological station for the period 1914–2013, and historical data for 1733–1855 were studied [10]. A later ice breakup of the river in the period from 1733 to 1855 was explained by the fact that this period belonged to the so-called Little Ice Age. For the dates of the beginning of ice phenomena for 1972–2012, a linear positive trend was obtained [10]. It was noted that the tendencies of deviation of the average air temperature from the norm and changes in the dates of ice formation were unidirectional.

On a 45-kilometer stretch in the delta of the Northern Dvina River almost every spring, ice jams are formed. A lot of historical evidence has been preserved about the spring floods with high water rises and their consequences for Arkhangelsk (high flood of 1621 with ice drift in Kholmogory, water rise of 5.3 m in the spring of 1779, flood of 1811) [11]. Almost annually, in the period from 1900 to 1915 in Arkhangelsk during the spring ice drift, the rise of water was 3-4 meters. To prevent ice jams and related floods in the city since 1915, icebreaking work began to be carried out. From 1922 to 1970, the icebreaking included bombing [12], and since 1954, radiation for ice weakening. Since 1962, directed explosions has became a part of the annual icebreaking works [13]. The early descent of ice into the river mouth has become a powerful anthropogenic factor affecting not only the occurrence of ice jams, but also the course of spring ice phenomena. The ice drift in the Arkhangelsk region began to advance a few days earlier [14]. Over the centuries, the population of the city has grown significantly (from 11 thousand in 1811 to 345 thousand in 2021). The ice regime of the Northern Dvina River is now affected by discharges of warm wastewater from

[1] Trudy Arkhangel'skogo gubernskogo statisticheskogo komiteta za 1867 i 1868 g. [Proceedings of the Arkhangelsk Provincial Statistical Committee for 1867 and 1868]. (rus)

[2] Rykachev, M.A. Vskrytiya i zamerzaniya vod v Rossiyskoy imperii [Breakup and freezing of waters in the Russian Empire]. St. Petersburg: printing house of the Imperial Academy of Sciences. 1886. 309 p. (rus)

[3] Orlov, P.N. Vskrytiye i zamerzaniye reki Severnoy Dviny v g. Arkhangel'ske po dannym za 1734-1915 gg. [Breakup and freezing of the Northern Dvina River in the city of Arkhangelsk according to data for 1734-1915]. Arkhangelsk: Provincial Printing House, 1915. 14 p.

the municipal economy and industrial enterprises. It is very problematic to distinguish the degree of anthropogenic influence and the influence of climate change on the characteristics of the ice regime at the mouth of the Northern Dvina River according to the hydrological data collected later than 1915.

The information basis for long-term analysis of the possible non-stationarity of ice phenomena and the search for statistically significant trends in the historical timing of the ice formation and the ice breakup at the mouth of the Northern Dvina River was the archival information of M.A. Rykachev, supplemented by the data of P.N. Orlov.

2.1.2. Dangerous hydrological and ice phenomena on the territory of Russia

The features of the distribution of DHP, including ice genesis, on the territory of Russia depend primarily on the natural and climatic conditions and characteristics of anthropogenic activity. The various aspects of the impact of DHP on natural and technical systems, flood hazard assessment in Russia and in its subjects are considered, for example, in works of [15, 16]. The use of methods of multidimensional data analysis and GIS technologies in the creation of regional information and cartographic databases on DHP is set out, for example, in the work of [17]. Integrated hydrometeorological modeling for early flood detection is used in foreign practice [18].

The starting material for studies of the long-term dynamics of dangerous hydrological and ice phenomena were Roshydromet data on adverse weather conditions and dangerous hydrometeorological phenomena that caused socio-economic losses in Russia for a 29-year period from 1991 to 2019 [19]. The total data set of DHP includes almost 1900 events.

2.1.3. Factors affecting the occurrence of ice jam and development of winter flooding in the regulated section of the river

The ice jams play an important role in the formation of catastrophic floods on rivers. Features, causes and consequences of the formation of ice jams both in natural and overregulated sections of rivers have been studied for several decades [20, 21, 22]. In the recent years, there have been more studies on regulated rivers as well [5, 23]. The studies showed that ice-hanging dams during the formation of ice covers and ice jams during its destruction mainly develop due to the presence of fractures in the longitudinal profile of the river, increased slopes and flow rates in the river section in combination with fluctuations in the mode of releases to the hydroelectric power station. The conditions for the formation of ice jams in the regulated section of the river differ from the natural conditions of ice jams by the presence of pre-flood discharge of the water level. One of the main reasons (factors) for ice jam is the insufficient flow capacity of the channel (both ice and water) associated with its morphological features [23].

The authors attempted to assess the factors that influenced the occurrence of ice jam and the development of winter flooding on the Volga River below the Rybinsk hydroelectric complex near Yaroslavl in February 2020. For this purpose, they compared this case with a similar situation that occurred in the winter of 2007. The authors used the results of monitoring observations based on operational reports of the Ministry of Emergency Situations of Russia, PJSC RusHydro and Roshydromet. Information from the Federal Agency of Water Resources on the water management situation in the territory of the Upper Volga Basin Water Management and the operating modes of the reservoirs of the Volga-Kama cascade was used as well.

The factor of insufficient throughput of the channel is relatively constant, but in the considered case (2020) on the river section of the Nizhny Novgorod reservoir of the Volga River in the Yaroslavl region, it played a decisive role in the formation of an ice jam.

2.1.4. Factors and methods of modeling river flows in the area of the bridge crossing in the conditions of ice jam formation

For the successful implementation of infrastructure projects in the river basins of Russia, modeling of ice phenomena and the capacity of river channels in the autumn-winter and winter-spring periods, including in the presence of engineering structures on rivers (bridges, crossings, power transmission towers, etc.), is of great importance. An overview of methods of mathematical modeling of ice processes and the experience of their implementation for practical problems is contained, for example, in the papers [23–25].

In [26] issues of dynamics of water flows with ice cover and a set of mathematical models of ice jams and their consequences are considered. The methods of calculation, forecast and comprehensive assessment of the impact of ice jams on the environment were set out in a monograph [27].

Researches [28, 29] are devoted to the creation of a physical model of the ice jammed section of the riverbed. In foreign practice, both one-dimensional mathematical models of ice processes implemented in computer programs RIVICE, RIVJAM, ICEJAM, and two-dimensional ones, for example, CRISSP, are widely used. A comparison of numerical models of river ice jams was made in papers [30, 31].

The object of the study was a new bridge across the Volga River in its middle course during the construction period. The estimated flow rate was assumed to be equal to the construction flow rate with a 10% security of 30,000 m^3/s. The corresponding water levels were determined taking into account the support from the Zhiguli hydroelectric complex, and the calculations were carried out at two levels at the output border, equal to 53.0 m and 54.0 m.

2.2. Research Methodology

The solution of the tasks was established on the methodological approaches based on the fundamental provisions of engineering hydrology and methods of scientific and cognitive activity: empirical (passive experiment) and universal general logical methods (analysis, synthesis, generalization, etc.), as well as methods of mathematical modeling of hydrological and hydraulic processes, mathematical statistics, multidimensional analysis and expert assessments.

The achievements of applied mathematical sciences and the development of the theory of ice processes at the present stage have provided a new way to assess the variability of the ice regime of the mouth of the Northern Dvina River in historical retrospective, which excludes the influence of anthropogenic factors. The methodological basis of the study were multidimensional data analysis and methods of mathematical statistics. Verification of the significance of the trend was carried out on the recommendations of the State Hydrological Institute (SHI, 2010) [32].

The classification of the subjects of Russia by type, number and frequency of occurrence of ice DHP in the development of work of [1] was carried out using the method of multidimensional data analysis – cluster analysis. The regression analysis methods were used to verify the stationarity of long-term DHP series by cluster, region, and type.

The authors generalized the features of ice jam processes in overregulated sections of rivers, and assessed the hydrological situation and ice conditions with an analysis of the causes and consequences of ice jams on the river section of the Gorky reservoir below the Rybinsk hydroelectric complex. The work was carried out as a result of a passive empirical experiment using meteorological, hydrological (on water flows and levels) data and information on ice phenomena on the river. The authors also employed a universal (general logical) method - analysis and synthesis, induction and deduction, generalization. The draft Rules for the Use of Water Resources of the Rybinsk and Gorky Reservoirs on the Volga River were useful for the study.

The assessment of ice impacts on the capacity of the Volga River bed and the temporary bridge crossing during the construction period was carried out by the method of mathematical modeling of the river flow in the area of the bridge crossing in the conditions of ice jam using the Russian software package STREAM 2D CUDA [33]. It was based on the numerical solution of the equations of shallow water in a two-dimensional (planned) formulation and the simplest model (with no consideration of the elastic properties of ice).

3. Results and Discussion

3.1. Statistical analysis of the characteristics of the ice regime in retrospective period

For statistically reliable conclusions about the possible non-stationarity of ice phenomena on the river over a retrospective observation period of more than 180 years (1734–1915), the Northern Dvina was tested for the hydrological homogeneity of the studied characteristics in accordance with the current methodological guidelines of the State Hydrological Institute (SHI, 2010) [32].

A method for estimating the significance of linear regression equations over time was used. If the trend was significantly different from zero, then the hydrological characteristic (including the date of occurrence of the ice event) was non-uniform in time.

The significance of the trend was assessed by comparing the correlation coefficient r of the linear regression equation with a random mean square error calculated by the formula:

$$\sigma_r = (1-r^2)/\sqrt{n-1}, \tag{1}$$

where n is the number of years of observations. At a 5 % significance level, the condition $r/\sigma_r \geq 2$ must be satisfied, at a 1 % significance level $r/\sigma_r \geq 3$.

Figure 1 shows the factor field of breakup dates from the ice of the Northern Dvina River. The date of the opening of the river corresponded to the first of the dates of the complete clearing of the river from ice. The earliest opening date is April 21, the latest date is June 7. Along the y-axis, the boundaries (Figure 1) of the studied field of opening dates are: April 15 – lower and June 14 – upper. The beginning of the series under consideration corresponds to the 1st year. The domain of definition is taken at 200 years.

The general trend of autopsy dates reversed after 120 years (1860). For verification, 2 periods were considered: observation data from 1734 to 1859 and from 1860 to 1915. The abscissa shows the years (1st – 1734 and 182nd – 1915) of the study series of observations of the opening of the Northern Dvina River. The ice breakup trend equation has the form in the format of numbers: y = -0.038x + 43227. It was obtained as a result of applying the STATISTICA package using the “encoding” of dates (converting the “date” format to the “number” format).

The trend of the ice breakup dates (April 15 to June 14) for the period of 1734–1859 is not statistically significant. The trend for the period of 1860–1915 is statistically significant: the coefficient of determination R2 is greater than 0.1. For the model of paired linear regression, the coefficient of determination is equal to the square of the usual correlation coefficient between y and x at both 5% and 1% (Figure 1).

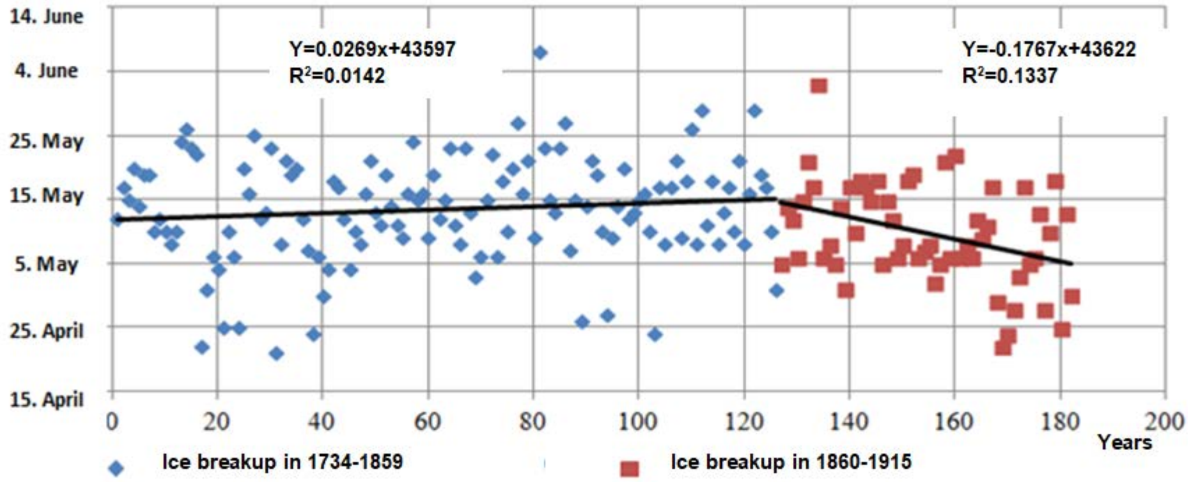

Figure 1. Ice breakup in 1734–1859 (blue) and 1860–1915 (red).

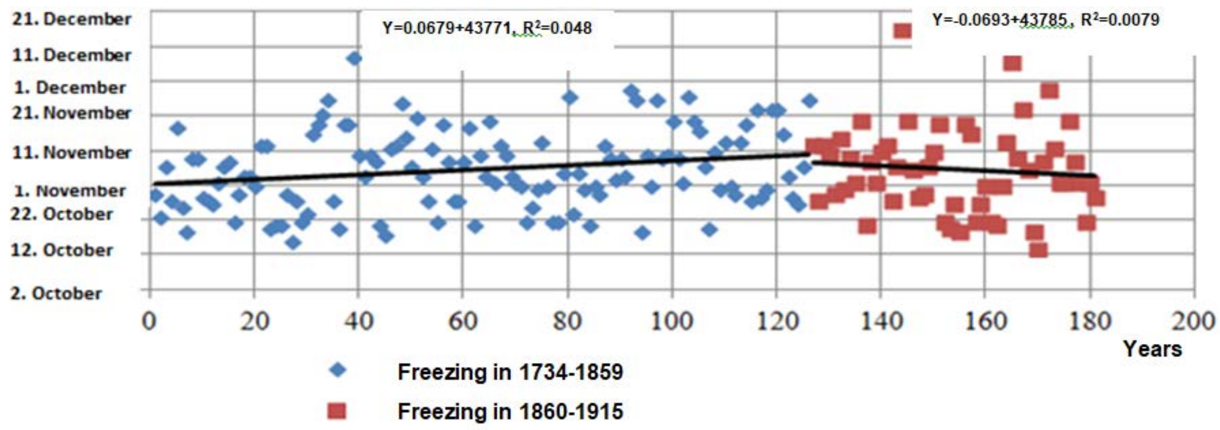

Figure 2. Freezing in 1734–1859 (blue) and 1860–1915 (red).

The trend of dates of river freezing (from October 12 to December 21) for 1734–1859 is statistically significant at the level of 5 %, and at the level of 1 % it is no longer significant. The trend of dates of river freezing in 1860–1915 is not statistically significant (Figure 2). In addition, the shift of the ice breakup dates in 1860–1915 towards earlier dates and the shift of freezing dates in the period 1734-1859 towards later dates were proven.

Analysis of retrospective data for 182 years (from 1734 to 1915) made it possible to exclude the influence of anthropogenic factors on the assessment of the variability of the ice regime on the mouth section of the Northern Dvina River. The identified trends indicated a possible warming of the climate in the northern latitudes. The findings could be useful for analyzing long-term regional and global climate change. Similar conclusions about shifts in the timing of ice breakup and freezing of the rivers of Central Siberia were made based on the results of a retrospective analysis of two-hundred-year observations.

3.2. Classification of the subjects of the Russian Federation by the spectrum of hazardous hydrological and ice phenomena

Floods (33.3%) and high waters (29.8%) caused the most material damage on the territory of Russia out of all the events of the DHP, and cases of recorded damage from ice jams and ice hanging dams amounted to 7.2% and 0.5%, respectively. Descriptive data statistics showed that the maximum number of DHP types found in a particular region (in 2% of the subjects of the Russian Federation) can reach up to six (ice jam and ice hanging dam, low baseflow, high water and flood, mudflow).

For each type of DHP within the territory of Russia, linear trends were built. The temporal homogeneity of the series was checked according to the recommendations of the State Hydrological Institute [32], with the ratio $r/\sigma_r \geq 2$ (r is correlation coefficient; σ_r is root mean square error; n = 29 is the number of years of observations) the trend was recognized as significant at 5 % of the level of significance, with the ratio $r/\sigma_r \geq 3$ trend was recognized as significant at 1 % level of significance [32]. The final conclusion about the significance of the trend or the non-stationarity of the series was made with the same conclusions for 5 %, and for 1 %. The results of assessing the significance of trends for all types of DHP, including ice jams, are shown in Table 1. For the period of 1991–2019, all DHP analyzed with recorded material damage had upward trends, but trends were recognized as statistically insignificant at both 5 % and 1 % significance levels.

Table 1. Significance of linear trends of dangerous hydrological and ice phenomena for 1991–2019.

DHP types	Trend equation	r	σ_r	r/σ_r
Ice jams	y = 0.0546x + 4.4507	0.13	0.19	0.71
All types of dangerous hydrological phenomena	y = 1.0128x + 50.015	0.34	0.17	2.03

Using cluster analysis, the DHP were grouped into 4 typical groups: ice difficulties (ice jam, ice hanging dam, early ice formation), high waters and floods, mudflows, low base flow. The combination of these phenomena is special for each subject of the Russian Federation. Each of the 85 subjects of Russia was assigned to one of nine clusters, depending on the combination of DHP types, which in different years caused material damage to the region [1].

The list of clusters, the combination of DHP types of which includes ice difficulties (ice jams and anchor ice dam, early ice formation), is given below in ranked order:

1. Cluster No. 3 (ice difficulties, high waters): 13 subjects (16 % of all subjects of the Russian Federation),

2. Cluster No. 4 (ice difficulties, high waters, low base flow): 8 subjects (9.9 % of all subjects of the Russian Federation),

3. Cluster No. 1 (ice difficulties, high waters, mudflows, low base flow): 3 subjects (3.7 % of all subjects of the Russian Federation),

4. Cluster No. 2 (ice difficulties, high waters, mudflows): 2 subjects (2.5 % of all subjects of the Russian Federation).

The lists of subjects of the Russian Federation corresponding to each of the clusters No. 3, 4, 1 and 2 are shown in Table 2.

In regions where two or more types of DHP are recorded, the frequency of their occurrence sometimes differs significantly. During the period under review from 1991 to 2019, some subjects of the Russian Federation could bear material losses from high waters, and others could suffer from ice difficulties, etc. Therefore, within clusters No. 3, 4, 1 and 2, a more detailed typing of subjects was carried out according to the share of DHP of each type in their total number.

The division of subjects of the Russian Federation into groups within these clusters was performed by means of cluster analysis in the STATISTICA program using the K-means method and grouping at constant intervals. The results of clustering are shown in Table 2.

Table 2. Clustering of Subjects of the Russian Federation within clusters by DHP frequency of each type.

% DHP case ratio	Subjects of the Russian Federation within each dedicated cluster
Cluster No. 3 (ice difficulties / high waters)	
10% / 90%	Omsk Region, Penza Region, Primorsky Krai, Ulyanovsk Region
30% / 70%	Leningrad Region, Murmansk Oblast, Nenets Autonomous Okrug, Orenburg Oblast, Pskov Oblast, Republic of Tatarstan
47% / 53%	Arkhangelsk Region, Ivanovo Region, Republic of Khakassia
Cluster No. 4 (ice difficulties / high water / low baseflow)	
42% / 57% / 1%	Krasnoyarsk Krai, Republic of Sakha (Yakutia)
10% / 40% / 50%	Novosibirsk Region, Tomsk Oblast
10% / 75% / 15%	Amur Region, Kemerovo Region, Tyumen Region, Khabarovsk Territory
Cluster No. 1 (ice difficulties / high waters / mudflow / low baseflow)	
20% / 75% /2%/ 3%	Altai Republic
24% / 70%/5%/1%	Altai Krai
5% / 50%/35%/10%	Krasnodar Krai
Cluster No. 2 (ice difficulties / high waters / mudflows)	
25% / 70% / 5%	Zabaykalsky Krai (Trans-Baikal Territory)
10% / 70% / 20%	Republic of Dagestan

Within each cluster, depending on the share of DHP of each type, the subjects of the Russian Federation were also divided into groups. For example, cluster No. 3 unites regions for which material damage was caused by such types of DHP as ice difficulties and high waters. In the Omsk, Penza and Ulyanovsk regions, as well as the Primorsky Krai, on average, only 10% of all cases of the recorded material damage were caused by ice difficulties, the remaining 90% of cases were due to high waters and floods. In addition, in cluster No. 4, which unites other subjects of the Russian Federation, material damage was caused by such types of DHP as ice difficulties, high waters and low baseflow. For example, in the Novosibirsk and Tomsk regions, on average, 10% of all cases of the recorded material damage was caused by ice difficulties, 40% were due to high waters and floods, and 50% were due to low baseflow. In the Krasnoyarsk Territory and the Republic of Sakha (Yakutia), an average of 42% of all cases of recorded material damage was caused by ice difficulties, 57% of cases were freshets and floods, and the remaining 1% of cases were caused by low baseflow.

The use of cluster analysis methods made it possible to zone the territory of Russia according to the predominant types of DHP (including ice) and to assess the degree of exposure of the subjects of the Russian Federation to their impact. The information obtained makes it possible to assess the territorial risks caused by DHP and to timely identify negative processes. The possible manifestation of that may affect the occurrence and development of emergency situations in water bodies and adjacent territories. Floods, freshets and ice difficulties (congestion and anchor ice dam) cause material damage in a significant part of the subjects of the Russian Federation. Therefore, the organization of monitoring of these DHP on the territory of Russia is a priority.

3.3. Assessment of the factors that influenced the occurrence of ice jam and the development of winter flooding in the regulated section of the river

On the longitudinal profile (Figure 3) of the Nizhny Novgorod Reservoir [4], a 50-kilometer "rapid" section of the channel near Nekrasovskoye village on the river section from Yaroslavl to Kostroma is visible. In addition, it is on this section of the Volga River that large morphometric obstacles are located: several islands, narrowings and turns of the channel. It is obvious that these morphometric barriers have led to the restriction of the living section and the formation of slush in some areas in this part of the reservoir. The combination of unfavorable morphological conditions, the alternation of strong thaws and significant cold snaps, unstable ice and short-term winter ice drift in an exceptionally ice jams area in the zone of wedging the water level of the Nizhny Novgorod Reservoir in the area of Mininsky Island have led to the formation of an ice jam above Nekrasovskoye village. The formation of ice jam caused a significant narrowing of the live section of the flow, but at the same time the decrease in capacity in this section of the channel (taking into account the additional rise in the water level above the ice jam) did not exceed 30–40%, and an ice survey of ice jam was not carried out.

A decisive role in the formation of ice jams in the river section of the Nizhny Novgorod Reservoir both in 2020 and in 2007 was played by the factor of insufficient ice and water capacity of the channel associated with the morphological features of the Volga River section. The time of formation of ice jams both in February 2020 and in January 2007 clearly coincided with the periods of significant fluctuations of tail-water volume at the Rybinsk hydroelectric complex with their overall significant growth. In both cases, during the formation of ice jams, the water level at the dam of the hydroelectric complex of the Nizhny Novgorod Reservoir was discharged by more than 0.3–0.35 m due to a corresponding increase in discharge costs at the Nizhny Novgorod hydroelectric complex.

This once again confirms the extremely negative impact of the water level in the reservoir before the flood on the conditions and the possibility of ice jams on the regulated section of the river above the hydraulic complexes.

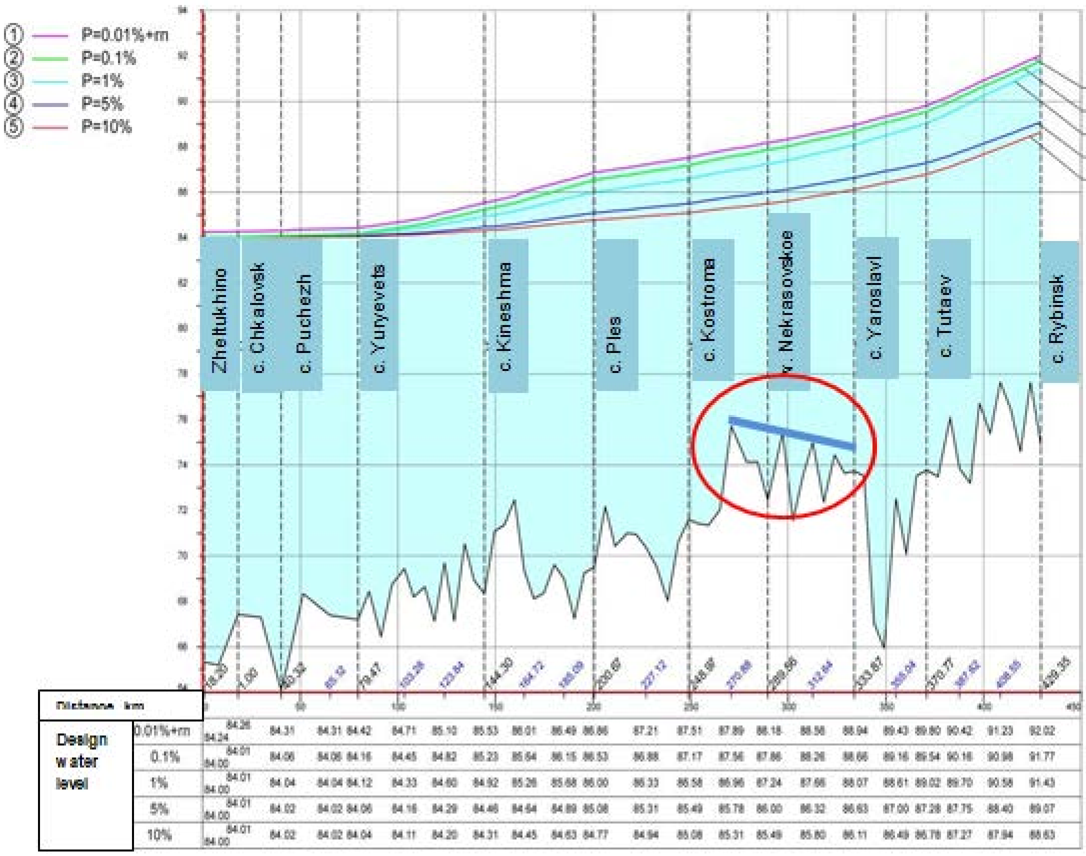

Figure 3. Calculated curves of the free surface of the Nizhny Novgorod Reservoir on a congestion-prone section of the Volga River 1, 2, 3, 4, 5 – water levels (m) for years of different probability of exceeding [4].

The magnitude of the maximum rise in ice dam levels in the Volga River near Yaroslavl in 2020 exceeded the maximum of 2007 by almost 1 m with even slightly smaller fluctuations in discharges from the Rybinsk reservoir. Under very similar weather and hydro meteorological conditions, in both cases, the main difference was the "lower background" of water levels in the upper stream near the dam of the Nizhny Novgorod hydroelectric complex (in 2020 in January-February they were 0.8 m lower than in 2007). Therefore, when establishing the operating modes of reservoirs, special account should be taken of the emerging water management and hydro meteorological situation, taking into account the analysis of observations of hazardous hydrological phenomena on the water body. The results of the study were used to substantiate the modes of operation of the reservoirs of the Volga-Kama cascade of hydraulic complexes and the development of a new edition of the regulations for the use of water resources of reservoirs.

3.4. Modeling of river flow in the bridge area under conditions of ice jam formation

The hydrodynamics of the streams was taken into account by additional friction on the inner surface of the ice cover. For tangential stresses on a free surface, a quadratic dependence on the average depth of the flow velocity with Manning roughness coefficients ***n*** was assumed. At the same time, the influence of wind was not taken into account, since the free surface of the water was shielded by ice. The problem of the vertical velocity profile in the subglacial stream was not considered, since it is not significant for determining water levels in ice jam floods.

Full-scale measurements of real currents showed that additional roughness coefficients from the presence of ice on the surface of the flow have values from 0.02−0.03 for the average winter period to 0.03−0.06 or more in the presence of ice jam during the flood period [34, 35]. In the calculations, the total roughness coefficient for the area with ice jam was taken to be equal to 0.05.

A digital elevation model (DEM) of the Volga River bed above and below the gate of the bridge crossing was constructed (Figure 4). Calculations of water levels and flow rates in the conditions of the ice jam formed along the entire width of the channel with an ice thickness of 0.73 m (with the probability of exceeding 10% and obtained from field measurements in early March 2021) were performed by means of the STREAM 2D CUDA software package development of NPP Aquarius Analytic LLC [33]. For numerical simulation in the computational domain, a hybrid grid of a triangular-quadrangular structure (63 thousand cells) was used.

In the calculations, the ice jam was located above the gate of the bridge crossing the entire width of the river at a distance of 6 km upstream. According to hydrological surveys, at water flows of 29800 m^3/s and 30200 m^3/s, the water levels in the gate of the bridge crossing were equal to 54.16 m and 54.34 m (during the ice age), respectively. At the same time, the slope of the water surface in the area above the bridge without ice is 3 cm/km (I = 0.00003), and taking into account the stable ice (ice jam is located above the bridge) – 6.7 cm/km (I = 0.000067), i.e. increases by more than 2 times. The depth of the flow along the line of the main fairway at such levels reaches 18–19 m, and in the shallow water zone is 5–6 m Fig.4.

The calculations taking into account ice phenomena for the conditions of spring 2021 have shown that the temporary structures that existed at that time practically do not affect the hydrodynamic characteristics of the flow and the ice itself cannot have a strong negative impact on them.

Forecast calculations of ice phenomena for the conditions of spring 2022, when the temporary bridge will be fully operational, can lead to a long ice jam (up to 10 km long). However, the ice cutters provided for the temporary bridge, according to the assessment, should cope with the regulatory load. With an ice jam length of 7.5 km, they should start cutting the ice floes.

The ice load on the supports of a permanent bridge during the period of the temporary bridge preservation can reach 60 Tf per support due to the effect of ice jam, in addition, a shock effect from floating single ice floes is possible (the strongest is in the deep-water part of the fairway, where speed reaches 2 m/s). These issues require further special studies and observations.

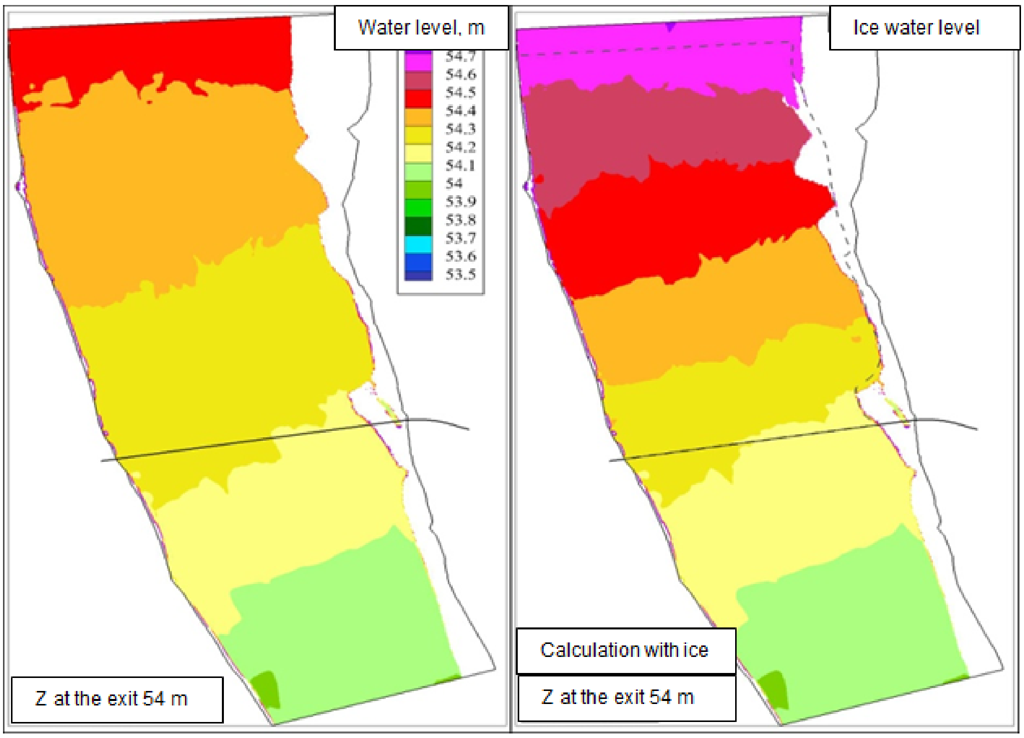

a) b)

Figure 4. Comparison of water levels calculated at Q=30000 m^3/s (a – without ice, b – with ice) with the water level at the output boundary of 54 m (dash line – ice boundary, solid line – gate of the bridge crossing).

4. Conclusion

In the context of climate change and the ice regime of water bodies as a result of human economic activity, the methods of forecasting ice phenomena are being transformed, which are mainly based on statistical dependencies established according to hydro meteorological observations.

The results of continuous monitoring of ice and hydrological regimes are important for timely forecasting, taking preventive measures and assessing the consequences of the impact of ice hazards on water bodies.

Russian territories were clustered by the genesis of ice phenomena and types of dangerous hydrological processes with recorded material damage, obtained using the cluster analysis method. Ensuring counteraction to technogenic and natural threats on water bodies, the developed information resource can be used in determining regional lists and criteria for dangerous ice hydrological phenomena, collecting information about the threat, possible consequences and monitoring of such processes. The results of qualitative and quantitative analysis can be used to collect information on the consequences of exposure and monitoring of ice hazards, as well as to provide public authorities and other organizations with factual and predictive data on hydrological hazards in the whole country and on the territory of the subjects of the Russian Federation. In addition, the results of the study can be used to substantiate the modes of operation of reservoirs of hydraulic complexes (cascades of hydraulic systems) and the development of regulations for the use of water resources.

Modern trends in the development of mathematical modeling of the processes of ice jam formation, transporting ability of sub glacial flows in sections of rivers with engineering structures are associated with a combination of hydrodynamic models, models of river flow formation and the functioning of water management systems.

References

1. Kozlov, D.V., Snezhko, V.L., Lagutina N.V. Hydrological hazards on the territory of the Russian Federation: multidimensional analysis and zoning. Meteorology and Hydrology. 2021. 10. Pp. 66–75. DOI: 10.52002/0130-2906-2021-10-66-75 (rus)
2. State report. On the state and use of water resources of the Russian Federation in 2020. Moscow: Rosvodresursy, NIA-Priroda, 2022. 510 p. (rus)
3. Agafonova, S.A., Frolova, N.L. Specific features of ice regime in rivers of the Northern Dvina basin. Water resources. 2007. 34(2). Pp. 141–149. (rus)
4. Bednaruk, S.E., Kozlov, D.V. Causes and consequences of the flood-prone ice situation below the Rybinsk hydroelectric power station. Environmental Engineering. 2020. 2. Pp. 81–98. DOI: 10.26897/1997-6011/2020-2-81-98 (rus)
5. Kozlov, D.V., Kuleshov, S.L. Multidimensional data analysis in the assessment of ice-jam formation in river basins. Water resources. 2019. 46. Pp. 132–141. DOI: 10.31857/S0321-0596462132-141 (rus)
6. Buzin, V.A. Zazhory i zatory l'da na rekakh Rossii [Congestion and ice jams on the rivers of Russia]. St. Petersburg: Publishing House of the State Hydrological Institute. 2016. 242 p. (rus)
7. Mokhov, I.I. Contemporary climate changes in the Arctic. Vestnik Rossiiskoi Akademii Nauk. 2015. 85(5-6). Pp. 478–484. DOI: 10.1134/S1019331615030168
8. Krasilnikova, V.V. Analysis of inter-annual variability of surface air temperature in the Dvina Bay of the White sea for the period 1915–2015. Hydrometeorological research and forecasting. 2018. 2(368). Pp. 110–119. (rus)
9. Agafonova, S.A., Frolova, N.L., Vasilenko, A.N., Shirokova, V.A. Ice regime and dangerous hydrological phenomena on rivers of the Arctic zone of European Russia. Vestnik Moskovskogo universiteta. Seriya 5, Geografiya. 2016. 6. Pp. 41–49.
10. Grishchenko, I.V. Characteristics of ice processes in the Northern Dvina river estuary and their development trends in a changing climate. Vestnik of Northern (Arctic) Federal University. 2016. 1. Pp. 5–11. DOI: 10.17238/issn2227-6572.2016.1.5
11. Borisenkov, E.P., Pasetsky, V.M. Ekstremal'nyye prirodnyye yavleniya v russkikh letopisyakh XI-XVII vv. [Extreme natural phenomena in Russian chronicles of the XI-XVII centuries]. Leningrad: Gidrometeoizdat, 1983. 240 p. (rus)
12. Magritsky, D.V., Skripnik, E.N. Hydrological hazards in the mouth of the Northern Dvina and the causes of their long-term changes. Vestnik Moskovskogo universiteta. Seriya 5, Geografiya. 2016. 6. Pp. 59–70.
13. Busin, M.V., Varfolomeev, A.Yu., Markov, Yu.V., Popov, A.N. Effect of flooding on state buildings in Arkhangelsk. Arctic and North. 2011. 3. Pp. 169–180. (rus)
14. Mikhailov, V.N. Ust'ya rek Rossii i sopredel'nykh stran: proshloye, nastoyashcheye i budushcheye [Estuaries of the rivers of Russia and adjacent countries: past, present, and future]. Moscow: GEOS, 1977. 413 p. (rus)
15. Gladkevich, G.I., Tersky, P.N., Frolova, N.L. Assesment of inundation hazard on the territory of the Russian Federation. Water Sector of Russia: Problems, Technologies, Management. 2012. 2. Pp. 29–46.
16. Taratunin, A.A. Navodneniya na territorii Rossiyskoy Federatsii [Floods on the territory of the Russian Federation]. Russian Research Institute for Integrated Use and Protection of Water Resources (RosNIIVKh), 2008. 432 p. (rus)
17. Abdullin, R.K., Shikhov, A.N. Synthetic mapping of hazardous meteorological phenomena at the regional scale level. Geodesy and cartography = Geodezia i Kartografia. 2017. 78(8). Pp. 39-48. DOI: 10.22389/0016-7126-2017-926-8-39-48 (rus)
18. Alfieri, L, Thielen Del Pozo, J, Pappenberger, F. Ensemble hydro-meteorological simulation for flash flood early detection in southern Switzerland. Journal of Hydrology.2012. 424–425. Pp. 143–153. DOI: 10.1016/j.jhydrol.2011.12.038
19. Official website of the Federal Service for Hydrometeorology and Environmental Monitoring. Typical list of natural hazards 2022. [Online] URL: http://meteo.ru/data/310 (reference date: 11.04.2022). (rus)

20. Donchenko, R.V. Ledovyy rezhim rek SSSR [Ice regime of the rivers of the USSR]. Leningrad:.Gidrometeoizdat, 1987. 242 p. (rus)
21. Gotlieb, Y.L., Donchenko, R.V., Pekhovich, A.I., Sokolov, I.N. Led v vodookhrannykh lishchakh i biologicheskikh infektsiyakh GES [Ice in reservoirs and lower streams of hydroelectric power plants]. Leningrad: Gidrometeoizdat, 1983. 200 p. (rus)
22. Ashton, G.D. (ed.). River and lake ice engineering. Littleton, Colorado, U.S.A.: Water Resources Publications, 1986. 485 p.
23. Buzin, V.A., Zinoviev, A.T. Ledovyye protsessy i yavleniya na rekakh i vodokhranilishchakh: metody matematicheskogo modelirovaniya i opyt realizatsii dlya prakticheskikh tseley (obzor sovremennykh sostoyaniy sostoyaniya) [Ice processes and phenomena on rivers and reservoirs. Methods of mathematical modeling and experience of their implementation for practical purposes (review of the current state of the problem)]. Barnaul: IVEP (IVEP) of Russian Academy of Sciences, Siberian brunch, 2009. 169 p. (rus)
24. Debolskaya, E.I. Mathematical models of ice jams and their consequences. RUDN University. 2014. 131 p.
25. Shen, H. Mathematical modeling of river ice processes. Cold Regions Science and Technology. 2010. 62(1). Pp. 3–13. DOI: 10.1016/j.coldregions.2010.02.007
26. Wang, J., Shi, F., Chen, P., Wu P., Sui, J. Simulations of ice jam thickness distribution in the transverse direction. Journal of Hydrodynamics. 2014. 26. Pp. 762–769. DOI: 10.1016/S1001-6058(14)60085-8
27. Kozlov, D.V., Buzin, V.A., Frolova, N.L., Agafonova, S.A., Baburin, V.L., Banshchikova, L.S., Goroshkova, N.I., Zavadskiy, A.S., Krylenko, I.N., Savel'yev, K.L., Kozlov, K.D., Buzina, L.F. Opasnyye ledovyye yavleniya na rekakh i vodokhranilishchakh Rossii [Dangerous ice phenomena on rivers and reservoirs of Russia]. Moscow: RGAU-MSKhA named after K.A. Timiryazev, 2015. 348 p. (rus)
28. Healy, D., Hicks, F. Experimental study of ice jam thickening under dynamic flow conditions. Journal of Cold Regions Engineering. 2007. 21(3). Pp. 72–91. DOI: 10.1061/(ASCE)0887-381X(2007)21:3(72)
29. Pahlavan, H., Clark, S., Wang, M., Malenchak, J. An experimental investigation of turbulent flow characteristics beneath an ice. Manitoba, Canada, 2016. 135 p.
30. Carson, R., Beltaos, S., Groeneveld, J., Healy, D., She, Y., Malenchak, J., Morris, M., Saucet, J.-P., Kolerski T., Shen H. Comparative testing of numerical models of river ice jams. Canadian Journal of Civil Engineering. 2011. 38(2). Pp. 669–678. DOI: 10.1139/l11-036
31. Tarasov, A.S. Modeling of ice dams in riverbeds (overview). Ice and Snow. 2020. 60(1). Pp. 121–133. DOI: 10.31857/S2076673420010028.
32. Metodicheskiye rekomendatsii po otsenke odnorodnosti gidrologicheskikh kharakteristik i ikh raschetnykh pokazateley po neodnorodnym dannym [Guidelines for assessing the homogeneity of hydrological characteristics and determining their calculated values from heterogeneous data]. St.Petersburg: Nestor-Istoriya. 2010. 162p.
33. Aleksyuk, A.I., Belikov, V.V. Simulation of shallow water flows with shoaling areas and bottom discontinuities. Computational Mathematics and Mathematical Physics. 2017. 57. Pp. 318–339. DOI: 10.1134/S0965542517020026
34. Krylenko, I., Alabyan, A., Aleksyuk, A., Belikov, V., Sazonov, A., Zavyalova, E., Pimanov, I., Potryasaev, S., Zelentsov, V. Modeling ice-jam floods in the frameworks of an intelligent system for river monitoring. Water Resources and the Regime of Water Bodies. 2020. 47. Pp. 387–398. DOI: 10.1134/S0097807820030069
35. Frolova, N.L., Agafonova, S.A., Belikov, V.V., Krylenko, I.N., Golovlev, P.P. Zatornyye navodneniya v rayone g.Tomska: geneticheskiy analiz i modelirovaniye [Jam floods near the city of Tomsk: genetic analysis and modeling]. Ledovyye i termicheskiye protsessy na vodnykh ob"yektakh Rossii: nauchnyye trudy IV Vserossiyskoy konferentsii [Ice and thermal processes in water bodies of Russia: proceedings of the IV All-Russian Conference]. 2013. Pp. 180–186. (rus)

Information about authors:

Dmitry Kozlov, *Doctor of Technical Sciences*
ORCID: https://orcid.org/0000-0002-9440-0341
E-mail: kozlovdv@mail.ru

Nazira Dzhumagulova, *PhD in Technical Sciences*
ORCID: https://orcid.org/0000-0002-0586-9464
E-mail: dnazira@rambler.ru

Received 11.04.2022. Approved after reviewing 08.06.2023. Accepted 13.06.2023.

Magazine of Civil Engineering

ISSN 2712-8172

journal homepage: http://engstroy.spbstu.ru/

Research article

UDC 624.15

DOI: 10.34910/MCE.120.2

Influence of industrial wastes and lime on strength characteristics of clayey soil

A. Bhardwaj* ✉, *R.K. Sharma

National Institute of Technology, Hamirpur, India

✉ *avinash@nith.ac.in*

Keywords: soil stabilization, additives, binders, stress-strain curves, scanning electron microscopy, environmental Impact, recycling

Abstract. The stress-strain and volumetric behavior, shear strength parameters, permeability and stiffness of soft clayey soil stabilised with various proportions of molasses, waste foundry sand, and lime are investigated in this article using the variable head permeability test and consolidated drained triaxial test. The results of the tests showed that the permeability, stress-strain and volumetric behavior of the soft clayey soil were significantly enhanced by the addition of molasses, waste foundry sand, and lime. At all confining pressures, the volumetric strain was found to decrease with the inclusion of additives. The additives to soft clayey soil reduced cohesion to a limited extent whereas significantly increasing the angle of shearing resistance. Furthermore, scanning electron microscope (SEM) images of all the optimum composites demonstrate that with the additives, a composite with higher strength and density is observed, and the geotechnical properties of soft clayey soil are improved, thereby making it suitable as a subgrade material in pavement construction.

Citation: Bhardwaj, A., Sharma, R.K. Influence of industrial wastes and lime on strength characteristics of clayey soil. Magazine of Civil Engineering. 2023. 120(4). Article No. 12002. DOI: 10.34910/MCE.120.2

1. Introduction

Expansive soil is a type of clayey soil that is prone to large volumetric variations caused by changes in water content. As expansive soils act differently than other types of soil, geotechnical engineers in particular have obstacles when working with them. Structures that are constructed on them are susceptible to damage as a result of their tendency to swell and shrink. Damage caused by swelling and shrinking behaviour of expansive soils owing to moisture fluctuations costs billions of dollars worldwide [1, 2]. Disruption caused by weak expansive soil is most evident on structures that are lightly stressed, such as single or double-story buildings, canal linings, earth retaining structures, pavements, etc.Soil stabilization is the technique of improving the engineering and index properties of poor soils [3, 4]. It is particularly of immense importance in civil engineering as it increases the shear strength of the soil and fulfils essential geotechnical requirements under specific environment. Efforts have been made in the past to stabilise expansive soils using a variety of materials such as molasses, waste foundry sand (WFS), construction demolition waste, cement, lime, polyurethane resin, and glass waste etc. [5–13]. It was observed that strength of expansive soil enhanced with the help of using these materials.

An enzyme is a biological system product that accelerates the chemical reactions in the cells by catalysis. Enzymes are hydrophilic organic catalysts that promote extremely particular chemical reactions under favourable circumstances [14]. According to a number of investigations, enzyme-based stabilisers result in maintenance-free roads with increased bearing capacity (UCS, CBR, and resilient modulus) [15–19]. The addition of molasses to sodic clay and soft murum soil modified structural strength of soil and proved to be economical in road construction [20]. The plasticity of the composite was reduced from 53 % to 19 % when 4 % molasses was added to the soil cement blend, and the CBR value was raised from 1 %

to 64 %. Lab tests conducted on mixtures of clayey soil and bio-enzyme revealed that the CBR value of the clayey soil was increased by 5–10 % in the presence of the bio-enzyme, compared to the CBR value of the untreated soil [21]. The unconfined compressive strength of kaolin clay increased from about 1.42 MPa to 2.04 MPa for samples with 0.1 wt% of fibres and 2.0 wt% molasses with respect to the dry weight of the soil [22].

The rapid development of industry has resulted in the production of a massive amount of waste, both solid and liquid. These wastes are often dumped on land or released into water bodies, without sufficient treatment, despite the fact that pollution control measures are required, and as a result they represent a significant source of environmental pollution and health hazard. High-quality silica sand, known as waste foundry sand (WFS) is a byproduct of the ferrous and non-ferrous metal casting industries. Because of its high thermal conductivity, it has been used for decades as a casting material for making moulds. The waste foundry sand is usually thrown away when the casting process is complete [23]. Every year, India produces nearly 1.8 million tonnes of waste foundry sands. More than 60 million tonnes of WFS were produced worldwide in 2016 and much of it was deposited in landfills [24]. The waste disposal problem of WFS might be overcome, and the environment would benefit, if it were utilized to stabilize expansive soils. Efforts to utilize WFS as a construction material have been increased significantly in recent years [25–29]. Standard proctor and CBR tests performed on combinations of lime, WFS, molasses, clayey soil and concluded that at 20 % WFS the CBR value of clayey soil was found to be the highest when compared with the other percentages of WFS used in the study [30]. Waste foundry sand materials (samples) from ten different industries were collected and investigated for use in road construction and as a structural fill. It was concluded that the finer sample may be used for the construction of the subbase layer of pavement [31].

The stabilization of clayey soil by the addition of lime is a method that is widely utilized across the globe to increase its suitability for construction. Lime is the oldest traditional stabilizer used for soil stabilization [32]. The term "lime stabilization" refers to the process of improving the quality of the soil by the incorporation of burned limestone products, such as calcium oxide (CaO) or calcium hydroxide (Ca $(OH)^2$). Lime stabilization is used to strengthen sub-bases and subgrades in roads, to build railroads and airports, embankments, to exchange soil in unstable slopes, to backfill bridge abutments and retaining walls, to line canals, to enhance the soil under foundation slabs, and to make lime piles [33, 34]. Stabilization of the expansive soil with 6 % lime decreased soil swelling without increasing soil pressure [35]. Eastern Croatian clay soils were combined with lime, and the results demonstrated an improvement in the geotechnical properties of the clays [36]. The unconfined compressive strength (UCS) and small-strain dynamic characteristics of lime- and water-stabilized soft clay specimens revealed that increasing the lime concentration up to 10 % resulted in increasing the shear wave velocity (Vs), shear modulus (Gmax) and UCS values [37].

It has become clear from reviewing the existing research that using molasses and WFS individually in soil stabilization not only enhanced the geotechnical properties of clayey soils, but also proved to be environmentally friendly by resolving WFS disposal issues. Strength characteristics of composites and the shear response of clayey soils were significantly enhanced by the separate addition of molasses, WFS, and lime.

However, the shear response of clayey soil blended with molasses (M), waste foundry sand (WFS), and lime (L) in combination with each other has been understudied in the past. In the present study, a set of permeability tests and consolidated drained triaxial tests was carried out on clayey soil stabilized with molasses, WFS, and lime separately and in combination. The effect of adding different amounts of additives to clayey soil on deviator stress was examined. In addition, the strength ratio and stiffness of stabilized soil at different strain levels were compared with those of unstabilized soil.

2. Materials and Methods

The soil samples were takenfrom the side of NH-88 (Kangra-Shimla route) near the Jukhala village in the Bilaspur district of Himachal Pradesh, India. After sample collection in airtight bags, samples were transported to the laboratory. The soil samples were pulverized in the pulverizing machine after drying. Then they were sealed again in air-tight bags to avoid any variation in moisture content. The soil was classified as clayey soil of high plasticity (CH) according to Unified Soil Classification System (USCS). Tables 1 and 2 present the geotechnical characteristics and mineral composition of the soft clayey soil investigated in the research.

Molasses used in the study was obtained from Budhewal Co-Operative Sugar Mill Ltd., located in the Punjab region of Ludhiana. Table 3 shows the chemical characteristics of molasses. The waste foundry sand used in this work is a recycling waste from Shakti Foundries in Ludhiana (Punjab). WFS has a dark colour and a sandy texture due to the angular shape of the waste particles and the fines adhering to the sand particles. Dry sieve analysis in accordance with ASTM D6913-04 gave the gradation curve for WFS.

The effective size (D10), coefficient of curvature (Cc) and coefficient of uniformity (Cu) for the sand are 0.14 mm, 0.89 and 1.44 respectively, indicating that WFS is poorly graded in nature, with the majority of the particles falling into the fine sand range. Fig. 1 displays the particle-size distribution curve of the sand used in this study. The various geotechnical and chemical properties of WFS were tabulated in Tables 4 and 5. The powdered lime utilized in this investigation was purchased from a hardware store in Hamirpur, Himachal Pradesh. The chemical composition of lime is presented in Table 6.

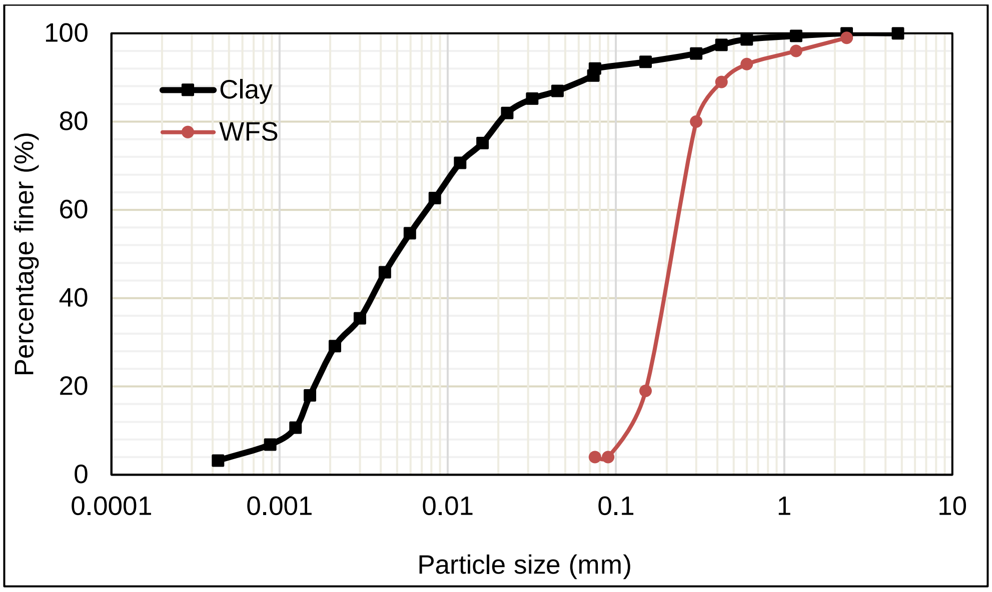

Figure 1. Particle size curve for soft clayey soil and WFS.

According to American society for testing and materials (ASTM) standards, grain size analysis (ASTM D6913-04, ASTM D422-63), pH (ASTM D4972-18), Atterberg limits (ASTM D4318-10), permeability (ASTM D5084-03), and consolidated drained (CD) triaxial compression tests (ASTM D7181-11) were performed on soft clayey soil, clay-molasses mix, clay-WFS mix, clay-lime mix, clay-molasses-WFS-lime mix, clay-molasses-lime mix, and clay-molasses-WFS-lime mix.

Using two 100 ml cylindrical beakers, one with distilled water and the other with 30 gm of soil mixed in 75 ml of distilled water, the pH of soft clayey soil alone and soil combined with varied amounts of molasses, WFS, and lime were tested in the lab. Soil and distilled water were combined and stirred every 15 minutes for an hour, following which the pH was recorded using an electronic pH metre inserted in the beaker. The laboratory tests confirmed that Atterberg limits of the soft clayey soil and stabilized soil conformed to standards. The samples used to determine the liquid limit and plastic limit were screened using a 0.425 mm sieve. The liquid limit of the sample is the water content corresponding to 25 blows determined using Casagrande test apparatus and plastic limit is the moisture content at which soil begins to crumble when rolled into a 3 mm diameter thread using a ground glass plate. The plasticity index of the soil is the numerical difference between the liquid and plastic limits.

To investigate the drainage properties of soft clayey soil and different composites of unstabilized and stabilized clayey soil a variable head permeability test was performed. A mould with a diameter of 100 mm and a height of 125 mm was used to conduct the variable head permeability test, and the sample was compacted in three layers at maximum dry density equal to optimum moisture content using 25 blows at each layer. The samples were soaked after preparation until water constantly came out of the mould. The starting and final heads were recorded, as well as the time it took for the heads to decrease, keeping the head difference constant. The triaxial tests were performed in a Perspex cell on 76×38 mm cylindrical materials compacted to the maximum dry density at optimum moisture content. The consolidated drained triaxial test was carried out in two stages: first, the sample was placed in the triaxial cell, confining pressure was applied, and drainage was allowed; secondly, an additional axial stress (also known as deviator stress) was applied, allowing drainage to occur, resulting in shear stresses in the sample. The sample was subjected to increasing axial stress until it failed. Applied stresses, axial strain, and sample volume change were all monitored during both phases.

Table 1. Geotechnical properties of clayey soil.

Soilproperties	Value
Soil type	CH
Liquid limit	55%
Plastic limit	20%
Plasticity index	35%
Specific gravity	2.6
Differential free swell index	35%
Optimum moisture content	16.5%

Table 2. Mineral composition of clayey soil.

Mineralcomposition	Content (%)
Oxygen, O	45.4
Silicon, Si	18.5
Aluminium, Al	8.69
Carbon, C	10.9
Iron, Fe	1.42
Potassium, K	1.86
Magnesium, Mg	2.30
Titanium, Ti	2.51

Table 3. Chemical properties of molasses used.

Constituents	Result
Color	Black
Brix	83.2
pH (1:1 at 20 ºC)	5.6
Specific Gravity	1.39
Viscosity	17500 mPa-s
Moisture	21.76%
Total sugar	47.83%
Invert sugar	10.20%
Sulphated sugar	15.50%
Ca	1.63%

Table 4. Geotechnical properties of WFS.

Property	Value
Specific Gravity	2.64
Optimum moisture content	8.20 %
Maximum dry density	1.59 g/cc

Table 5. Chemical properties of WFS.

Chemical composition	Percentage
SiO_2	84.90
Al_2O_3	5.21
Fe_2O_3	3.32
CaO	0.58
MgO	0.67
SO_3	0.29
MnO	0.08
TiO_2	0.19
K_2O	0.97
P_2O_5	0.05
Na_2O	0.50
Loss of ignition	2.87

Table 6. Chemical composition of lime used.

Chemicalcomposition	Content (%)
SiO_2	2.1
Al_2O_3	1.3
Fe_2O_3	1.2
CaO	82.8
MgO	0.3
SO_3	0.4
Na_2O	0.4
K_2O	-
C	2.2
$CaCO_3$	4.3
Impurities	5.0
Loss of ignition at 800°C	-

3. Results and Discussion

The following sections provide a summary of the effect of varying molasses, WFS, and lime percentages on pH, Atterberg limits, permeability, and shear strength parameters of soft clayey soils.

3.1. pH tests

The influence of molasses, WFS, and lime on soft clay pH is discussed in this section. pH of clayey soil treated with 5, 10, 15, and 20 % molasses was measured. Fig. 2 depicts the change in clay pH as a result of the addition of molasses. Soft clayey soil had a pH of 7.56, which was somewhat alkaline, whereas molasses had a pH of 5.8, which was slightly acidic. When molasses was added to soft clay, the pH of the composite decreased and reached neutral (pH = 7) at 10 % molasses concentration, and continued to drop as the molasses percentage was increasing. Molasses with a concentration of 10 % may be used for fixation in clay-molasses mixtures. Because molasses has a lower pH than soft clayey soil, it causes the pH of the mixture to drop when it is added [38].

Fig. 3 depicts the change in soft clay pH as a result of the addition of WFS (10, 20, 30, and 40 %). Soft clayey soil had a pH of 7.56, which was somewhat alkaline, whereas WFS had a pH of 6.42, which was slightly acidic. When WFS was added to soft clay, the pH of the composite decreased and reached neutral (pH = 7) at 20 % WFS concentration, and continued to drop as the WFS percentage was increasing. WFS with a concentration of 20 % may be used for fixation in clay-WFS mixtures. Because WFS has a lower pH than soft clayey soil, it causes the pH of the mixture to drop when it is added [39].

As shown in Fig. 4, the pH of the soft clay-lime mix rises as the lime concentration rises. The alkaline nature of lime causes a rise in pH with its addition. At 9% lime concentration in clay-lime combination, a maximum pH of 12.2 (pH of commercial lime employed in this research, which includes some impurities) was attained, suggesting that it might be utilized for soil stabilization. According to ASTM-C977, if the pH of the soil is 12.40 or above, the lowest proportion that yields a pH of 12.40 is the optimum lime concentration. When lime was added to soft clay, a reaction between the lime and the soil particles occurred, resulting in cation exchange up to a specific lime content, at which point the pH reached its maximum value, beyond which further lime dose had no effect on the pH value [40–42].

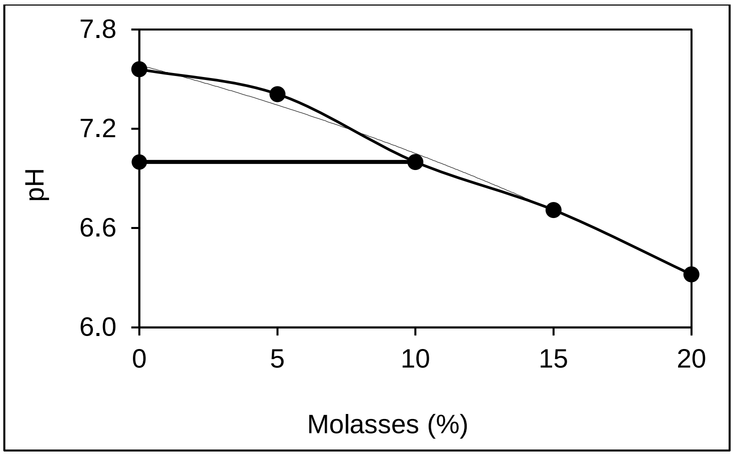

Figure 2. pH of clay-molasses mixes.

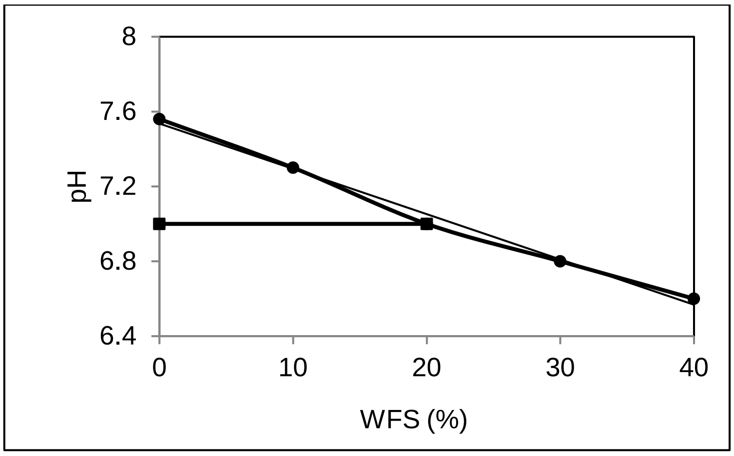

Figure 3. pH of clay-WFS mixes.

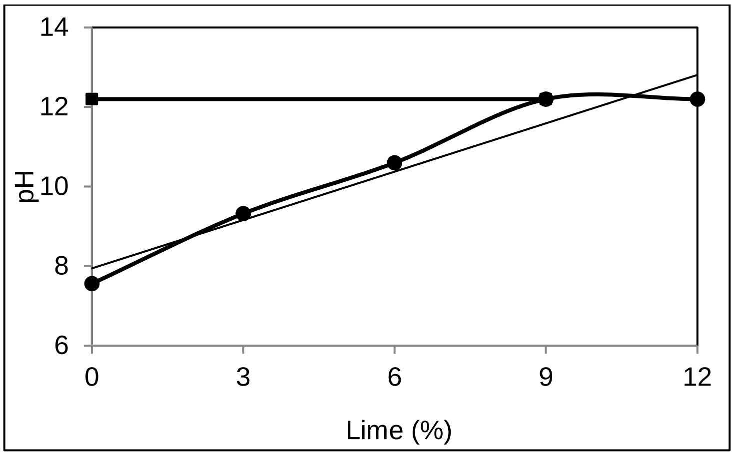

Figure 4. pH of clay-lime mixes.

3.2. Consistency limit tests

For soft clayey soil the liquid limit was 55 % and plastic limit was 20 % and from plasticity index chart it was observed that clayey soil can be categorized as CH (clay of high plasticity) (Fig. 5). Adding molasses (at 5 %, 10 %, 15 %, and 20 % concentrations) to soft clayey soil lowered the plasticity index (Ip) from 35 % to 21 %. Noteworthy, Ip value dropped more significantly when 10 % molasses was used compared to other percentages of WFS. The points of the curve in the plasticity index chart shifted from the high plastic (CH) zone to the intermediate plastic clay (CI) zone, as shown in Fig. 5. Similar trend was observed in the past by some researchers [6, 43]. The Ip in soft clayey soil was lowered from 35 % to 29 % after WFS (10, 20, 30, and 40 %) was added. It is worth noting that the percentage of WFS at which the Ip value dropped the most was 20 %. Fig. 5 shows a shift from the high plastic (CH) to the intermediate plastic clay (CI) region on the plasticity index chart. Similar trend was observed in the past by some researchers [39, 44]. The plasticity index (Ip) dropped from 35 % to 9 % with the addition of lime (3, 6, 9, and 12 %) to the soft clayey soil. It is important to note that the Ip value dropped significantly at 9 % lime compared to other lime concentrations. Variations in the plasticity index chart are depicted in Fig.5, where the points of the curve moved from the high plastic (CH) zone to the MI zone sufficiently below the A-line. Similar trend was observed in the past by some researchers [45, 46].

A combination of molasses and WFS reduced the Ip value of clayey soil to 17 %, by keeping molasses content constant at 10 % and varying the WFS content (10, 20, 30, and 40 %). Low plastic clay (CL) is represented by a variation in the plasticity index chart shown in Fig. 5. When WFS was added to soft clayey soil containing 10 % molasses and 10 % WFS, the plasticity index of the composite dropped, and it continued to drop considerably as higher percentages of WFS were added. As a result, the combination C: M: WFS:: 80: 10: 10 may be considered the optimum combination for soil stabilization from clay-molasses-WFS mix.

Plasticity index was reduced from 10 % to 3 % when soft clayey soil was treated with molasses and lime, by keeping molasses content at 10 % and varying lime content (3, 6, 9, and 12 %). The points of the plasticity index curve in Fig. 5 deviate from the standard chart by shifting to the MI region below the A-line. The plasticity index of the composite decreased when 6 % lime was added to clayey soil with 10 % molasses, followed by a considerable increase in the value of the Ip the next percentages of lime, suggesting that the combination C: M: L:: 84:10:6 is the optimal combination for soil stabilization from clay-molasses-lime mix.

Plasticity index value was reduced from 14 % to 8 % when WFS and lime were added to clayey soil, with WFS held constant at 20 % and varying lime content. The points of the plasticity index curve in Fig. 5 deviate from the plasticity index chart by shifting to the MI region below the A-line. The plasticity index of the composite decreased with the addition of lime 6 % to clayey soil containing 20 % WFS, followed by a considerable improvement in the value of the plasticity index for the subsequent percentages of lime, suggesting that the combination C: WFS: L:: 74:20:6 may be considered the optimum combination for soil stabilization from clay-WFS-lime mix.

Adding molasses, WFS, and lime to clayey soil lowered the Ip value down to 2 %, by keeping 10 % molasses, 20 % WFS constant, and varying lime content. The points of the curve in Fig.5 of the plasticity index chart shift to the ML region, which is sufficiently below the A-line. The plasticity index of the composite decreased with the addition of 3 % lime to clayey soil containing 10 % molasses and 20 % WFS, followed by a considerable increase in the value of the Ip for the next percentages of lime, suggesting that the combination C: M: WFS: L:: 67: 10: 20: 3 may be the optimum combination for soil stabilization from clay-molasses-WFS-lime mix.

From the above performed tests it was concluded that the geotechnical characteristics of soft clayey soil were improved significantly with the following proportions:

- 10 % molasses in clay-molasses mix;
- 20 % WFS in clay-WFS mix;
- 9 % lime in clay-lime mix;
- 10 % molasses and 10 % WFS in clay-molasses-WFS mix;
- 10 % molasses and 6 % lime in clay-molasses-lime mix;
- 20 % WFS and 6 % lime in clay-WFS-lime mix;
- and 10 % molasses, 20 % WFS and 3 % lime in clay-molasses-WFS-mix.

Hence all these mentioned combinations, considered optimum combinations, were further subjected to permeability test and consolidated drained triaxial tests.

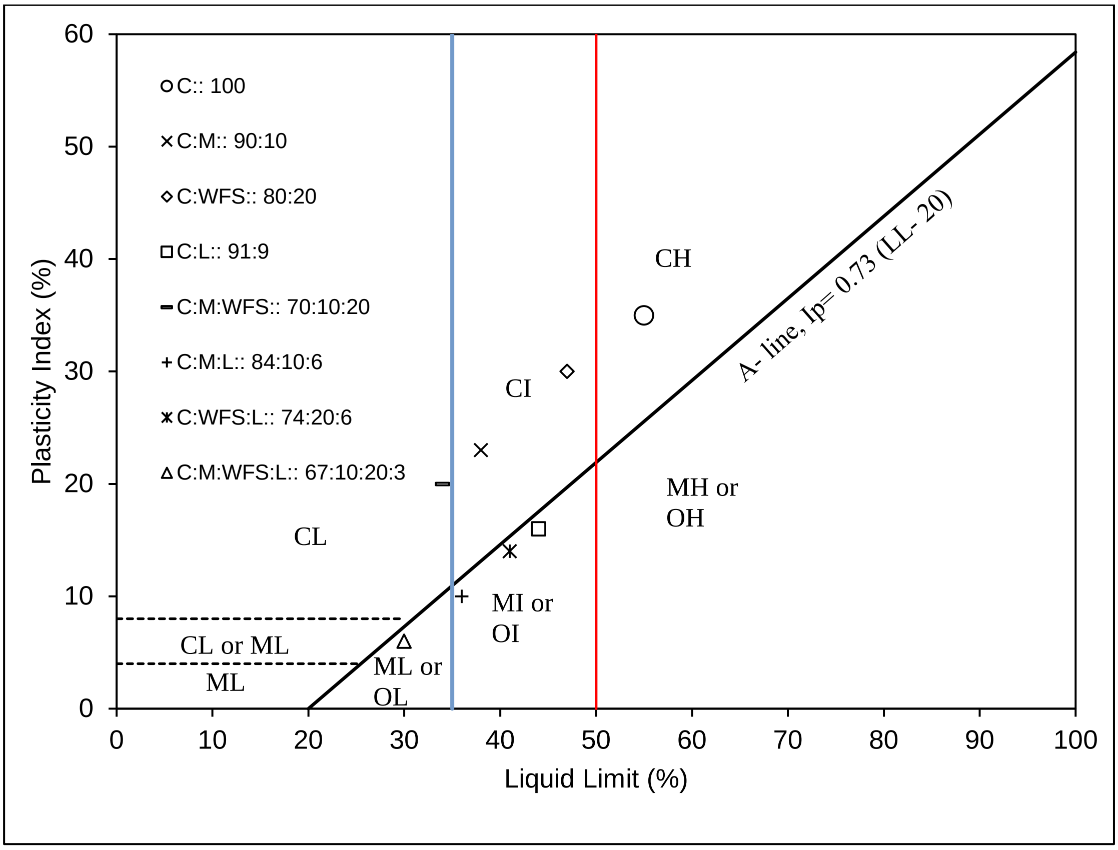

Figure 5. Plasticity index chart showing additives effect on classification of soft clayey soil.

3.3. Permeability tests

Permeability tests were conducted to assess the drainage characteristics of soft clayey soil alone and combined with optimum contents of molasses, WFS, and lime. The coefficient of permeability (k) of soft clayey soil was 3.4×10^{-8} cm/sec. On adding optimum percentage of molasses (10 %) individually the coefficient of permeability of soft clayey soil decreased and it increased with the addition of optimum percentages of WFS (20 %), and lime (9 %). Fig. 6 shows the coefficient of permeability values observed for soft clay and optimum combinations.

The addition of molasses to soft clayey soil caused an increase in the force of attraction between soil particles, which, in turn, reduced the amount of pore space between them resulting in a reduction of the soil permeability. The percentage of coarser particles in WFS was more than in clayey soil which may be the cause of the rise in permeability value of soft clayey soil after the addition of WFS. The pozzolanic interaction between lime and clay particles may be the cause of rise in permeability value observed after the addition of molasses and lime to clayey soil. Similar trend was observed in the past by some researchers [47, 48].

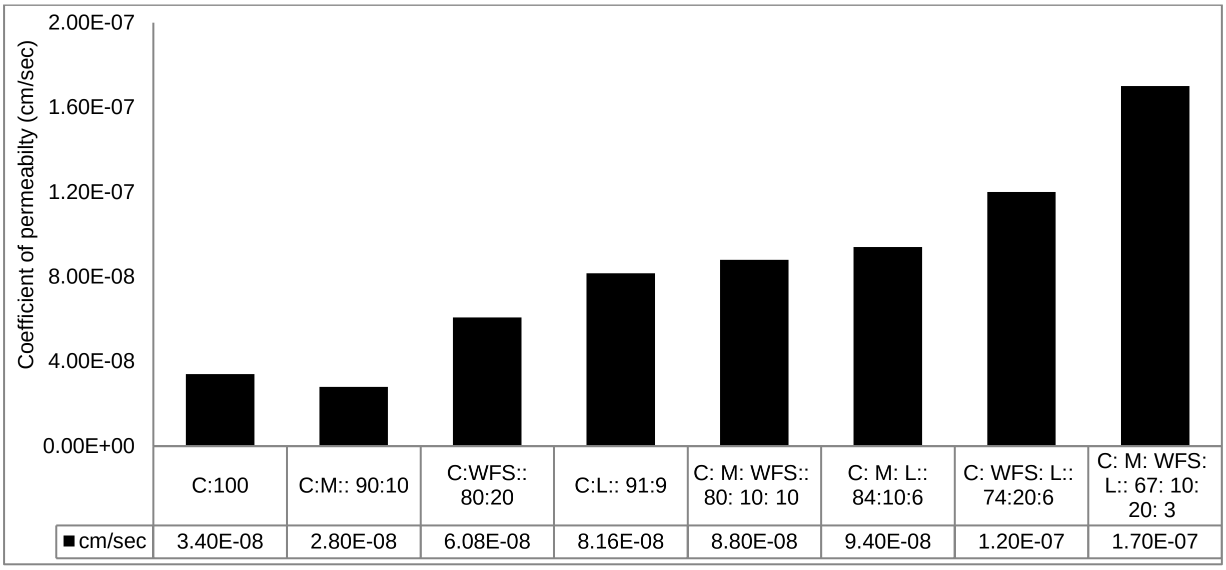

Figure 6. Permeability coefficient values of soft clay and optimum combinations.

3.4. Consolidated drained triaxial tests

3.4.1. Stress-strain curves from triaxial tests

Fig. 7–9 show typical stress–strain curves for soft clayey soil and optimum combinations of clayey soil blended with molasses, WFS, and lime at confining pressures of 49.03 kPa, 98.06 kPa, and 147.1 kPa, respectively. A significant increase in deviator stress was seen when clayey soil was stabilized using molasses, WFS, and lime, when compared to unstabilized clayey soil. With the addition of the optimum combination (C:M:WFS:L:: 67:9:20:3), the maximum deviator stress enhanced by 185 % for confining pressure of 49.03 kPa, 203 % for confining pressure of 98.06 kPa, and 179 % for confining pressure of 147.1 kPa. The deviator stress enhanced with increasing confining pressure for the samples stabilized with optimum percentages of additives (molasses, WFS, and lime), as shown in Fig. 10. The substantial impact of molasses, WFS, and lime as stabilizers occurred at high strain values, but at low strain (up to 2 %), the stabilization with these additives had no significant effect on the axial stress–strain behavior of the samples. Similar trend was observed in the past by some researchers [49–51].

3.4.2. Volumetric strain behavior

Fig. 11 shows volumetric strain curves on soft clayey soil stabilized with varied molasses, WFS, and lime concentrations for a confining pressure of 98.06 kPa. For moderate strains, the volumetric strain during shearing remained relatively constant and increased strain levels resulting in a higher volumetric strain reduction. The soft clayey soil showed the most significant reduction in volumetric strain. When the stabilization of soil was done using additives, decreased rate of volumetric strain was observed more for clay:molasses:WFS:lime mix followed by clay:WFS:lime mix, clay:molasses:lime mix, clay:molasses:WFS mix, clay:lime mix, clay:WFS mix, and clay:molasses mix. For soft clayeysoil, the rate of change in volumetric strain increased significantly up to strains of 10 %, after whichit decreased. The rate of change in volumetric strain was significantly lower for soil stabilized with molasses, WFS, and lime when compared to soft clayey soil.

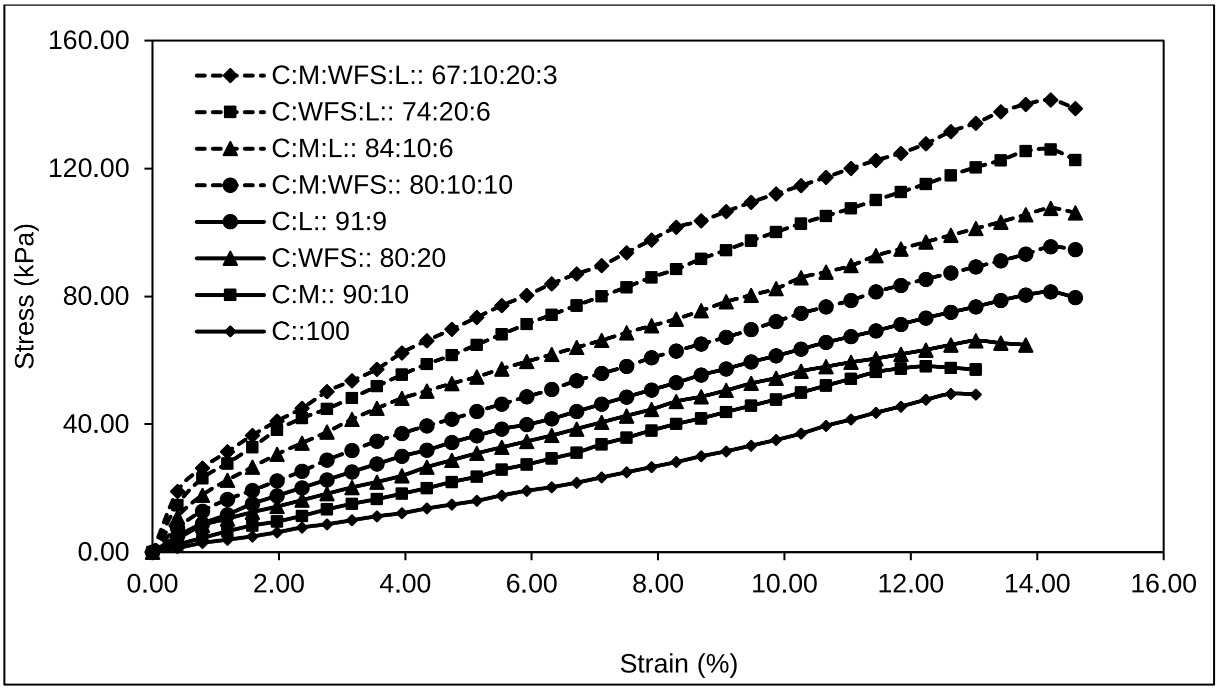

Figure 7. Deviator stress versus axial strain for soft clay and optimum combinations for confining pressure 49.03 kPa.

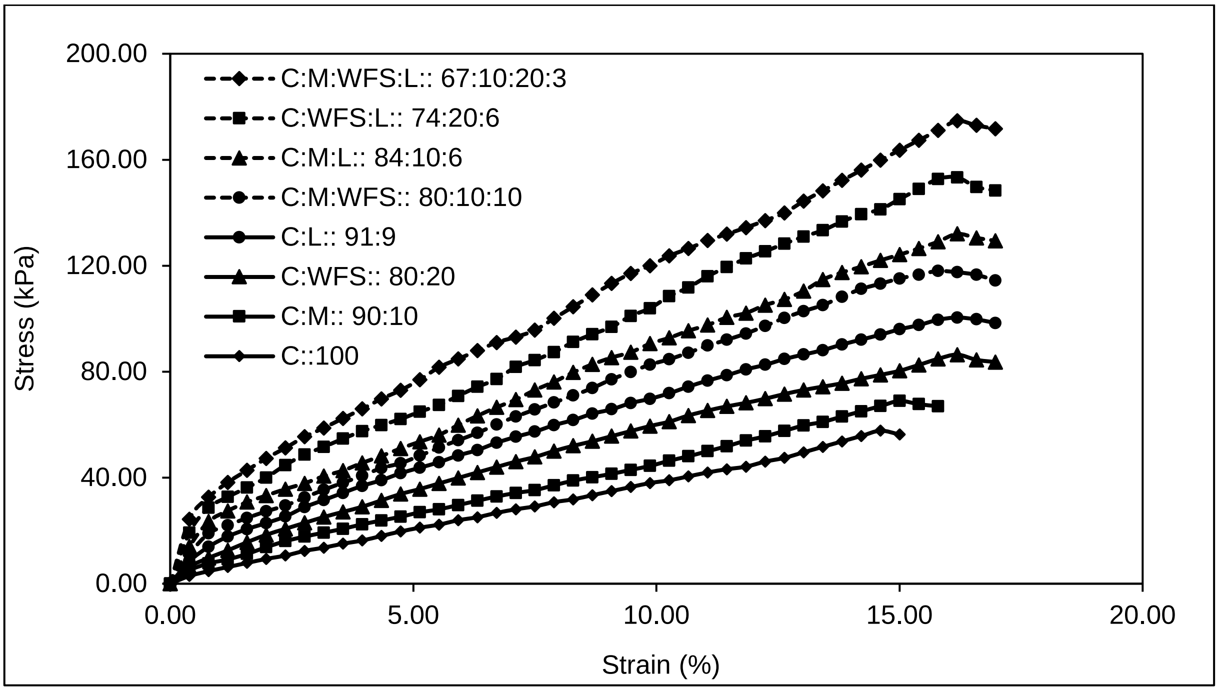

Figure 8. Deviator stress versus axial strain for soft clay and optimum combinations for confining pressure 98.06 kPa.

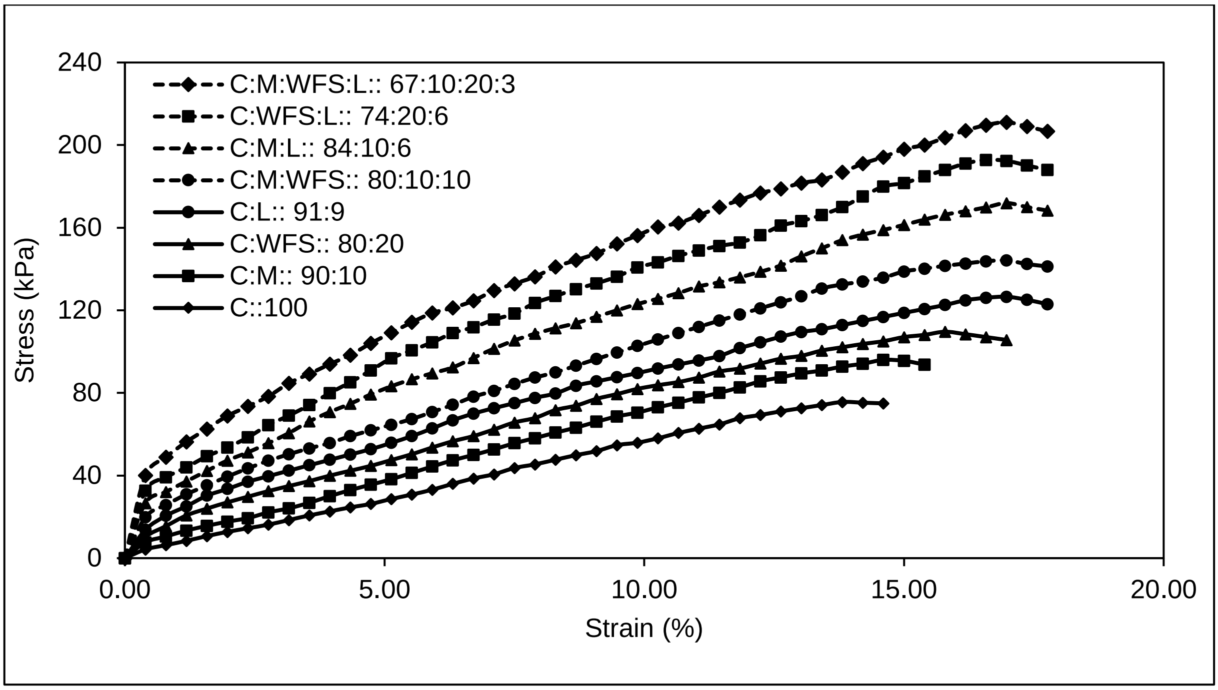

Figure 9. Deviator stress versus axial strain for soft clay and optimum combinations for confining pressure 147.1 kPa.

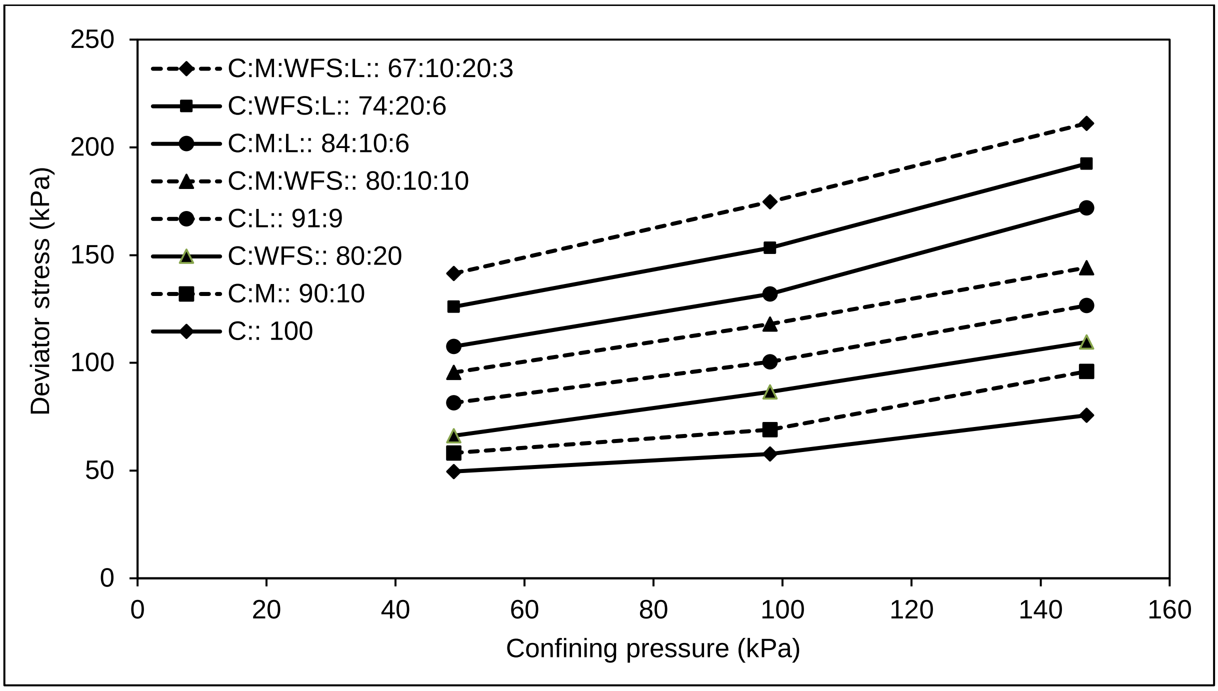

Figure 10. Deviator stress versus confining pressure for soft clay and optimum combinations.

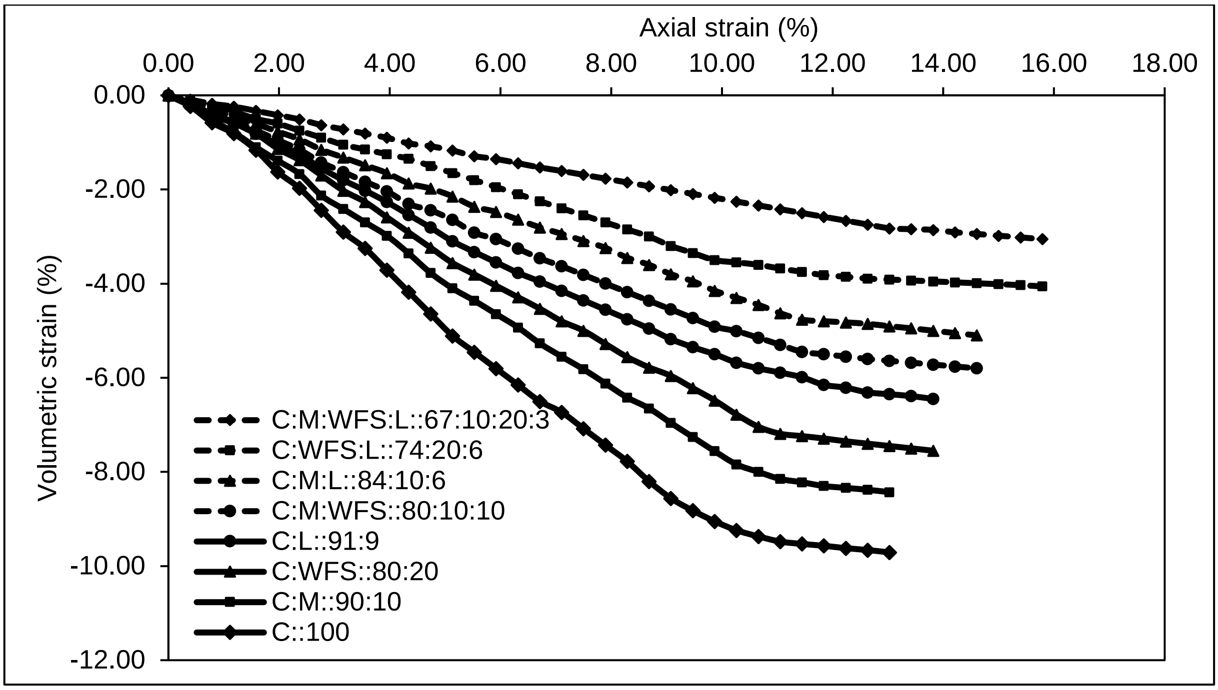

Figure 11. Volumetric strain-axial strain curves for soft clay and optimum combinations at confining pressure 96.06 kPa.

3.4.3. Effect of additives on deviator stress

Fig.12–14 illustrate the influence of altering optimum percentages of molasses, WFS, and lime in clayey soil for confining pressures of 49.03, 98.06, and 147.1 kPa for two axial strain values 6 % and 12 %. It was observed that the deviator stress of the optimum combinations was substantially higher when compared to the unstabilized soil.

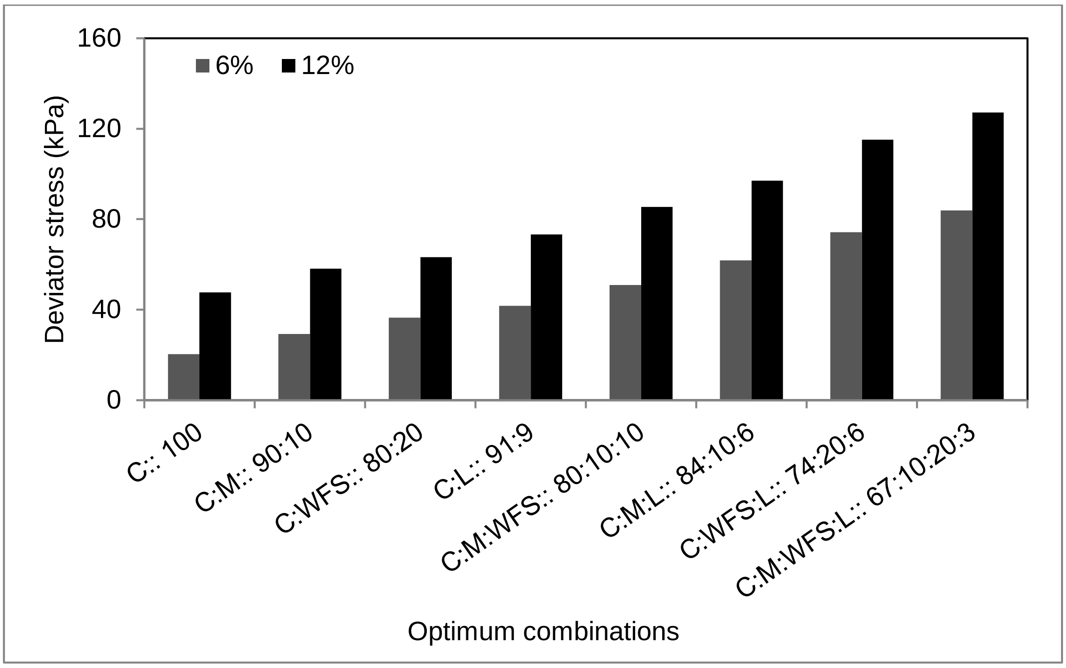

Figure 12. Maximum deviator stress for soft clay and optimum combinations of the composites (confining pressure 49.03 kPa).

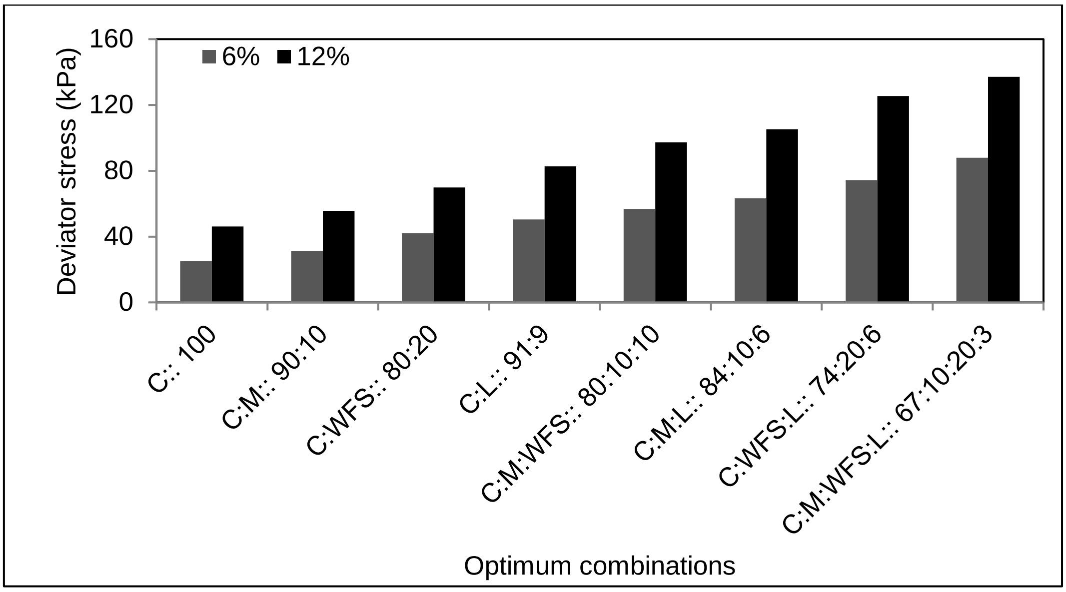

Figure 13. Maximum deviator stress for soft clay and optimum combinations of the composites (confining pressure 98.06 kPa).

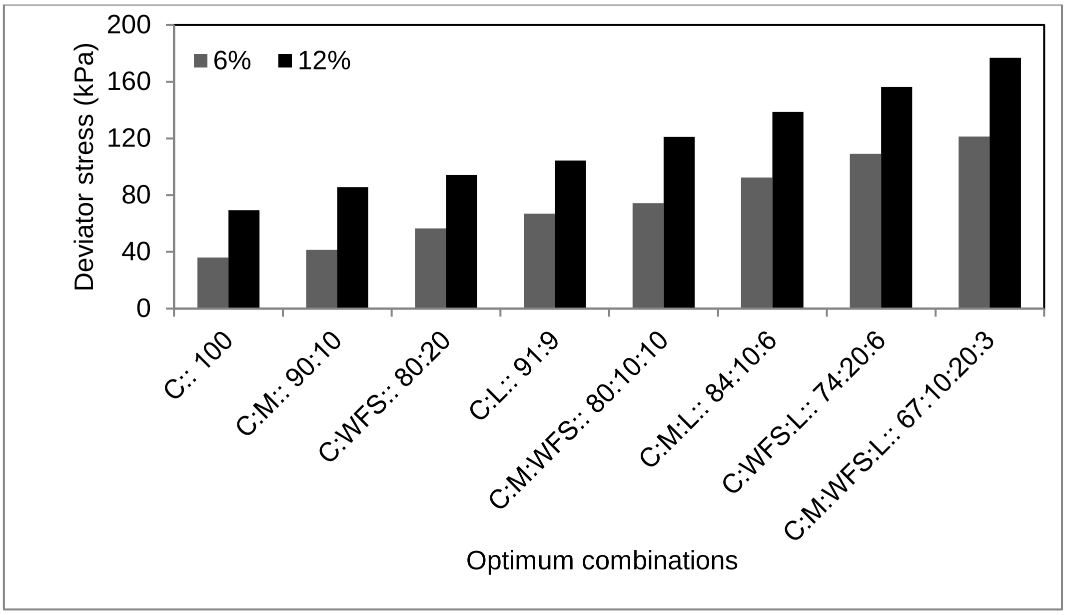

Figure 14. Maximum deviator stress for soft clay and optimum combinations of the composites (confining pressure 147.1kPa).

3.4.4. Shear strength parameters

The p-q diagram for unstabilized clayey soil and stabilized soil is shown in Fig. 15. The shear strength characteristics of clayey soil were shown to be significantly influenced by the addition of molasses, WFS, and lime.

As shown in Fig. 16, the friction angle increases as the percentage of additives in unstabilized clayey soil varied. The friction angle was greatly improved when molasses, WFS, and lime content blended with soft clayey soil. As the percentage of molasses, WFS, and lime increased, there was a fairly linear shift in the friction angle; hence, it ranged from 17° to 29.68°. The friction angle was around 14.86° for soft clayey soil. The friction angle value increased by 19.4 % on addition of 10 % molasses content, 35.5 % on addition of 20 % WFS content, 50.6 % on addition of 9 % lime content, 67.8 % for soil stabilized with 10 % molasses, and 10 % WFS content, 80.5 % for soil stabilized with 10 % molasses, and 6 % lime content, 98.02 % for soil stabilized with 20 % WFS, and 6 % lime content and 113.8 % for soil stabilized with 10 % molasses, 20% WFS, and 3 % lime content, when compared to un-stabilized soil.

Fig. 17 shows that stabilised soil cohesion value (range from 19.92 to 13.89 kPa) is lower than soft clayey soil cohesion value (about 21.771 kPa). The cohesion value decreased by 8.5 % on addition of 10 % molasses content, 12.36 % on addition of 20 % WFS content, 19.06 % on addition of 9 % lime content, 24.48 % for soil stabilized with 10 % molasses, and 10 % WFS content, 28.34 % for soil stabilized with 10 % molasses, and 6 % lime content, 32.11 % for soil stabilized with 20 % WFS, and 6 % lime content and 36.19 % for soil stabilized with 10 % molasses, 20 % WFS, and 3 % lime content, when compared to un-stabilized soil.

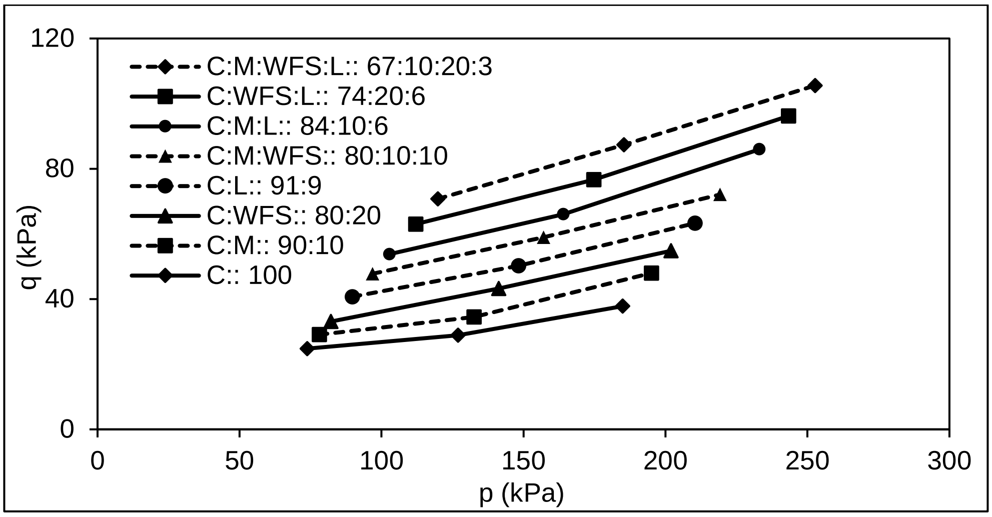

Figure 15.p-q diagram for the soft clay and optimum combinations.

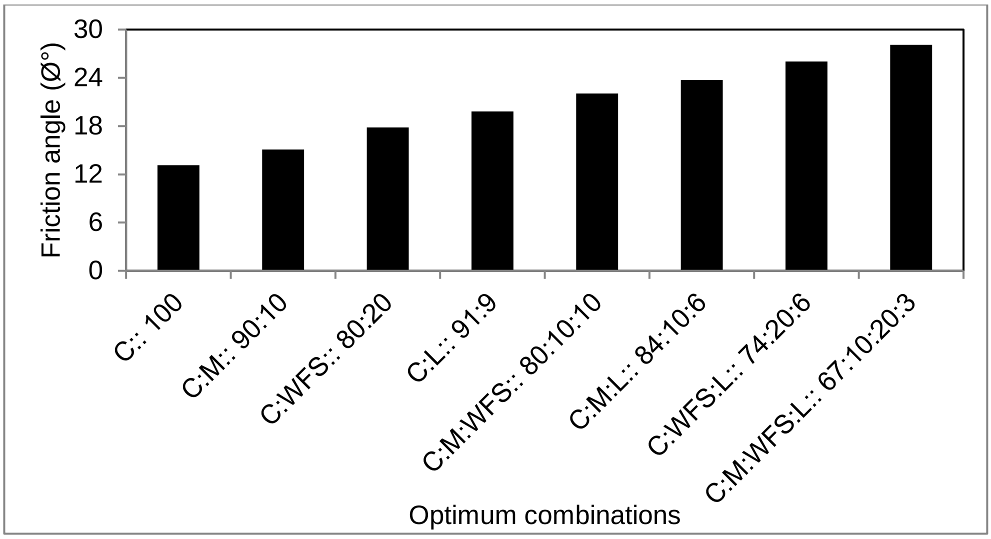

Figure 16. Effect of optimum content of molasses, WFS, and lime on friction angle of soft clayey soil (confining pressure 98.06 kPa).

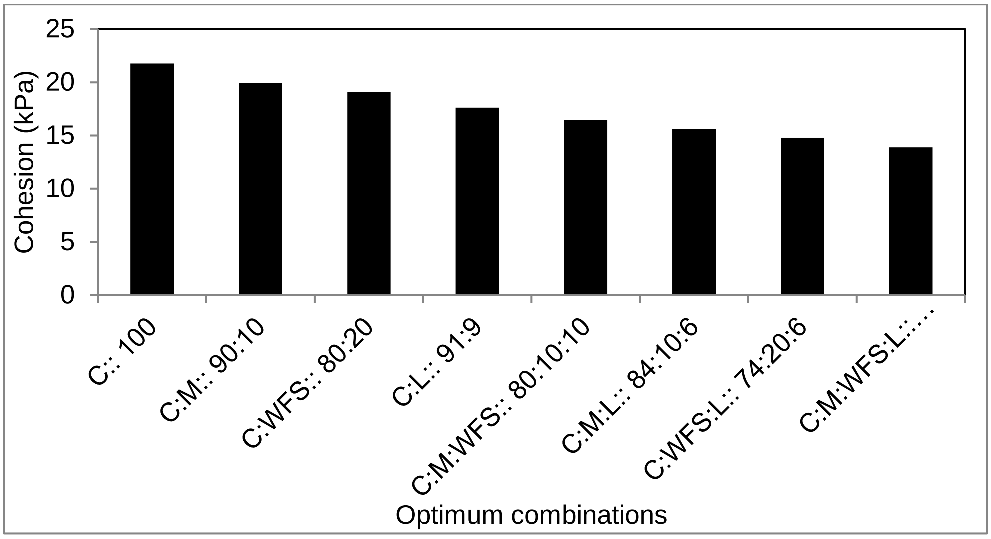

Figure 17. Effect of optimum content of molasses, WFS, and lime on cohesion value of soft clayey soil (confining pressure 98.06 kPa).

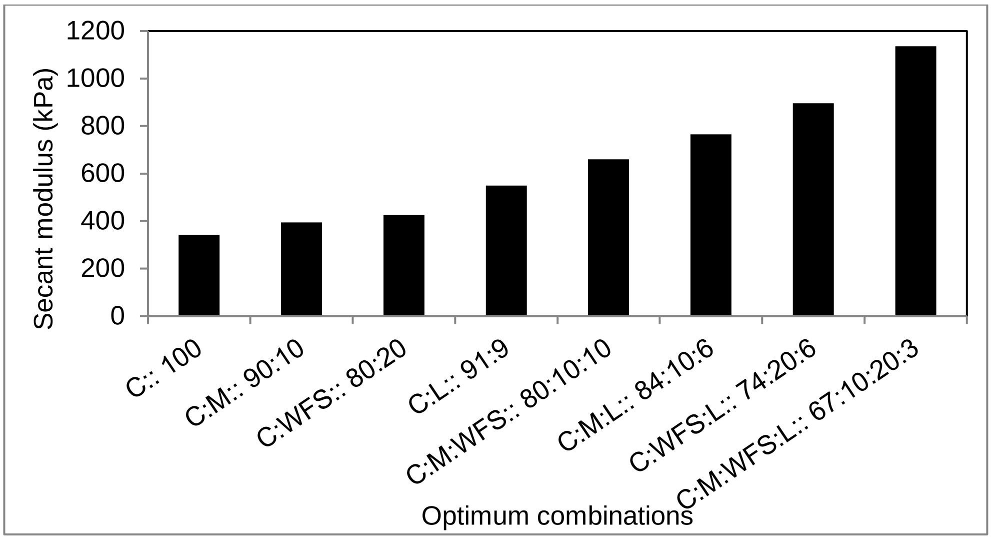

Figure 18. Secant modulus versus soft clayey soil and optimum combinations of the composites (confining pressure 49.03 kPa).

3.4.5 Effect of stiffness

For a confining pressure of 49.03 kPa, Fig. 18 depicts the difference between the secant modulus of soft clayey soil and stabilized clayey soil with the optimum content of molasses, WFS, and lime at lower strain levels (3 %). Initially, for clay-molasses and clay-WFS mixes, the rate increment in secant modulus was low; for clay:lime mix, clay:molasses:WFS mix, clay:molasses:lime mix, and clay:WFS:lime mix, the rate of increment in secant modulus value was somewhat higher; but for clay:molasses:WFS:lime mix, the secant modulus increased abruptly. The percentage increase in stabilized soil was 15.5 % for clay:molasses mix; 24.3 % for clay-WFS mix; 60.8 % for clay:lime mix; 93 % for clay:molasses:WFSmix; 123.7 % for clay:molasses:lime mix ;162 % for clay:WFS:lime mix; and 232 % for clay:molasses:WFS:lime mix soil. For red clayey deposits, [52] found that as confining pressure and saturation increased, the stiffness value also improved.

3.5. Microstructure

The addition of optimum proportions of additives was studied for their effects on the clayey soil structure using the scanning electron microscope (SEM) approach. Plate-like structures and numerous cavities can be seen in the SEM picture of the clayey soil (Fig.19). When the proper amount of molasses (about 10 percent) was mixed with clayey soil, a jelly-like structure formed (Fig. 20) and the gaps in the soil were filled, leading to an increase in the composite's strength. When clayey soil was mixed with the optimum percentage of waste foundry sand, a compact structure was created (Fig. 21), which helped in boosting the composite's strength. By adding lime to the clayey soil at the optimum content of 9 %, the void ratio was reduced because the finer particles of lime helped to fill the gaps, creating a denser and thread-like structure (Fig. 22), which in turn increased the strength of the composite.

Fig. 23 is a SEM image of a composite consisting of clay, molasses, and WFS, showing that the voids present in the composite were reduced and a compact structure was formed. When compared to clay-molasses or clay-lime composites, the SEM image of the clay-molasses-lime composite (Fig. 24) shows a more uniform and compact structure. Fig. 25 displays the result of combining WFS with lime, which is a denser structure than both clay-WFS or clay-lime composites alone. In Fig. 26, a thick micro-structure was observed that was formed when clay blended with molasses, WFS, and lime. Hence it can be concluded that by combining the right proportions of molasses, WFS, and lime with clay, a composite with increased strength and a more compact structure is produced, which in turn enhances the geotechnical properties of clay.

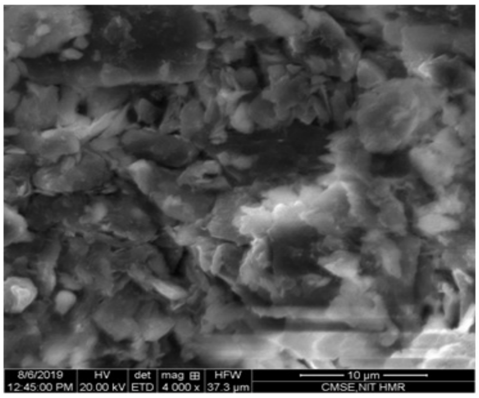

Figure 19. SEM image of clay.

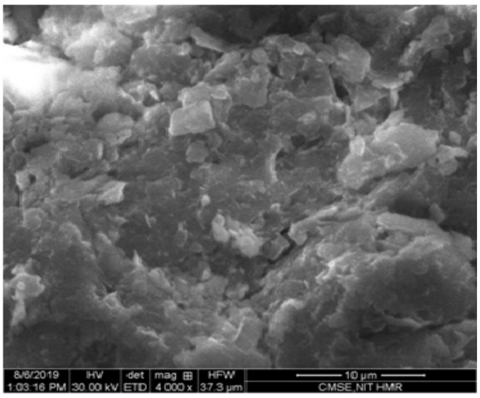

Figure 20.SEM of clay-molasses.

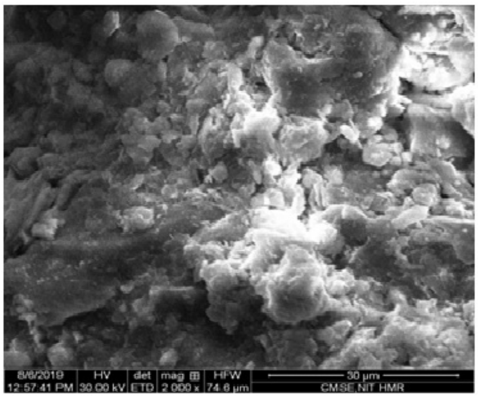

Figure 21.SEM of clay-WFS.

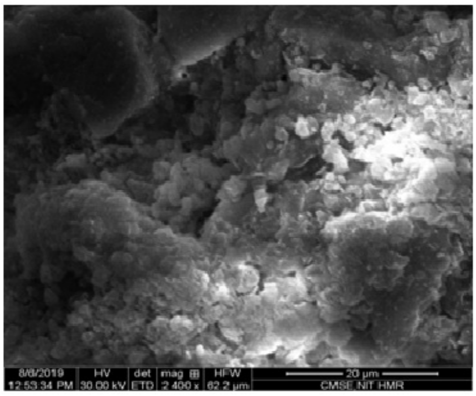

Figure 22. SEM of clay-lime.

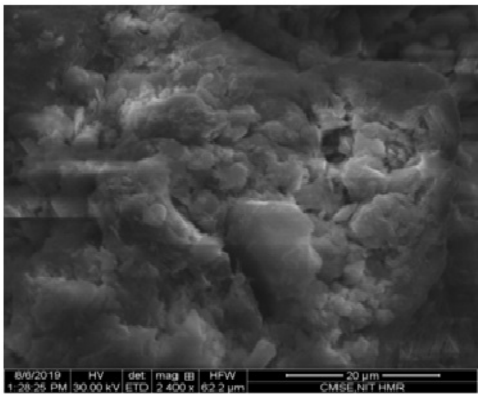

Figure 23. SEM of clay-molasses-WFS

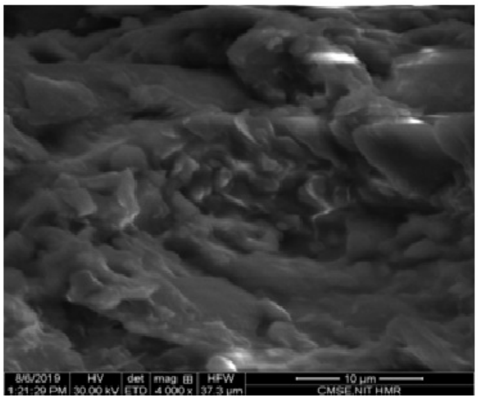

Figure 24. SEM of clay-molasses-lime.

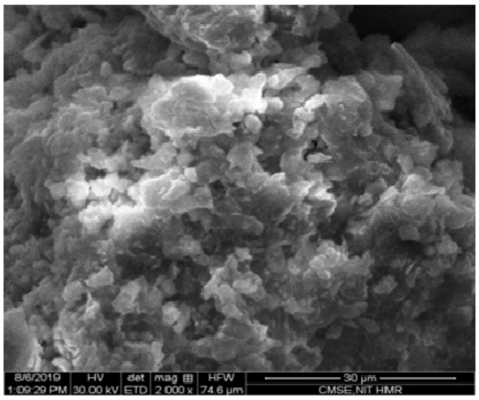

Figure 25. SEM of clay-WFS-lime.

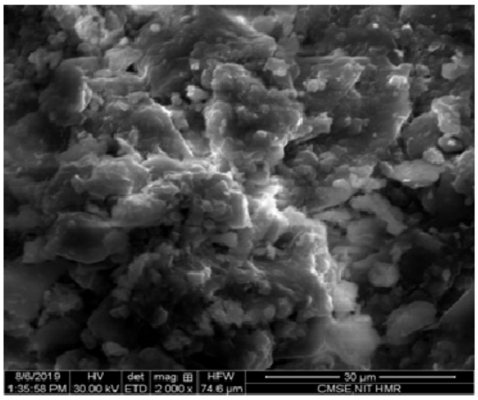

Figure 26. SEM of clay-molasses-WFS-lime.

4. Conclusion

Atterberg limits tests and pH tests on soft clayey soil and stabilized clayey soil were conducted to study about the behavior of soft clayey soil. The engineering characteristics of both soft clayey soil and optimum combinations were studied using permeability and consolidated drained triaxial tests. The following conclusions were drawn from this study:

1. The pH of soft clayey soil decreased with the addition of molasses and WFS and reached neutral value at 10 % molasses and 20 % WFS. The alkaline nature of lime caused a rise in pH of soft clayey soil with its addition and reached a maximum of 12.2 pH with 9 % lime.

2. The addition of molasses, WFS, and lime separately and in combination to each other decreased the plasticity index value of the soft clayey soil. For clay-molasses-WFS mix 10 % WFS, for clay-molasses-lime mix 6 % lime, for clay-WFS-lime mix 6 % lime and for clay-molasses-WFS-lime mix 3 % lime was found to be satisfactory to improve the workability of the clayey soil.

3. The considerable improvements in the deviator stress of soft clayey soil are obtained by 9 % lime, followed by 20 % WFS and 10 % molasses. Furthermore, among the optimum combinations, the clay-molasses-WFS-lime mix showed the most significant improvements in the deviator stress of soft clayey soil, followed by the clay-WFS-lime mix, the clay-molasses-lime mix, and the clay-molasses-WFS mix.

4. Scanning electron microscope (SEM) results showed that addition of molasses and WFS filled the voids between the soft clayey soil particles rendering a compact composite thus improving the strength characteristics. A combination of all the three additives in optimum proportion produced a composite possessing higher strength and dense structure, the geotechnical characteristics of clayey soil were improved making it suitable as a foundation material.

Based on the findings of this study, it is evident that clayey soil can be adequately stabilized for use as a foundation material. The significance of the results is that in contrast to other lime stabilization cases where larger amounts of lime (and invariably higher construction costs) were involved, the findings show that smaller amounts of lime (and thus lower construction costs) used in this study can provide a stronger foundation material. Optimum stabilization of clayey soil was achieved with 10 % molasses, 20 % WFS, and only 3 % lime.

References

1. Jayawardane, S., Anggraini, V., Emmanuel, E., Yong, L.L., Mirzababaei, M. Expansive and compressibility behaviour of lime stabilized fiber-reinforced marine clay. Journal of Materials in Civil Engineering. 2020. 32(11). Pp. 04020328.
2. Miah, M.T., Oh, E., Chai, G., Bell, P. Effect of Swelling Soil on Pavement Condition Index of Airport Runway Pavement. Transportation Research Record. 2022. 2676(10). Pp. 553–569. DOI: 10.1177/03611981221090517
3. Raja, K., Venkatachalam, S., Vishnuvardhan, K., Krishnan, R.S.R., Selvan, V.T., Vetriselvan, N. A review on soil stabilization using rice husk ash and lime sludge. Materials Today: Proceedings. 2022. 65(5). DOI: 10.1016/j.matpr.2022.04.178
4. Gidday, B.G., Mittal, S. Improving the characteristics of dispersive subgrade soils using lime. Heliyon. 2020. 6(2). Pp 03384.
5. Bozbey, I., Garaisayev, S. Effects of soil pulverization quality on lime stabilization of expansive clay. Environmental Earth Sciences. 2010. 60(6). Pp. 1137–1151.
6. Guney, Y., Aydilek, A.H., Demirkan, M.M. Geoenvironmental behavior of foundry sand amended mixtures for highway subbases. Waste Management. 2006. 26(9). Pp. 932–945.
7. Bhardwaj, A., Sharma, R.K. Effect of industrial wastes and lime on strength characteristics of clayey soil. Journal of Engineering, Design and Technology. 2020. 18(6). Pp. 1749–1772. DOI: 10.1108/JEDT-12-2019-0350
8. Jamei, M., Alassaf, Y., Ahmed, A., Mabrouk, A. Fibers reinforcement of the fissured clayey soil by desiccation. Magazine of Civil Engineering. 2022. 109(1). Article No. 10914. DOI: 10.34910/MCE.109.14
9. Polyankin, A.G., Korolev, K.V., Kuznetsov, A.O. Analysis of reinforced soil sustainability while tunnel construction. Magazine of Civil Engineering. 2020. 3(95). Pp. 80–89. DOI: 10.18720/MCE.95.8
10. Jose, A., Kasthurba, A. Stabilization of lateritic soil for masonry applications. Magazine of Civil Engineering. 2021. 101(1). Article No. 10109. DOI: 10.34910/MCE.101.9
11. Sharma, R.K., Bhardwaj, A. Effect of construction demolition and glass waste on stabilization of clayey soil. In International conference on sustainable waste management through design. Springer, Cham, 2018. Pp. 87–94.
12. Bhardwaj, A., Walia, B.S. Influence of cement and polyester fibers on compaction and CBR value of clayey soil. Indian Geotechnical Conference 2017 GeoNEst.. IIT Guwahati, India, 2017.
13. Bhardwaj, A., Sharma, R.K. Bearing Capacity Evaluation of Shallow Foundations on Stabilized Layered Soil using ABAQUS. Studia Geotechnica et Mechanica. 2022. 45(1). DOI: 10.2478/sgem-2022-0026
14. Agarwal, P., Kaur, S. Effect of bio-enzyme stabilization on unconfined compressive strength of expansive soil. International Journal of Research in Engineering and Technology. 2014. 3(5). Pp. 30–33.
15. Eujine, G.N., Chandrakaran, S., Sankar, N. Accelerated subgrade stabilization using enzymatic lime technique. Journal of Materials in Civil Engineering. 2017. 29(9). Pp. 04017085–4017087. DOI: 10.1061/(ASCE)MT.1943-5533.0001923.
16. Eujine, G.N., Chandrakaran, S., Sankar, N. Influence of enzymatic lime on clay mineral behavior. Arabian Journal of Geosciences. 2017. 10(20). Pp. 454–62. DOI: 10.1007/s12517-017-3238-z
17. Patel, U., Singh, S., Chaudhari, S. Effect of bio enzyme–terrazyme on compaction, consistency limits and strength characteristics of expansive soil. International Journal of Research in Engineering and Technology. 2018. 5(3). Pp. 1602–1605.

18. Velasquez, R.A., Marasteanu, M.O., Hozalski, R.M. Investigation of the effectiveness and mechanisms of enzyme products for subgrade stabilization. International Journal of Pavement Engineering. 2006. 7(3). Pp. 213–220. DOI: 10.1080/10298430600574395
19. Venkatasubramanian, C., Dhinakaran, G. Effect of bio-enzymatic soil stabilisation on unconfined compressive strength and California bearing ratio. Journal of Engineering and Applied Science. 2011. 6(5). Pp. 295–298.
20. Suriadi, A., Murray, R.S., Grant, C.D., Nelson, P.N. Structural stability of Sodic soils in sugarcane production as influenced by gypsum and molasses. Australian Journal of Experimental Agriculture. 2002. 42. Pp. 315–322.
21. Raheem, B. S., Oladiran, G.F., Oke, D.A., Musa, S.A. Evaluation of Strength Properties of Subgrade Materials Stabilized with Bio-Enzyme. European Journal of Engineering and Technology Research. 2020. 5(5). Pp. 607–610.
22. Jiménez, J.E., Fontes Vieira, C.M., Colorado, H.A. Composite Soil Made of Rubber Fibers from Waste Tires, Blended Sugar Cane Molasses, and Kaolin Clay. Sustainability. 2022. 14(4). Pp. 2239. DOI: 10.3390/su14042239
23. Basar, H.M., Aksoy, N.D. Pretreatment of Waste Foundry Sand via Solidification/Stabilization. CLEAN–Soil, Air, Water. 2013. 41(1). Pp. 94–101.
24. Dyer, P.P.O.L., Gutierrez Klinsky, L.M., Silva, S.A., Silva, R.A., Lima, M.G. Macro microstructural characterisation of waste foundry sand reused as aggregate. Road Material Pavement Design. 2019. Pp. 1–14. DOI: 10.1080/14680629.2019.1625807
25. Kirk, P.B. Field demonstration of highway embankment constructed using waste foundry sand. Doctoral dissertation, Ph. D. Dissertation, Purdue University, West Lafayette, IN. 1998. 202 p.
26. Mast, D.G., Fox, P.J. Geotechnical performance of a highway embankment constructed using waste foundry sand. Recycled Materials in Geotechnical Applications, Geotechnical Special Publication. 1998. 79. Pp. 66–85.
27. Javed, S., Lovell, C.W. Uses of waste foundry sands in civil engineering. Transportation Research Record. 1995. 1486. Pp. 109– 113.
28. Yazoghli-Marzouk, O., Vulcano-Greullet, N., Cantegrit, L., Friteyre, L., Jullien, A. Recycling foundry sand in road construction-field assessment. Construction Building and Materials. 2014. 61. Pp. 69–78. DOI: 10.1016/j.conbuildmat.2014.02.055.
29. Aneke, F., Ikechukwu, C. Green-Efficient Masonry Bricks Produced from Scrap Plastic waste and Foundry Sand. Case Studies in Construction Materials. 2021. Pp. 00515. DOI: 10.1016/j.cscm.2021.e00515
30. Bhardwaj, A., Sharma, R.K. Designing thickness of subgrade for flexible pavements incorporating waste foundry sand, molasses, and lime. Innovative Infrastructure Solutions. 2022. 7. Pp. 132. DOI: 10.1007/s41062-021-00723-6
31. Vinoth, M., Sinha, A.K., Guruvittal, U.K., Havanagi, V.G. 2022. Strength of Stabilised Waste Foundry Sand Material. Indian Geotechnical Journal. 2022. 52(3). Pp. 707–719.
32. Mallela, J., Harold, P., Smith, K.L. Consideration of lime-stabilized layers in mechanistic-empirical pavement design. Arlington, Virginia, USA: The National Lime Association. 2004.
33. Anon, Lime Stabilization Construction Manual. Eighth Edition. National Lime Association, Arlington, VA. 1985.
34. Anon, Lime Stabilization Manual. British Aggregate Construction Materials Industry. London. 1990.
35. López-Lara, T., Hernández-Zaragoza, J.B., Horta-Rangel, J., Rojas-González, E., López-Ayala, S., Castaño, V.M. Expansion reduction of clayey soils through Surcharge application and Lime Treatment. Case Studies in Construction Materials. 2017. 7. Pp. 102–109. DOI: 10.1016/j.cscm.2017.06.003
36. Zagvozda, M., Tatjana, R., Sanja, D. Wood bioash effect as lime replacement in the stabilisation of different clay subgrades. International Journal of Pavement Engineering. 2020. 23(8). Pp. 1–11. DOI: 10.1080/10298436.2020.1862839
37. Jafari, S.H., Lajevardi, S.H., Sharifipour, M. Correlation between Small-Strain Dynamic Properties and Unconfined Compressive Strength of Lime-Stabilized Soft Clay. Soil Mechanics and Foundation Engineering. 2022. 59(4). Pp. 331. DOI: DOI: 10.1007/s11204-022-09819-2
38. Bhardwaj, A., Sharma, R.K., Sharma, A. (2021) Stabilization of clayey soil using waste foundry sand and molasses. In: Singh H., Singh Cheema P.P., Garg P. (eds) Sustainable development through engineering innovations. Lecture notes in civil engineering, Springer, Singapore. 2021. 113. DOI: 10.1007/978-981-15-9554-7_57
39. Dong, Q., Huang, V., Huang, B. Laboratory evaluation of utilizing waste heavy clay and foundry sand blends as construction materials. Journal of Materials in Civil Engineering. 2013. 26(9). Pp. 04014065. DOI: 10.1061/(ASCE)MT.1943-5533.0000968
40. Davidson, L.K., Demeril T., Handy, R. L. Soil pulverization and lime migration in soil lime stabilization. Highway Research Board, National Research Council, Washington DC. 1965. 92. Pp. 103–126.
41. Yong, R., Ouhadi, V. Experimental study on instability of bases on natural and lime/cement-stabilized clayey soils. Applied Clay Science. 2007. 35(3). Pp. 238–249.
42. Sharma, N.K., Swain, S.K., Sahoo, U.C. Stabilization of a clayey soil with fly ash and lime: a micro level investigation. Geotechnical and Geological Engineering. 2012. 30. Pp. 1197–1205. DOI: 10.1007/s10706-012-9532-3
43. Vinodhkumar, S., Kulanthaivel, P., Kabilan, A., Lokeshkanna, K.M. Study of black cotton soil characteristics with molasses. Asian Journal of Engineering and Applied Technology. 2018. 7(1). Pp. 73–77. DOI: 10.51983/ajeat-2018.7.1.857
44. Kale, R.Y., Wawage, R., Kale, G. Effect of foundry waste on expansive soil (black cotton soil). International Journal for Scientific Research and Development. 2019. 7(2) Pp. 1800–1804.
45. Harichane, K., Ghrici, M., Kenai, S., Grine, K. Use of natural pozzolana and lime for stabilization of cohesive soils. Geotechnical and Geological Engineering. 2011. 29(5). Pp. 759–769.
46. Nalbantoglu, Z. Lime stabilization of expansive clay. Expansive Soils – Recent advances in characterization and treatment, Taylor and Francis, London. 2006. Pp. 341–348.
47. Shirsavkar, S.S., Koranne, S. Innovation in road construction using natural polymer. Electronic Journal of Geotechnical Engineering. 2010. 15(1). Pp. 1614–1624.
48. Grower, K., Goyal, T. Experimental study of waste foundry sand and marble dust as a soil stabilizing material. International Research Journal of Engineering and Technology. 2019. 6(6). Pp. 1265–1272.
49. M'Ndegwa, J.K. The effect of cane molasses on strength of expansive clay soil. Journal of Emerging Trends in Engineering and Applied Sciences. 2011. 2(6). Pp. 1034–1041.
50. Kumar, A., Kumari, S., Sharma, R.K. Influence of use of additives on engineering properties of clayey soil. Proceedings of National conference: Civil Engineering Conference-Innovation for Sustainability. 2016.

51. Zhu, F., Li, Z., Dong, W., Yangyun, Ou. Geotechnical properties and microstructure of lime-stabilized silt clay. Bulletin of Engineering Geology and the Environment. 2019. 78(4). Pp. 2345–2354. DOI: 10.1007/s10064-018-1307-5

52. Ma, S.K., Mao, S.H., Ping, H., Chao, Y. Soil–water characteristics and shear strength in constant water content triaxial tests on Yunnan red clay. Journal of Central South University. 2013. 20(5). Pp. 1412–1419. DOI: 10.1007/s1177 1-013-1629-1

Information about authors:

Avinash Bhardwaj,
ORCID: https://orcid.org/0000-0002-1183-6407
E-mail: avinash@nith.ac.in

Ravi Kumar Sharma, *PhD*
ORCID: https://orcid.org/0000-0003-0031-642X
E-mail: ravi@nith.ac.in

Received 14.11.2022. Approved after reviewing 13.01.2023. Accepted 17.01.2023.

Magazine of Civil Engineering

ISSN 2712-8172

journal homepage: http://engstroy.spbstu.ru/

Research article

UDC 539.3

DOI: 10.34910/MCE.120.3

Stress-strain state of elastic shell based on mixed finite element

***Yu.V. Klochkov*[1], *V.A. Pshenichkina*[2], *A.P. Nikolaev*[1], *O.V. Vakhnina*[1] ✉, *M.Yu. Klochkov*[2]**

[1] *Volgograd State Agrarian University, Volgograd, Russian Federation*
[2] *Volgograd State Technical University, Volgograd, Russian Federation*
✉ *ovahnina@bk.ru*

Keywords: thin-walled shell-type structure, modified mixed functional, compliance matrix, four-node sampling element, force and kinematic unknowns

Abstract. In a mixed formulation, a four-node finite element was developed, which is a fragment of the middle surface of the elastic shell. Longitudinal forces and bending moments, as well as displacements and their first derivatives with respect to curvilinear coordinates, were taken as nodal unknowns. To obtain the compliance matrix, the Reissner functional was used, in which the stresses, when using the direct normal hypothesis, are represented by dependences on the forces and bending moments of the middle surface, the approximation of which was carried out by bilinear functions. In the interpolating expressions for the kinematic sought quantities, Hermite polynomials of the third degree were used. As a result of minimizing the transformed functional with respect to the force and kinematic nodal unknowns, the compliance matrix of the accepted discrete element was formed. Verification of the developed discrete element in a mixed formulation was carried out on the examples of calculations of cylindrical shells with circular and elliptical cross sections. The values of the force parameters found using the developed algorithm adequately satisfied the conditions of static equilibrium (the calculation error was less than 0.5 %). An analysis of the obtained finite element solutions showed the effectiveness of the developed algorithm and made it possible to note the possibility of its use in calculations of thin-walled structures made of incompressible materials.

Citation: Klochkov, Yu.V., Pshenichkina, V.A., Nikolaev, A.P., Vakhnina, O.V., Klochkov, M.Yu. Stress-strain state of elastic shell based on mixed finite element. Magazine of Civil Engineering. 2023. Article no. 12003. DOI: 10.34910/MCE.120.3

1. Introduction

Definition of the object of the study. The current widespread use of thin-walled shell-type structures (pipelines, tanks, hangars, domed roofs, wide-span ceilings, and others) puts forward a rather urgent task of creating domestic computational algorithms for analyzing the stress-strain state of such technospheric systems and objects.

Literature review. At present, when choosing the optimal shapes and sizes of thin-walled shell-type structures, numerical methods for analyzing their SSS [1–6] come to the fore, with FEM taking the priority position. It is widely used in calculations of plates and shells both under elastic [7–12] and elastoplastic [13, 14] deformation. FEM is essential in the analysis of SSS structures made of composite materials [15–17], as well as in matters of shell stability [18]. Three-dimensional finite elements are used both in the analysis of the stress-strain state of bulk structures and thin-walled structures [19–21].

The relevance of the research. Most of the currently created finite element computing systems are based on FEM in the formulation of the displacement method, which inevitably leads to the need to calculate second-order partial derivatives of the normal component of the displacement vector when using the theory of thin shells [22] based on the Kirchhoff-Love hypotheses. At the same time, finite element algorithms for determining the stress-strain state of shell structures in a mixed formulation [23, 24] make it possible to obtain the desired internal force quantities (longitudinal forces and bending moments) directly in the process of solving the system of equations formed as a result of minimizing the mixed Reissner functional. This can also achieved without organizing additional computational procedures that greatly complicate the finite element algorithm for calculating thin-walled shell-type structures.

The purpose and objectives of the study. This paper presents the derivation of the modified Reissner functional, in which the total specific work of stresses is expressed in terms of the specific work of longitudinal forces and bending moments at a point of the middle surface on deformations and curvatures of the middle surface at this point. By minimizing the modified mixed functional with respect to force (longitudinal forces and bending moments) and kinematic (displacement vector components and their first-order partial derivatives) nodal unknowns, the compliance matrix and the column of nodal forces of a quadrangular discretization element, which is a fragment of the middle surface of a thin-walled shell-type structure, are assembled.

The verification of the developed algorithm was carried out on the example of determining the SSS of cylindrical shells with circular and elliptical cross sections. An analysis of the results of the obtained finite element solutions made it possible to conclude that the developed algorithm is effective and that the calculation accuracy of the required force and kinematic nodal unknowns is acceptable.

2. Materials and Methods

The median surface of a thin-walled shell-type structure can be given by the radius vector

$$\vec{R}^0 = x\vec{i} + y(x,\ t)\,\vec{j} + z(x,\ t)\vec{k}, \tag{1}$$

where t is a parameter counted from the vertical axis in a plane perpendicular to the axis $Ox,$ which is at a distance of x from the origin.

Basis vectors of a point M^0 are determined by derivatives

$$\vec{a}_1^0 = \vec{R}_{,x}^0;\ \ \vec{a}_2^0 = \vec{R}_{,t}^0;\ \ \vec{a}^0 = \vec{a}_1^0 \times \vec{a}_2^0 \big/ \sqrt{a_0}\,, \tag{2}$$

where $a_0 = \left(\vec{a}_1^0 \cdot \vec{a}_1^0\right)\left(\vec{a}_2^0 \cdot \vec{a}_2^0\right) - \left(\vec{a}_1^0 \cdot \vec{a}_2^0\right)^2.$

The derivatives of the basis vectors of point M^0 are determined by the components in the same basis [25]

$$\vec{a}_{\alpha,\beta}^0 = \Gamma_{\alpha\beta}^{0\rho}\vec{a}_\rho^0 + b_{\alpha\beta}^0\vec{a}^0;\ \ \vec{a}_{,\beta}^0 = -b_\beta^{0\rho}\vec{a}_\rho^0, \tag{3}$$

where indices $\alpha,$ $\beta,$ ρ take values 1, 2; $\Gamma_{\alpha\beta}^{0\rho}$ are Christoffel symbols of the second kind; $b_\beta^{0\rho}$ are mixed components of the curvature tensor.

The position of the point of the shell at a distance of ζ from the point of the middle surface $M^0,$ as well as its position after the application of a given load, are determined by the radius vectors

$$\vec{R}^{0\zeta} = \vec{R}^0 + \zeta\vec{a}^0;\ \ \vec{R}^\zeta = \vec{R}^{0\zeta} + \vec{V}. \tag{4}$$

The displacement vector $\vec{V}$ of point $M^{0\zeta}$ according to the direct normal hypothesis [22] can be represented by the following expression

$$\vec{V} = \vec{v} + \zeta\left(\vec{a} - \vec{a}^0\right), \tag{5}$$

where $\vec{v} = v^\rho\vec{a}_\rho^0 + v\vec{a}^0$ is the displacement vector of point $M^{0\zeta};$ $\vec{a} = \vec{a}_1 \times \vec{a}_2 \big/ \sqrt{a}$ is unit vector of the normal at point $M;$ $\vec{a}_\rho = \vec{a}_\rho^0 + \vec{v}_{,\rho}$ are covariant vectors of the local basis of point M of the deformed state.

Here and below, the comma means the operation of differentiation with respect to global coordinates x and t.

The basis vectors of points $M^{0\zeta}$ and M^{ζ} are determined by the corresponding differentiation (4) with respect to x and t

$$\vec{g}_{\rho}^{0} = \vec{R}_{,\rho}^{0\zeta} = \vec{a}_{\rho}^{0} - \zeta b_{\rho}^{0\gamma}\vec{a}_{\gamma}^{0}; \quad \vec{g}_{\rho} = \vec{R}_{,\rho}^{\zeta} = \vec{g}_{\rho}^{0} + \vec{v}_{,\rho} + \zeta\left(\vec{a}_{,\rho} - b_{\rho}^{0\gamma}\vec{a}_{\gamma}^{0}\right). \tag{6}$$

Deformations at point M^{ζ} of a thin-walled shell-type structure are determined by the difference between the components of the metric tensors at the point of the initial and deformed states [26]

$$\varepsilon_{\rho\gamma}^{\zeta} = \left(g_{\rho\gamma} - g_{\rho\gamma}^{0}\right)/2. \tag{7}$$

Four-node element. The finite element is represented by a quadrangular part of the middle surface with nodes $i,\ j,\ k,\ l.$ Taking into account that when implementing the mixed formulation of the FEM, there is no need to include the desired unknown higher-order derivatives in the structure, the column of nodal variable parameters of the used quadrangular sampling element in the local $-1 \le \xi, \eta \le 1$ and global $x,\ t$ coordinate systems was chosen in the form

$$\underset{1\times 60}{\left\{U^{L}\right\}^{T}} = \left\{ \underset{1\times 12}{\{N\}^{T}} \underset{1\times 12}{\{M\}^{T}} \underset{1\times 12}{\left\{v^{1L}\right\}^{T}} \underset{1\times 12}{\left\{v^{2L}\right\}^{T}} \underset{1\times 12}{\left\{v^{L}\right\}^{T}} \right\}; \tag{8}$$

$$\underset{1\times 60}{\left\{U^{G}\right\}^{T}} = \left\{ \underset{1\times 12}{\{N\}^{T}} \underset{1\times 12}{\{M\}^{T}} \underset{1\times 12}{\left\{v^{1G}\right\}^{T}} \underset{1\times 12}{\left\{v^{2G}\right\}^{T}} \underset{1\times 12}{\left\{v^{G}\right\}^{T}} \right\}, \tag{9}$$

where $\underset{1\times 12}{\{N\}^{T}} = \left\{N^{11i}N^{11j}N^{11k}N^{11l}N^{22i}\ldots N^{22l}N^{12i}\ldots N^{12l}\right\};$

$\underset{1\times 12}{\{M\}^{T}} = \left\{M^{11i}M^{11j}M^{11k}M^{11l}M^{22i}\ldots M^{22l}M^{12i}\ldots M^{12l}\right\}$ are columns of power parameters;

$\underset{1\times 12}{\left\{q^{L}\right\}^{T}} = \left\{q^{i}q^{j}q^{k}q^{l}q_{,\xi}^{i}\ldots q_{,\xi}^{l}q_{,\eta}^{i}\ldots q_{,\eta}^{l}\right\};$ $\underset{1\times 12}{\left\{q^{G}\right\}^{T}} = \left\{q^{i}q^{j}q^{k}q^{l}q_{,x}^{i}\ldots q_{,x}^{l}q_{,t}^{i}\ldots q_{,t}^{l}\right\}$ are columns of kinematic parameters in local $-1 \le \xi, \eta \le 1$ and global $x,\ t$ coordinate systems, respectively.

Here, q means the values $v^{\rho},\ v.$

Bilinear functions of local coordinates $\xi,\ \eta$ [27] were used as shape functions for the force unknowns

$$N^{\alpha\beta} = \underset{1\times 4}{\{\varphi\}^{T}} \underset{4\times 1}{\left\{N^{\alpha\beta}\right\}}; \quad M^{\alpha\beta} = \underset{1\times 4}{\{\varphi\}^{T}} \underset{4\times 1}{\left\{M^{\alpha\beta}\right\}}, \tag{10}$$

and for the kinematic required unknowns, the products of Hermite polynomials of the third order were applied [27]

$$q = \underset{1\times 12}{\{\psi\}^{T}} \underset{12\times 1}{\left\{q^{L}\right\}}. \tag{11}$$

Compliance matrix of a four-node bin. To obtain the compliance matrix of a four-node discretization element, one can use the Reissner functional written in the following form

$$\Pi_{S} = \int_{V}\left\{\sigma^{\rho\gamma}\right\}^{T}\left\{\varepsilon_{\rho\gamma}^{\zeta}\right\}dV - 0.5\int_{V}\left\{\sigma^{\rho\gamma}\right\}^{T}[C]\left\{\sigma^{\rho\gamma}\right\}dV - 0.5\int_{F}\{U\}^{T}\{P\}dF, \tag{12}$$

where $\left\{\sigma^{\rho\gamma}\right\}^T=\left\{\sigma^{11}\sigma^{22}\sigma^{12}\right\}$; $\left\{\varepsilon^{\rho\gamma}\right\}^T=\left\{\varepsilon^{\zeta}_{11}\varepsilon^{\zeta}_{22}2\varepsilon^{\zeta}_{12}\right\}$; $\left\{U\right\}^T=\left\{v^1v^2v\right\}$; $\left\{P\right\}^T=\left\{p^1p^2p\right\}$ is column of the external surface load vector.

In accordance with [26], the elasticity matrix $\left[C\right]$ included in (12) determines the relationship between columns $\left\{\varepsilon^{\zeta}_{\rho\gamma}\right\}$ and $\left\{\sigma^{\rho\gamma}\right\}$

$$\left\{\varepsilon^{\zeta}_{\rho\gamma}\right\}=\left[C\right]\left\{\sigma^{\rho\gamma}\right\}. \tag{13}$$

Column $\left\{\sigma^{\rho\gamma}\right\}$, on the basis of the theory of thin shells [22], can be expressed in terms of the required force unknowns, which are the longitudinal forces $N^{\alpha\beta}$ and bending moments $M^{\alpha\beta}$

$$\underset{3\times1}{\left\{\sigma^{\rho\gamma}\right\}}=\underset{3\times6}{\left[D_{\sigma}\right]}\underset{6\times1}{\left\{NM\right\}}, \tag{14}$$

where $\underset{3\times6}{\left[D_{\sigma}\right]}=\begin{bmatrix}1/h & 0 & 0 & \zeta/I & 0 & 0\\ 0 & 1/h & 0 & 0 & \zeta/I & 0\\ 0 & 0 & 1/h & 0 & 0 & \zeta/I\end{bmatrix}$; $\left\{NM\right\}^T=\left\{N^{11}N^{22}N^{12}M^{11}M^{22}M^{12}\right\}$; h is the shell thickness; $I=h^3/12$ is moment of inertia.

The column of covariant components of the strain tensor at point M^{ζ}, taking into account the direct normal hypothesis [22], Cauchy relations (7), and interpolation dependence (11), can be represented by the matrix relation

$$\left\{\varepsilon^{\zeta}_{\rho\gamma}\right\}=\underset{3\times6}{\left[D_{\varepsilon}\right]}\underset{6\times1}{\left\{\varepsilon_{\rho\gamma}\right\}}=\underset{3\times6}{\left[D_{\varepsilon}\right]}\underset{3\times36}{\left[B\right]}\underset{36\times1}{\left\{u^L\right\}}=\underset{3\times6}{\left[D_{\varepsilon}\right]}\underset{3\times36}{\left[B\right]}\underset{36\times36}{\left[T\right]}\underset{36\times1}{\left\{u^G\right\}}, \tag{15}$$

where $\underset{3\times6}{\left[D_{\varepsilon}\right]}=\begin{bmatrix}1 & 0 & 0 & \zeta & 0 & 0\\ 0 & 1 & 0 & 0 & \zeta & 0\\ 0 & 0 & 1 & 0 & 0 & \zeta\end{bmatrix}$; $\underset{1\times6}{\left\{\varepsilon^{\rho\gamma}\right\}^T}=\left\{\varepsilon_{11}\varepsilon_{22}2\varepsilon_{12}\aleph_{11}\aleph_{22}2\aleph_{12}\right\}$ is a column of deformations and curvatures at point M of the middle surface; $\underset{1\times36}{\left\{u^L\right\}^T}=\left\{\underset{1\times12}{\left\{v^{1L}\right\}^T}\underset{1\times12}{\left\{v^{2L}\right\}^T}\underset{1\times12}{\left\{v^{L}\right\}^T}\right\}$;
$\underset{1\times36}{\left\{u^G\right\}^T}=\left\{\underset{1\times12}{\left\{v^{1G}\right\}^T}\underset{1\times12}{\left\{v^{2G}\right\}^T}\underset{1\times12}{\left\{v^{G}\right\}^T}\right\}$; $\left[T\right]$ is transformation matrix of the column of kinematic quantities from the local coordinate system ξ, η to the global one x, t.

The column of power variable parameters $\left\{NM\right\}$ is interpolated through its nodal values using relations (10)

$$\underset{6\times1}{\left\{NM\right\}}=\underset{6\times24}{\left[H\right]}\underset{24\times1}{\left\{G^{\alpha\beta}\right\}}, \tag{16}$$

where $\left\{G^{\alpha\beta}\right\}^T=\left\{\underset{1\times4}{\left\{N^{11}\right\}^T}\underset{1\times4}{\left\{N^{22}\right\}^T}\underset{1\times4}{\left\{N^{12}\right\}^T}\underset{1\times4}{\left\{M^{11}\right\}^T}\underset{1\times4}{\left\{M^{22}\right\}^T}\underset{1\times4}{\left\{M^{12}\right\}^T}\right\}.$

Functional (12), taking into account (14) and (16), can be represented as

$$
\begin{gathered}
\Pi_S = \underset{1\times24}{\left\{G^{\alpha\beta}\right\}^T} \int\limits_V \underset{24\times6}{\left[H\right]^T} \underset{6\times3}{\left[D_\sigma\right]^T} \underset{3\times6}{\left[D_\varepsilon\right]} \underset{6\times36}{\left[B\right]} dV \underset{36\times36}{\left[T\right]} \underset{36\times1}{\left\{u^G\right\}} - \\
- 0.5 \underset{1\times24}{\left\{G^{\alpha\beta}\right\}^T} \int\limits_V \underset{24\times6}{\left[H\right]^T} \underset{6\times3}{\left[D_\sigma\right]^T} \underset{3\times3}{\left[C\right]} \underset{3\times6}{\left[D_\sigma\right]} \underset{6\times24}{\left[H\right]} dV \underset{24\times1}{\left\{G^{\alpha\beta}\right\}} - \\
- 0.5 \underset{1\times36}{\left\{u^G\right\}^T} \underset{36\times36}{\left[T\right]^T} \int\limits_F \underset{36\times3}{\left[A\right]^T} \underset{3\times1}{\left\{P\right\}} dF,
\end{gathered} \tag{17}
$$

where $\underset{3\times36}{\left[A\right]} = \begin{bmatrix} \underset{1\times12}{\{\psi\}^T} & 0 & 0 \\ 0 & \underset{1\times12}{\{\psi\}^T} & 0 \\ 0 & 0 & \underset{1\times12}{\{\psi\}^T} \end{bmatrix}.$

Applying to (17) the procedure of minimization with respect to the required unknowns $\left\{G^{\alpha\beta}\right\}^T$, we can obtain the following matrix expression

$$
\partial\Pi_S \Big/ \partial\left\{G^{\alpha\beta}\right\}^T = \underset{24\times36}{\left[S\right]} \underset{36\times1}{\left\{u^G\right\}} - \underset{24\times24}{\left[Z\right]} \underset{24\times1}{\left\{G^{\alpha\beta}\right\}} = 0, \tag{18}
$$

where $\underset{24\times36}{\left[S\right]} = \int\limits_V \underset{24\times6}{\left[H\right]^T} \underset{6\times3}{\left[D_\sigma\right]^T} \underset{3\times6}{\left[D_\varepsilon\right]} \underset{6\times36}{\left[B\right]} dV \underset{36\times36}{\left[V\right]}; \quad \underset{24\times24}{\left[Z\right]} = \int\limits_V \underset{24\times6}{\left[H\right]^T} \underset{6\times3}{\left[D_\sigma\right]^T} \underset{3\times3}{\left[C\right]} \underset{3\times6}{\left[D_\sigma\right]} \underset{6\times24}{\left[H\right]} dV.$

The first integral in functional (12) can be represented in the following form

$$
\begin{gathered}
\int\limits_V \underset{1\times3}{\left\{\sigma^{\rho\gamma}\right\}} \underset{3\times1}{\left\{\varepsilon^{\zeta}_{\rho\gamma}\right\}} dV = \int\limits_V \underset{1\times3}{\left\{\varepsilon^{\zeta}_{\rho\gamma}\right\}^T} \underset{3\times1}{\left\{\sigma^{\rho\gamma}\right\}} dV = \\
= \underset{1\times36}{\left\{u^G\right\}^T} \underset{36\times36}{\left[T\right]^T} \int\limits_V \underset{36\times6}{\left[B\right]^T} \underset{6\times3}{\left[D_\varepsilon\right]^T} \underset{3\times6}{\left[D_\sigma\right]^T} \underset{6\times24}{\left[H\right]} dV \underset{24\times1}{\left\{G^{\alpha\beta}\right\}}.
\end{gathered} \tag{19}
$$

By minimizing the functional (17) taking into account (19) with respect to the kinematic unknown unknowns $\left\{u^G\right\}^T$, we can write the following matrix relation

$$
\partial\Pi_S \Big/ \partial\left\{u^G\right\}^T = \underset{36\times24}{\left[S\right]^T} \underset{24\times1}{\left\{G^{\alpha\beta}\right\}} - \underset{36\times1}{\left\{R\right\}} = 0, \tag{20}
$$

where $\left\{R\right\} = \left[T\right]^T \int\limits_F \left[A\right]^T \left\{P\right\} dF.$

The system of equations obtained as a result of minimizing the functional Π_S with respect to $\left\{G^{\alpha\beta}\right\}^T$ and $\left\{u^G\right\}^T$ can be represented in the matrix form

$$
\begin{bmatrix} -\underset{24\times24}{\left[Z\right]} & \underset{24\times36}{\left[S\right]} \\ \underset{36\times24}{\left[S\right]^T} & \underset{36\times36}{\left[0\right]} \end{bmatrix} \begin{Bmatrix} \underset{24\times1}{\left\{G^{\alpha\beta}\right\}} \\ \underset{36\times1}{\left\{u^G\right\}} \end{Bmatrix} = \begin{Bmatrix} \underset{24\times1}{\left\{0\right\}} \\ \underset{36\times1}{\left\{R\right\}} \end{Bmatrix} \tag{21}
$$

or in a more compact form

$$\underset{60\times60}{[K]}\underset{60\times1}{\left\{U^G\right\}}=\underset{60\times1}{\{f\}},\tag{22}$$

where $\underset{60\times60}{[K]}=\begin{bmatrix}-\underset{24\times24}{[Z]} & \underset{24\times36}{[Z]}\\ \underset{36\times24}{[S]^T} & \underset{36\times36}{[0]}\end{bmatrix}$ is the flexibility matrix of a four-node sampling element; $\underset{1\times60}{\{f\}^T}=\left\{\underset{1\times24}{\{0\}^T}\;\underset{1\times36}{\{R\}^T}\right\}$ is column of nodal forces.

An analysis of the structures of matrices $[Z]$ and $[S]$ in the compliance matrix $[K]$ shows that matrix $[K]$ is also a determinable value in the case of an incompressible material at a transverse strain coefficient of $\nu=0.5.$

Analyzing the resulting compliance matrix $[K],$ it can be noted that it contains a significant zero block $\underset{36\times36}{[0]}$, which can significantly reduce the conditionality of the global compliance matrix of the entire shell-type structure. To eliminate this problem, this paper proposes to carry out the following transformations.

Let us express from equation (18) the column of force nodal unknowns

$$\underset{24\times1}{\left\{G^{\alpha\beta}\right\}}=\underset{24\times24}{[Z]^{-1}}\underset{24\times36}{[S]}\underset{36\times1}{\left\{u^G\right\}}\tag{23}$$

and substitute relation (23) into equation (20)

$$\underset{36\times24}{[S]^T}\underset{24\times24}{[Z]^{-1}}\underset{24\times36}{[S]}\underset{36\times1}{\left\{u^G\right\}}-\underset{36\times1}{\{R\}}=0.\tag{24}$$

Transforming (24), we can obtain the following matrix expression

$$\underset{36\times36}{[L]^T}=\underset{36\times1}{\left\{u^G\right\}}=\underset{36\times1}{\{R\}},\tag{25}$$

where $\underset{36\times36}{[L]}=\underset{36\times24}{[S]^T}\underset{24\times24}{[Z]^{-1}}\underset{24\times36}{[S]}$ is the modified compliance matrix of the four-node bin.

Analyzing (25), it can be noted that $\underset{36\times36}{[L]}$ does not contain a zero block and differs from $\underset{60\times60}{[K]}$ in a significantly smaller dimension, which reduces the requirements for the amount of RAM used by computer equipment when studying the stress-strain state of a thin-walled shell-type structure.

Based on the obtained modified compliance matrix $\underset{36\times36}{[L]}$, with the help of the index matrix [28], the global compliance matrix of the entire calculated thin-walled shell-type structure is assembled and the solution of the global system of algebraic equations is performed, the unknowns of which are only the kinematic nodal unknowns $\left\{u^G\right\}.$

After calculating the kinematic nodal unknowns $\left\{u^G\right\}$ using (23), without any difficulty, one can obtain the values of the desired force unknowns at any point of interest to the designer in the considered thin-walled shell-type structure.

Verification of the developed computational algorithm based on the use of the modified compliance matrix of the four-node discretization element $\underset{36\times36}{[L]}$ was performed on specific calculation examples.

3. Results and Discussion

Calculation example 1. As a test example, a circular cylinder was calculated, rigidly clamped on the right end and having a free edge on the left end. The radius vector (1) in this case will look like

$$\vec{R}^0 = x\vec{i} + R\sin t\ \vec{j} + R\cos t\ \vec{k}. \tag{26}$$

The cylinder was loaded with an internal pressure of intensity q_w and a uniformly distributed axial load q_u applied along the free left end. The design scheme of the shell is shown in Fig. 1.

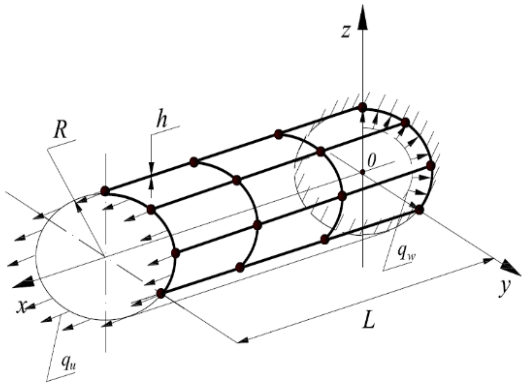

Figure 1. Calculation scheme of a circular cylinder with a uniformly distributed axial load q_u and internal pressure q_w.

The following initial values are accepted: R = 0.9 m; h = 0.02 m; L = 0.8 m; E = 2·10^5 MPa; ν = 0.3; q_w = 5 MPa; q_u = 500 kN/m.

The values of stresses in the edge sections of the shell are presented in Table 1 for various variants of discretization of the shell fragment, considered according to the symmetry conditions.

Table 1. Stress values in sections of a cylindrical shell.

Characteristic section	Stress, MPa	Grid of Discretization Nodes				Analytical Solution
		21×21	41×41	51×51	61×61	
Rigid termination	σ_{11}^{in}	410.5	417.5	418.3	418.8	–
	σ_{11}^{out}	–360.5	–367.5	–368.3	–368.8	–
	σ_{11}^{midl}	25.00	25.00	25.00	25.00	25.00
	σ_{22}^{in}	117.5	122.3	123.0	123.3	–
	σ_{22}^{out}	–113.7	–113.1	–113.0	–112.9	–
	σ_{22}^{midl}	4.48	7.24	7.62	7.84	–
Free end	σ_{11}^{in}	24.98	24.99	25.00	25.00	–
	σ_{11}^{out}	25.02	25.01	25.00	25.00	–
	σ_{11}^{midl}	25.00	25.00	25.00	25.00	25.00
	σ_{22}^{in}	226.8	226.8	226.8	226.8	–
	σ_{22}^{out}	222.0	222.0	222.0	222.0	–
	σ_{22}^{midl}	224.5	224.5	224.5	224.5	225.0

An analysis of the data presented in Table 1 allows us to state the fact of a fairly fast convergence of the computational process as the grid of discretization nodes thickens. In addition, it should be noted that the numerical values of normal stresses correspond to the physical meaning of the problem being solved. Meridional stresses σ_{11} on the middle surface in the outer and inner fibers of the edge sections of the cylindrical shell correspond to a given axial external load

$$\sigma_{11}^{midl} = q_u / h = 500 \text{ kN/m}/0.02 \text{ m} = 25.0 \text{ MPa}.$$

Ring stresses of the middle surface at the free end of the cylinder σ_{22}^{midl} = 224.5 MPa correspond to the specified internal pressure q_w with an acceptable level of error δ = 0.22 %.

$$\sigma_{22}^{midl} = \frac{q_w \cdot R}{h} = \frac{5 \text{ MPa} \cdot 0.9 \text{ m}}{0.02 \text{ m}} = 225.0 \text{ MPa}.$$

The developed algorithm for determining the stress-strain state of thin shells, which implements a mixed version of the FEM, makes it possible to immediately obtain internal force factors (longitudinal forces and bending moments) at any point of the shell structure of interest to the researcher without excessive labor-intensive calculations. "Physical" values of forces and moments in the edge sections of the cylindrical shell, referred to the middle surface, are presented in Table 2, the structure of which is similar to Table 1.

Table 2. Values of forces and moments in a circular cylinder.

Characteristic section	Efforts, N; moments, N·m	Grid of discretization nodes				Analytical Solution
		21×21	41×41	51×51	61×61	
Rigid termination	N_{11}	500.0	500.0	500.0	500.0	500.0
	N_{22}	89.7	144.7	152.5	156.8	–
	M_{11}	–2570.0	–2616.6	–2622.3	–2625.4	–
	M_{22}	–771.2	–785.8	–787.6	–788.6	–
Free end	N_{11}	500.0	500.0	500.0	500.0	500.0
	N_{22}	4490.5	4490.3	4490.3	4490.3	4500.0
	M_{11}	0.131	0.035	0.023	0.016	0.000
	M_{22}	–49.3	–49.3	–49.3	–49.3	–

The data in Table 2 testify to the stable convergence of the computational process in terms of forces and moments. The values of the axial longitudinal forces N_{11} in the edge sections of the cylindrical shell correspond to a given axial load of q_u = 500 kN/m. The value of the longitudinal ring force also corresponds to a given internal pressure q_w with a minimum error δ = 0.2 %.

The bending moment M_{11} tends monotonically to zero in the end section.

On the basis of the foregoing, it can be concluded that the developed algorithm is correct and that the accuracy of calculating the controlled strength parameters of the SSS of shell structures is sufficient for engineering practice.

Calculation example 2. The stress-strain state of a cylindrical shell with an elliptical cross section, rigidly fixed at the ends, loaded with an internal pressure of q = 5 MPa is determined. Due to the presence of symmetry, 1/8 of the shell was considered. The design scheme is shown in Fig. 2.

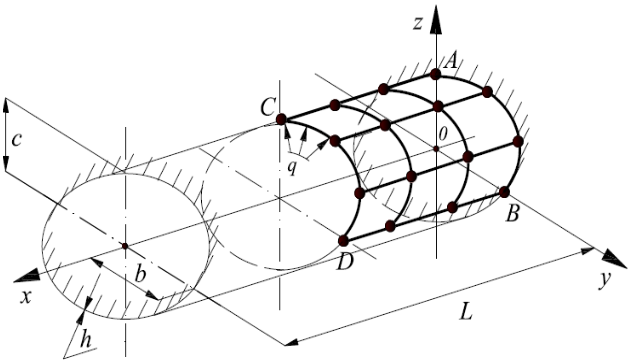

Figure 2. Calculation scheme of a cylindrical shell with elliptical cross section.

The radius vector expression (1) for an elliptical cylinder will look like this:

$$\vec{R}^0 = x\vec{i} + b\sin t\,\vec{j} + c\cos t\,\vec{k}. \tag{27}$$

In the problem under consideration, the following initial data are accepted: b = 1.0 m; c = 0.8 m; L = 1.0 m; h = 0.02 m; E = 2·10^5 MPa; ν = 0.3.

The values of normal stresses and bending moments in the shell sections for various variants of discretization of the calculated fragment of the shell are presented in Table 3.

Table 3. Values of normal stresses and bending moments in an elliptical cylinder.

Characteristic section	Stress, MPa; moments, N•m	Grid of discretization nodes					Solution in the formulation of the displacement method, 61×61
		41×41	51×51	61×61	81×81	101×101	
Rigid termination, x = 0.0; t = 0.0 rad. (point A)	σ_{11}^{in}	642.1	642.4	642.5	642.7	642.8	642.4
	σ_{11}^{out}	–544.6	–544.9	–545.0	–545.2	–545.2	–544.8
	σ_{22}^{in}	183.5	185.1	186.1	187.4	188.1	192.7
	σ_{22}^{out}	–172.5	–171.1	–170.1	–169.0	–168.3	–163.4
	M_{11}	–395.6	–395.8	–395.8	–396.0	–396.0	–
	M_{22}	–118.7	–118.8	–118.9	–118.9	–118.9	–
Rigid termination, x = 0.0; $t = \pi/2$ rad. (point B)	σ_{11}^{in}	264.8	265.2	265.4	265.6	265.7	265.5
	σ_{11}^{out}	–118.3	–118.7	–118.9	–119.1	–119.2	–119.0
	σ_{22}^{in}	85.21	84.00	83.16	82.06	81.38	79.65
	σ_{22}^{out}	–29.70	–31.12	–32.10	–33.32	–34.06	–35.70
	M_{11}	–127.7	–128.0	–128.1	–128.2	–128.3	–
	M_{22}	–38.90	–38.95	–39.00	–39.00	–39.00	–
Mid-span, $x = L/2$; t = 0.0 rad. (point C)	σ_{11}^{in}	71.35	71.34	71.33	71.33	71.32	71.27
	σ_{11}^{out}	95.77	95.79	95.80	95.80	95.81	95.67
	σ_{22}^{in}	312.4	312.3	312.3	312.3	312.3	312.0
	σ_{22}^{out}	338.5	338.5	338.5	338.5	338.5	338.1

Characteristic section	Stress, MPa; moments, N•m	Grid of discretization nodes					Solution in the formulation of the displacement method, 61×61
		41×41	51×51	61×61	81×81	101×101	
Mid-span, $x = L / 2$; $t = \pi / 2$ rad. (point D)	σ_{11}^{in}	37.72	37.72	37.73	37.73	37.73	37.84
	σ_{11}^{out}	9.81	9.81	9.81	9.81	9.81	9.83
	σ_{22}^{in}	173.9	173.9	174.0	174.0	174.0	174.7
	σ_{22}^{out}	144.2	144.2	144.2	144.3	144.3	144.8

As follows from the analysis of tabular data, the convergence of the computational process in terms of both stresses and moments is very stable. In order to verify the developed algorithm, the rightmost column contains the stress values found based on the use of a quadrangular finite element, the stiffness matrix of which was composed on the basis of a finite element procedure in the formulation of the displacement method [27]. As shown by a comparative analysis of the finite element solutions obtained on the basis of the developed algorithm, and the FEM in the formulation of the displacement method, the numerical values of the normal stresses practically coincide at all characteristic points with an acceptable minimum discrepancy in the values of σ_{22} at points A and B. When performing this comparative analysis one should take into account the fact that when implementing the developed algorithm in a mixed formulation, it is possible to directly obtain the numerical values of force factors (forces and moments) and stresses at any of the nodal points of the calculated shell. When using FEM in the formulation of the displacement method, to obtain numerical values of stresses, it is required to perform several stages of computational procedures, namely: after obtaining the displacement values and their first derivatives, it is necessary to calculate the values of the second derivatives of the normal displacement using an interpolation procedure. Then, using the Cauchy relation [22], it is necessary to calculate the deformations of the midsurface point. Next, it is necessary to proceed, on the basis of the Kirchhoff-Love hypotheses, to deformations at a point of an arbitrary layer of the shell, and only after that, using the relations of Hooke's law, it is possible to obtain the stress values. All the above computational procedures complicate the calculation algorithm and increase the calculation error. The use of a mixed formulation of the FEM implemented in the developed algorithm makes it possible to avoid additional cumbersome computational procedures and makes it possible to directly obtain the desired strength parameters of the calculated shell structure, which ultimately makes the developed algorithm the most preferable in the analysis of SSS of shell structures of various configurations.

Calculation example 3. The quadrangular discretization element developed in this work in a mixed formulation can be effectively used to study the SSS of shells made of an incompressible material. The problem was solved to determine the strength parameters of an elliptical cylinder, the design scheme, the geometric and physical characteristics of which coincide with the data of calculation example 2. The difference was that Poisson's ratio was taken equal to $\nu = 0.5$, i.e. it was assumed that the shell is made of an incompressible material. The results of the numerical experiment are presented in tabular and graphical forms. Table No. 4, the structure of which is similar to the structure of Table No. 3, presents the numerical values of normal stresses and bending moments in the support and span sections of an elliptical cylinder, depending on the degree of refinement of the grid of discretization nodes of the calculated shell fragment. Analyzing the tabular data, one can state the stable convergence of the computational process as the grid of discretization nodes becomes denser.

Table 4. Values of normal stresses and bending moments in an elliptical cylinder made of incompressible material.

Characteristic section	Stress, MPa; moments, N•m	Grid of discretization nodes				
		41×41	51×51	61×61	81×81	101×101
Rigid termination, x = 0.0; t = 0.0 rad. (point A)	σ_{11}^{in}	689.8	690.0	690.1	690.2	690.3
	σ_{11}^{out}	–493.3	–493.5	–493.6	–493.7	–493.8
	σ_{22}^{in}	334.4	336.0	337.1	338.4	339.1
	σ_{22}^{out}	–257.0	–255.6	–254.7	–253.6	–252.9
	M_{11}	–394.3	–394.5	–394.6	–394.6	–394.7
	M_{22}	–197.6	–197.7	–197.8	–197.8	–197.8
Rigid termination, x = 0.0; $t = \pi / 2$ rad. (point B)	σ_{11}^{in}	247.8	248.1	248.3	248.5	248.6
	σ_{11}^{out}	–41.27	–41.60	–41.77	–41.95	–42.03
	σ_{22}^{in}	129.5	128.3	127.4	126.3	125.7
	σ_{22}^{out}	–14.97	–16.52	–17.55	–18.83	–19.60
	M_{11}	–96.36	–96.57	–96.69	–96.81	–96.86
	M_{22}	–49.39	–49.47	–49.51	–49.55	–49.56
Mid-span, $x = L$ / 2; t = 0.0 rad. (point C)	σ_{11}^{in}	108.7	108.7	108.7	108.7	108.7
	σ_{11}^{out}	156.3	156.3	156.3	156.3	156.3
	σ_{22}^{in}	305.4	305.4	305.4	305.4	305.4
	σ_{22}^{out}	347.3	347.2	347.2	347.2	347.2
Mid-span, $x = L$ / 2; $t = \pi$ / 2 rad. (point D)	σ_{11}^{in}	73.92	73.92	73.92	73.91	73.91
	σ_{11}^{out}	34.0	34.0	34.0	34.0	34.0
	σ_{22}^{in}	179.4	179.4	179.4	179.5	179.5
	σ_{22}^{out}	139.2	139.2	139.3	139.3	139.3

Fig. 3 shows the graphs of changes in normal stresses on the inner σ^{in} and outer σ^{out} surfaces of the shell, as well as bending moments M_{11}, M_{22} on the middle surface along the generatrix of the elliptical cylinder.

The analysis of the graphical material shows that the maximum values of the edge effect appear directly in the rigid embedment, gradually fading towards the zone located at a distance of 0.1 L from the reference section, which corresponds to the physical meaning of the problem being solved.

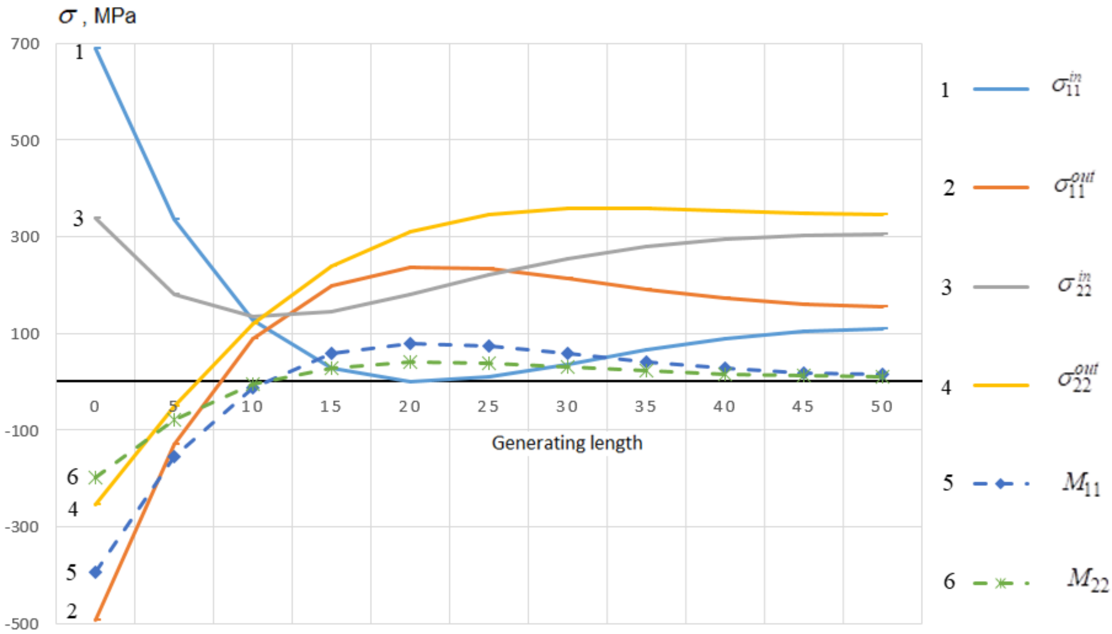

Figure 3. Diagrams of normal stresses and bending moments along the generatrix at *t* = 0.0 rad.

Fig. 4 shows the changes in the normal stresses σ^{in} and σ^{out}, as well as the bending moment M_{11}, M_{22} along the arc of the shell cross section in a rigid enclosure (x = 0.0 m).

Analyzing the graphs presented in Figure 4, it can be noted that the controlled strength characteristics (normal stresses and bending moments) reach a maximum at the value of parameter t equal to zero. Then the values of normal stresses and bending moments gradually decrease (by about two times) to their minimum values in the reference section at the value of parameter t equal to $\pi/2$.

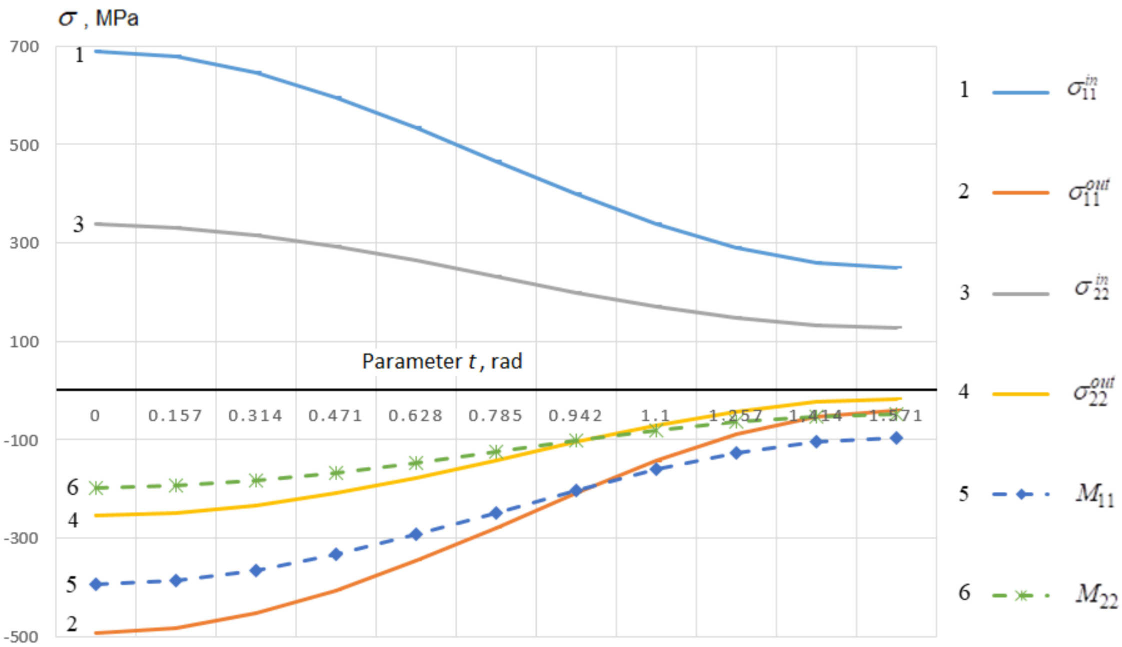

Figure 4. Diagrams of normal stresses and bending moments in rigid termination at *x* = 0.0 m.

4. Conclusions

Taking into account the results of the numerical studies, we can draw the following conclusions.

1. The convergence of the computational process using the developed finite element in a mixed formulation is stable in terms of both force and kinematic factors.

2. The obtained numerical values of the stresses at the controlled points are in adequate agreement with the stress values found from the conditions of static equilibrium (the calculation error does not exceed 0.5 %).

3. The use of the developed mixed finite element leads to the possibility of determining the power parameters directly as a result of solving the system of resolving equations.

4. The developed finite element in a mixed formulation is suitable for determining the SSS of thin-walled structures made of incompressible materials ($\nu = 0.5$).

References

1. Krysko, A.V., Awrejcewicz, J., Bodyagina, K.S., Zhigalov, M.V., Krysko, V.A. Mathematical Modeling of Physically Nonlinear 3D Beams and Plates Made of Multimodulus Materials. Acta Mechanica. 2021. 232 (2). Pp. 3441–3469. DOI: 10.1007/s00707-021-03010-8
2. Storozhuk, E.A. Stress–Strain State and Stability of a Flexible Circular Cylindrical Shell with Transverse Shear Strains. International Applied Mechanics. 2021. 57 (5). Pp. 554–567. DOI: 10.1007/s10778-021-01106-1
3. Abrosov, Y.Y., Maximyuk, V.A., Chernyshenko, I.S. Physically Nonlinear Deformation of a Long Orthotropic Cylindrical Shell with Elliptic Cross-Section. International Applied Mechanics. 2021. 57. Pp. 282–289. DOI: 10.1007/s10778-021-01079-1
4. Raspopina, V., Perelygina, A., Shemetov, L., Grigorov, P. Dependence between the Mechanical Characteristics of the Material and the FDM Sample Made From This Material. Safety in Aviation and Space Technologies. Select Proceedings of the 9th World Congress "Aviation in the XXI Century". Cham, 2022. Pp. 215–227. DOI: 10.1007/978-3-030-85057-9_18
5. Paimushin, V.N., Gazizullin, R.K., Polyakova, N.V., Shishov, M.A. Sandwich Shells with Composite Facings and a Transversally Flexible Core: Refined Equations and Buckling Modes of Specimens under Four-Point Bending Tests. Advanced Structured Materials. 2021. 141. Pp. 391–411. DOI: 10.1007/978-3-030-54928-2_29
6. Ubaydulloev, M.N., Serazutdinov, M.N. Simulation and Calculation of Stress–Strain State of Thin-Walled Structures Strengthened under Load. Lecture Notes in Mechanical Engineering. 2022. Pp. 332–340. DOI: 10.1007/978-3-030-85233-7_40
7. Rozin, L.A. Zadachi teorii uprugosti i chislennyye metody ikh resheniya [Problems of the theory of elasticity and numerical methods for their solution]. St. Petersburg: Publishing house of SPbSTU, 1998. 531 p.
8. Klochkov, Y.V., Nikolaev, A.P., Vakhnina, O.V. Calculation of Rotation Shells Using Finite Triangular Elements with Lagrange Multipliers in Variative Approximation of Displacements. Journal of Machinery Manufacture and Reliability. 2016. 45 (1). Pp. 51–58. DOI: 10.3103/S1052618816010076
9. Leonetti, L., Magisano, D., Madeo, A., Garcea, G., Kiendl, J., Reali, A. A simplified Kirchhoff–Love large deformation model for elastic shells and its effective isogeometric formulation. Computer Methods in Applied Mechanics and Engineering. 2019. 354. Pp. 369–396. DOI: 10.1016/j.cma.2019.05.025
10. Lalin, V., Rybakov, V., Sergey, A. The finite elements for design of frame of thin-walled beams. Applied Mechanics and Materials. 2014. 578–579. Pp. 858–863. https://doi.org/10.4028/www.scientific.net/amm.578-579.858
11. Tyukalov, Yu.Ya. Quadrilateral Finite Element for Thin and Thick Plates. Construction of Unique Buildings and Structures. 2021. 5 (98). Pp. 9802. DOI: 10.4123/CUBS.98.2
12. Rozin, L.A., Terpugov, V.N. Variatsionnyye zadachi uprugogo ravnovesiya s odnovremenno zadannymi skachkami napryazheniy i peremeshcheniy [Variational problems of elastic equilibrium with simultaneously given jumps of stresses and displacements]. Scientific and technical statements of the St. Petersburg State Polytechnic University. 2009. 1 (74). Pp. 65–72. (rus)
13. Klochkov, Yu., Nikolaev, A., Vakhnina, O., Sobolevskaya, T., Klochkov, M. Physically Nonlinear Shell Deformation Based on Three-Dimensional Finite Elements. Magazine of Civil Engineering. 2022. 5 (113). Pp. 11314. DOI: 10.34910/MCE.113.14
14. Sultanov, L.U. Analysis of Finite Elasto-Plastic Strains: Integration Algorithm and Numerical Examples. Lobachevskii Journal of Mathematics. 2018. 39 (9). Pp. 1478–1483. DOI: 10.1134/S1995080218090056
15. Zheleznov, L.P., Kabanov, V.V., Boiko, D.V. Nonlinear Deformation and Stability of Discrete-Reinforced Elliptical Cylindrical Composite Shells under Torsion and Internal Pressure. Russian Aeronautics. 2018. 61 (2). Pp. 175–182. DOI: 10.3103/S1068799818020046
16. Bakulin, V.N. Model for Analysis of the Stress-Strain State of Three-Layer Cylindrical Shells with Rectangular Cutouts. Mechanics of Solids. 2022. 57 (1). Pp. 102–110. DOI: 10.3103/S0025654422010095
17. Agapov, V. The Family of Multilayered Finite Elements for the Analysis of Plates and Shells of Variable Thickness. E3S Web of Conferences. 2018 Topical Problems of Architecture, Civil Engineering and Environmental Economics, TPACEE 2018. 2019. Pp. 02013. DOI: 10.1051/e3sconf/20199102013
18. Lalin, V.V., Rybakov, V.A., Ivanov, S.S., Azarov, A.A. Mixed finite-element method in V.I. Slivker's semi-shear thin-walled bar theory. Magazine of Civil Engineering. 2019. 5 (89). P. 79–93. DOI: 10.18720/MCE.89.7
19. Magisano, D., Liang, K., Garcea, G., Leonetti, L., Ruess, M. An efficient mixed variational reduced-order model formulation for nonlinear analyses of elastic shells. International Journal for Numerical Methods in Engineering. 2018. 113 (4). Pp. 634–655. DOI: 10.1002/nme.5629
20. Garcea, G., Liguori, F.S., Leonetti, L., Magisano, D., Madeo, A. Accurate and efficient a posteriori account of geometrical imperfections in Koiter finite element analysis. Int. J. Numer. Methods Eng. 2017. 112 (9). Pp. 1154–1174. DOI: 10.1002/nme.5550
21. Yakupov, S.N., Kiyamov, H.G., Yakupov, N.M. Modeling a Synthesized Element of Complex Geometry Based Upon Three-Dimensional and Two-Dimensional Finite Elements. Lobachevskii Journal of Mathematics. 2021. 42 (9). Pp. 2263–2271. DOI: 10.1134/S1995080221090316
22. Novozhilov, V.V. Teoriya tonkikh obolochek [Theory of thin shells]. St. Petersburg: Publishing House of the St. Petersburg University, 2010. 378 p.
23. Rickards, R.B. Metod konechnykh elementov v teorii obolochek i plastin [Finite element method in the theory of shells and plates]. Riga: Known, 1988. 284 p.

24. Lei, Zh., Gillot, F., Jezeguel, L. Developments of the mixed grid isogeometric Reissner-Mindlin shell: serendipity basis and modified reduced. Int. J. Mech. 2015. 54. Pp. 105–119.
25. Pogorelov, A.V. Differentsial'naya geometriya [Differential geometry]. 6th ed., stereotype. Moscow: Nauka, 1974. 176 p.
26. Sedov, L.I. Mekhanika sploshnoy sredy [Mechanics of a continuous medium]. v. 1. Moscow: Nauka, 1976. 536 p.
27. Klochkov, Yu.V., Nikolaev, A.P., Sobolevskaya, T.A., Vakhnina, O.V., Klochkov, M.Yu. The calculation of the ellipsoidal shell based FEM with vector interpolation of displacements when the variable parameterisation of the middle surface. Lobachevskii Journal of Mathematics. 2020. 41 (3). Pp. 373–381. DOI: 10.1134/S1995080220030117
28. Postnov, V.A., Kharkhurim, I.Ya. Metod konechnykh elementov v raschetakh sudovykh konstruktsiy [Finite element method in calculations of ship structures]. L .: Shipbuilding, 1974. 342 p.

Information about authors:

Yuriy Klochkov, *Doctor of Technical Sciences*
ORCID: https://orcid.org/0000-0002-1027-1811
E-mail: klotchkov@bk.ru

Valeria Pshenichkina, *Doctor of Technical Sciences*
ORCID: https://orcid.org/0000-0001-9148-2815
E-mail: vap_hm@list.ru

Anatoly Nikolaev, *Doctor of Technical Sciences*
ORCID: https://orcid.org/0000-0002-7098-5998
E-mail: anpetr40@yandex.ru

Olga Vakhnina, *PhD in Technical Sciences*
ORCID: https://orcid.org/0000-0001-9234-7287
E-mail: ovahnina@bk.ru

Mikhail Klochkov,
ORCID: https://orcid.org/0000-0001-6751-4629
E-mail: m.klo4koff@yandex.ru

Received 01.03.2023. Approved after reviewing 26.04.2023. Accepted 27.04.2023.

Magazine of Civil Engineering

ISSN 2712-8172

journal homepage: http://engstroy.spbstu.ru/

Research article

UDC 692.526

DOI: 10.34910/MCE.120.4

Behavior of timber-timber composite structure connected by inclined screws

T.P. Chernova[1,2] ✉ **,** ***V.I. Melekhov***[2]

[1] *Department of State Expertise, Arkhangelsk, Russian Federation*

[2] *Northern (Arctic) Federal University named after M.V. Lomonosov, Arkhangelsk, Russian Federation*

✉ *zhuravleva.t.pav@mail.ru*

Keywords: stress-strain state, cross laminated timber (CLT), glulam (GLT), bending tests, timber-timber composite (TTC), dowels, inclined screws, strength, stiffness, finite element method, numerical model

Abstract. The behavior of timber composite structure made of cross laminated timber (CLT) panel and glued laminated timber (GLT) beam was considered in this paper. Bending tests of a CLT-GLT composite structures with and without fasteners were conducted. CLT panel and GLT beam were connected by screws installed at a 45° angle to the GLT axis grain. It was experimentally proved that the application of inclined screws increases the strength of the CLT-GLT composite structure by 1.3 and 1.6 times, stiffness – by 1.6 and 2.1 times, shear capacity – by 2.1 and 3.5 times for two orientation types of CLT panel (CI and CII), respectively. Two types of CLT panel orientations were considered: with the top layer oriented parallel to the GLT axis (CI) and oriented perpendicular to the GLT axis (CII). The CLT-GLT composite structure with the top layer oriented parallel to the axis of the GLT beam has 50 % more strength and 14 % more stiffness than a composite structure with the top layer oriented perpendicular to the GLT axis. Based on numerical and experimental results, a design procedure was suggested to determine the strength and strain characteristics of the CLT-GLT composite structure connected by inclined screws.

Funding: The authors acknowledge the financial support given to this study by the Foundation for Assistance to Small Innovative Enterprises, the program “U. M. N. I. K.” (contract No. 14123GU/2019 dated 10.06.2019).

Acknowledgements: The authors also gratefully acknowledge the support given to this study by LLC Promstroyles.

Citation: Chernova, T.P., Melekhov, V.I. Behavior of timber-timber composite structure connected by inclined screws. Magazine of Civil Engineering. 2023. 120(4). Article no. 12004. DOI: 10.34910/MCE.120.4

1. Introduction

The successful development of engineered wood products (such as CLT, LVL, OSB, etc.), nowadays a building materials of global interest, offered further favorable opportunities for copious application of construction wood. One of the directions for the application of engineered wood products is the research of new design solutions for CLT composite structures.

In the composite structures the CLT panel is connected with GLT beam in forms of a ribbed or box-shaped cross-section, supported by metal beams or profiled sheeting, formed into a timber-concrete composite structure, i.e. timber composite systems (Fig. 1, a-d).

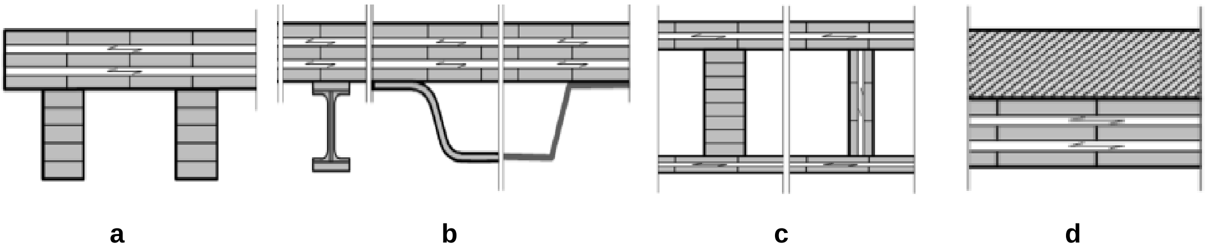

Figure 1. Timber composite systems [1]: a – ribbed cross-section of the CLT-GLT structure; b – CLT with metal beams; c – box-shaped cross-section of the CLT-GLT structure; d – composite cross-section of CLT-concrete.

CLT panels formed into steel-timber composite (STC) were considered by [2, 3], etc.; timber-concrete composite (TCC) – by [4–9], etc.; timber-timber composite (TTC) – by [10–24], etc.

The research results of timber composite structures connected by screws were given in the papers of J.M. Branco [11], A.A. Chiniforush [12], I. Giongo [14, 15], R. Masoudnia [18–21], D. Riccadonna [22], G. Schiro [23], etc.; by glued perforated steel plates – in the paper of J. Estévez-Cimadevila [13], etc.; by punched metal plates – in the papers of N. Jacquier [16, 17], etc.; by glue – in the papers of S. Aicher [10], I. Sustersic [24], etc.

The studies of R. Masoudnia et al. [18–21] present the effect of the panel and beam configuration on the effective flange width of timber composite beam. Research of J.M. Branco et al. [11] confirms the increase in strength and stiffness characteristics of TTC connections with screws installed at an angle of 45° to the grain of wood, compared with TTC connections with screws installed perpendicular to the grain of wood.

The issues of composite action between elements and reinforcement of timber composite structures by dowel fasteners installed at an angle to the grain of wood were investigated by [25–31], etc.

The research results of reinforcement of timber composite structures by screws were given in the papers [25–27]; by glued-in steel rods – in papers [28, 29]; by screws with anchorage details – in paper [30]; by twisted cruciform rods – in paper [31].

The models for predicting the behavior of the composite structures can be classified into three groups: numerical, empirical, and analytical.

Nowadays, numerical methods are widely used. In particular, finite element models are the most common way to analyze composite structures. Unfortunately, a finite element model of a composite structure that has not been checked against analytical results or experimental data does not guarantee high reliability, since many factors impinge on a numerical solution. The most precise design method for composite structures is an experimental one, but it is characterized by increased workability. Therefore, analytical methods, which are the most general and economical, are used. There are several analytical design procedures for composite structures [32], including mechanically jointed beams theory (gamma method), composite theory (k-method) [33], shear analogy method and transformed section method. In addition, other methods [34–36] are used for the designing of composite structures subjected to flexure. None of the above mentioned analytical design procedures has been universally accepted yet.

The aim of the study was to verify the suggested design procedure for determining the strength and strain characteristics of a composite structure made of CLT panel and GLT beam connected by inclined screws.

Study objectives:

- to determine the strength and strain characteristics of a composite structure made of CLT panel and GLT beam connected by inclined screws;
- to compare the results obtained by the suggested design procedure, the numerical and experimental results for a composite structure made of CLT panel and GLT beam connected by inclined screws.

2. Methods

The research program includes numerical, analytical and experimental analyses of the strength and strain characteristics of a timber-timber composite structure.

Numerical analysis of the strength and strain characteristics of composite structures made of CLT panel and GLT beam connected by inclined screws, without fasteners and the CLT-GLT solid structure with rigid connection was carried out.

Numerical analysis of the behavior of the CLT-GLT composite structure was conducted using the ANSYS software (Fig. 2), taking into account the anisotropic properties of wood (Orthotropic Elasticity) for the GLT beam and the layers of the CLT panel. Solid elements (SOLID 186) were used for the numerical analyses. Boundary conditions were applied to the numerical model of timber composite structure by constraining the necessary nodes to represent the simply-supported condition. The CLT-GLT composite structures with a span of 3,000 mm were loaded according to a 2-point scheme for each GLT beam. A contact region between the layers of the CLT panel was modeled using “bonded” configuration. Contact regions between CLT panel and GLT beam were applied using different configurations: “no separation” for the CLT-GLT composite structures connected by inclined screws and without fasteners, “bonded” for the CLT-GLT solid structure with rigid connection.

Figure 2. Numerical model of CLT-GLT composite structure.

The coefficients k_W and k_{EI} were obtained from numerical analysis:

$$k_W = \frac{\sigma^{solid}}{\sigma^{composite}}, \; k_{EI} = \frac{w^{solid}}{w^{composite}} \tag{1}$$

where σ^{solid}, w^{solid} are normal stress and mid-span deflection of the CLT-GLT solid structure with rigid connection; $\sigma^{composite}$, $w^{composite}$ are normal stress and mid-span deflection of the CLT-GLT composite structure.

The suggested design procedure for determining the strength and strain characteristics of a composite structure made of CLT panel and GLT beam connected by inclined screws includes:

- calculation of normal stresses and mid-span deflection of the CLT-GLT solid structure with rigid connection;
- application of coefficients k_W and k_{EI} for calculation of normal stresses and mid-span deflection of a composite structure made of CLT panel and GLT beam connected by inclined screws.

Normal stresses σ and mid-span deflection w of the CLT-GLT solid structure loaded according to a 2-point scheme can be determined by the equations:

$$\sigma = \frac{M}{W_{red} \cdot k_W} \le R \cdot m, \; w = \frac{N \cdot l^3}{24 \cdot E \cdot I_{red} \cdot k_{EI}} \cdot \left(3\frac{a}{l} - 4\frac{a^3}{l^3} \right) \tag{2}$$

where M is a bending moment; W_{red} is a section modulus of the cross-section of a structure relative to its own neutral axis; R is a design resistance taking into account a coefficient m; N is a magnitude of concentrated load; l is a span of the structure; a is a distance between support and concentrated load; E is a modulus of elasticity of the GLT beam in longitudinal direction; I_{red} is the second moment of area of the structure relative to its own neutral axis; k_W, k_{EI} are coefficients (k_W = 1, k_{EI} = 1 for the CLT-GLT solid structure with rigid connection).

Section modulus of the cross-section of the CLT-GLT solid structure with rigid connection relative to its own neutral axis can be determined by equation (3):

$$W_{red} = \frac{I_{red}}{e} = \frac{\sum_{i=1}^{n} I_i + \sum_{i=1}^{n} A_i \cdot e_i^2}{e} \tag{3}$$

where A_i is cross-sectional area of separate element (layer or GLT beam); I_i is second moment of area of separate element (layer or GLT beam) relative to its own main axis; e_i is distance from the neutral axis of the whole structure to the neutral axis of separate element (layer or GLT beam); e is distance from the neutral axis of the whole structure to the point on the cross section of the structure at which the normal stress is to be determined.

The following simplifications must be taken into account during the design procedure for determining the strength and strain characteristics of a composite structure made of CLT panel and GLT beam connected by inclined screws:

- cross-sectional area of the CLT panel layer must be determined using the reduction factor, which depends on the ratio of modulus of elasticity of the layer and GLT beam;
- coefficients k_W and k_{EI} depend on geometrical parameters and strength characteristics of connection;
- modulus of elasticity of CLT panel in transverse direction can not be taken into account.

Experimental analysis of two groups of CLT-GLT composite specimens was carried out.

The first group included four CLT-GLT composite specimens without fasteners where CLT panel was simply-supported by GLT beam. Two variants of the CLT panel's orientation were considered: with the top layer of the panel oriented parallel to the GLT axis (CI) and oriented perpendicular to the GLT axis (CII). Nondestructive tests of the first group specimens were conducted during elastic stage. The tested specimens were used later to second group of CLT-GLT composite specimens.

The second group included four CLT-GLT composite specimens, which were prepared with compliant joint provided by inclined screws SPAX with length and diameter equal to 300 and 8 mm, respectively. The screws were placed under the angle of 45° relatively to longitudinal axis of the specimens. The screw spacing was taken as 150 mm. Two variants of the CLT panel's orientation (CI and CII) were considered. Tests of the second group were conducted until failure.

The characteristics of the materials used in the experimental tests were as follows:

- GLT beams with a strength class of GL20h were formed into cross-section of 150×60 mm (3 parts with a cross-section of 50×60 mm). The moduli of elasticity of the spruce GLT beams (9,465 MPa in longitudinal direction, 410 MPa in transverse direction) were experimentally determined;
- CLT panels with a strength class of C14 were 57 mm thick and were composed of three layers of 19 mm. The moduli of elasticity of the spruce CLT longitudinal boards (7,000 MPa in longitudinal direction, 230 MPa in transverse direction) were defined from technical approval;
- SPAX screws were made of carbon steel with characteristics from European Technical Approval ETA-12/0114.

The simply supported composite structure with the span of 3,000 mm was tested in a 4-point bending setup (Fig. 3). The loading scheme was selected so that the shear forces in the connection of timber composite structure were most fully manifested. The CLT-GLT composite structure was loaded by a jack with a developing load of 200 kN. The loading was applied to the structure through a steel distribution beams. Steel plates 20 mm thick were installed on the supports and under the distribution beams to avoid compression perpendicular to the grain of the wood. The tests were conducted at the temperature of 20–24 °C and relative humidity of 50–60 %.

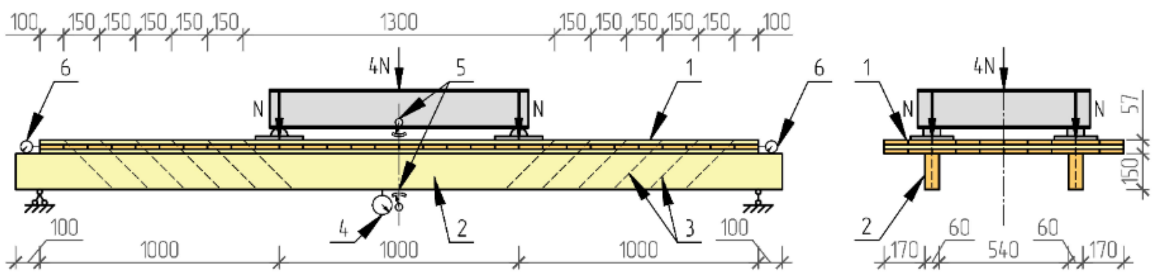

a **b**

c

Figure 3. Test setup: a – longitudinal section; b – cross-section; c – general view; 1 – CLT panel; 2 – GLT beam; 3 – screws; 4 – flexometer; 5 – strain gauges; 6 – displacement transducers.

The mid-span deflections of the structures were measured by flexometers. Measurements of wood grain strain were obtained using strain gauges installed at the compressed surface of the CLT panel and the tensile surfaces of the GLT beams. Slips between the CLT panel and the GLT beams were determined using displacement transducers installed at the edges of the CLT panel.

The sequence of the experiments:

1. Bending tests of composite structures by loading in stages of 1.4 kN at intervals of 5 minutes until failure. The mid-span deflections, slips between the CLT panel and the GLT beams, wood grain strain at each loading step are recorded and the destructive load $N_{\max}$ is determined.

2. Graphic documenting and analysis of the failure mode of the CLT-GLT composite structures.

3. Drawing of mid-span normal stresses distributions along cross-sectional depth of composite structures, load-deflection and load-slip curves.

4. Calculation of reliability coefficient for brittle failure of timber in accordance with the requirements of Interstate Standard GOST 33082-2014:

$$\gamma_{\nu} = 1.64 \cdot \left(1.94 - 0.116 \cdot \lg t\right), \tag{4}$$

where $t = t_{\max} / 38.2$ is loading time to failure adjusted to a constant destructive load $N_{\max}$, sec; $t_{\max} = n^2 \cdot t_n$ is test time, sec; n is number of load stages; t_n is stage time, sec.

5. Calculated load-carrying capacity of the CLT-GLT composite structure:

$$R_{\exp \nu} = N_{\max} / \gamma_{\nu}. \tag{5}$$

6. Comparison of the results obtained by the suggested design procedure, the numerical and experimental results for composite structure made of CLT panel and GLT beam connected by inclined screws.

3. Results and Discussion

The mid-span deflections and slips derived from the numerical analysis of the CLT-GLT composite structure were compared with the experimental deflections and slips (Table 1).

Table 1. Experimental and numerical results for timber composite structures.

Type of structure		At N = 3.5 kN				At N_{max} = 25.44 kN for CI At N_{max} = 16.97 kN for CII			
		Mid-span deflection, mm		Slip, mm		Mid-span deflection, mm		Slip, mm	
		Exp.	Num.	Exp.	Num.	Exp.	Num.	Exp.	Num.
Rigid connection	CI	–	4.90	–	0	–	35.65	–	0
	CII	–	6.19	–	0	–	30.03	–	0
With fasteners	CI	8.28	8.67	0.594	0.600	63.30	63.00	4.943	4.365
	CII	9.41	9.97	0.606	0.594	47.00	48.33	3.325	2.881
Without fasteners	CI	13.10	15.00	1.275	1.254	(95.24)	(109.08)	(9.269)	(9.119)
	CII	19.63	21.29	2.114	2.191	(95.15)	(103.22)	(10.248)	(10.624)

Fig. 4 shows the load-deflection and load-slip curves for CI and CII composite structures made of CLT panel and GLT beam connected by inclined screws (B+P+S), without fasteners (B+P+0) and the CLT-GLT solid structure with rigid connection (B+P).

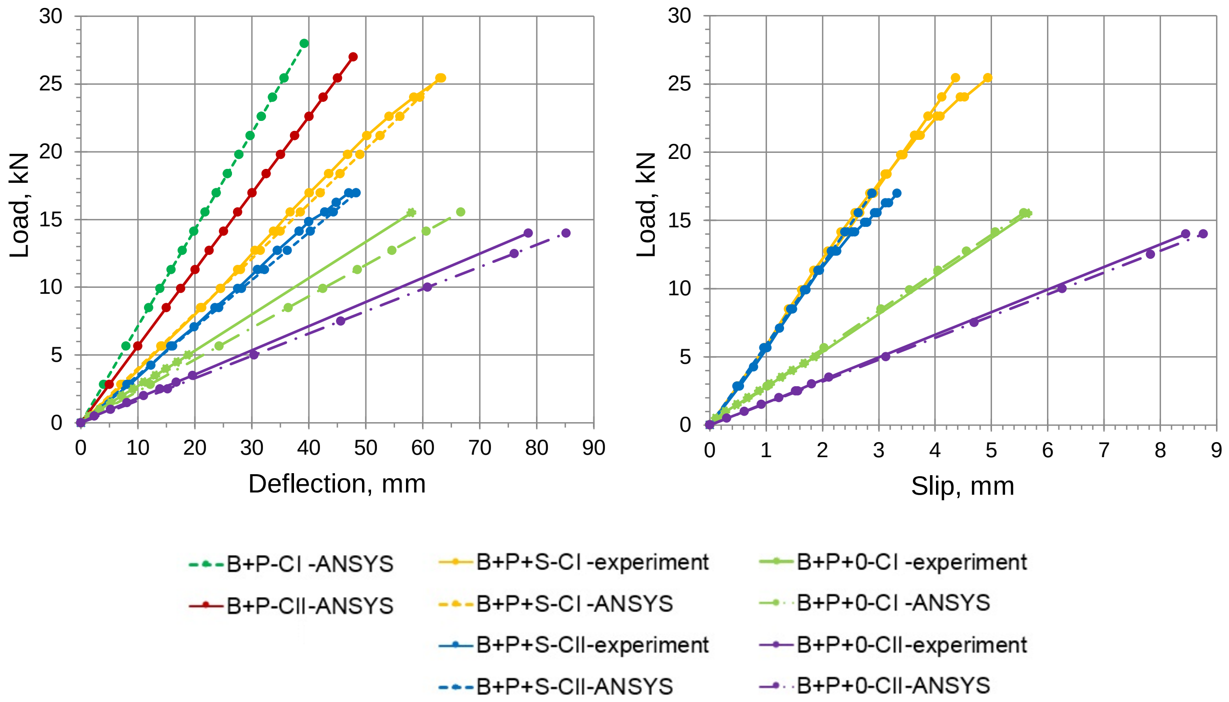

Figure 4. Load-deflection and load-slip curves for the CLT-GLT composite structures bending tests.

As a result of the stress-strain characteristics studies carried out for the CLT-GLT composite structure, it can be noted:

- the CI composite structure has 50 % more strength and 14 % more stiffness than the CII composite structure;
- the application of inclined screws increases the strength of the CLT-GLT composite structure by 1.3 and 1.6 times, the stiffness by 1.6 and 2.1 times, and the shear capacity by 2.1 and 3.5 times for CI and CII, respectively.

Fig. 5 shows the mid-span normal stresses distributions along cross-sectional depth of CI and CII composite structures (MPa) obtained by numerical and experimental analyses. The experimental values are shown in brackets.

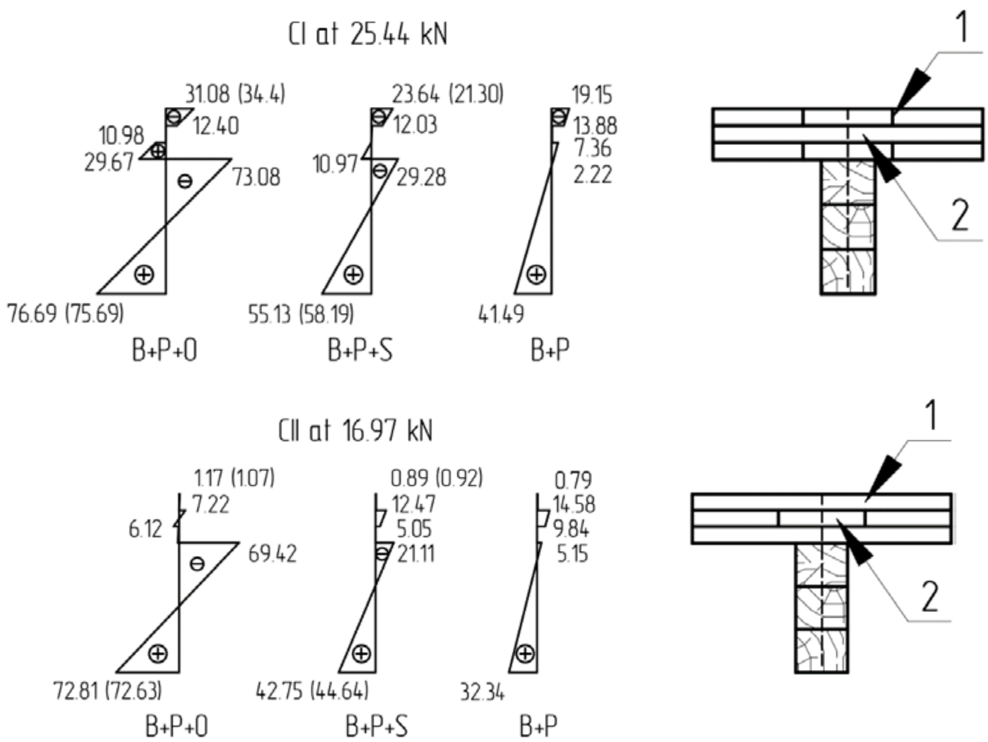

Figure 5. Mid-span normal stresses distributions along cross-sectional depth of CI and CII composite structures: 1 – top layer of CLT panel; 2 – cross layer of CLT panel.

When bending tests of CI and CII composite structures connected by inclined screws, brittle failure of the GLT beams in the middle of the span caused by normal tensile stresses was observed (Fig. 6, a-d).

The failure of the CI composite structure occurred in the tensile zone of the GLT beam with subsequent cracking along the plane perpendicular to the longitudinal axis of the beam.

The failure of the CII composite structure occurred in the tensile zone of the GLT beam. The crack developed from a knot along the plane inclined to the longitudinal axis of the beam. During loading, a gap developed between the lamellas of the bottom CLT layer.

The brittle failure of GLT beams in the middle of the span caused by bending tensile stresses corresponds to the results of studies in the publications [12–15].

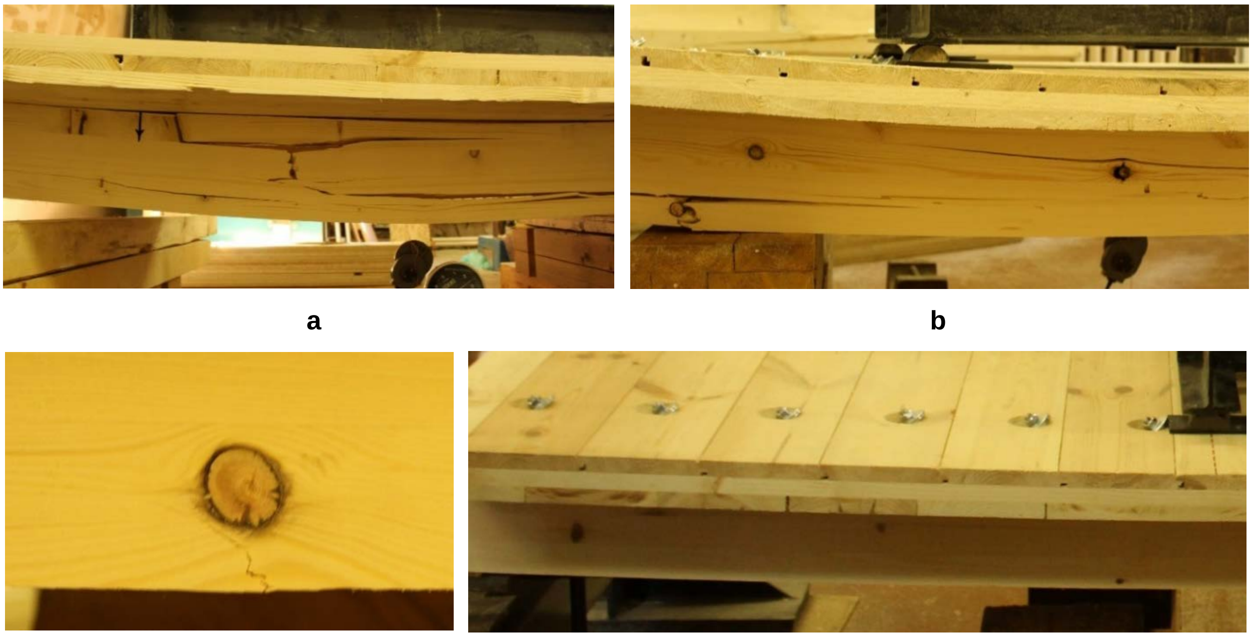

a b

c d

Figure 6. Failure of the CLT-GLT composite structures: a – CI; b – CII; c – knot in the tensile zone of the GLT beam (CII); d – gap between lamellas of the CLT panel.

A comparison of the results obtained by the suggested design procedure, the numerical and experimental results for the CLT-GLT composite structures is provided in Table 2.

Table 2. Comparison of experimental and numerical results for the CLT-GLT composite structures.

Method	Numerical analysis (1)		Design procedure (2), (3)		Experimental analysis	
	CI	CII	CI	CII	CI	CII
Destructive load $N_{\max}$, kN	–	–	–	–	25.44	16.97
Reliability coefficient, γ_v	–	–	–	–	2.81	2.88
Load-carrying capacity R_{expv}, kN	8.31	5.36	8.51	5.98	9.04	5.89
Differences between load-carrying capacity, %	**8.10**	**9.00**	**5.90**	**1.48**	**–**	**–**
Mid-span deflection of composite structure $w^{composite}$, mm	63.00	48.33	56.57	47.16	63.30	47.00
Differences between mid-span deflection, %	**0.47**	**2.75**	**10.64**	**0.33**	**–**	**–**
Mid-span deflection of solid structure w^{solid}, mm	35.65	30.03	32.01	29.3	–	–
Coefficient k_{EI}	0.57	0.62	0.57	0.62	–	–
Normal stresses of composite structure $\sigma_{c,CLT}^{composite}$, MPa	–23.64	–0.89	–26.63	0.00	–21.30	–0.92
Normal stresses of composite structure $\sigma_{t,GLT}^{composite}$, MPa	55.13	42.75	57.43	45.43	58.19	44.64
Differences between normal stress in tensile zone, %	**5.26**	**4.42**	**1.31**	**1.75**	**–**	**–**
Normal stresses of solid structure $\sigma_{c,CLT}^{solid}$, MPa	-19.15	-0.79	-21.57	0	–	–
Normal stresses of solid structure $\sigma_{t,GLT}^{solid}$, MPa	41.49	32.34	43.22	34.37	–	–
Coefficient k_W for $\sigma_{c,CLT}$	0.81	0.89	0.81	0.89	–	–
Coefficient k_W for $\sigma_{t,GLT}$	0.75	0.76	0.75	0.76	–	–
Slip υ, mm	4.365	2.881	–	–	4.943	3.325
Differences between slip, %	**11.69**	**13.35**	–	–	–	–

Table 2 presents determining of a coefficients k_W and k_{EI} from numerical analysis, calculation of normal stresses and mid-span deflection of the CLT-GLT solid structure with rigid connection and application of coefficients k_W and k_{EI} for calculation of normal stresses and mid-span deflection of a composite structure made of CLT panel and GLT beam connected by inclined screws.

For the CI (CII) composite structure connected by inclined screws the differences between numerical and experimental results are as follows:

- load-carrying capacity is 8.1 % (9.0 %);
- mid-span deflection is 0.47 % (2.75 %);
- normal stress in tensile zone is 5.26 % (4.42 %);
- slip between the CLT panel and the GLT beam is 11.69 % (13.35 %).

The differences between the slips obtained by numerical and experimental analyses can be explained by determining slips between the CLT panel and the GLT beam in the elastic stage of numerical modeling.

For the CI (CII) composite structure connected by inclined screws the differences between the results obtained by the suggested design procedure and experimental tests are as follows:

- load-carrying capacity is 5.9 % (1.48 %);
- mid-span deflection is 10.64 % (0.33 %);
- normal stress in tensile zone is 1.31 % (1.75 %).

The close agreement between results obtained by design procedure, the numerical and experimental results confirmed that the suggested design procedure is sufficiently accurate for determining strength and strain characteristic of a composite structure made of CLT panel and GLT beam connected by inclined screws.

4. Conclusions

1. A numerical model for determining the strength and strain characteristics of a composite structure made of CLT panel and GLT beam connected by inclined screws was developed. The accuracy of the proposed numerical model of timber composite structure was verified. The maximum differences between the load-carrying capacity, mid-span deflection, normal stress in tensile zone and slip between CLT panel and GLT beam calculated using numerical model and experimentally were equal to 9.0 %, 2.75 %, 5.26 % and 13.35 %, respectively.

2. A design procedure for determining the strength and strain characteristics of a composite structure made of CLT panel and GLT beam was suggested. The suggested engineering method for the CLT-GLT composite structure was verified. The maximum differences between the load-carrying capacity, mid-span deflection and normal stress in tensile zone of the CLT-GLT composite structure obtained by the suggested design procedure and experimental tests were equal to 5.9 %, 10.64 % and 1.75 %, respectively

3. It was experimentally proved that the application of inclined screws increases the strength of the CLT-GLT composite structures by 1.3 and 1.6 times, stiffness – by 1.6 and 2.1 times, and shear capacity – by 2.1 and 3.5 times for CI and CII, respectively.

4. The CLT-GLT composite structure with the top layer oriented parallel to the axis of the GLT beam has 50 % more strength and 14 % more stiffness than composite structure with the top layer oriented perpendicular to the GLT axis.

References

1. Brandner, R., Flatscher, G., Ringhofer, A., Schickhofer, G., Thiel, A. Cross laminated timber (CLT): overview and development. European Journal of Wood and Wood Products. 2016. 74(3). Pp. 331–351. DOI: 10.1007/s00107-015-0999-5
2. Hassanieh, A., Valipour, H.R., Bradford, M.A. Experimental and numerical investigation of short-term behavior of CLT-steel composite beams. Engineering Structures. 2017. 144. Pp. 43–57.
3. Loss, C., Piazza, M., Zandonini, R. Connections for steel-timber hybrid prefabricated buildings. Part I: Experimental tests. Construction and Building Materials. 2016. 122. Pp. 781–795. DOI: 10.1016/j.conbuildmat.2015.12.002
4. Du, H., Hu, X., Sun, Z., Meng, Y., Han, G. Load carrying capacity of inclined crossing screws in glulam-concrete composite beam with an interlayer. Composite Structures. 2020. 245. 112333. DOI: 10.1016/j.compstruct.2020.112333
5. Huber, C., Deix, K. Comparison of calculation methods of elastic bonding: limits of the gamma method using an example of a wood-concrete composite floor with single loads. Materials. 2021. 14(23). 7211. DOI: 10.3390/ma14237211
6. Labudin, B.V., Popov, E.V., Sopilov, V.V., Nikitina, T.A., Karelsky, A.V., Bardin, I.N., Vakhlov, D.G. Structural solutions of wood-concrete floors using shear-resistant joints. IOP Conference Series: Materials Science and Engineering. 2020. 896. 012028. DOI: 10.1088/1757-899X/896/1/012028
7. Vasiljevs, R., Serdjuks, D., Buka-Vaivade, K., Podkoritovs, A, Vatin, N. I. Load-carrying capacity of timber-concrete composite panels. Magazine of Civil Engineering. 2020. 93(1). Pp. 60–70. DOI: 10.18720/MCE.93.6
8. Buka-Vaivade, K., Serdjuks, D. Behavior of timber-concrete composite with defects in adhesive connection. Procedia Structural Integrity. 2022. 37. Pp. 563–569. DOI: 10.1016/j.prostr.2022.01.123
9. Sustersic, I., Brank, B., Dujic, B., Brezocnik, J., Gavric, I., Aicher, S., Dill-Langer, G., Winter, W., Fadai, A., Demschner, T., Ledinek, G. Hybrid cross laminated timber plates (HCLTP) – numerical optimisation modelling and experimental tests. 14th World Conference on Timber Engineering. Vienna, Austria, 2016.
10. Aicher, S., Zisi, N., Sustersic, I. Load sharing and damage redundancy of ribbed wooden elements. Otto-Graf-Journal. 2019. 18. Pp. 15–30.
11. Branco, J.M., Kekeliak, M., Lourenço, P.B. In-plane stiffness of traditional timber floors strengthened with CLT. European Journal of Wood and Wood Products. 2015. 73. Pp. 313–323. DOI: 10.1007/s00107-015-0892-2
12. Chiniforush, A.A., Valipour, H.R., Ataei, A. Timber-timber composite (TTC) connections and beams: An experimental and numerical study. Construction and Building Materials. 2021. 303. 124493. DOI: 10.1016/j.conbuildmat.2021.124493
13. Estévez-Cimadevila, J., Suárez-Riestra, F., Otero-Chans D., Martín-Gutíerrez E. Experimental analysis of pretensioned CLT-glulam T-section beams. Advances in Materials Science and Engineering. 2018. 1528792. DOI: 10.1155/2018/1528792
14. Giongo, I., Schiro, G., Riccadonna, D. Innovative pre-stressing and cambering of timber-to-timber composite beams. Composite Structures. 2019. 226. 111195. DOI: 10.1016/j.compstruct.2019.111195
15. Giongo, I., Schiro, G., Walsh, K., Riccadonna, D. Experimental testing of pre-stressed timber-to-timber composite (TTC) floors. Engineering Structures. 2019. 201. 109808. DOI: 10.1016/j.engstruct.2019.109808

16. Jacquier, N., Girhammar, U.A. Evaluation of bending tests on composite glulam-CLT beams connected with double-sided punched metal plates and inclined screws. Construction and Building Materials. 2015. 95. Pp. 762–773. DOI: 10.1016/j.conbuildmat.2015.07.137
17. Jacquier, N., Girhammar, U.A. Tests on glulam-CLT shear connections with double-sided punched metal plate fasteners and inclined screws. Construction and Building Materials. 2014. 72. Pp. 444–457. DOI: 10.1016/j.conbuildmat.2014.08.095
18. Masoudnia, R., Hashemi, A., Quenneville, P. Evaluation of effective flange width in timber composite beams. New Zealand Timber Design Journal. 2018. 26(2). Pp. 14–24.
19. Masoudnia, R., Hashemi, A., Quenneville, P. Predicting the effective flange width of a CLT slab in timber composite beams. Journal of Structural Engineering. 2018. 144(7). DOI: 10.1061/(ASCE)ST.1943-541X.0001979
20. Masoudnia, R., Masoudnia, S. Numerical investigation of effective flange width in the CLT-GLT composite T-beams. New Zealand Timber Design Journal. 2019. 27 (3). Pp. 7–16.
21. Masoudnia, R. State of the art of the effective flange width for composite T-beams. Construction and Building Materials. 2020. 244. 118303. DOI: 10.1016/j.conbuildmat.2020.118303
22. Riccadonna, D., Walsh, K., Schiro, G., Piazza, M., Giongo, I. Testing of long-term behaviour of pre-stressed timber-to-timber composite (TTC) floors. Construction and Building Materials. 2020. 236. 117596. DOI: 10.1016/j.conbuildmat.2019.117596
23. Schiro, G., Giongo, I., Sebastian, W., Riccadonna, D., Piazza, M. Testing of timber-to-timber screw-connections in hybrid configurations. Construction and Building Materials. 2018. 171. Pp. 170–186. DOI: 10.1016/j.conbuildmat.2018.03.078
24. Sustersic, I., Dujic, B., Aicher, S. Less is more – optimised ribbed CLT plates – the future. New Zealand Timber Design Journal. 2017. 25 (2). Pp. 19–26.
25. Blaß, H.J., Steige, Y. Steifigkeit axial beanspruchter vollgewindeschrauben. KIT Scientific Publishing. Karlsruhe, 2018. 174 p. DOI: 10.5445/KSP/1000085040
26. Dietsch, P., Brandner, R. Self-tapping screws and threaded rods as reinforcement for structural timber elements – a state-of-the-art report. Construction and Building Materials. 2015. 97. Pp. 78–89. DOI: 10.1016/j.conbuildmat.2015.04.028
27. Franke, S., Franke, B., Harte, A.M. Failure modes and reinforcement techniques for timber beams – state of the art. Construction and Building Materials. 2015. 97. Pp. 2–13. DOI: 10.1016/j.conbuildmat.2015.06.021
28. Merkulov, A.T., Turkovskij, S.B., Grill', A.A., Sazonov, A.I., Pogorel'tsev, A.A., Grigor'ev, S.A., Tarasov, M.A. Composite-section wood beam on inclined glued braces. Patent Russia no. 2173376, 2001.
29. Roshchina, S.I., Lukin, M.V., Labudin, B.V., Melekhov, V.I. Design of composite laminated wooden joists on the engineering method basis. Bulletin of the Higher Education Institutions. Forest Journal. 2012. 327(3). Pp. 90–94.
30. Trautz, M., Koj, C. Mit schrauben bewehren – neue ergebnisse. Bautechnik. 2009. 86 (4). Pp. 228–238.
31. Zhadanov, V.I., Arkayev, M.A., Stolpovsky, G.A. Strengthening of wooden constructions with the use of twisted cruciform rods. Civil engineering. 2017. 5. Pp. 25–31.
32. Buka-Vaivade, K., Serdjuks, D., Goremikins, V., Pakrastins, L., Vatin, N.I. Suspension structure with cross-laminated timber deck panels. Magazine of Civil Engineering. 2018. 83(7). Pp. 126–135. DOI: 10.18720/MCE.83.12
33. Blaß, H.J., Sandhaas, C. Timber engineering: principles for design. KIT Scientific Publishing. Karlsruhe, 2017. 644 p. DOI: 10.5445/KSP/1000069616
34. Ecsedi, I., Baksa, A. Analytical solution for layered composite beams with partial shear interaction based on Timoshenko beam theory. Engineering Structures. 2016. 115. Pp. 107–117. DOI: 10.1016/j.engstruct.2016.02.034
35. Focacci, F., Foraboschi, P., Stefano, M.D., Composite beam generally connected: analytical model. Composite Structures. 2015. 133. Pp. 1237–1248. DOI: 10.1016/j.compstruct.2015.07.044
36. Karelskiy, A.V., Zhuravleva, T.P., Labudin, B.V. Load-to failure bending test of wood composite beams connected by gang nail. Magazine of Civil Engineering. 2015. 54(2). Pp. 77–85. DOI: 10.5862/MCE.54.9

Information about authors:

Tatyana Chernova, *PhD in Technical Sciences*
ORCID: https://orcid.org/0000-0002-2471-4062
E-mail: zhuravleva.t.pav@mail.ru

Vladimir Melekhov, *Doctor of Technical Sciences*
ORCID: https://orcid.org/0000-0002-2583-3012
E-mail: v.melekhov@narfu.ru

Received 18.01.2023. Approved after reviewing 06.04.2023. Accepted 03.05.2023.

Magazine of Civil Engineering. 2023. 120(4). Article No. 12005

Magazine of Civil Engineering

ISSN 2712-8172

journal homepage: http://engstroy.spbstu.ru/

Research article

UDC 624.1

DOI: 10.34910/MCE.120.5

Soil-structure interaction: theoretical research, in-situ observations, and practical applications

M.M. Sabri [1] ✉ , ***K.G. Shashkin*** [2]

[1] *Peter the Great St. Petersburg Polytechnic University, St. Petersburg, Russian Federation*

[2] *PI Georeconstruction, St. Petersburg, Russian Federation*

✉ *mohanad.m.sabri@gmail.com*

Keywords: soil-structure interaction, design methods, structural response, seismic response, elasto-visco-plastic model, soil model, long-term settlement, restoration, historical buildings, finite element method, non-linear analysis

Abstract. This research paper presents a comprehensive investigation on soil-structure interaction, combining theoretical research and in-situ observations. Detailed calculations and a thorough comparison of the results with long-term settlement observations are provided, accompanied by the validation of the proposed elasto-visco-plastic soil model through rigorous calculations. Real-world examples showcasing the application of design methods incorporating soil-structure interaction calculations in civil and industrial engineering, as well as in the reinforcement and restoration of historical buildings, are also presented. The study reveals that neglecting the spatial behavior of soil leads to significant underestimation of stresses in structures. For buildings on spread footings, the underestimation can range from 150% to 400%, while for buildings on pile foundations, it can be as high as 200% to 900%. Furthermore, an innovative architectural solution employed in a high-rise building successfully mitigated settlement issues by utilizing longer piles. The calculated settlement was reduced to 60 mm, and the actual settlement observed three years after construction was only 32 mm, indicating the effectiveness of the implemented solution. By emphasizing the importance of soil-structure interaction calculations, this research fosters a unified approach among various stakeholders involved in construction design. The findings and methodologies presented in this paper hold great potential to significantly enhance the field of geotechnical engineering, enabling more accurate and effective design approaches for various structures and applications.

Funding: This research was supported by a grant from the Russian Science Foundation No. 22-79-10021, https://rscf.ru/project/22-79-10021/

Citation: Sabri, M.M., Shashkin, K.G. Soil-structure interaction: theoretical research, in-situ observations, and practical applications. Magazine of Civil Engineering. 2023. 120(4). Article no. 12005. DOI: 10.34910/MCE.120.5

1. Introduction

The impacts of soil-structure interaction on calculations have been extensively studied and validated by the behavior of structures and soils [1-13]. When a rigid plate is loaded, contact pressure contours emerge in the deformed half-space. The Boussinesq analytical solution, which is widely recognized, indicates that these contours are parabolic with asymptotes running along the edges of the plate, assuming the plate is entirely rigid and circular [14-16] (Fig. 1):

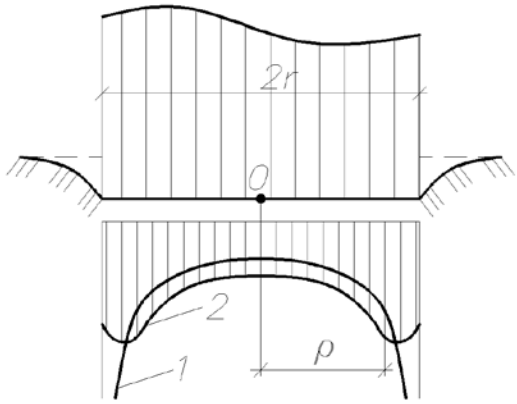

Figure 1. Contact pressure contours in the deformed half-space under a plate: 1 – according to the analytical solutions, 2 – in reality considering the development of plastic deformations.

In reality, the contact contours are typically saddle-shaped (contours 2 in Fig. 1, experimental values in Fig. 2).

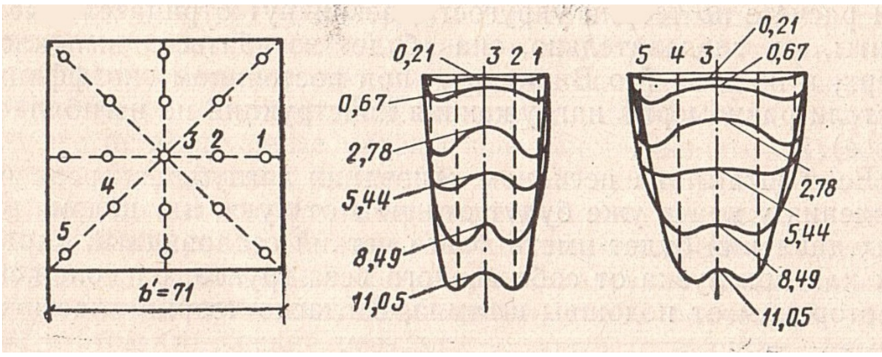

a. b. c.

Figure 2. Experimental diagrams of reactive pressures: under a square plate 71×71 cm on the surface of sand soil at pressures 0.2–8 kgs/cm^2 (from 20 to 800 kPa) [17, 18]: a – layout of pressure gauges; b – contours along the middle axis; c –contours along the diagonal [19].

The same contours of vertical forces form within the plate, reflecting the contract contours under the plate in the deformed half-space. The values of reactive forces in the plate depend on the rigidity of the deformed half-space. It is also apparent that while considering a real structure of a final rigidity instead of the rigid plate, the contact contours will also depend on the rigidity of this structure (Fig. 3).

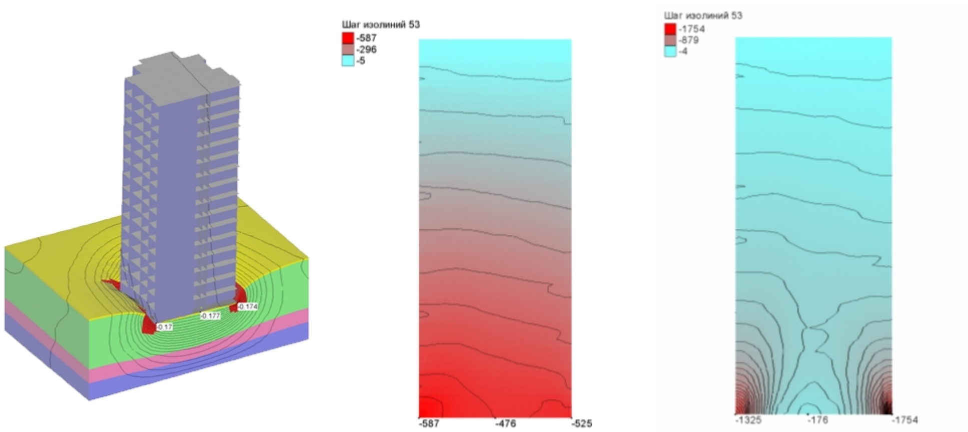

a. b. c.

Figure 3. The results of calculation of a building on a slab foundation with subsoil: a – calculation model (cross-section), the areas of limit state are marked in red; b – linear forces (kN/m) in a transversal wall at calculation on inflexible soil; c – forces considering of spatial soil behavior.

Although there is clear evidence of the regularities in soil-structure interaction, differential pressure in the subsoil of rigid structures is not always considered in design practice, raising the question of whether it is necessary to consider this feature in structural design.

2. Methods

2.1. Idealized models of reinforced concrete buildings

In order to investigate the effects of soil-structure interaction, idealized models of reinforced concrete buildings were used, with different structural schemes including transversal bearing walls at a spacing of 3 and 6 meters, longitudinal and transversal bearing walls, and longitudinal bearing walls. The use of idealized models enabled to obtain of the fundamental regularities of soil-structure interaction without being distracted by the details of the structural scheme (openings, changes in the spacing of bearing walls etc.). To compare the results, the calculations for each building on elastoplastic soil were compared with the results of a corresponding calculation on a completely inflexible subsoil (on rigid supports), which is equivalent to the loading of a building on a subsoil per loaded area, as commonly accepted in design practice. This comparison was highly informative as it ultimately identified the studied effect, which was completely absent when considering a structure on rigid supports. Figure 4 shows a comparison of stresses in the walls of the building on rigid supports and a flexible subsoil with medium compressibility (with a strain modulus of approximately 10 MPa).

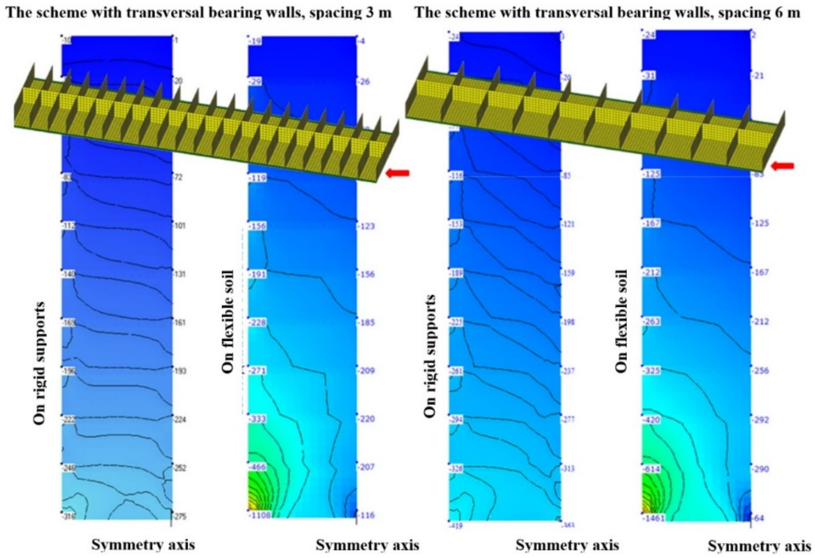

Figure 4. Distribution of vertical forces in a face wall of the building (kN) at various structural schemes.

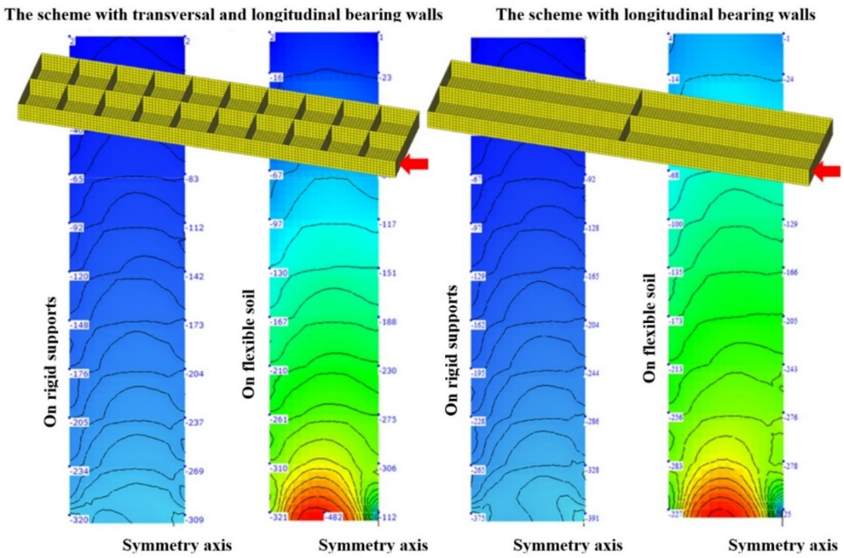

Figure 5. The contours of distribution of vertical forces (kN) in a transversal face wall of the building at calculation on nonlinear deformed soil made of soils of medium deformability, and KSSI contour.

2.2. Account of nonlinear soil behavior in time, account of nonlinear properties of structural materials

Based on the analysis of behavior models used for solving problems related to soil-structure interaction, models with double or independent strain hardening at volumetric and shape-changing deformations are considered the most promising. It has been demonstrated that strains in buildings and structures are not only caused by the consolidation process but also by the process of shape-changing, which is often the deciding factor in practical situations [20]. To accurately predict changes in the stress-strain behavior of soil during loading, models with independent descriptions of the behavior of soil during consolidation and shape-changing are necessary. A model with independent strain hardening has been verified through a series of in situ investigations of building strain development [21-23].

The central concept behind creating a visco-plastic model of soil behavior is to develop an independent description of the reversible deformations area, also known as the strain hardening area, for both consolidation and shape-changing. In this model, the relationships between the shear strain $\gamma_p(p,q)$ and volumetric strain $\varepsilon_{vp}(p,q)$ are determined based on laboratory soil tests and can be graphically represented by contours in p–q coordinates (Fig. 7). As the limit stress approaches, strains increase, and the contours of $\gamma_p(p,q)$ align along the Coulomb law line.

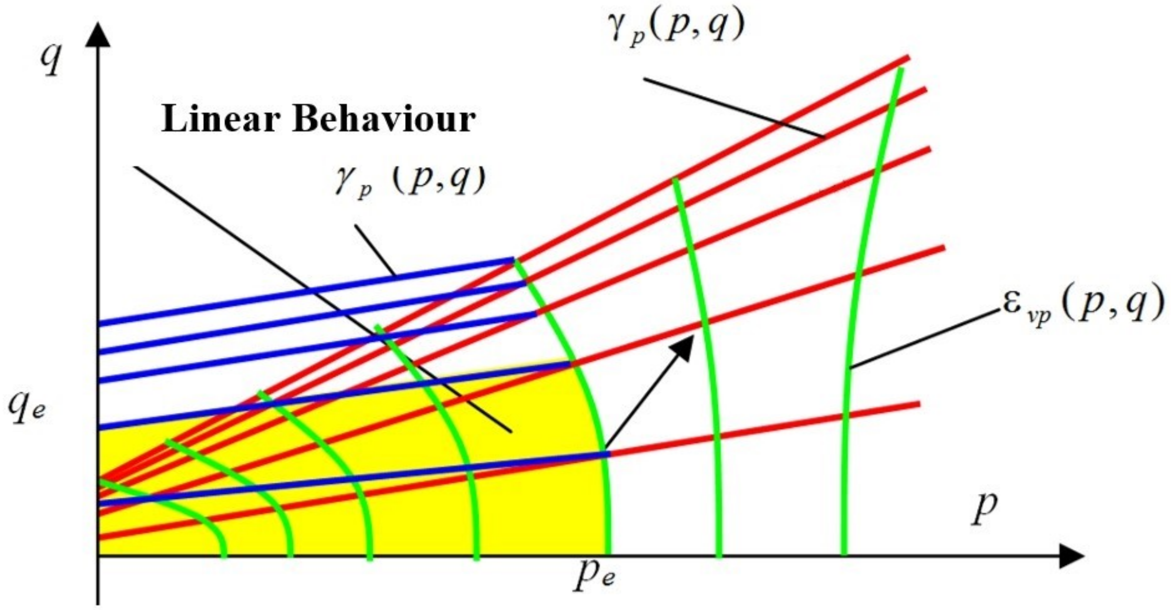

Figure 8. The scheme of making an elastoplastic model with independent strain hardening.

The approach described here involves defining the complete set of dependencies between shear $\gamma_p(p,q)$ and volumetric strains $\varepsilon_{vp}(p,q)$ and varying values of stress deviator. These dependencies can be represented as contours in p-q coordinates, with the contours of $\gamma_p(p,q)$ concentrating along the Coulomb law line as strains increase, approaching the limit stress. Points above the limit line of Coulomb law correspond to stress states that are impossible for the soil milieu and should not be considered in the model. The vector of plastic deformation for a given increment of stresses is then defined by the set of $\gamma_p(p,q)$ and $\varepsilon_{vp}(p,q)$ dependencies. This approach does not require any theoretical assumptions about the shape of a "tent" or other mathematical abstractions, allowing the maximum approximation of the model behavior to experimental results. Any differences between the model and experiment are primarily due to inaccuracies in approximating the $\gamma_p(p,q)$ and $\varepsilon_{vp}(p,q)$ functions.

The limitations of existing models in describing soil behavior over time and predicting the strains of buildings and structures are acknowledged. Specifically, there is a lack of models that can accurately describe the development of shear strains in time. Most models assume immediate development of shear strains, which is inconsistent with the accumulated construction experience. Therefore, there is a need to develop more advanced models that can better capture soil behavior over time and provide more accurate predictions of strain development.

The Creep Model is a method of modeling the development of creeping deformations over time. It relates the strains caused by creeping in shear and secondary consolidation as two projections of a vector that is orthogonal to the tent surface in the Cam Clay model. However, the tent surface and the associated law of plastic flow are mathematical abstractions that may not be applicable to describing the actual soil behavior. As a result, it is uncertain whether using these abstractions will lead to success in describing shear creeping based on the dependency for compression.

The proposed model used the simplest linear dependency: viscosity decreases according to the linear law with an increase of shear stress and approaches null at reaching the strength limit:

$$\eta(\tau) = \eta_0 \frac{\tau_{\lim} - \tau}{\tau_{\lim}}. \tag{1}$$

The model incorporates a linear relationship between the rate of development of shear strains and acting stresses, which aligns well with previous research [24]. This enables the model to integrate different soil behaviors, where slow strain development occurs at small shear stresses and quick failure occurs at stresses approaching the strength limit. As the strength limit approaches, the shear viscosity resistance decreases to zero, leading to soil failure.

To validate the proposed model, a database of long-term observations of settlements of buildings and structures was compiled and analyzed (Fig. 9).

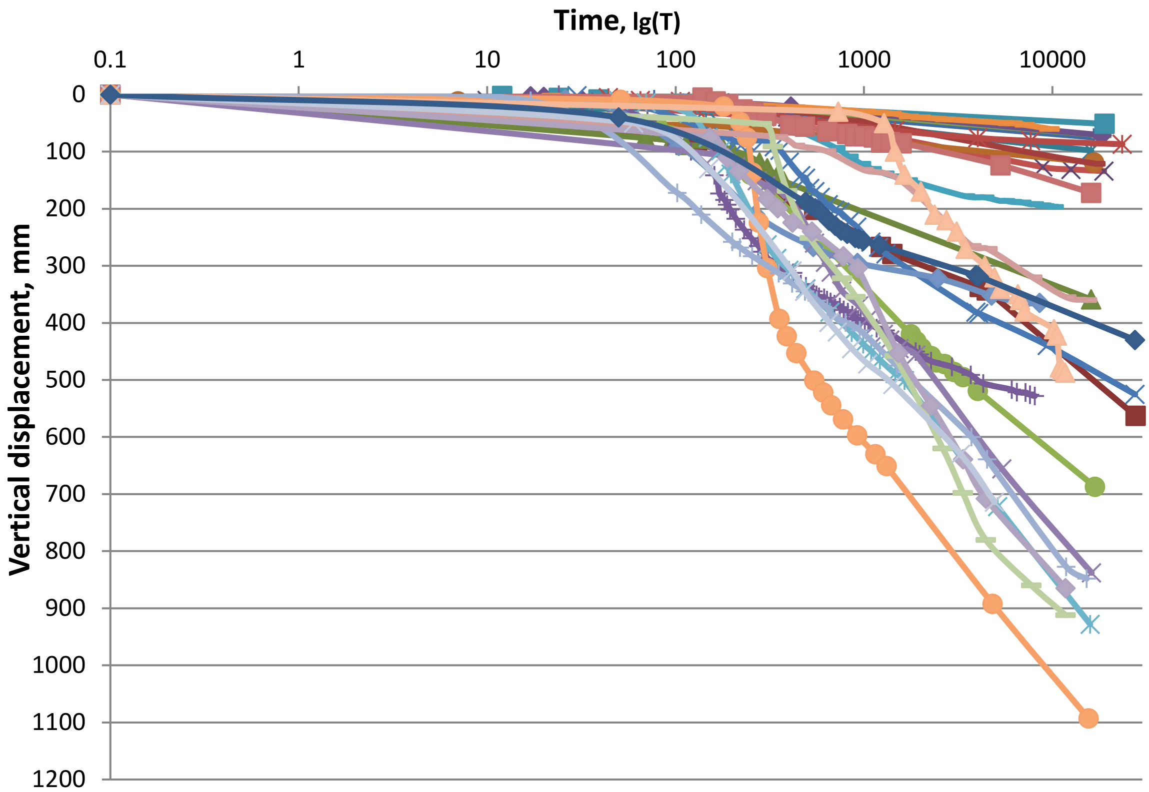

Figure 9. The results of long-term observations of 30 buildings on soft soils (duration of observations 23–77 years [25]).

3. Results and Discussion

3.1. The results of the Numerical modeling using the proposed soil-structure interaction ideology

The ratio between a force in a point of structure at the flexible soil solution and a force in the same point in the rigid support solution is called "an indicator of the effect of soil-structure interaction, denoted as KSSI. Fig. 5 displays the KSSI graphs for various structural schemes of the building on medium compressive soil. Its shows that the stresses in structures are evidently affected by the soil-structure rigidity ratio. Fig. 6 and 7 exhibit the KSSI dependencies on the soil-structure rigidity ratio for different structural schemes and various types of foundations.

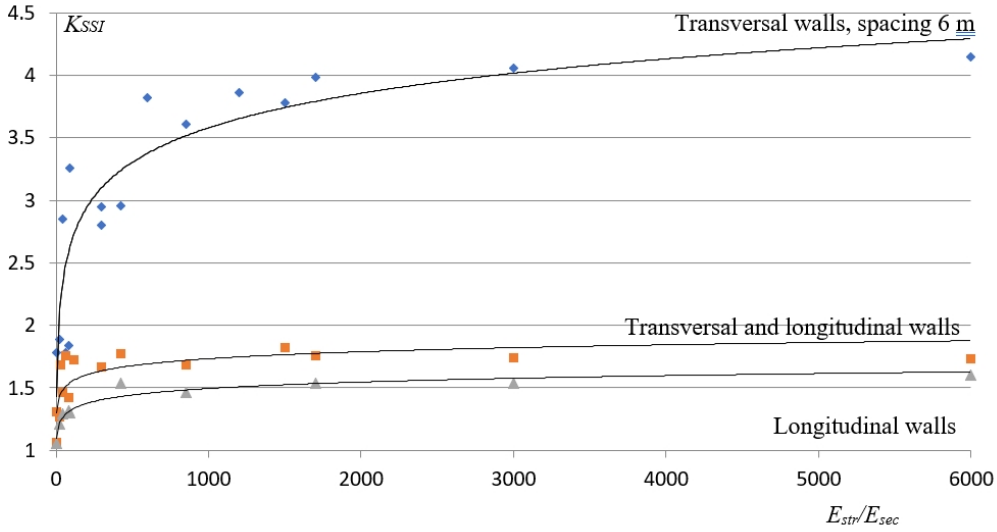

Figure 6. The dependency of an indicator of non-linearly deformed soil-structure interaction effect on their ridigity ratio for different structural schemes.

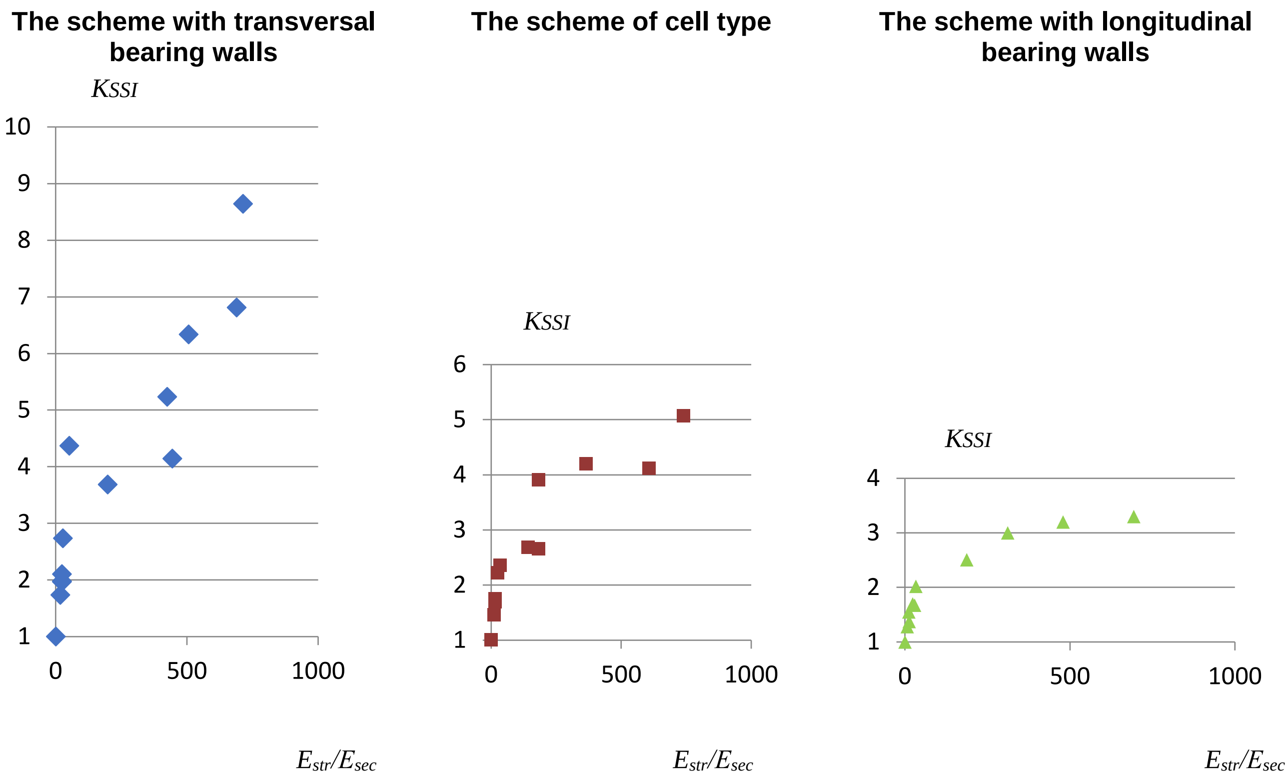

Figure 7. The graphs of dependency of an indicator of soil-structure interaction effect for the building on pile foundation and non-linearly deformed soil on their ratios for various structural schemes of buildings.

The results of numerical experiments indicate a significant underestimation of stresses in structures when the spatial behavior of soil is not considered. The underestimation can range from 150 to 400% for buildings on spread footings, while for buildings on pile foundations, it can be as high as 200–900%. Despite the importance of this issue, both in Russia and abroad, it is often ignored in design practice. One reason for this is the division of experts involved in structural and geotechnical calculations, which results in using different software suites that do not interact well. Furthermore, practical design experience highlights the importance of accounting for soil-structure interaction to design more durable and cost-effective structures. Despite this, doubts remain about the accuracy of soil calculations, which hinders the adoption of soil-structure interaction calculations. To address these doubts, extensive work has been done to compare calculated and observed strain values, discussed in detail below.

3.2. Comparison of the calculated results according to different methods and observation results

Fig. 9 demonstrates that considering buildings on soft soils, the notion of "final settlement" loses its sense as settlements develop as per logarithmical law, which does not have an asymptote. Therefore, a clear scientific setting of the task of comparison of calculations and observations requires a comparison of settlements in a certain time moment. Fig. 10 compares results according to the simplified method of strata summing (set in the Russian regulations) and nonlinear calculations according to the abovementioned model with results of long-term observations. The figure shows that the accuracy of geotechnical calculations using nonlinear models increases significantly.

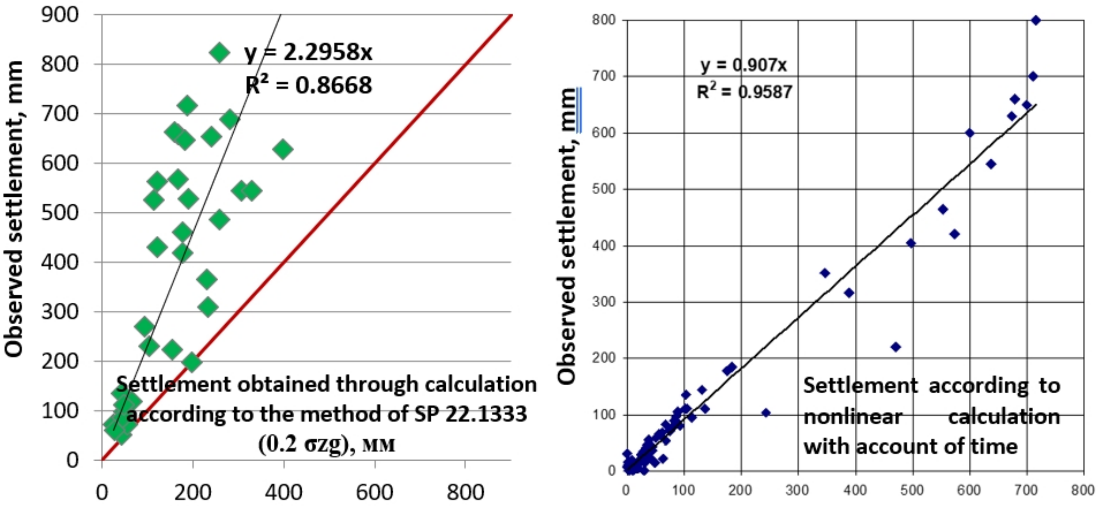

Figure 10. Comparison of the results of calculations according to different methods and observation results.

With the correct account of soil deformations, there is a problem of the correct account of structural rigidity since the values of forces in soil-structure interaction calculations largely depend on a rigidity ratio. There is a need to consider the long-term creeping of concrete and cracking for reinforced concrete structures. N.A. Evseev [26] has elaborated on convenient methods of accounting for the rigidity of RC structures in soil-structure interaction calculations.

3.3. Application of the design ideology considering the soil-structure behavior

3.3.1. Design of the unique high-rise building

The account of soil-structure behavior is essential for both usual and unique high-rise buildings. An example of a unique high-rise building constructed in difficult soil conditions in St. Petersburg is considered. At the pre-design stage, soil-structure interaction calculations were performed for the unique building for different configurations of its underground floor (Fig. 11). As a result, a structural scheme was proposed, which minimized settlements and tilts and formed the basis of the architectural solution (Fig. 12). The proposal was to increase the area of building spread on soil and simultaneously deepen the underground part, and construct rigid radial walls to provide transfer of pressure throughout the foundation area.

The concept, which was accepted as the basis of the architectural solution, allowed minimizing settlement of the high-rise building (Fig. 13). Increasing the pile length provided reduced the calculated settlement to about 60 mm, according to the observation results, the actual settlement three years after completion of the construction was 32 mm. At the same time, soil-structure interaction calculations allowed considering the development of forces in radial walls of the underground part and ensuring the strength of these structures.

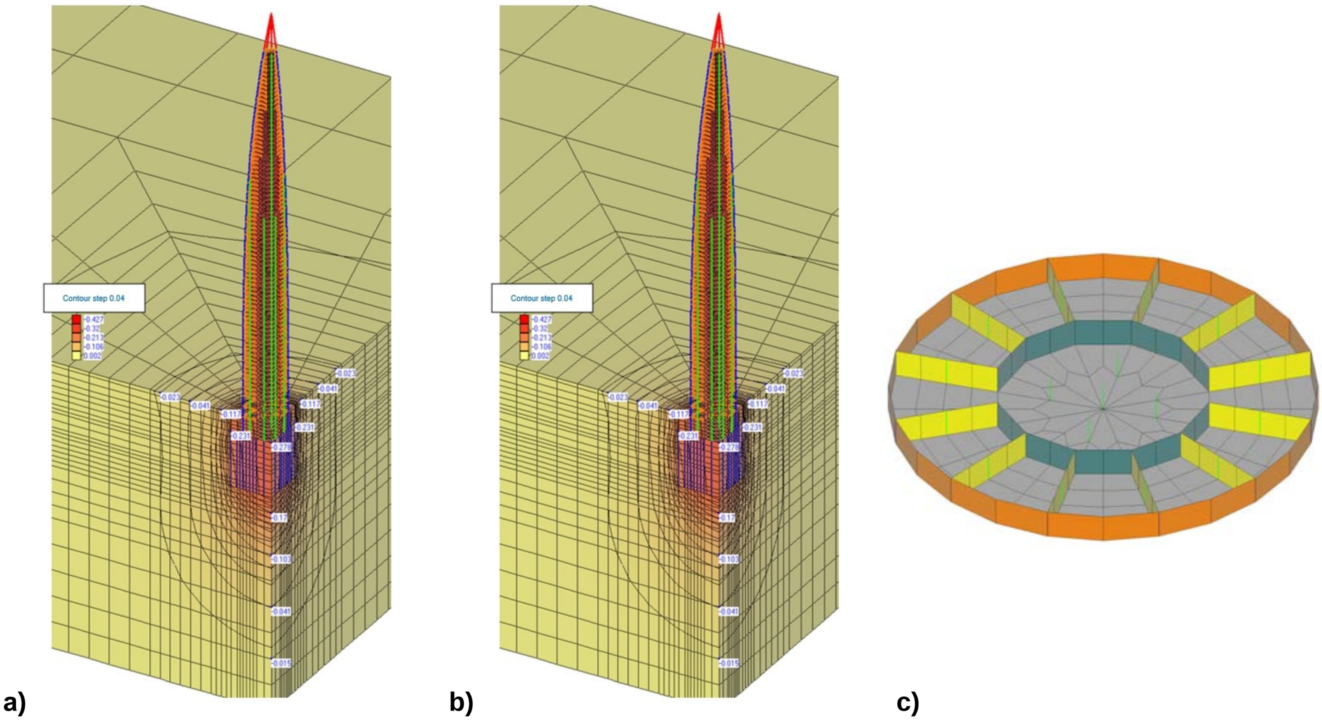

a) b) c)

Figure 11. Pre-design calculations of the high-rise building on dispersed soils in St. Petersburg: a – the settlement at the underground part diameter of 55 m (the maximum value 64 cm); b – the settlement at the underground part diameter of 80 m (the maximum value 28 cm), c – the plan of the underground floor with radial walls proposed at pre-design stage.

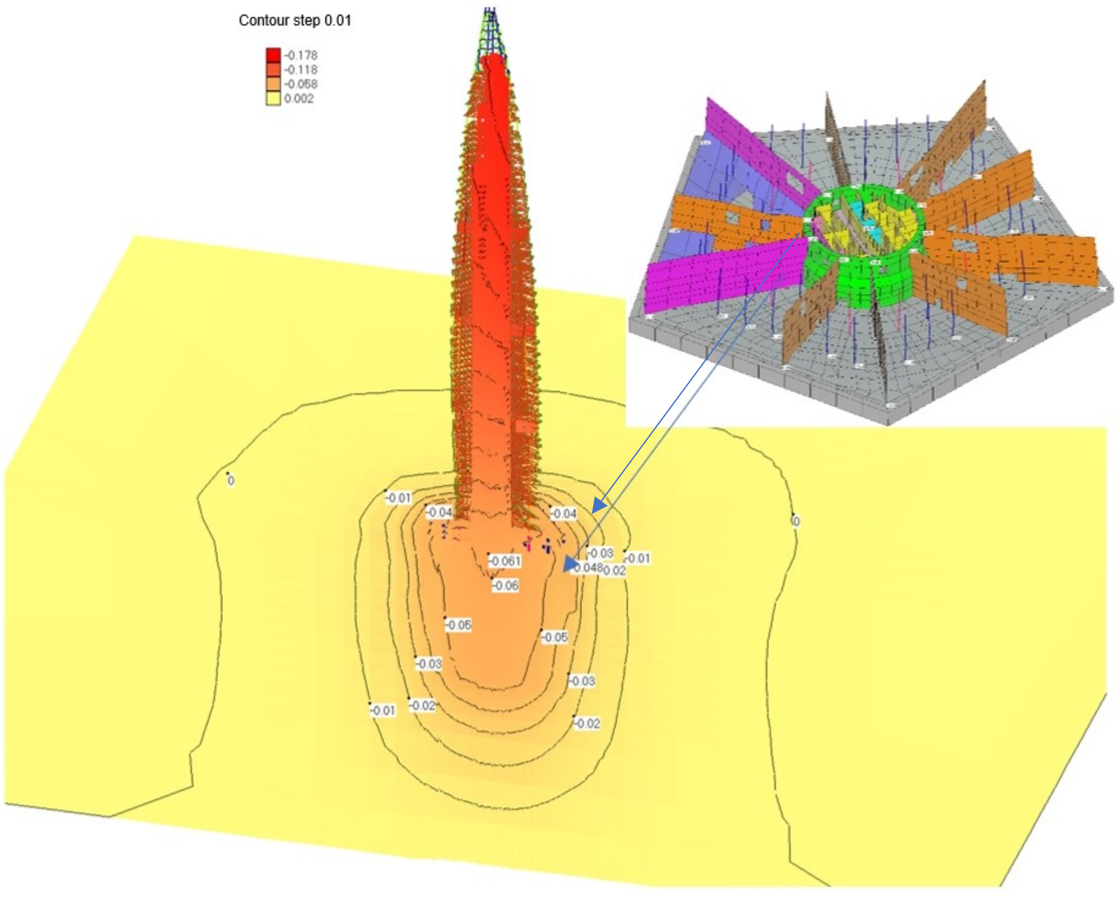

Figure 13. Calculation of settlements of the high-rise building, m (in the top right corner, there is a fragment of the calculation model for the configuration of the underground part accepted in the design).

3.3.2. Account of soil-structure interaction in industrial construction

In contrast to civil engineering, where traditional structural schemes are used for most buildings (as discussed in detail in part 1), complex shapes are more common in industrial construction structures due to the requirements of technological processes. In these cases, adequate consideration of soil behavior is necessary to determine the forces acting on superstructures accurately. For example, an 80-meter-high silo tower for production (Fig. 14) experiences the same loads as a 200-meter-high skyscraper, while a clinker brick warehouse (Fig. 15) applies almost the same pressure to the soil as the 500-meter-high building discussed earlier. In the latter case, a unique technical solution was implemented involving cutting structures with numerous deformation joints to allow the structures to adapt to the significant soil deformations that could not be minimized using long piles.

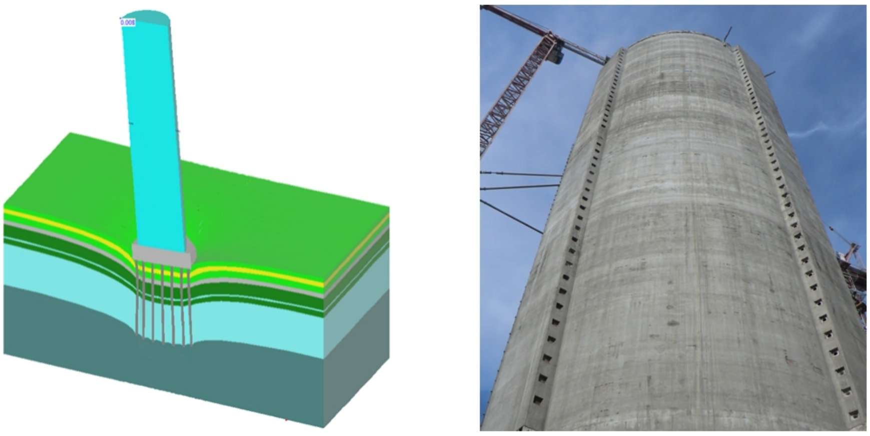

Figure 14. The calculation model (the exaggerated strain model at the calculation for wind action) and view of the erected structure of the silo tower for ready production, the cement plant in Novorossiysk.

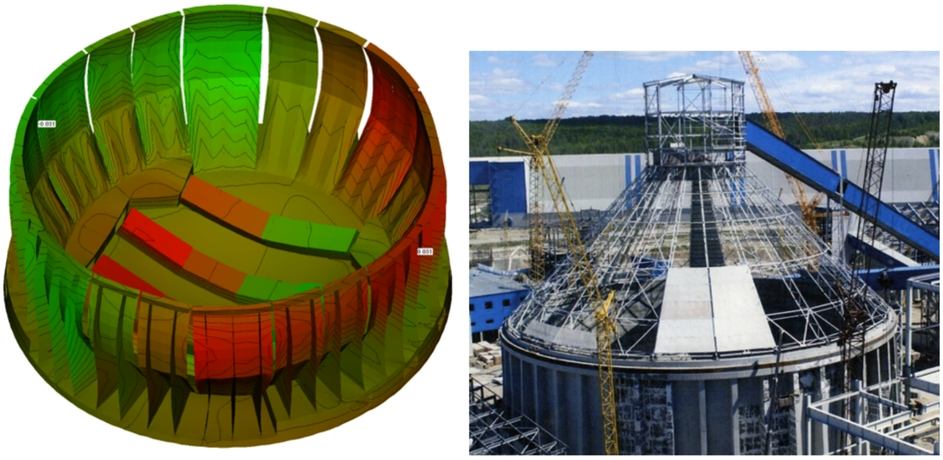

Figure 15. The strain model (in a larger scale) and view of the erected structure of the clinker warehouse, the cement plant in Novorossiysk.

3.3.3. Soil-structure interaction calculation at the analysis of causes of deformation of historical buildings

The consideration of soil-structure interaction also proves to be beneficial for diagnosing the causes of defects in historical buildings and selecting the most effective options for strengthening foundations and structures. The analysis of the strains of the Marine Cathedral in Kronshtadt, for instance, revealed characteristic settlement features for cross and cupola temples, where the four central pillars, on which the dome rests, experienced the largest settlement (Fig. 16), while the surrounding structures were less deformed. Based on the structure calculation, tensile areas prone to cracking were identified. These were found to be the areas where cracks had occurred (Fig. 17), allowing for unequivocal conclusions about the reasons for the development of defects. The clearly stated reason for the development of defects allowed for substantiating the lack of necessity to reinforce foundations and avoid the dangerous influence of technology on the building structures.

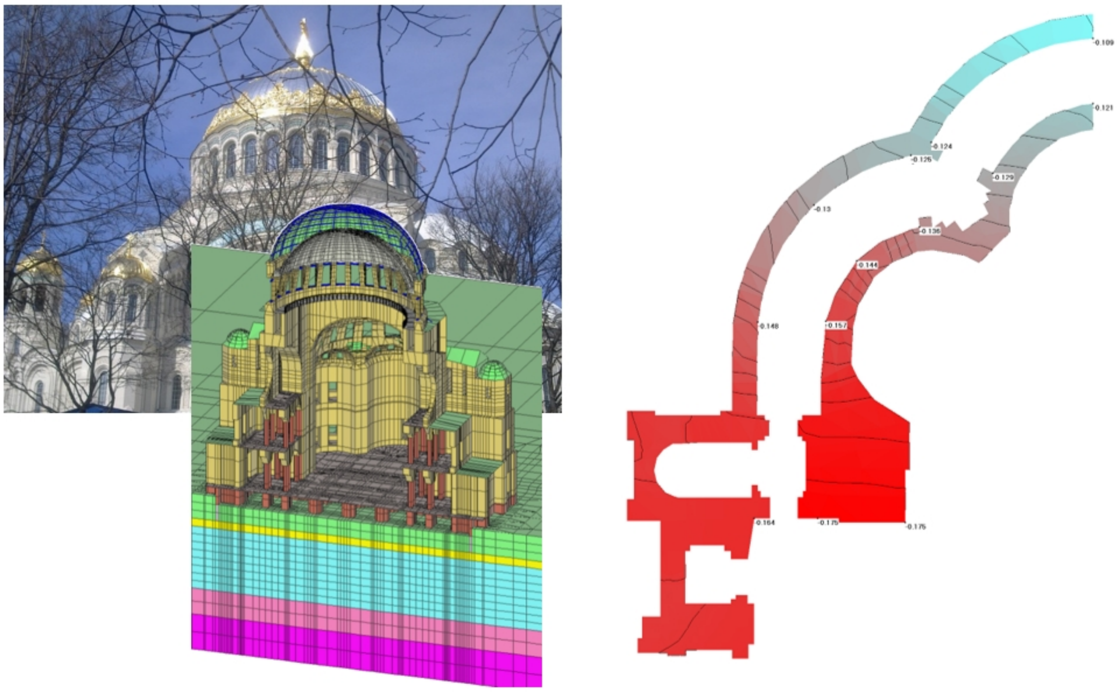

a) b)

Figure 16. Calculation of Kronshtadt Marine Cathedral:
a – photo and calculation model (cross-section);
b – settlement contours in one-fourth of the building plan.

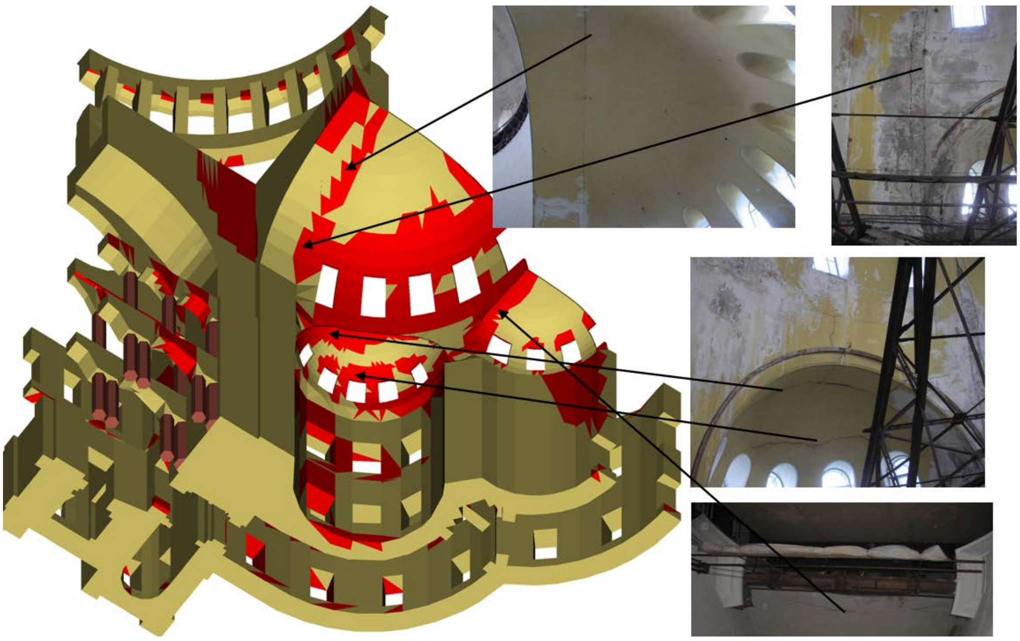

Figure 17. Matching of the expected areas of cracking according to the calculation and the examination results.

4. Conclusions

The paper highlights the importance of considering soil-structure interaction in construction design, particularly for high-rise buildings, industrial structures, and historical monuments. Based on the calculation analysis, the main findings of the research are:

1. Soil-structure interaction calculations are essential for both usual and unique high-rise buildings, industrial construction structures, and historical buildings. These calculations help correctly define forces in superstructures and diagnose causes of defects in historical buildings.

2. The results of numerical experiments indicate a significant underestimation of stresses in structures when the spatial behavior of soil is not considered. The underestimation can range from 150 to 400% for buildings on spread footings, while for buildings on pile foundations, it can be as high as 200–900%.

3. Based on the information provided, the architectural solution implemented in the high-rise building successfully minimized settlement using longer piles. The calculated settlement was reduced to 60 mm, and the actual settlement three years after construction was only 32 mm, indicating that the solution was effective.

4. Adequate consideration of soil behavior is necessary for industrial construction structures with complex shapes due to the requirements of technological processes. The results of calculation of an 80-meter-high silo tower and a clinker brick warehouse shows that such structures can experience similar loads and pressures on the soil as much taller buildings in civil engineering.

5. The calculation model of soils and structures plays a unifying role, interconnecting geological data, foundation engineering details, and features of structural behavior.

6. Reliable investigation data and application of nonlinear models in soil calculations provide the accuracy required for calculation of structures.

7. The calculation of structures considers expected and differential settlements, which increase the reliability of structures and exclude additional costs in foundation construction.

8. Soil-structure interaction calculations provide a reliable tool for diagnostics of causes of development of strains and defects in historical structures and rational designating measures to strengthen foundations and structures.

9. Using soil-structure interaction calculations results in a single ideology of interaction of different participants of construction design.

References

1. Vicencio, F., Alexander, N.A. Dynamic Structure-Soil-Structure Interaction in unsymmetrical plan buildings due to seismic excitation. Soil Dynamics and Earthquake Engineering. 2019. 127. 105817. DOI: 10.1016/j.soildyn.2019.105817
2. Gičev, V., Kisomi, H.B., Trifunac, M.D., Jalali, R.S. Flexibility of foundation increases the base shear and horizontal strains during an out–of–plane response to an SH pulse in linear and nonlinear soil. Soil Dynamics and Earthquake Engineering. 2019. 127. 105837. DOI: 10.1016/j.soildyn.2019.105837
3. Ge, Q., Xiong, F., Xie, L., Chen, J., Yu, M. Dynamic interaction of soil – Structure cluster. Soil Dynamics and Earthquake Engineering. 2019 123. Pp. 16–30. DOI: 10.1016/j.soildyn.2019.04.020
4. François, S., Pyl, L., Masoumi, H.R., Degrande, G. The influence of dynamic soil-structure interaction on traffic induced vibrations in buildings. Soil Dynamics and Earthquake Engineering. 2007. 27. Pp. 655–674, DOI: 10.1016/j.soildyn.2006.11.008
5. Worku, A., Lulseged, A. Kinematic pile-soil interaction using a rigorous two-parameter foundation model. Soil Dynamics and Earthquake Engineering. 2023. 165. DOI: 10.1016/j.soildyn.2022.107701
6. Mashhadi, S., Homaei, F. Soil-structure interaction and frequency components of near-fault records on the performance-based confidence levels of steel setback MRFs. Soil Dynamics and Earthquake Engineering. 2023. 166. DOI: 10.1016/j.soildyn.2023.107759
7. Lai, H., Gu, X., Tu, W., Lin, Y., Xiao, J. Effects of soil small strain nonlinearity on dynamic impedance of horizontally loaded suction caisson for offshore wind turbines. Soil Dynamics and Earthquake Engineering. 2023. 165. 107731. DOI: 10.1016/j.soildyn.2022.107731
8. Sabri, M.M., Shashkin, K.G. Subsoil stabilized by polyurethane resin injection: FEM calculation. Construction of Unique Buildings and Structures. 2020. 98(6). DOI: 10.18720/CUBS.91.8
9. Ulitsky, V.M., Shashkin, A.G., Shashkin, K.G., Shashkin, V.A., Lisyuk, M.B. Soil-structure interaction effects. Geotechnical Engineering for Infrastructure and Development - Proceedings of the XVI European Conference on Soil Mechanics and Geotechnical Engineering, ECSMGE 2015, 2015.
10. Yáñez-Godoy, H., Mokeddem, A., Elachachi, S.M. Influence of spatial variability of soil friction angle on sheet pile walls' structural behavior. Georisk Assessment and Management of Risk for Engineered Systems and Geohazards. 2017. 11(4). Pp. 299–314. DOI: 10.1080/17499518.2017.1297465
11. Stefanidou, S.P., Sextos, A.G., Kotsoglou, A.N.,Lesgidis, N., Kappos, A.J. Soil-structure interaction effects in analysis of seismic fragility of bridges using an intensity-based ground motion selection procedure. Engineering Structures. 2017. 151. Pp. 366–380. DOI: 10.1016/j.engstruct.2017.08.033
12. Martínez-De La Concha, A., Cifuentes, H., Medina, F." Finite element methodology to study soil-structure interaction in high-speed railway bridges. Journal of Computational and Nonlinear Dynamics. 2018. 13(3). 031010. DOI: 10.1115/1.4038819
13. Fu, X., Xie, Q. Spatial distribution of soil pressure based on soil arching effect of full-buried anti-slide pile. Electronic Journal of Geotechnical Engineering. 2013. 18 U. Pp. 5193–5202.
14. Bezih, K., Chateauneuf, A., Kalla, M., Bacconnet, C. Effect of soil-structure interaction on the reliability of reinforced concrete bridges. Ain Shams Engineering Journal. 2015. 6(3). Pp. 755–766. DOI: 10.1016/j.asej.2015.01.007
15. Mayoral, J.M., Castañon, E., Albarran, J. Regional subsidence effects on seismic soil-structure interaction in soft clay. Soil Dynamics and Earthquake Engineering. 2017. 103. Pp. 123–140. DOI: 10.1016/j.soildyn.2017.09.014
16. Maheshwari, B.K., Truman, K.Z., El Naggar, M.H., Gould, P.L. Three-dimensional nonlinear analysis for seismic soil–pile-structure interaction. Soil Dynamics and Earthquake Engineering. 2004. 24. Pp. 343–356. DOI: 10.1016/j.soildyn.2004.01.001

17. López Jiménez, G.A., Dias, D., Jenck, O. Effect of the soil–pile–structure interaction in seismic analysis: case of liquefiable soils. Acta Geotechnica. 2018. 14. Pp. 1509–1525. DOI: 10.1007/s11440-018-0746-2
18. Murzenko, Y.N. Experimental results on the distribution of normal contact pressure on the base of a rigid foundation resting on sand. Soil Mechanics and Foundation Engineering. 1965. 2. Pp. 69–73.
19. Evtushenko, S.I., Krakhmal'nyi, T.A. Investigation of the behavior of strip foundations with complex configuration of the base. Soil Mechanics and Foundation Engineering. 2017. 54. Pp. 169–172. DOI: 10.1007/s11204-017-9452-6
20. Gorbunov-Posadov, M.I. Raschet konstruktsiy na uprugom osnovanii. [Calculation of structures on elastic subsoil]. Moscow: Stroyizdat, 1973. 627 p.
21. Shahskin, A.G. Description of deformation behavior of clayey soil with a help of visco-elasto-plastic model. Engineering Geology. 2010. 4. Pp. 22–32.
22. Ulitsky, V., Shashkin, A., Shashkin, K., Lisyuk, M. Preservation and reconstruction of historic monuments in Saint Petersburg with provisions for soil-structure interaction. Geotechnical Engineering for the Preservation of Monuments and Historic Sites. 2013. Pp. 735–742. DOI: 10.1201/b14895-85
23. Semenov, A.S., Melnikov, B.E. Multimodel analysis of the elasto-plastic and elasto-visco-plastic deformation processes in materials and structures. Low Cycle Fatigue and Elasto-Plastic Behaviour of Materials. 1998. Pp. 659–664. DOI: 10.1016/b978-008043326-4/50110-0
24. Shahskin, A.G. Account of shape-changing strains at calculation of soils of buildings and underground structures. Residential construction. 2011. Pp. 17–21.
25. Wei, H., Dong-yan, L., Bao-yun, Z., Yan-bo, F., Yu-chao, X. Study on the rheological properties and constitutive model of Shenzhen mucky soft soil. Journal of Engineering Science and Technology Review. 2014. 7(3). Pp. 55–61.
26. Vasening, V.A., Shahskin, A.G. Vekovyye osadki zdaniy Sankt-Peterburga [Age-long settlement of buildings in St. Petersburg]. St.Petersburg: "Georeconstruction" Publishing house, 2022. 448 p.
27. Evseev, N.A. Accounting of physical nonlinearity of reinforced concrete structures at computation of structural systems. Bulletin of Civil Engineers. 2017. 5. Pp. 66–70. DOI: 10.23968/1999-5571-2017-14-5-66-70

Information about authors:

***Mohanad Sabri**, PhD in Technical Sciences*
ORCID: https://orcid.org/0000-0003-3154-8207
E-mail: mohanad.m.sabri@gmail.com

***Konstantin Shashkin**, PhD in Technical Sciences*
E-mail: cshashkin@yandex.ru

Received 17.02.2023. Approved after reviewing 05.05.2023. Accepted 10.05.2023

Magazine of Civil Engineering

ISSN 2712-8172

journal homepage: http://engstroy.spbstu.ru/

Research article

UDC 624.154:624.139.32:519.87

DOI: 10.34910/MCE.120.6

Prismatic face slope piles operating under frost heaving

O.V. Tretiakova [1, 2]✉

[1] *Perm National Research Polytechnic University, Perm, Russian Federation*

[2] *Perm State Agro-Technological University named after academician D.N. Prianishnikov, Perm, Russian Federation*

✉ *olga_wsw@mail.ru*

Keywords: frost heaving, prismatic face slope pile, equilibrium equation, stability

Abstract. The effectiveness of piles with reverse surface slope in frost heaving of soil has been the subject of discussion in many papers. In the previous works, the author considered cylindrical piles with an upper reverse taper and calculation method for the piles under these conditions. However, in order to extend the area of their use it is necessary to consider other configurations of piles as well. In this study, prismatic face slope piles are modeled for soil frost heaving conditions; equilibrium equations for calculating prismatic piles with four, six and eight faces are derived. The equilibrium equation for prismatic face slope piles in general form is also given. The equations make it possible to determine geometric parameters of piles ensuring their stability in soil under the action of tangential frost heaving forces. The author analyzes material capacity of cylindrical taper piles and prismatic face slope piles. The piles have the same bearing capacity in thawed soil and operate under the same geological and climatic conditions set before. The square pile with a sloping face shows the lowest material capacity. The proposed approach can be used for prismatic piles with a different number of faces in various conditions.

Citation: Tretiakova, O.V. Prismatic face slope piles operating under frost heaving. Magazine of Civil Engineering. 2023. 120. Article no. 12006. DOI: 10.34910/MCE.120.6

1. Introduction

The effectiveness of a pile under frost heaving is characterized by its stability, which can be achieved through the equilibrium of the acting forces. This equilibrium prevents the pile from being lifted by frost heaving forces, which contributes to the integrity of the structure above. The pile uplift can be avoided in various ways. The first way is to increase the load on the pile by changing the weight of the structures above. However, this might lead to unjustified cost increases. Another way is to use piles that reduce the impact of frost heaving forces on the structures. The design of such piles involves creation of surface slope resulting in additional restraining forces. The latter counteract the frost forces that cause the piles to rise.

The surface slope for a cylindrical pile can be created by means of a truncated taper at the top of the pile. The bottom base of the taper corresponds to the diameter of the pile, which creates the surface slope where forces are formed to counteract the frost heaving. The author of the paper [1] has developed a pile with an upper reverse taper.

If the pile is prismatic and has a square cross-section, the necessary counter-bulging forces can be obtained by shaping the upper section of the pile into a pyramid, with the upper square base being smaller. This makes it possible to create a slope on the side faces of the pile resulting in counter-bulging forces. Prismatic piles can have a cross-section with a different number of faces.

The effectiveness of surface slope piles has been verified by numerous experimental studies and practical use. V.F. Zhukov [2] described the practice of using piles with an expanded base in harsh climatic conditions of Magadan. K.A. Linell and E.F. Lobacz [3] reviewed the practice of applying foundations in frozen soil. They gave recommendations on designing trapezoidal foundations with expansion in the lower part and on pile foundations with a developed base in the form of an anchor plate. P.A. Abbasov and A.A. Kovalevskii [4] developed piles with ribbed surfaces, which they recommended to use in frost heaving soil conditions. F.G. Gabibov [5] confirmed the effectiveness of such piles in soils increasing in volume. O.P. Medvedeva, I.N. Kazakov and N.F. Bulankin [6] analyzed the performance of pyramidal-prismatic piles in conditions of Siberian climate. The prismatic part of the pile made it possible to use such piles in conditions of freezing and frost heaving. B.S. Yushkov and his colleagues [7–8] conducted research into the performance of the double taper pile ('double cone pile') in seasonally freezing soils. They proved the effectiveness of such a pile under soil frost heaving due to the upper reverse taper. S.V. Feshchenko, A.V. Veshkurtsev, G.B. Barskaya [9] proposed to increase the cross-section of the lower part of the pile in order to anchor it in permafrost. L. Domaschu k[10–11] studied foundations with expanded bases and their performance in heaving soils. In his paper [10] he considered a tower foundation consisting of inclined elements forming a truncated pyramid. The test results indicated that the influence of frost heaving on the inclined elements decreased as the angle of inclination increased. X. Huang, Y. Sheng and others [12–13] tested bell-shaped piles in freezing soil. They found increased resistance of such piles to lifting caused by tangential forces of frost heaving. M. Schafer and S.P. Madabhushi [14] conducted experimental studies of small pile models with an expanded base in soils increasing in volume. The results showed that the expanded base increased the resistance of piles to uplift, which is efficient under frost heaving. Z. Zhu, L. Han [15] proposed a taper-cylindrical foundation for a tower in frozen soil. D.C. Sego, K.W. Biggar and G. Wong [16] extended traditionally used investigation methods for straight piles to bell-shaped piles under permafrost. They pointed out that the bearing capacity of a pile in permafrost can be increased by base expansion. Thus, experimental studies reliably confirm the effectiveness of surface slope piles under frost heaving conditions.

However, practical design of such piles requires calculation methods taking into account frost heaving forces and other factors. The latter include climatic and hydrogeological conditions and also the thermal regime of the soil. The existing calculation regulations are based on the theory of elasticity and Fourier laws related to thermal conductivity of frozen soil. Calculation models of soil frost heaving have been developed by Russian and foreign authors. V.M. Ulitsky, I.I. Sakharov, V.N. Paramonov and S.A. Kudryavtsev [17–18] published a series of papers where they proposed a mathematical model to determine the thermal characteristics and stress-strain state of freezing soil. S. Nishimura and others [19] presented a thermo-hydro-mechanical formulation for frost heaving suitable for assessment of foundation stability. J.H. Dong, X.L. Wu and others [20] developed a computational model of horizontal frost heaving. A.G. Alekseev [21] compared the simulation results obtained by means of various software tools with the analytical solution of the soil frost heaving problem. Based on their work, the author of the paper [22] has developed a method for calculating normal frost heaving forces. However, calculation of piles of complex configurations, including surface slope piles, under frost heaving requires consideration of additional factors.

Many scientists have worked on calculation methods for piles with reverse surface slope and other configurations. Among them are A.Z. Ter-Martirosyan and Z.G. Ter-Martirosyan [23], who used analytical and numerical methods to calculate interaction of a pile with an enlarged base with the surrounding soil. They obtained the dependence of stress-strain state of soil on pile geometric parameters. Their approach can be applied to evaluate pile operation both in thawed and in frozen soil. V.S. Sazhin [24] analyzed frost heaving forces and deformations for shallow foundations. He investigated foundations of trapezoidal section and truncated pyramid-shaped blocks [25]. V.S. Sazhin presented the sloping faces of a trapezoidal foundation as stepped ones in the calculation scheme. To calculate heaving deformations, V.S. Sazhin proposed a design model of freezing soil in the form of a cylinder, with a taper representing a pyramidal pile being placed in it [26]. He used the equation of axisymmetric thermal stress of the soil cylinder. Z.G. Ter-Martirosyan [27] considered the stress-strain state of a freezing cylindrical soil element surrounding the pile. X.Y. Xu and others [28] suggested calculating foundations by the finite difference method, taking into account the stiffness of the foundation that limits soil heaving. G.Q. Kong and others [29, 30] conducted analytical study of a taper pile with an expanded base. They analyzed side resistance of the pile, taper angle and diameter of the lower base by numerical simulation methods and obtained increased load-bearing capacity of the taper pile for its lifting and under the action of negative soil friction. This is of interest for piles under conditions of soil frost heaving and soil thawing. M. Schafer and S.P. Madabhushi [14] mathematically described the behaviour of expanded base piles in layered soils increasing in volume. This mechanism of pile-soil interaction may find its application in frost heaving conditions. P. He et al [31] obtained analytical solution for calculation of trapezoidal channel in frost heaving. H. Jiang and others [32] developed a method for designing a parabolic channel in frozen soil using digital technology. Wu Y. and others [33] calculated stresses and strains of soil around a single bridge pile during freezing and used non-linear finite-element model of pile-soil interaction. S. Jianzhong and others [34] presented a numerical three-dimensional model of a bridge pile foundation in permafrost. It is evident from their research that calculation methods for piles of complex configurations have received attention in scientific practice.

Piles with reverse surface slope, on the one hand, are effective in conditions of soil frost heaving due to their configuration, on the other hand, they require more complex approaches to their calculation than piles of constant section. B.S. Yushkov and others [35–36] gave an analytical quantitative assessment of the effect of the angle of surface slope on pile displacement. However, the angle in each case was not calculated, but was set from a limited number of values, as the pile was manufactured in factory conditions. So this method of selecting geometric parameters of piles is time-consuming. The author of the paper [37–38] has developed a method for calculating the pile with the upper reverse taper, which makes it possible not to select, but to calculate the geometric parameters of the pile with the least time and labor consumption. As the upper reverse taper pile is only one of the variants of piles with reverse surface slope, other pile configurations need to be considered for design practice.

The aim of the study is to extend the taper pile design method developed by the author to prismatic piles with sloping faces (prismatic face slope piles). To achieve the aim, the following tasks have been set:

- to model square, hexagonal and octagonal prismatic piles with the upper part in the form of truncated pyramid;
- to obtain equations with respect to geometric parameters of piles in the soil under the action of heaving forces;
- to estimate material capacity of piles.

2. Methods

A cylindrical pile with the upper reverse taper in frost heaving conditions was developed by the author [37–38] in previous works. However, a special case of a taper is a pyramid, i.e. taper is a pyramid with an infinite number of faces. This paper describes behavior of a cylindrical reverse taper pile and several prismatic face slope piles under frost heaving, the cross-sections of the prismatic ones being square, hexagonal and octagonal. The upper part of the prismatic piles is designed as a truncated pyramid. Calculation schemes for two cases of frost boundary position along the height of the piles are shown in Fig. 1.

In Fig. 1 S_f, T_{fi} are the frost heaving normal and tangential forces and F_i is the frictional force on the side of the pile in the thawed soil, respectively; P is the sum of the external load and the pile weight and α is the pile surface angle. The figure also shows the position of the inherent sections of the pile: z_0 is the bed of non-heaving material under the grillage; $z_{tp(pr)}$ is the bottom base of the taper (pyramid), z_{pl} is the base of the pile.

Table 1 shows the input data for the pile design, where the soil conditions are represented by a stiff clay loam with a liquidity index of 0.4.

Table 1. Initial data for piles calculation

№	Parameter name	Parameter designation	Parameter value
1	Frost heaving tangential stresses	τ_f	100 kPa
2	Frost heaving normal stresses	σ_f	200 kPa
3	Sum of the external load on the pile and the pile weight	P	130 kN
4	Side resistance of the pile in the thawed soil	f_i	26 kPa
5	Frost boundary position	ξ	2.1 m

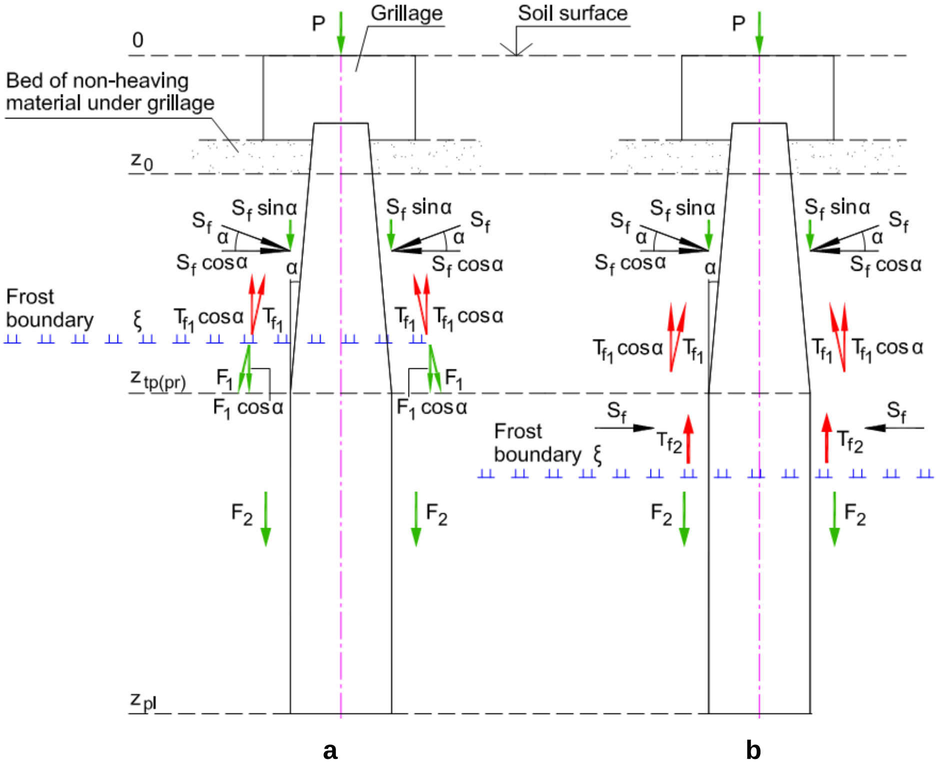

Figure 1. Two cases of frost boundary position of the pile:
a) frost boundary within the part of the pile with a surface slope;
b) frost boundary within the part of the pile of constant section.

2.1. Cylindrical pile with upper reverse taper

The bearing capacity of the cylindrical pile (Fig. 2a) for tangential frost heaving forces is 198.6 kN and tangential frost heaving forces is 231.2 kN. Thus, the tangential frost heaving forces that cause pile uplift exceed its bearing capacity and the condition of pile stability is not met. In this case we propose to specify the taper of the pile and determine the taper angle required for pile stability in the soil, the latter referring to the absence of vertical displacement, i.e. lifting. The taper angle is determined from the equation (1) obtained by the author [37–38].

Fig. 2b illustrates the cylindrical pile with an upper reverse taper and the coordinates of inherent sections. Fig. 2b shows a part of the taper L_{tp}, subject to the influence of frost heaving forces. R_{cl} is the radius of the cylindrical part of the pile.

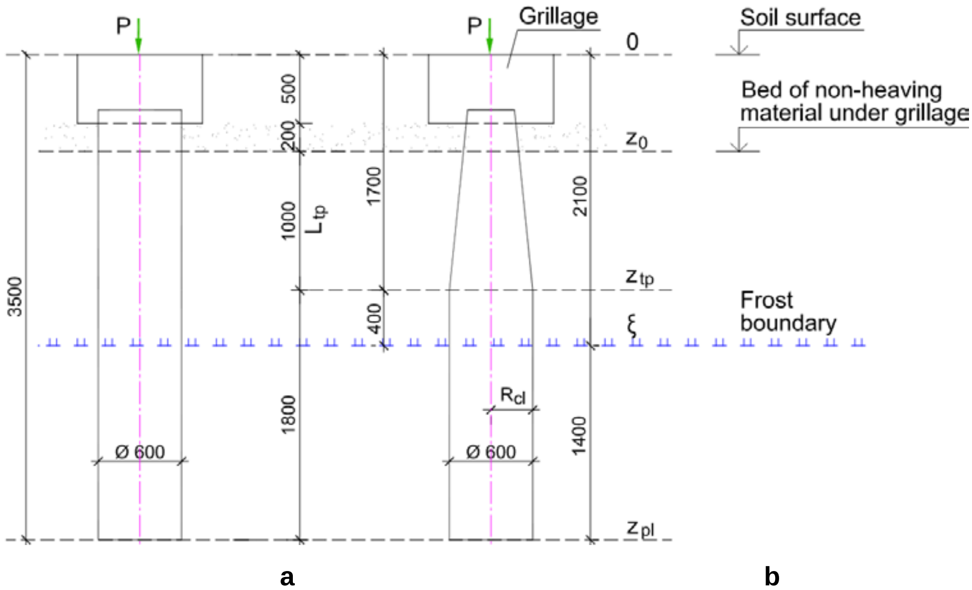

Figure 2. Piles with (a) constant section and (b) upper reverse taper, mm.

The equilibrium equation for the pile under the action of frost heaving forces [37–38] is illustrated in Fig. 1b and 2b.

$$0.5\sigma_f\left(z_{tp}-z_0\right)^2\left(\sin\alpha\right)^2+\left[-R_{cl}\sigma_f\left(z_{tp}-z_0\right)-0.5\tau_{f1}\left(z_{tp}-z_0\right)^2\right]\left(\sin\alpha\right)+$$
$$+R_{cl}\left[\tau_{f1}\left(z_{tp}-z_0\right)+\tau_{f2}\left(\xi-z_{tp}\right)-f_2\left(z_{pl}-\xi\right)\right]-0.5\pi^{-1}P=0. \quad (1)$$

The equation will make it possible to determine the taper angle required to ensure stability of the pile in the soil under frost heaving.

2.2. Prismatic square pile

A prismatic pile with a square cross section having sloping faces (hereinafter, prismatic square pile) is considered in the same soil conditions as the cylindrical taper pile discussed above, and their lengths are equal. Fig. 3 shows the pile and coordinates of its inherent sections. In Fig. 3 L_{pr} is a part of the pyramid subject to the influence of frost heaving forces; a_{pr} is the side of the upper base of the pyramid exposed to frost heaving forces; $a_{pr}(z)$ is the variable face width; a_{pl} is the side of the bottom base of the pyramid.

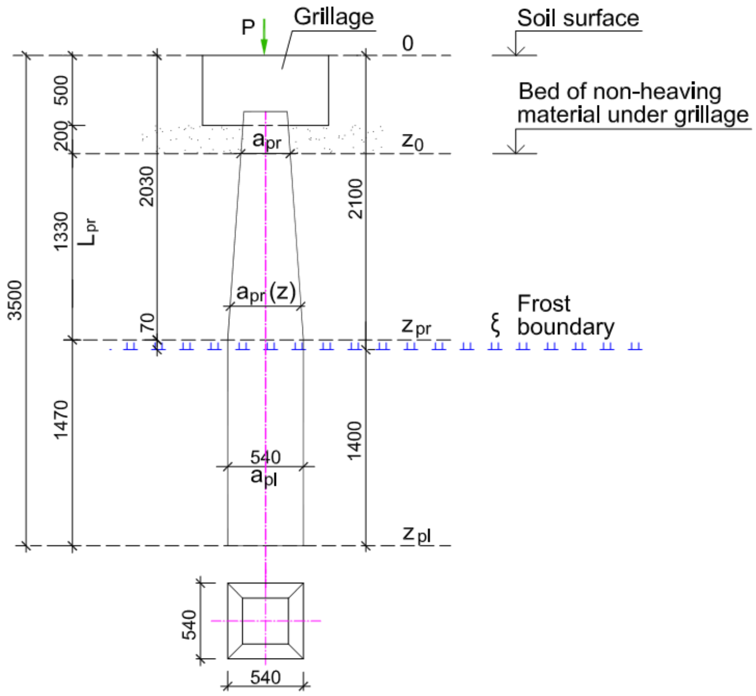

Figure 3. Prismatic square pile with sloping faces, mm.

Fig. 1b shows the forces acting on sloping and vertical faces of piles. The upper part of the prismatic pile is designed as a truncated pyramid.

The normal frost heaving force acting on the sloping faces of the pyramid (Fig. 1b) is presented as follows:

$$S_f=\int_{z_0}^{z_{pr}}\sigma_f dF_{pr}, \quad (2)$$

where F_{pr} is the side surface area (hereinafter surface area) of the pyramidal part of the pile.

The tangential frost heaving force acting on the sloping faces of the pyramid is presented by the equation

$$T_{f1}=\int_{z_0}^{z_{pr}}\tau_{f1}dF_{pr}. \quad (3)$$

And equation (4) presents tangential frost heaving force acting on vertical faces of the constant-section pile in the frozen zone.

$$T_{f2} = \int\limits_{z_{pr}}^{\xi} \tau_{f2} dF_{pl}, \tag{4}$$

where F_{pl} is the side surface area (hereinafter surface area) of the pile part with constant cross-section.

The frictional force on the side of constant section pile in the thawed soil is as follows:

$$F_2 = \int\limits_{\xi}^{z_{pl}} f_2 dF_{pl}. \tag{5}$$

Equation for the face slope angle of the square pile is based on equilibrium of acting forces. The equilibrium equation at frost boundary position $z_0 < z_{pr} < \xi$ (see Fig. 1b) is as follows:

$$-P - S_f \sin\alpha + T_{f1}\cos\alpha + T_{f2} - F_2 = 0. \tag{6}$$

Supposing that at small angles of face slope $\cos\alpha \approx 1,$ we rewrite the equation (6) as follows:

$$-P - S_f \sin\alpha + T_{f1} + T_{f2} - F_2 = 0. \tag{7}$$

Taking into account inherent sections in Fig. 1b and 3 and expressions (2–5), equation (7) will look like

$$-P - \left(\int\limits_{z_0}^{z_{pr}} \sigma_f dF_{pr} \right) \sin\alpha + \int\limits_{z_0}^{z_{pr}} \tau_{f_1} dF_{pr} + \int\limits_{z_{pr}}^{\xi} \tau_{f_2} dF_{pl} - \int\limits_{\xi}^{z_{pl}} f_2 dF_{pl} = 0. \tag{8}$$

The upper part of the square pile is designed as a truncated pyramid. Fig. 4 shows the projection of the pyramid face to the vertical plane, where z is an arbitrary coordinate; dF_{pr} is a variable area of the elementary stripe of the pyramid face. For small angles, it is assumed that the face area is equal to the area of its projection.

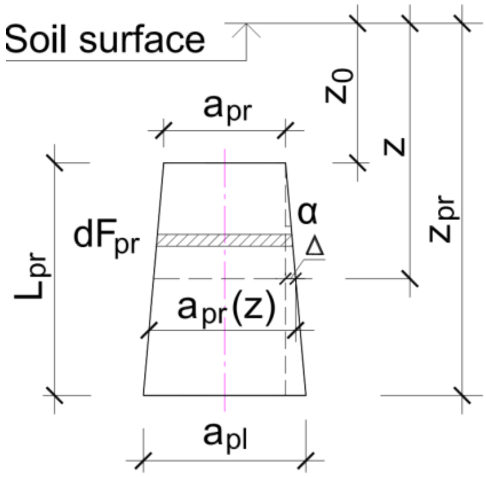

Figure 4. Pyramid face.

The variable area of the elementary stripe of the pyramid face, according to Fig. 4 is as follows:

$$dF_{pr} = 4a_{pr}(z)dz. \tag{9}$$

Its variable width is as follows:

$$a_{pr}(z) = a_{pr} + 2\Delta. \tag{10}$$

Taking into account $\Delta = (z - z_0) tg\alpha,$ and at small angles $tg\alpha \approx \sin\alpha,$ we obtain

$$a_{pr}(z) = a_{pr} + 2(z - z_0)\sin\alpha. \tag{11}$$

From the condition

$$\frac{(a_{pl}/2) - (a_{pr}/2)}{z_{pr} - z_0} = tg\alpha \approx \sin\alpha, \tag{12}$$

we have

$$a_{pr} = a_{pl} - 2(z_{pr} - z_0)\sin\alpha. \tag{13}$$

After substituting (13) in expression (11), we obtain

$$a_{pr}(z) = \left(a_{pl} - 2(z_{pr} - z_0)\sin\alpha\right) + 2(z - z_0)\sin\alpha. \tag{14}$$

After simplifying (14), the variable width of the elementary stripe will be written as the expression

$$a_{pr}(z) = a_{pl} - 2\sin\alpha(z_{pr} - z). \tag{15}$$

Taking into account (15), the variable area of the elementary stripe of the pyramid surface along its perimeter (9) will be

$$dF_{pr} = 4\left[a_{pl} - 2\sin\alpha(z_{pr} - z)\right]dz. \tag{16}$$

The elementary stripe area of the constant section pile along its perimeter is

$$dF_{pl} = 4a_{pl}dz. \tag{17}$$

Equation (8) after substituting (16) and (17) will be written as

$$\begin{gathered} -P - \left(\int_{z_0}^{z_{pr}} \sigma_f 4\left[a_{pl} - 2\sin\alpha(z_{pr} - z)\right]dz\right)\sin\alpha + \\ + \int_{z_0}^{z_{pr}} \tau_{f_1} 4\left[a_{pl} - 2\sin\alpha(z_{pr} - z)\right]dz + \int_{z_{pr}}^{\xi} \tau_{f_2} 4a_{pl}dz - \int_{\xi}^{z_{pl}} f_2 4a_{pl}dz = 0. \end{gathered} \tag{18}$$

After transformations, the equation (18) will take the form of a quadratic equation with respect to the sine of the face slope angle of the pyramidal part of the pile.

$$\begin{gathered} \sigma_f (z_{pr} - z_0)^2 (\sin\alpha)^2 + \left[-a_{pl}\sigma - \tau_{f_1}(z_{pr} - z_0)^2\right](\sin\alpha) + \\ + a_{pl}\left[\tau_{f_1}(z_{pr} - z_0) + \tau_{f_2}(\xi - z_{pr}) - f_2(z_{pr} - \xi)\right] - 0.25P = 0. \end{gathered} \tag{19}$$

The equation will make it possible to determine the taper angle required to ensure stability of the pile in the soil under frost heaving.

2.3. Prismatic hexagonal pile

A prismatic hexagonal pile with sloping faces (hereinafter prismatic hexagonal pile) is considered under the same soil conditions as the cylindrical taper pile discussed above and their lengths are equal. Fig. 5 shows the pile with the coordinates of the inherent sections. In Fig. 5 R_{cl} is radius of the circle inscribed in the bottom base of the pyramid, i.e. radius of the cylinder inscribed in the hexagonal constant-section of the pile.

Equation for the face slope angle of the hexagonal pile is based on equilibrium of acting forces. The equilibrium equation at frost boundary position $z_0 < z_{pr} < \xi$ (see Fig. 1b and 5) with regard to the inherent sections and expressions (2-5) is as follows:

$$-P - \left(\int_{z_0}^{z_{pr}} \sigma_f dF_{pr} \right) \sin\alpha + \int_{z_0}^{z_{pr}} \tau_{f_1} dF_{pr} + \int_{z_{pr}}^{\xi} \tau_{f_2} dF_{pl} - \int_{\xi}^{z_{pl}} f_2 dF_{pl} = 0. \quad (8)$$

The upper part of the pile is designed as a truncated hexagonal pyramid. The bottom base of the pyramid corresponds to a cross-section of a part of the pile with constant size. The angle of face slope for the truncated pyramid is calculated through the variable radius of the taper inscribed in the pyramid (Fig. 6). Fig. 6 shows: dF_{tp} is the variable surface area of the elementary strip of the inscribed taper; R_{tp} is the radius of the upper base of the inscribed taper subjected to soil frost heaving; $R_{tp}(z)$ is the variable radius of the taper; R_{cl} is the radius of the bottom base of the inscribed taper.

Radius of the circle inscribed in the bottom base of the pyramid, i.e. radius of the cylinder inscribed in the hexagonal section of the pile, is calculated as follows:

$$R_{cl} = \frac{a_{pl}}{2tg(\pi/6)} = 285.8 \text{ mm}, \quad (20)$$

where a_{pl} is the face width of the hexagonal constant section pile (Fig. 5).

The variable area of the elementary stripe around the perimeter of the truncated hexagonal pyramid will be

$$dF_{pr} = P(z)dz, \quad (21)$$

where $P(z)$ is the perimeter of the elementary pile stripe at its pyramidal part.

The perimeter of the elementary stripe of the pyramid surface is calculated through the radius of the inscribed circle.

$$P = 2Rntg(\pi/n), \quad (22)$$

where n is the number of faces of the pyramid; R is the radius of the inscribed circle.

The perimeter of the hexagonal pyramid is

$$P = 6.928R. \quad (23)$$

If the radius of the inscribed circle is assumed to be the variable radius of the taper inscribed in the pyramid, the area of the elementary stripe on the pyramidal part of the pile (21) will be as follows:

$$dF_{pr} = P(z)dz = 6.928R_{tp}(z)dz, \quad (24)$$

where $R_{tp}(z)$ is the variable radius of the taper inscribed in the pyramid (Fig. 6).

According to Fig. 6, the expression for the variable radius of the inscribed taper is presented as the equation

$$R_{tp}(z) = R_{tp} + \Delta. \quad (25)$$

Taking into account $\Delta = (z - z_0)tg\alpha,$ we obtain the equation

$$R_{tp}(z) = R_{tp} + (z - z_0)tg\alpha. \quad (26)$$

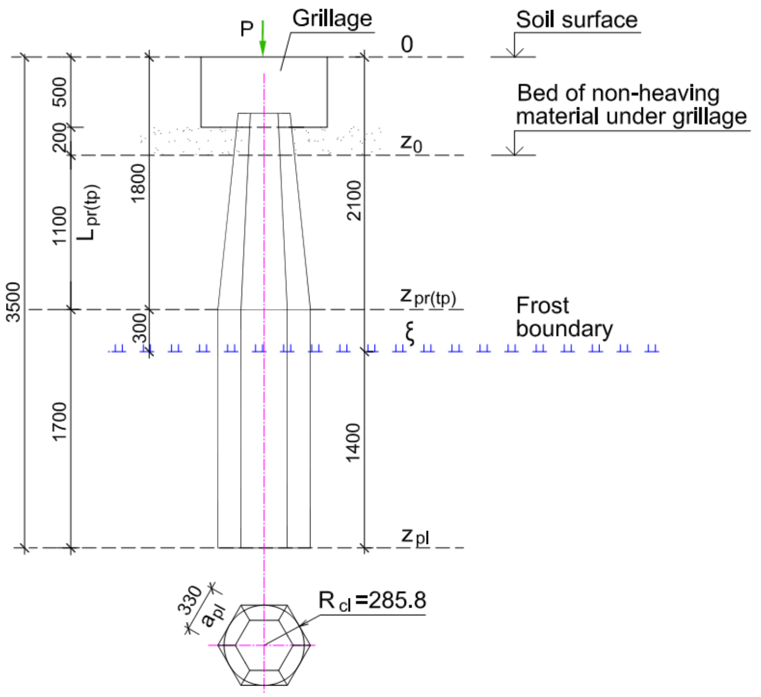

Figure 5. Prismatic hexagonal pile with sloping faces, mm.

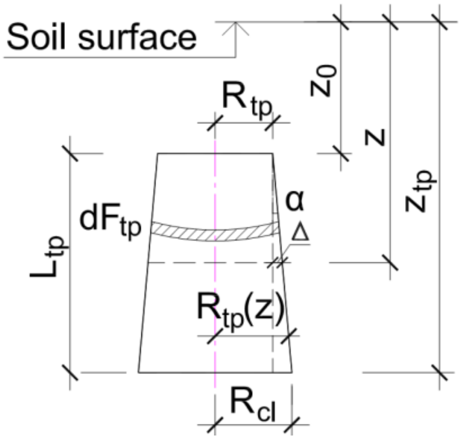

Figure 6. Taper inscribed in the pyramid.

Based on the condition

$$\left(R_{cl}-R_{tp}\right)/\left(z_{tp}-z_0\right)=tg\alpha, \tag{27}$$

the expression for radius of the inscribed taper will be as follows:

$$R_{tp}=R_{cl}-\left(z_{tp}-z_0\right)tg\alpha. \tag{28}$$

Then the expression for the variable radius of the taper (26) in view of (28) will be

$$R_{tp}\left(z\right)=\left[R_{cl}-\left(z_{tp}-z_0\right)tg\alpha\right]+\left(z-z_0\right)tg\alpha=R_{cl}-tg\alpha\left(z_{tp}-z\right). \tag{29}$$

Taking into account the variable radius of the inscribed taper (29), the expression for the area of the elementary stripe on the hexagonal pyramidal part of the pile (24) is written as

$$dF_{pr}=6.928\left(R_{cl}-tg\alpha\left(z_{tp}-z\right)\right)dz. \tag{30}$$

Given $tg\alpha\approx\sin\alpha$ for small angles, we obtain an expression for the area of the elementary stripe of the pyramid along its perimeter

$$dF_{pr} = 6.928\left(R_{cl} - \sin\alpha\left(z_{tp} - z\right)\right)dz. \tag{31}$$

where α is the angle of formatrix slope of the inscribed taper, R_{cl} is the radius of the circle inscribed in the hexagonal base of the pyramid.

As for the elementary surface stripe of the constant section pile, its area along the perimeter will be

$$dF_{pl} = 6a_{pl}dz. \tag{32}$$

Then equation (8) with account of (31) and (32) will be written as a quadratic equation with respect to the sine of the face slope angle of the pyramidal part of the pile.

$$\begin{gathered} 3.464\sigma_f\left(z_{tp} - z_0\right)^2(\sin\alpha)^2 + \\ +\left[-6.928R_{cl}\sigma_f\left(z_{tp} - z_0\right) - 3.464\tau_{f_1}\left(z_{tp} - z_0\right)^2\right](\sin\alpha) + \\ +6.928R_{cl}\tau_{f_1}\left(z_{tp} - z_0\right) + 6a_{pl}\left[\tau_{f_2}\left(\xi - z_{tp}\right) - f_2\left(z_{cl} - \xi\right)\right] - P = 0. \end{gathered} \tag{33}$$

The equation will make it possible to determine the taper angle required to ensure stability of the pile in the soil under frost heaving.

2.4. Prismatic octagonal pile

A prismatic pile with an octagonal cross section and sloping faces (hereinafter a prismatic octagonal pile) is considered in the same soil conditions as the cylindrical pile with a taper discussed above. The lengths of the prismatic pile and cylindrical one discussed above are the same. Fig. 7 shows the pile with coordinates of the inherent sections.

Equation for the face slope angle of an octagonal pile is based on equilibrium of acting forces. Taking into account inherent sections and expressions (2–5), the equilibrium equation at frost boundary position $z_0 < z_{pr} < \xi$ (see Fig. 1b) is as follows:

$$-P - \left(\int_{z_0}^{z_{pr}} \sigma_f dF_{pr}\right)\sin\alpha + \int_{z_0}^{z_{pr}} \tau_{f_1} dF_{pr} + \int_{z_{pr}}^{\xi} \tau_{f_2} dF_{pl} - \int_{\xi}^{z_{pl}} f_2 dF_{pl} = 0. \tag{8}$$

The upper part of the pile is designed as a truncated octagonal pyramid. The bottom base of the pyramid corresponds to a cross-section of the part with constant size. The angle of face slope of the pyramid is calculated through the variable radius of the taper inscribed in the pyramid (Fig. 6). Radius of the circle inscribed in the bottom base of the pyramid (Fig. 7) is calculated as follows:

$$R_{cl} = \frac{a_{pl}}{2tg\left(\pi/8\right)} = 298.7 \text{ mm}. \tag{34}$$

Variable surface area of the elementary stripe of the truncated pyramid is

$$dF_{pr} = P\left(z\right)dz. \tag{21}$$

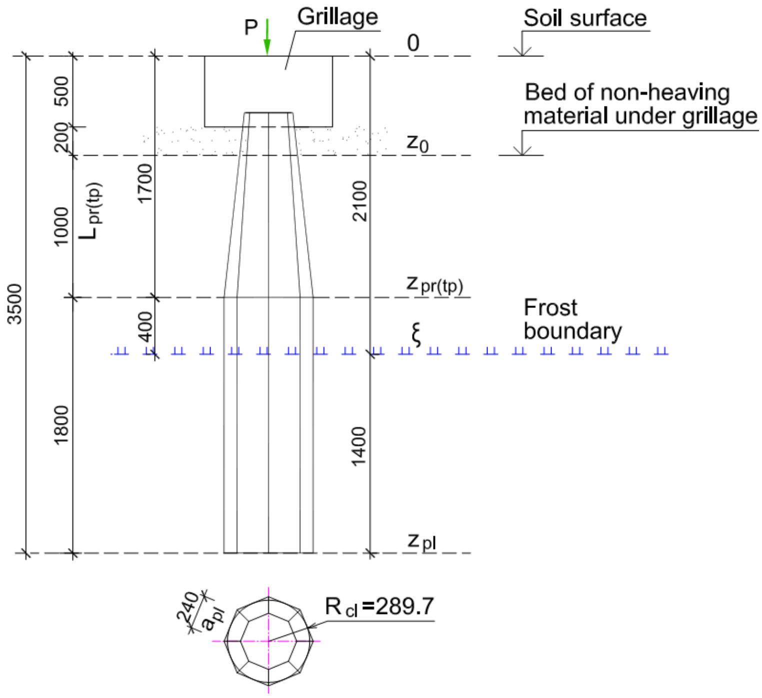

Figure 7. Prismatic octagonal pile with sloping faces, mm.

The perimeter of the elementary stripe of an octagonal pyramid is

$$P = 6.627R, \tag{35}$$

where R is the radius of the inscribed circle.

The radius of the circle inscribed will be considered as a variable radius of the taper inscribed in the pyramid. Then, taking into account the variable radius of the taper (21), the area of the elementary stripe on the pyramidal part of the pile is written as

$$dF_{pr} = P(z)dz = 6.627R_{tp}(z)dz. \tag{36}$$

When substituting the equation (29) in the expression (36) we obtain the equation

$$dF_{pr} = 6.627\left(R_{cl} - tg\alpha\left(z_{tp} - z\right)\right)dz. \tag{37}$$

Given $tg\,\alpha \approx \sin\alpha$ for small angles, the expression for the area of the elementary stripe of the pyramid along its perimeter can be written as

$$dF_{pr} = 6.627\left(R_{cl} - \sin\alpha\left(z_{tp} - z\right)\right)dz. \tag{38}$$

The area of the elementary surface stripe of the constant section pile along its perimeter is as follows:

$$dF_{pl} = 8a_{pl}dz. \tag{39}$$

where a_{pl} is the width of the face of the octagonal constant section pile.

Equation (8) with regard to (38) and (39) will be written as a quadratic equation with respect to the sine of the face slope angle of the pyramidal part pile.

$$\begin{gathered}3.314\sigma_f\left(z_{tp} - z_0\right)^2(\sin\alpha)^2 + \\ +\left[-6.627R_{cl}\sigma_f\left(z_{tp} - z_0\right) - 3.314\tau_{f_1}\left(z_{tp} - z_0\right)^2\right](\sin\alpha) + \\ +6.627R_{cl}\tau_{f_1}\left(z_{tp} - z_0\right) + 8a_{pl}\left[\tau_{f_2}\left(\xi - z_{tp}\right) - f_2\left(z_{cl} - \xi\right)\right] - P = 0.\end{gathered} \tag{40}$$

The equation will make it possible to determine the taper angle required to ensure stability of the pile in the soil under frost heaving.

2.5. Equation of face slope piles in general form

The equation for prismatic pile with sloping faces in general form is based on the equilibrium of all forces acting on the piles in the freezing soil.

$$-P-\left(\int_{z_0}^{z_{pr}} \sigma_f dF_{pr}\right)\sin\alpha+\int_{z_0}^{z_{pr}} \tau_{f_1} dF_{pr}+\int_{z_{pr}}^{\xi} \tau_{f_2} dF_{pl}-\int_{\xi}^{z_{pl}} f_2 dF_{pl}=0. \tag{8}$$

The upper part of the piles is designed as a truncated pyramid. The variable elementary surface area of the pyramid is

$$dF_{pr}=P(z)\,dz. \tag{21}$$

The perimeter of the elementary stripe of the pyramid surface through the radius of the inscribed circle is

$$P=2Rntg(\pi/n), \tag{22}$$

where n is the number of faces of the pyramid, R is the radius of the inscribed circle.

If the radius of the incircle is assumed to be the variable radius of the taper inscribed in the pyramid, then the expression (21) considering (22) will be as follows:

$$dF_{pr}=P(z)\,dz=2n\,tg(\pi/n)\,R_{tp}(z)\,dz, \tag{41}$$

where $R_{tp}(z)$ is the variable radius of the taper inscribed in the pyramid.

Then the area of the elementary stripe of the pyramidal part of the pile (41) with account of the variable radius of the taper (29) will be written as

$$dF_{pr}=2n\,tg(\pi/n)\left(R_{cl}-tg\alpha\left(z_{tp}-z\right)\right)dz. \tag{42}$$

where R_{cl} is the radius of the circle inscribed in the base of the pyramid.

Given $tg\alpha \approx sin\alpha$ for small angles, the expression (42) will be as follows:

$$dF_{pr}=2n\,tg(\pi/n)\left(R_{cl}-\sin\alpha\left(z_{tp}-z\right)\right)dz. \tag{43}$$

The elementary stripe area of a constant section pile along its perimeter will be

$$dF_{pl}=na_{pl}dz. \tag{44}$$

where a_{pl} is the face width of the constant section pile.

Equation (8) with (43) and (44) will be written as a quadratic equation with respect to the sine of the face slope angle of the pyramidal part of the pile.

$$\begin{gathered}ntg(\pi/n)\sigma_f\left(z_{tp}-z_0\right)^2(\sin\alpha)^2+\\+\left[-2ntg(\pi/n)R_{cl}\sigma_f\left(z_{tp}-z_0\right)-ntg(\pi/n)\tau_{f_1}\left(z_{tp}-z_0\right)^2\right](\sin\alpha)+\\+2ntg(\pi/n)R_{cl}\tau_{f_1}\left(z_{tp}-z_0\right)+\\+na_{pl}\left[\tau_{f_2}\left(\xi-z_{tp}\right)-f_2\left(z_{cl}-\xi\right)\right]-P=0.\end{gathered} \tag{45}$$

The equation will make it possible to determine the taper angle required to ensure stability of the pile in the soil under frost heaving.

3. Results and Discussion

The paper considers a cylindrical pile with an upper reverse taper and prismatic pile with sloping faces in the upper part, operating under frost heaving conditions. The cylindrical pile was developed by the author earlier. Prismatic piles with four, six and eight faces are modeled in this study. The upper part of the cylindrical pile is a truncated taper while that of the prismatic pile looks like a truncated pyramid with a different number of faces.

The author provides equations of equilibrium for prismatic piles with sloping faces, the equations being presented in integral form. These equations establish a relationship between the geometric parameters of the piles and the magnitudes and ratios of these forces, which makes it possible to determine the parameters of the piles. Considering the soil in the framework of elasticity theory, the integral values of forces within the given intervals are taken equal to their average values. In view of this and also sectional variability, the equilibrium equations are transformed into second-order equations with respect to geometric parameters of piles. To derive the second-order equations, the area of a truncated pyramid is used, the area being represented through the variable width of the faces and the variable radius of the taper inscribed in the pyramid. The calculation method developed by the author can be used for prismatic piles with any number of faces. The equations are given in Table 2.

Table 2. Pile equations.

Pile type	Equation regarding the geometric parameters of the pile	Equation number
Cylindrical pile with upper reverse taper	$0.5\sigma_f (z_{tp}-z_0)^2(\sin\alpha)^2 + {}$ $+[-R_{cl}\sigma_f (z_{tp}-z_0)-0.5\tau_{f1}(z_{tp}-z_0)^2](\sin\alpha)+{}$ $+R_{cl}[\tau_{f1}(z_{tp}-z_0)+\tau_{f2}(\xi-z_{tp})-f_2(z_{pl}-\xi)]-0.5\pi^{-1}P=0.$	(1)
Prismatic octagonal pile	$3.314\sigma_f (z_{tp}-z_0)^2(\sin\alpha)^2 + {}$ $+[-6.627R_{cl}\sigma_f (z_{tp}-z_0)-3.314\tau_{f1}(z_{tp}-z_0)^2](\sin\alpha)+{}$ $+6.627R_{cl}\tau_{f1}(z_{tp}-z_0)+8a_{pl}[\tau_{f2}(\xi-z_{tp})-f_2(z_{cl}-\xi)]-P=0.$	(40)
Prismatic hexagonal pile	$3.464\sigma_f (z_{tp}-z_0)^2(\sin\alpha)^2 + {}$ $+[-6.928R_{cl}\sigma_f (z_{tp}-z_0)-3.464\tau_{f1}(z_{tp}-z_0)^2](\sin\alpha)+{}$ $+6.928R_{cl}\tau_{f1}(z_{tp}-z_0)+6a_{pl}[\tau_{f2}(\xi-z_{tp})-f_2(z_{cl}-\xi)]-P=0.$	(33)
Prismatic square pile	$\sigma_f (z_{pr}-z_0)^2(\sin\alpha)^2+[-a_{pl}\sigma-\tau_{f1}(z_{pr}-z_0)^2](\sin\alpha)+{}$ $+a_{pl}[\tau_{f1}(z_{pr}-z_0)+\tau_{f2}(\xi-z_{pr})-f_2(z_{pl}-\xi)]-0.25P=0$	(19)
Equation of a prismatic pile in general form	$n\,tg\,(\pi/n)\,\sigma_f (z_{tp}-z_0)^2(\sin\alpha)^2 + {}$ $+[-2n\,tg(\pi/n)\,R_{cl}\sigma_f (z_{tp}-z_0)-n\,tg(\pi/n)\,\tau_{f1}(z_{tp}-z_0)^2](\sin\alpha)+{}$ $+2n\,tg(\pi/n)\,R_{cl}\tau_{f1}(z_{tp}-z_0)+na_{pl}[\tau_{f2}(\xi-z_{tp})-f_2(z_{cl}-\xi)]-P=0.$	(45)

For the conditions, given in Table 1, the geometric parameters of the piles such as cylindrical piles with upper reverse taper and prismatic piles with sloping four, six and eight faces have been obtained. The piles operate in the same soil and climatic conditions and are loaded with the same vertical load. All piles meet the design requirements for the section size at the point of embedding in the pile grillage. The length of all the piles is 3.0 m. The cross-section of the lower part of the piles is constant. The length and cross-section of the lower part is calculated from the condition of the vertical compressive load in the thawed soil, i.e. in summer. The cross-section of the upper part of the pile is variable with a sloping surface. The corresponding top length and angle are limited by the cross-section of the pile at the embedment point in the pile grillage. The surface slope angle is obtained from the equilibrium condition of the pile in the soil under the action of frost heaving forces. The parameters of the pile are shown in Table 3.

Table 3. Parameters of piles.

Parameters of piles / Piles type	Bearing capacity of piles in thawed soil, кN	Pile (inscribed circle) radius, m	Taper (pyramid) length, m	Taper (inscribed taper) angle, degree	Pile volume, m^3
Cylindrical pile with taper	134.92	0.3	1.0	5.96	0.73
Prismatic octagonal pile	134.29	0.2897	1.0	6.13	0.71
Prismatic hexagonal pile	134.72	0.2858	1.1	5.57	0.71
Prismatic square pile	135.0	0.54, face width	1.33	4.6, face angle	0.70

A comparison of the piles (Table 3) for the geological conditions given in the article has shown that under equal geological conditions with the same vertical load, the square pile with sloping faces has the smallest volume. Consequently, the minimum material capacity has been shown by the prismatic square pile. As the pile spacing in the group is determined by the cross-section, the square piles with sloping faces require the smallest space between them.

Surface slope piles have been the subject of attention of many scientists. Piles with expanded base were investigated by V.F. Zhukov [2], B.S. Yushkov [7–8], S.V. Feshchenko [9], L. Domaschuk [10–11], M. Schafer and S.P. Madabhushi [14] and others. Huang and Sheng [12–13] tested bell-shaped piles. However, in existing studies the range of configurations is mostly limited to cylindrical piles, although prismatic piles also occur in design and construction practice. The author of the paper has considered the performance of both cylindrical and prismatic piles in heaving soil and developed a method for calculating the geometric parameters of piles under the set conditions.

Another important aspect is applicability and practical relevance of the calculation factors. V.S. Sazhin [39] investigated the behavior of the soil under a strip foundation and derived an equation for the soil uplifting and internal forces of the foundation. Relying on the equality of works [26] performed by the forces that contribute to the pile uplift and prevent it, V.S. Sazhin [26] also determined the displacement of a pile in the swelling soil. He pointed out that, despite different nature of soil swelling and heaving, the deformations of foundations caused by these processes were due to similar laws. Therefore, in his calculations he used the same methods both for swelling and frost heaving soils. V.S. Sazhin obtained a universal formula for the vertical displacement of piles with any cross-section under heaving forces.

Later on B.S. Yushkov and D.S. Repetsky [40] proposed a formula for calculating the displacements of a 'double cone pile' [40] under the action of tangential frost heaving forces. These equations can be successfully used to verify the displacements of piles operated under frost heaving. However, based on the personal experience, the author considers the geometric parameters of foundations that ensure zero displacement under specified conditions more important than displacements themselves. So, in construction design, the author emphasizes the importance of using the equations for calculating geometrical parameters of foundations, which is especially true for piles of complex shapes, in particular those with a surface slope.

In the paper the author presents solutions to determine the required geometric parameters of cylindrical piles with upper reverse taper and prismatic piles with sloping faces, where the equilibrium is zero displacement of piles under the action of frost heaving forces. The author follows the system approach to the solution of the problem, i.e. takes into account the frost boundary position, values of soil frost heaving forces, etc.

When deriving equations for calculating prismatic piles with a pyramidal part, the author uses the expression for the variable radius of the inscribed taper and the same experimental approaches [38] as for the pile with taper. It is due to the fact that the cylindrical pile with the upper reverse taper is effective in frost heaving conditions due to the taper part, while the prismatic pile with sloping faces provides such efficiency due to the pyramidal part. Taking into account that a taper is a pyramid with an infinite number of faces, the latter may be considered as a special case of a taper.

Modern methods of calculating piles under frost heaving conditions do not distinguish between cylindrical and prismatic piles. Only the surface area of the pile subject to frost heaving forces is taken into account. However, the author's experience reveals that in seasonally freezing soils the ribs of a prismatic pile affect the size and speed of its lifting by frost heaving forces. The rib effect and the difference in the operation of prismatic and cylindrical piles under frost heaving have become the subject of the author's further research.

4. Conclusion

With large areas affected by frost heaving, protection methods based on the properties of constructions, without use of additional elements and measures, are of particular interest. Such constructions are piles with reversed surface slope, whose configuration makes it possible to reduce the negative effect of frost heaving.

In this study, the calculation method for cylindrical piles with an upper reverse taper is extended to prismatic piles with sloping faces. Equations for calculating geometric parameters of piles with sloping faces are derived and conclusions on the material capacity of the piles are drawn. The equations make it possible to determine geometric parameters of piles ensuring their stability in soil under the action of tangential frost heaving forces.

Further research will be aimed at performance of face slope piles in a group, as well as technological provisions for manufacturing piles at the construction site and in the factory. Attention will be paid to the automation of the developed calculation method for surface slope piles.

References

1. Tretyakova, O.V., Yushkov, B.S. Inverted-Cone Piles for Transport Constructions in Seasonally Freezing Soils. Soil Mechanics and Foundation Engineering. 2017. 54(3). Pp. 173–176. DOI: 10.1007/s11204-017-9453-5
2. Zhukov, V.F. Conference on design and construction of pile foundations in permafrost soils. Soil Mechanics and Foundation Engineering. 1970. 7(3). Pp. 213–215. DOI: 10.1007/BF01704636
3. Linell, K.A., Lobacz, E.F. Design and Construction of Foundations in Areas of Deep Seasonal Frost and Permafrost. CRREL Special Report (US Army Cold Regions Research and Engineering Laboratory). 1980. (80–34). Pp. 310.
4. Abbasov, P.A., Kovalevskii, A.A. Behavior of piles with ribbed surfaces in sand soils. Soil Mechanics and Foundation Engineering. 1984. 21(2). Pp. 69–75. DOI: 10.1007/BF01710704
5. Gabibov, F.G. New pile foundation structures for swelling clay soils. Journal of Physics: Conference Series. 2021. 1928(1). Pp. 012064. DOI: 10.1088/1742-6596/1928/1/012064
6. Kozakov, Y.N., Medvedeva, O.P., Bulankin, N.F. Studying the operational features of composite pyramidal-prismatic piles. Osnovaniya, Fundamenty i Mekhanika Gruntov. 1994. (1). Pp. 16–18.
7. Yushkov V., R.D. Construction of foundations in oil industry. Environmental protection in oil and gas complex. 2008. (12). Pp. 12–17.
8. Yushkov, B.S., Degtyar, A.A., Shakhova, A.B. Reinforcement of weak seasonally freezing soils at road consructing by double-cone hollow pile method. Proceedings of the IOP Conference Series: Materials Science and Engineering. 2018. 451 (1). Pp. 012044. DOI: 10.1088/1757-899X/451/1/012044
9. Feshchenko, S.V., Veshkurtsev, A.V., Barskaya, G.B. Use of the combined pile – Anchor in permafrost soil. Neftyanoe khozyaystvo – Oil Industry. 2004. (9). Pp. 115–117.
10. Domaschuk, L. Frost Heave Forces on Embedded Structural Units. Proceedings of the 4th Canadian Permafrost Conference. 1982. Pp. 487–496.
11. Domaschuk, L. Frost heave resistance of pipe piles with expanded bases. In Proceedings of the International Offshore Mechanics and Arctic Engineering Symposium. 1984. 3. Pp. 58–63.
12. Huang, X., Sheng, Y. Experimental study on anti-frost jacking of belled pile in seasonally frozen ground regions. Springer Series in Geomechanics and Geoengineering. 2018. 216849. Pp. 1368–1371. DOI: 10.1007/978-3-319-97115-5
13. Huang, X., Sheng, Y., Huang, L., Peng, E., Cao, W., Zhang, X., He, B. Experimental Study on the Anti-frost Jacking Ability of Belled Pile Under Unidirectional Freezing Condition. Gongcheng Kexue Yu Jishu/Advanced Engineering Science. 2021. 53(1). Pp. 122–131. DOI: 10.15961/j.jsuese.201901193
14. Schafer, M., Madabhushi, S.P.G. Uplift Resistance of Enlarged Base Pile Foundations. Indian Geotechnical Journal. 2020. 50(3). Pp. 426–441. DOI: 10.1007/s40098-019-00369-3
15. Zhu, Z., Han, L. Discussions on tower base design principles and geological conditions from Budongquan to Fenghuo Mountain in the project of ± 400 KV AC-DC Network in Qinghai-Tibet plateau. Proceedings of the 2011 International Conference on Multimedia Technology, ICMT 2011. 2011. Pp. 1030–1033. DOI: 10.1109/ICMT.2011.6002863
16. Sego, D.C., Biggar, K.W., Wong, G. Enlarged Base (Belled) Piles for Use in Ice or Ice-Rich Permafrost. Journal of Cold Regions Engineering. 2003. 17(2). Pp. 68–88. DOI: 10.1061/(asce)0887-381x(2003)17:2(68)
17. Ulitskii, V.M., Sakharov, I.I., Paramonov, V.N., Kudryavtsev, S.A. Bed – Structure System Analysis for Soil Freezing and Thawing Using the Termoground Program. Soil Mechanics and Foundation Engineering. 2015. 52(5). Pp. 240–246. DOI: 10.1007/s11204-015-9335-7
18. Sakharov, I.I., Paramonov, V.N., Kudryavtsev, S.A. The account of frost heave and thawing processes when designing road embankments in cold regions. Lecture Notes in Civil Engineering. 2020. 49. Pp. 19–24. DOI: 10.1007/978-981-15-0450-1_3
19. Nishimura, S., Gens, A., Olivella, S., Jardine, R.J. Thm-coupled finite element analysis of frozen soil: Formulation and application. Geotechnique. 2009. 59(3). Pp. 159–171. DOI: 10.1680/geot.2009.59.3.159
20. Dong, J.H., Wu, X.L., Shi, L.J., Yu, X.Y., He, P.F. Calculation method and analysis of horizontal frost heave effect of L-shaped retaining wall in permafrost regions. Yantu Lixue/Rock and Soil Mechanics. 2022. 43(4). Pp. 879–890. DOI: 10.16285/j.rsm.2021.0894.
21. Alekseev, A., Gribovskii, G., Vinogradova, S. Comparison of analytical solution of the semi-infinite problem of soil freezing with numerical solutions in various simulation software. Proceedings of the IOP Conference Series: Materials Science and Engineering. 2018. 365 (4). Pp. 042059. DOI: 10.1088/1757-899X/365/4/042059
22. Tretiakova, O.V. Normal stresses of frost heaving as function of excess moisture. Magazine of Civil Engineering. 2017. 76(8). Pp. 130–139. DOI: 10.18720/MCE.76.12

23. Ter-Martirosyan, A.Z., Ter-Martirosyan, Z.G. Interaction between finite stiffness broadened heellong pile and the surrounding soil. Procedia Engineering. 2015. 111. Pp. 756–762. DOI: 10.1016/j.proeng.2015.07.142
24. Sazhin, V.S., Borshchev, V.V., Sazhin, A.V. Interaction between shallow foundations and slightly heaving bed soil. Soil Mechanics and Foundation Engineering. 1984. 21(4). Pp. 177–180. DOI: 10.1007/BF01710610
25. Sazhin, V.S., Borshchev, V.V. Interaction of shallow strip foundations and heaving soils. Soil Mechanics and Foundation Engineering. 1987. 24(4). Pp. 129–133. DOI: 10.1007/BF01716861
26. Sazhin, V.S. Method of determining the magnitude of rise of piles following flooding of swelling soils. Soil Mechanics and Foundation Engineering. 1968. 5(1). Pp. 49–52. DOI: 10.1007/BF01707231
27. Ter-Martirosyan, Z.G., Gorbachev, P.A. Stress-strain state of a freezing layer of clayey soil. Soil Mechanics and Foundation Engineering. 2011. 48(2). Pp. 43–51. DOI: 10.1007/s11204-011-9127-7
28. Xu, X.Y., Li, H.S., Qiu, M.G., Tao, Z.X. Calculation of frost heave in seasonal frozen soil under piled foundation restrain condition. Harbin Jianzhu Daxue Xuebao/Journal of Harbin University of Civil Engineering and Architecture. 2001. 34(6). Pp. 8–11.
29. Kong, G.Q., Yang, Q., Liu, H.L., Liang, R.Y. Numerical study of a new belled wedge pile type under different loading modes. European Journal of Environmental and Civil Engineering. 2013. 17(SUPPL.1). Pp. s65–s82. DOI: 10.1080/19648189.2013.834586
30. Kong, G.Q., Zhou, L.D., Gu, H.W., Qin, H.Y. An Approach for Capacity Calculation of Shaped Pile Group Under Uplift Load. Soil Mechanics and Foundation Engineering. 2018. 55(4). Pp. 270–276. DOI: 10.1007/s11204-018-9536-y
31. He, P., Ma, W., Mu, Y., Dong, J., Huang, Y. Elastic foundation beam model for frost heave damage of trapezoidal canal lining considering frost heave force and adfreeze force. Zhongnan Daxue Xuebao (Ziran Kexue Ban)/Journal of Central South University (Science and Technology). 2021. 52(11). Pp. 4148–4157. DOI: 10.11817/j.issn.1672-7207.2021.11.034
32. Jiang, H., Li, L., Wang, Z., Gong, J., Sun, T., Li, H. Anti-frost heave design method for a parabolic canal based on the hydraulic optimal solution set in seasonally frozen regions. Cold Regions Science and Technology. 2022. 193. Pp. 103433. DOI: 10.1016/j.coldregions.2021.103433
33. Wu, Y., Zhu, Y., Guo, C., Su, Q., Ma, W. Multifield coupling model and its applications for pile foundation in permafrost. Science in China, Series D: Earth Sciences. 2005. 48(7). Pp. 968–977. DOI: 10.1360/082004-175
34. Jianzhong, S., Chunxiang, G., Xu, W., Weijia, Z. Numerical analysis of the forming process of the bearing capacity of the auxiliary pile foundation in Permafrost area. Proceedings of the E3S Web of Conferences. 2020. 198. Pp. 02002. DOI: 10.1051/e3sconf/202019802002
35. Yushkov, B.S.; Repetskii, D.S. The method of forces frost heaving of the ground on two conical pile. Bulletin of Perm National Polytechnic University Construction and Architecture. 2014. 4. Pp. 59–67.
36. Yushkov. Experimental and theoretical basics for the calculation of biconical pile foundation that install in frost heave soils. Perm: Permskiy Natsionalnyy Issledovatelskiy Politekhnicheskiy Universitet 2015. Pp. 311.
37. Tretiakova, O.V. Modeling a reverse taper pile for frost heave conditions. Journal of Physics: Conference Series. 2021. 1928(1). Pp. 012045. DOI: 10.1088/1742-6596/1928/1/012045
38. Tretiakova, O.V. Model of pile-frozen soil interaction in a closed form. Magazine of Civil Engineering. 2022. 115(7). Pp. 11501. DOI: 10.34910/MCE.115.1
39. Sazhin, V.S. Determination of deformations of a base of expansive soil with consideration of its joint action with the structure. Soil Mechanics and Foundation Engineering. 1970. 7(1). Pp. 49–54. DOI: 10.1007/BF01703624
40. Repetskii D.S., Y.B.S. Computation of a single twoconic pile in the sasonally freezing frost heaving soil. Nauchno-tekhnicheskiy vestnik Povolzh'ya. 2011. (3). Pp. 163–166.

Information about author:

Olga Tretiakova, *PhD in Technical Sciences*
E-mail: olga_wsw@mail.ru

Received 11.12.2022. Approved after reviewing 28.02.2023. Accepted 28.02.2023.

Magazine of Civil Engineering. 2023. 120(4). Article No. 12007

Magazine of Civil Engineering

ISSN
2712-8172

journal homepage: http://engstroy.spbstu.ru/

Research article

UDC 691.3

DOI: 10.34910/MCE.120.7

Phase structure of cement pastes with antifreeze agents

E.A. Vdovin , ***V.F. Stroganov***

Kazan State University of Architecture and Engineering, Kazan, Russian Federation

vdovin007@mail.ru

Keywords: phase structure, cement paste, antifreeze agents, X-ray phase analysis, differential thermal and thermogravimetric analysis, electron microscopy, cement-crushed stone mixtures

Abstract. This paper is concerned with changes in the phase structure of cement paste modified by complex antifreeze agents based on sodium formate, calcium chloride and S-3 superplasticizer. Complex modifiers were developed for cement-crushed mixtures hardening at low temperatures (down to –15.0 °C) used in pavement structures. In countries where construction and operation of highways occur at low air temperatures (below 0 °C), it is promising to use the method of modifying cement-crushed mixtures with complex antifreeze agents. The structural studies of cement paste with these additives are poorly described in scientific literature. Therefore, the aim of this work was to consider the impact of complex antifreeze agents in cement paste on the peculiarities of phase structure formation and the relationship between the structure and the properties of the obtained materials. The cement paste was tested for compressive strength using the standard technique; then after preparation, the samples were tested by X-ray, differential thermal and thermogravimetric analyses. It was established that the modification provides the possibility to increase the content of the crystalline phase compared with the amorphous one in the form of new formations (portlandite and dicalcium hydrosilicates). The developed complex modifiers contribute to activation of hydration processes in cement paste, which is confirmed by the level of the hydration degree up to 0.6 and the integral value of weight loss up to 20.5 %. The relationships between the increase in the compressive strength of cement paste and the increase in the hydration degree of calcium silicates and the integral value of weight loss were established. It was shown that the combined use of components of the complex three-component additive provided synergism of processes of structure formation and, as a consequence, an increase in the strength of cement paste. The use of the developed compositions of antifreeze agents in the technology of construction of cement-crushed bases at subzero temperatures (up to –15 °C) prolongs the road construction season and improves the operational indicators of road pavement materials.

Citation: Vdovin, E.A., Stroganov, V.F. Phase structure of cement pastes with antifreeze agents. Magazine of Civil Engineering. 2023. 120(4). Article no. 12007. DOI: 10.34910/MCE.120.7

1. Introduction

The priority tasks in the development of building materials science include the creation of materials with improved physical and mechanical characteristics by modifying them with complex multifunctional additives [1, 2].

In countries where construction and operation of highways occur at low air temperatures (below 0 °C) [3–5], these tasks can be solved using technologies for constructing structural layers of road pavements made of low-strength stone materials and soils, reinforced with cement and modified with functional additives [6–9].

For example, the effect of combined use of hydromechanical activation of cement and antifreeze agents on the physical and technical properties of fine-grained materials, hardening at low temperatures, was studied in [10]. The proposed approach made it possible to increase the effectiveness of the studied additives and opened up additional possibilities for their application in winter concreting.

The admixtures for winter concreting were studied in [11, 12]. It was shown that calcium chloride was effective, but its use as an antifreeze agent was not recommended due to the serious danger of corrosiveness. The impact of chloride-containing antifreeze additives with two types of chloride-containing components ($NaCl$ and $CaCl_2$) on the rheological properties of cement concrete at negative temperatures was studied [13] the modification with two types of chlorides provides a decrease in the yield strength and an increase in viscosity. Increase in antifreeze concentration and cement content, decrease in sub-zero curing temperature, and addition of slag were found to have significant effects on the rheological properties of cement-mineral mixtures. In addition, chlorides promote early cement hydration, reduce the freezing temperature and prevent early freezing of cement-mineral materials. The authors [14] additionally found that chloride-based accelerators adversely affect the strength of concrete, while non-chloride-based accelerators provide an alternative use if mixed with the appropriate type and amount of cement.

Accelerators are used at low temperatures for patching the road surface using fast-hardening concrete mixtures of high strength and construction of cement-mineral road pavement bases [12, 15, 16]. It is noted that at subzero temperatures the accelerator promotes cement hydration, shortening the setting time and increasing the strength gain at an early age.

It should be noted that one-component antifreeze agents in cement-mineral materials do not provide the required level of cement paste (CP) hydration at subzero temperatures, especially at air temperatures below –5 °C [12]. It was found that in some cases the chloride antifreeze deteriorates the physical and mechanical properties of materials [12, 17].

A chemical mechanism of concrete destruction under the action of magnesium chlorides was discussed in [12, 18]. The authors explain it by the formation of multiphase nanosized crystals in the material, including $CaCl_2$, $Mg(OH)_2$ and $Mg_3(OH)_5Cl(H_2O)_4$. Additionally, the destruction of concrete by the proposed mechanism is indirectly confirmed by testing concrete samples taken from several selected concrete bridge decks. It is shown that the cumulative effect of $MgCl_2$ antifreeze caused a significant decrease in splitting tensile strength (up to 50 %), as well as a decrease in microhardness (up to 60 %), even at a depth of 25 to 50 mm.

The use of advanced composite materials with magnesium oxychloride cement and mineral aggregates was discussed in [19]. It was found that the problem of magnesia composites hardening under freezing temperatures hadn’t been solved yet.

The studies on replacing chlorides or reducing their negative effects in antifreeze agents are of high versatility. For example, in [20], urea was discussed as an antifreeze agent instead of chlorides for concreting in cold weather. However, its effectiveness as an antifreeze agent has been confirmed only at temperatures down to –5 °C. The use of calcium nitrate as an additive in antifreeze was considered in [20]. The negative effect of corrosion processes on the physical and mechanical characteristics of concrete was shown in [21], where calcium nitrate was studied as an antifreeze agent. The authors [22] believe that sodium nitrite ($NaNO_2$) and potassium carbonate (K_2CO_3) are the most common antifreeze additives that ensure the required level of properties of concrete (compressive strength, tensile strength, flexural strength, modulus of elasticity and Poisson's ratio) at negative temperatures. The effect of chloride-free antifreeze additives (calcium nitrite ($Ca(NO_2)_2$), calcium nitrate ($Ca(NO_3)_2$) and urea ($CO(NH_2)_2$)) on the rheological properties of cement-mineral materials with different types and content of binders (Portland cement, ground blast furnace slag) at negative temperatures were also studied [23–25].

High-strength calcium sulfoaluminate was also used as a mineral accelerator in winter construction [26–28].

The process of cement hydration acceleration during winter concreting can be performed through the use of accelerating additives of various chemical structures: calcium formate and nitrate, CSH crystals, and triethanolamine [29–31]. It was shown that additives based on calcium nitrate, calcium formate, and CSH crystals were the most efficient for Portland cement mortars, and triethanolamine was the most efficient for cement with the addition of ground granulated blast furnace slag.

The positive effect of sodium formate (SF) on the process of concrete hardening at subzero temperatures and its effective anti-icing properties was experimentally confirmed in works [32, 33]. This work presented a regression equation, which predicted the strength of concrete with the addition of sodium formate used in winter works. The effect of an antifreeze additive on the flexural strength of road concrete was also studied in [34]. Here the authors used the method of orthogonal planning of the experiment and took into account water-cement ratio, the content of antifreeze modifier, fly ash and technological factors of the works.

It is important to take into account that cement-crushed stone mixtures (CCSMs) have significant porosity. When CCSMs are exposed to subzero temperatures, the number of pores and capillaries increases, in which stresses are formed during the transition of water into ice, causing material destruction [2]. To solve this problem, it is necessary to develop multifunctional antifreeze additives that provide the greatest compaction of the material to reduce open porosity and determine their effect on the formation of a frost-resistant and durable phase structure of the material.

It is recommended to develop complex antifreeze additives using mixtures of nitrate and thiocyanate, and in some cases using alkanolamines, carboxylic acids, or their salts [11, 35]. These studies also confirm that chemical combinations can provide synergistic effects when combined antifreeze additives are used.

The effective implementation of multifunctional additives is exampled by the development of a nano-modified high-tech additive [36], applied in concreting at outside air temperatures up to –5 °C. The multifunctionality of this additive consists in the combined use of four components (sulfonaphthalene-formaldehyde, amorphous nano-silica, saponified wood resin, and sodium nitrite). The proposed ratio of plasticizing, stabilizing, air-entraining, and antifreeze components made it possible to provide optimal conditions for the cement hydration during winter concreting and, as a consequence, the required strength and workability.

O. Tene carried out similar studies on the development of a multifunctional antifreeze additive for modifying cement-based pavements during work under subzero temperatures [37]. As components of complex additives, he proposed a combination of plasticizing (solutions of melamine-formaldehyde polymers, technical lignosulfonates), antifreeze (sodium and calcium formates), and hydrophobizing substances (sodium liquid glass, ethyl silicones, and sodium methylsiliconates) with hardening accelerators (sodium, ammonium and iron sulfates), and the introduction of mineral fillers and stabilizers (fly ash, active microsilica, dolomite flour, slaked lime).

The authors [38, 39] point out that when developing complex antifreeze additives, it is necessary to consider the nature of the effect of the components of antifreeze modifiers on the composition of hydration products, processes and features of the formation of structure and hardening of concrete.

While developing a method for modifying CCSMs hardening at low temperatures, we took into account the positive experience and previous results on the complex antifreeze additives. We used the multifunctional antifreeze compositions, including sodium formate, calcium chloride, and superplasticizer S-3. It should be noted that superplasticizer S-3 as part of a complex multifunctional modifier, is intended to reduce moisture, improve technological properties and increase the density of the central chemical mixture [2]. In addition to accelerating the hardening process, calcium chloride enhances the antifreeze effect of sodium formate, and its reduced content in the complex additive should prevent the development of destructive processes during hardening of cement-mineral materials. Modification of cement-crushed mixtures with the developed additives makes it possible to increase the material compressive strength by 3.6, splitting tensile strength by 4.3, frost-resistance by 7.0, crack-resistance by 1.5, elasticity modulus by 1.9 times as compared to unmodified compositions (at a hardening temperature of –15 °C). The use of the developed compositions of antifreeze agents in the technology of construction of cement-crushed bases at subzero temperatures (up to –15 °C) prolongs the road construction season and improves the operational indicators of road pavement materials.

The performed analysis shows the prospects of CCSMs modification with complex antifreeze additives in countries where construction and operation of highways occur at low air temperatures (below 0 °C). It also indicates the need for research on the cumulative positive effect of antifreeze additives, plasticizers, and hardening accelerators in cement pastes on the formation of the phase structure and the identification of the relationship between the structure and the properties of the materials obtained.

Given the lack of structural surveys of cement pastes with antifreeze additives, this work aims to study the effect of multifunctional antifreeze compositions, including sodium formate, calcium chloride, and superplasticizer S-3, on the formation of the phase structure of cement pastes.

To achieve this aim, the following tasks were solved:

1. Determination of the phase compositions of cement paste and the ratio of amorphous and crystallization phases in the material.

2. Investigation of the impact of the components of antifreeze multifunctional additives on the degree of cement hydration, the qualitative and quantitative composition of the hardening products.

3. Determination of the relationship between CP strength and the degree of cement hydration in the presence of antifreeze agents used.

2. Materials and Methods

The research was carried out in the laboratories of the Scientific and Educational Center "Roads" of the Institute of Transport Structures of the Kazan State University of Architecture and Civil Engineering. The studied materials were CP without additives, with one-, two- and three-component antifreeze compositions and with each component of complex additives after hardening for 28 days at a temperature of –15 °C.

The studies used CEM I 42.5N Portland cement of the following mineral and chemical compositions (Tables 1 and 2).

Table 1. Mineral composition of cement.

Material	C 3 S	C 2 S	C 3 A	C 4 AF
Content, %	58	17	8	13

Table 2. Chemical composition of cement.

Material	SiO_2	Al_2O_3	Fe_2O_3	CaO	MgO	SO_3	R_2O (Na_2O+ +0.65 K_2O)	CaO_{free}
Content, %	21.1	5.85	4.2	65.4	1.13	1.03	1.07	0.16

The following substances were used as components of complex antifreeze agents (Table 3), by analogy to [2]:

- sodium formate is the sodium salt of formic acid (HCOONa), a chemically pure water-soluble product;
- crystalline calcium chloride (CC) ($CaCl_2$), a chemically pure water-soluble product;
- superplasticizer S-3 is the sodium salt of the condensation product of naphthalenesulfonic acid and formaldehyde. It was used as a 2.5 % aqueous solution, pH 7-9.
- tempering water, according to EN 1008:2002.

The CP samples after 28 days of curing were tested for compressive strength, according to EN 1 96-1: 2005. The prepared samples were examined by X-ray, differential thermal and thermogravimetric analyzes.

The X-ray diffraction of samples was studied using the DRON-3 X-ray diffractometer. The following operation mode was used: CuK_α with a wavelength of 1.54178 Å, exposure 10 sec., step 0.05°, interval from 2° to 78°.

Differential thermal analysis (DTA) and differential thermogravimetry (DTG) of samples were carried out on the 3425-1500-OD optical derivatograph of the F. Paulik, J. Paulik and L. Erdey system (MOM, Hungary). The sample weighed portions varied from 400 to 1700 mg, with a thermal balance sensitivity of 100 mg. The recording modes were DTA, DTG – 1/5, heating rate was 15 deg./min up to 1000 °C. Air was used as a comparison standard (empty crucible on the T-junction).

Diagnostics of each crystalline phase was carried out by identifying the corresponding characteristic reflections with specific interplanar distances (d) and relative intensities (l) on the obtained diffractograms. The identification procedure was carried out by comparing the obtained diffraction patterns with the international database of powder diffractometric data (JCPDS database), which contains the l and d values of reference minerals.

The relative contents of the amorphous and crystalline components in the studied CP were calculated using the XRYTOOL interactive computer program (Russia).

The hydration degree (HD) of cement pastes was determined by two independent methods.

- in X-ray technique, HD was assessed using the ratio of the intensities of reflexes of non-hydrated components of cement (alite, belite) and reflections of hydrated new formations (portlandite and aqueous dicalcium hydrosilicates):

$$\mathbf{HD} = \left(\mathbf{I}_{\mathrm{Ca2SiO4*nH2O}} + \mathbf{I}_{\mathrm{Ca(OH)2}}\right) \Big/ \left(\mathbf{I}_{\mathrm{Ca2SiO4*nH2O}} + \mathbf{I}_{\mathrm{Ca(OH)2}} + \mathbf{I}_{\mathrm{C2S+C3S}}\right), \quad (1)$$

where $\mathbf{I}_{\mathrm{Ca2SiO4*nH2O}}$ is the intensity of dicalcium hydrosilicate reflection, d = 9.6 Å; $\mathbf{I}_{\mathrm{Ca(OH)2}}$ is the intensity of portlandite reflection, d = 4.9 Å; $\mathbf{I}_{\mathrm{C2S+C3S}}$ is the intensity of alite and belite reflection, d = 2.78 Å.

– in differential thermal analysis and differential thermogravimetry, HD was assessed using the mass loss $(\Delta \mathrm{m})$ within the limits of the considered effect on thermoanalytical curves.

3. Results and Discussion

Phase composition of cement pastes hardened at subzero temperatures was determined using the X-ray, differential thermal and thermogravimetric analyzes.

The CP samples hardened for 28 days were tested for compressive strength R_{comp} (Table 3).

Table 3. Compressive strength of CP hardened at –15 °C.

Sample No.	Content of additives in cement pastes, % by weight of cement			W/C	R_{comp}, MPa, of CP samples hardened for 28 days at -15 °C
	CC	SF	SP		
1	-	-	-	0.26	4.7
2	-	6	-	0.23	20.2
3	3	-	-	0.26	33.3
4	3	6	-	0.23	25.9
5	3	6	2	0.20	48.4
6	-	-	2	0.21	7.5
7	-	6	2	0.20	22.6
8	3	-	2	0.21	35.4

The studied CPs have a similar composition of crystalline phases. The main predominant compound in them is unhydrated C_3S. Calcium aluminate and aluminoferrites remained at the same level in quantitative terms, i.e. they underwent insignificant hydration in contrast to alite. New hydration formations in cement pastes are represented by portlandite $Ca(OH)_2$ and dicalcium hydrosilicate ($Ca_2SiO_4 \cdot nH_2O$). Along with the crystalline phases, CP also contains an amorphous component, which consists of new hydration formations of colloidal dimension, with a probable composition of $Ca_2SiO_4 \cdot nH_2O$ (Table 4).

Analysis of X-ray diffraction patterns for CPs without additives shows that in Portland cement the most hydrated were alite and belite, while calcium aluminates and alumoferrites were hydrated to a much lesser extent.

Table 4. Relative phase content and hydration degree for alite and belite in CP.

Sample No	Sample composition	Relative phase content,%		Relative HD, r.u.
		Crystalline	Amorphous	
1	Cement paste without additives	49.5	50.5	0.45
2	Cement paste with 6% SF	53.6	46.4	0.58
3	Cement paste with 3% $CaCl_2$	62.0	38.0	0.7
4	Cement paste with 3% $CaCl_2$; 6% SF	61.4	38.6	0.51
5	Cement paste with 3% $CaCl_2$; 6% SF; 2% S-3	62.6	37.4	0.6
6	Cement paste with 2% S-3	64.4	35.6	0.37
7	Cement paste with 6% SF; 2% S-3	67.2	32.8	0.31
8	Cement paste with 3% $CaCl_2$; 2% S-3	61.5	38.5	0.56

The scheme of hydration transformation that took place in CPs can be described by two main reactions:

$$Ca_3SiO_5 + nH_2O \rightarrow Ca_2SiO_4 * nH_2O + Ca\left(OH\right)_2, \quad (2)$$

$$Ca_2SiO_4 + nH_2O \rightarrow Ca_2SiO_4 * nH_2O, \quad (3)$$

These equations show that both compounds (alite and belite) are converted into dicalcium hydrosilicate, which in the initial period of Portland cement hardening exists in the form of colloidal particles. The appearance of $Ca_2SiO_4*nH_2O$ results in the presence of a significant amount of amorphous component in CPs (Table 4), when the main part of the new formations is in colloidal form and the process of Portland cement hydration is fixed at the initial stage. Only a small part of the colloid crystallizes into portlandite $Ca(OH)_2$ and calcium hydrosilicate $2CaO*SiO_2*nH_2O$. The number of water molecules in its structure is from 3 to 4 and it belongs to the group of highly basic hydrosilicates of the CSH (II) type by H. Taylor or C_2SH_2 by R. Bogg.

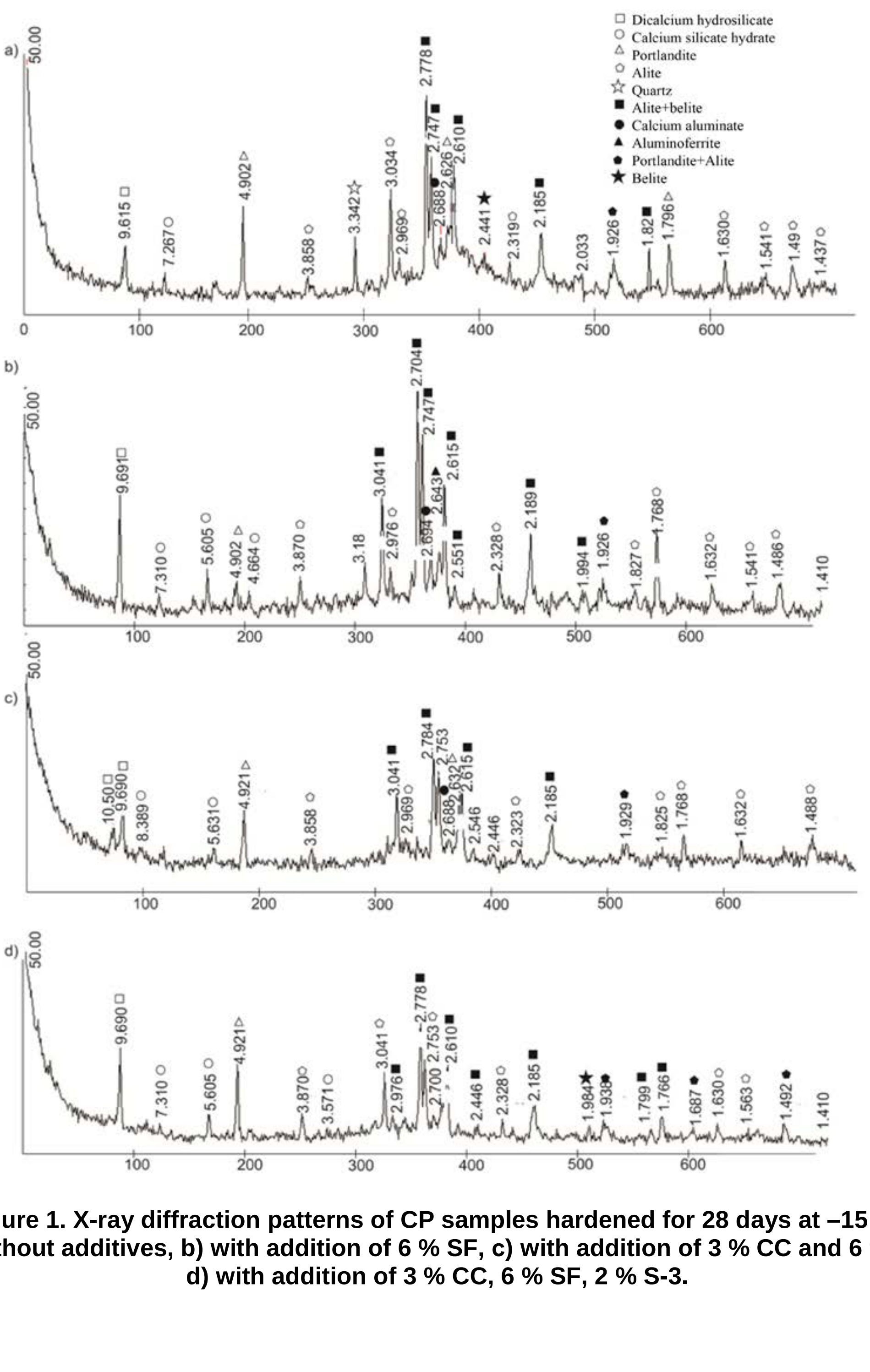

Figure 1. X-ray diffraction patterns of CP samples hardened for 28 days at –15 °C:
a) without additives, b) with addition of 6 % SF, c) with addition of 3 % CC and 6 % SF,
d) with addition of 3 % CC, 6 % SF, 2 % S-3.

It should be noted that CP with addition of 6 % SF shows a higher degree of hydration. It results in a larger crystallization of the amorphous component into portlandite $Ca(OH)_2$ and calcium hydrosilicate $2CaO*SiO_2*nH_2O$. The latter is represented by two varieties: one modification is characterized by reflection d = 10.5 Å, the other one has d = 9.69 Å (Fig. 1), their position is explained by the different content of water molecules. The deeper hydration process is explained by the fact that the addition of SF under the conditions of formation of cement paste at –15 °C has a multifunctional effect on the hydration of Portland cement. Firstly, SF helps to lower the freezing point of water, which ensures hydration in CP at subzero temperatures. Secondly, SF enhances the hydrolysis of compounds that make up Portland cement, i.e. increases the rate of hydration of the crystalline phases of the clinker. Thirdly, when SF dissolves in water, free sodium ions are formed in the solution, which, being activators of hardening, accelerate the hydration of Portland cement. The listed factors together determine the increase in CP strength.

It was shown that the CC additive, being an accelerator of the hardening process, to a greater extent promotes the hydration transformation of di- and tricalcium silicates. It works like SF additive, lowers the freezing point of water, thereby increasing the hydration time of Portland cement. It should be noted that at this stage chloride does not form independent phases, since the concentration of chlorine ions in the solution is obviously insufficient for the formation of independent compounds.

In the considered variants of CP modification with the superplasticizer, a lower degree of hydration was noted than that obtained by joint addition of SF and CC. Such CPs are characterised by hydration degree similar to that of CPs without additives. The absence of a significant amount of amorphous phase in them is probably explained by the lower water-cement ratio (W/C) compared to that of CP without additives. It can be concluded that the SP additive is not a stimulator of the hydration transformation of Portland cement at subzero temperatures. Its effective impact is explained by a decrease in the water-cement ratio, which reduces the destructive effect of the liquid phase at subzero temperatures and affects improvement of the CP strength characteristics.

Cement paste with a complex additive of SF, CC and SP shows a fairly high degree of hydration of the cement silicate components. The X-ray diffraction pattern of this sample shows high intensities of reflections of calcium hydrosilicate d = 9.69 Å, portlandite d = 4.921 Å, d = 2.632 Å, and a significant decrease in the intensities of reflections of alite d = 3.041 Å and belite d = 2.778 Å. The combined use of SF and CC promotes the activation of hydrolysis and hydration of Portland cement, and addition of SP results in a decrease in the W/C ratio, which leads to acceleration of the hardening process and achievement of maximum CP strength at subzero temperatures.

It should be noted that each complex additive, especially a three-component one, maximally manifests its activity in hydration processes. This is confirmed by the strength characteristics of cement pastes.

The considered cases confirmed that the XRD method does not allow to unambiguously estimate the contribution of the X-ray amorphous component for assessing the hydration degree. In this regard, we carried out additional thermal studies to obtain more reliable information. The content of hydrated water in CP was used to assess the hydration degree of CP, the weight loss was used to determine the new formations (Fig. 2, Table 5).

It is shown that in the temperature range of 40–350 °C an endothermic effect is recorded, which characterizes the process of removing weakly bound, mainly adsorbed water (Fig. 2). The DTA curves for CP without additives in the range of 440–500 °C recorded the process of dehydration of calcium hydroxide $Ca(OH)_2$ (Fig. 2a). The endothermic effect is a consequence of two processes' superposition, it is observed on thermoanalytical curves with a maximum of 720–760 °C. The first process is dehydration of newly formed dicalcium hydrosilicates $2CaOSiO_2*nH_2O$ of the CSH (II) type. The second process is dissociation of calcium carbonate $CaCO_3$, formed as a result of calcium hydroxide carbonization.

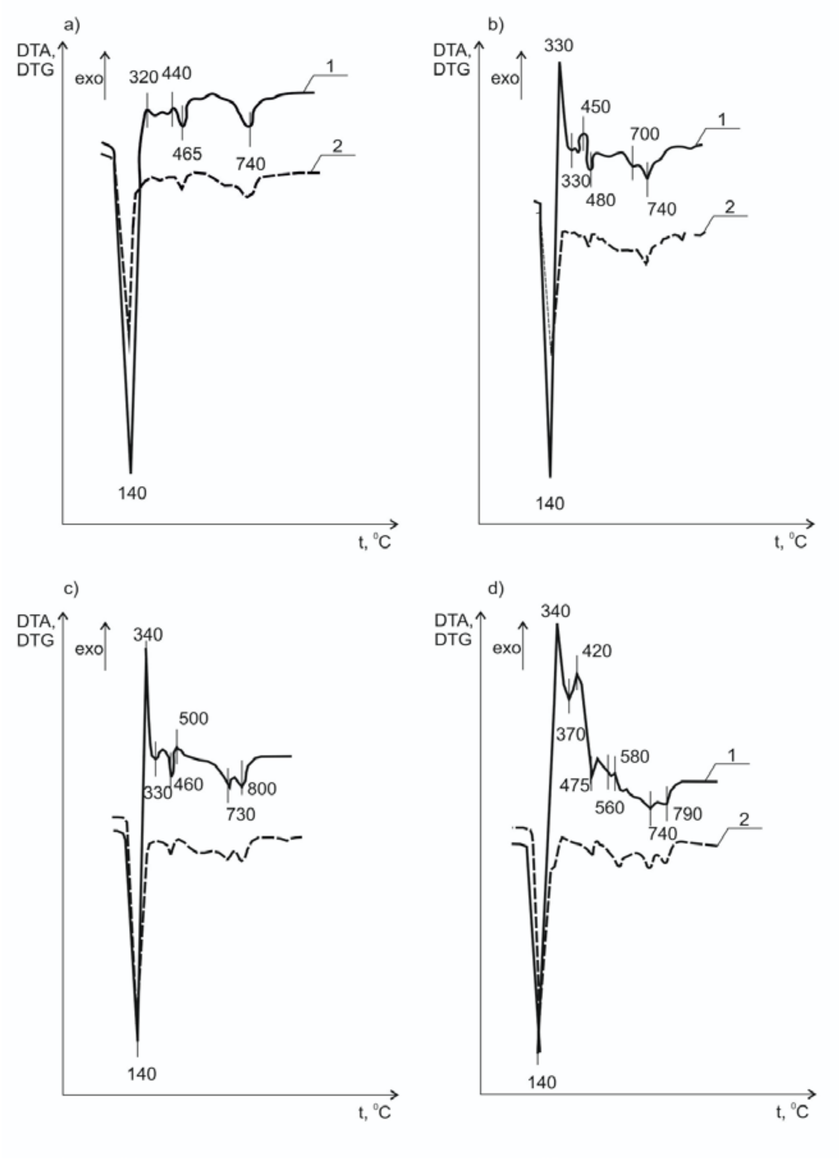

Figure 2. Thermoanalytical curves DTA (1) and DTG (2) of CP samples hardened for 28 days at –15 °C: a) without additives, b) with addition of 6 % SF, c) with addition of 3 % CC and 6 % SF, d) with addition of 3 % CC, 6 % SF, 2 % S-3.

It should be noted that a slight increase in total weight loss is observed in CP without additives (Table 5). This indicates a slow process of hydration of cement minerals and is confirmed by the minimum CP strength achieved.

A characteristic feature of the DTA curves of cement paste with SF (Fig. 2 b) is the appearance of peaks with maxima in the range of 330–450 °C, characterizing exothermic transformations. They are obviously associated with the destruction of organic substances of additive components. This indicates a deeper hydration process in CP with SF additive and provides an increase in the intensity of weight loss over the entire investigated temperature range (Table 5).

The positive impact of CC on the hydration process in CP was established. The active role of CC additive during the hydration transformation of alite and belite to CP is to increase the process of portlandite dehydration.

The SP additive has an insignificant impact on the hydration transformation of Portland cement in conditions of subzero temperatures.

When using a three-component additive from SF, CC and SP, the presence of thermal effects typical for each component is observed (Fig. 2d). However, each component of the additive is involved in the acceleration of the hydration of the clinker crystalline phases. The combination of additives provides an enhancement and deeper course of the hydration process, which is confirmed by the maximum total weight loss – 20.5 % (Table 5) and the highest CP strength – 48.4 MPa.

Table 5. Weight loss of CP with various additives and temperature modes.

Sample No	Material and content of additives in CP, %	Weight loss, % mass, In the temperature interval, °C				
		20 -350	20 -500	20 -700	20 -800	20 -1000
1	Without additives	7.7	9.2	10.7	13.2	13.3
2	SF 6.0	10.0	11.3	17.4	18.6	19.1
3	CC 3.0	12.6	14.8	16.2	18.5	19.3
4	CC 3.0; SF 6.0	11.4	12.5	15.4	19.3	20.0
5	CC 3.0; SF 6.0 SP 2.0	11.6	13.0	16.3	20.0	20.5
6	SP 2.0	6.8	8.0	10.0	11.9	12.0
7	SF 6.0 SP 2.0	8.8	10.1	14.2	17.2	18.5
8	CC 3.0; SP 2.0	9.8	11.2	12.6	15.7	16.2

Data from Tables 3, 4, and 5 were used to build the relationships between the compressive strength of cement pastes (σ_{CS}), the hydration degree of calcium silicates in them (α) and the integral weight loss. Analysis of these curves confirmed an increase in the level of compressive strength of cement pastes with an increase in the hydration degree of alite and belite (Fig. 3). It is important to note that the nature of the obtained dependencies was confirmed by independent methods: X-ray and differential thermal analysis. The established dependences testify to the effectiveness of practical application of the developed antifreeze modifiers and explain the role of hydration processes in providing improved operational reliability of cement-mineral materials.

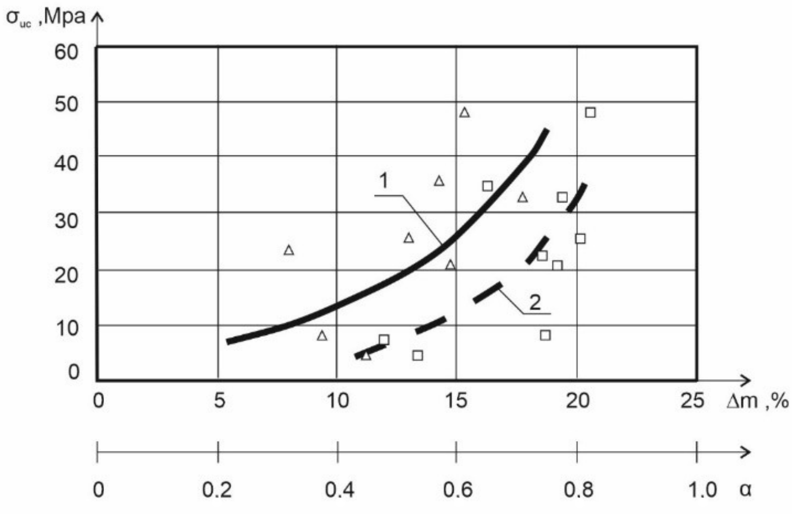

Figure 3. Relationships between the compressive strength of cement pastes (σ_{CS}) and the hydration degree (α) – 1 and the integral weight loss (∆m) – 2.

Thus, the combined use of the components of the complex three-component additive provides synergism of processes of structure formation and, as a consequence, an increase in the CP strength. It is recommended to use the developed antifreeze additives in the technologies of construction of cement concrete bases of pavements at temperatures up to –15 °C. The composition of additives is determined depending on the hardening temperature to ensure a given level of operational indicators and durability of pavement layers based on the results of previous research [40].

The results obtained are relevant as evidenced by the existing literature [11, 41]. As noted by the authors [11], action mechanisms of new non-chloride modifiers for cement paste have not been fully studied. The novelty of the present research consists in the establishment of synergistic effect of combinations of chemicals on the rate of hydration.

The effect of three-component modifiers on acceleration of cement hydration and increase in early strength [42, 43] in conditions of positive temperatures has been previously described. In contrast to [42, 43], it is shown that the modification with complex additives developed by us makes it possible to provide acceleration of cement hydration processes and increase the strength level of cement paste, not only at positive but also at subzero temperatures, during both fast and prolonged hardening. It should be noted that the modification provides an opportunity to increase the content of new formations [41, 42, 43] in the form of hydrosilicates. When using the developed compositions of additives, the new formations can be formed even at subzero temperatures, which increases the strength of the modified cement paste.

The authors [11, 41, 42] note the prospects of continuation and development of structural studies and examination of mechanisms of cement paste modification by complex modifiers of synergistic action in connection with insufficient information on this subject of research.

4. Conclusions

1. The features of formation of the phase structure of cement pastes hardened at subzero temperatures were established. They depend on the qualitative and quantitative compositions of the hardening products and the ratio of amorphous and crystallization phases in them, the rate and depth of the processes of cement hydration. These features determine the level of the achieved material strength.

2. The phase compositions of cement pastes and the ratio of amorphous and crystallization phases in them were determined. Hydrated new formations in cement pastes are represented by portlandite and dicalcium hydrosilicate. Along with crystalline phases, cement paste also contains an amorphous component, which comprises hydrated new formations of colloidal dimension, with a probable composition of $Ca_2SiO_4 \cdot nH_2O$.

3. The influence of complex additives and their components on the degree of cement hydration, the qualitative and quantitative composition of the hardening products was investigated. It is noted that the developed complex additives, especially the three-component ones, ensure the maximum manifestation of their activity in hydration processes.

4. It was confirmed that compressive strength of cement pastes increased with an increase in the degree of cement hydration and the integral weight loss in the presence of the used antifreeze agents. The combined use of the components of the complex three-component additive provides synergism of processes of structure formation and, as a consequence, an increase in the CP strength. The established dependences testify to the effectiveness of practical application of the developed antifreeze modifiers and explain the role of hydration processes in providing improved operational reliability of cement-mineral materials.

5. Modification of cement-crushed mixtures with the developed additives makes it possible to improve the construction and technical indicators of materials in road pavements of highways. Application of the developed polyfunctional compositions of antifreeze additives in technologies of cement concrete bases at subzero temperatures (up to –15 °C) extends of road construction season and improves the operational indicators of road pavement materials. The composition of additives is determined depending on the hardening temperature to ensure a given level of operational indicators and durability of pavement layers based on the results of the previous research.

References

1. Stroganov, V., Sagadeev, E., Ibragimov, R., Potapova L. Mechanical activation effect on the biostability of modified cement compositions. Construction and Building Materials. 2020. 246. 118506. DOI: 10.1016/j.conbuildmat.2020.118506
2. Vdovin, E.A., Stroganov, V.F. Properties of cement-bound mixes depending on technological factors. Magazine of Civil Engineering. 2020. 93. Pp. 147–155. DOI: 10.18720/MCE.93.12
3. Sha, A., Ma, B., Wang, H., Hu, L., Mao, X., Zhi, X., Chen, H., Liu, Y., Ma, F., Liu, Z., He, R. Si, W. Wang, X., Li, C. Highway constructions on the Qinghai-Tibet Plateau: Challenge, research and practice. Journal of Road Engineering. 2022. 2. Pp. 1–60. DOI: 10.1016/j.jreng.2022.02.002
4. Li, L., Liu, J., Zhang, X., Li, P., Saboundjian, S. Characterizing Permanent Deformation of Alaskan Granular Base–Course Materials. Journal of Materials in Civil Engineering. 2019. 31. DOI: 10.1061/(asce)mt.1943-5533.0002911
5. Lin, T., Ishikawa, T., Tokoro, T., Maruyama, K., Ueno, C. Modification of Japanese Pavement Fatigue Life Criteria by Considering Climatic Effects in Cold Regions. Lecture Notes in Civil Engineering. 2022. 164. Pp. 29–39. DOI: 10.1007/978-3-030-77230-7_3
6. Beck, R., Yu, B., Green, R. The Performance and Economic Benefits of Thick Granular Base for Flexible Pavement Design in Frost Susceptible Regions. GeoShanghai International Conference. 2010. Pp. 500–509. DOI: 10.1061/41104(377)64
7. Souliman, M.I., Bastola, N.R., Zeiada, W.A. Improvement of fatigue and rutting performance with different base treatments. Material Science & Engineering International Journal. 2020. 4. Pp. 122–129. DOI: 10.15406/mseij.2020.04.00138
8. Bodhgire, R., Shinde, A., Kakade, V. Cost Comparison of Flexible Pavement Designed with Cement Treated Base and Granular Base. SSRN Electronic Journal. 2019. DOI: 10.2139/ssrn.3368171

9. Eissa, A., Yasien, A., Bassuoni, M., Alfaro, M. Performance of Treated Soft Clay with Nano-Modified Cementitious Binders at Reference and Cold Temperatures. International Journal of Geosynthetics and Ground Engineering. 2022. 8. 52. DOI: 10.1007/s40891-022-00398-8
10. Karmaza, M.V., Motylev, R.V. Technologies for the use of antifrosty additives in winter concreting. International Conference Technical and Natural Sciences. Journal of Technical and Natural Sciences. 2018. Pp. 8–14.
11. Myrdal, R. Accelerating admixtures for concrete. SINTEF REPORT Building and Infrastructure Concrete and Innovation Center, Project. 2007. Pp. 1–35.
12. Liu, Z., Lou, B., Barbieri, D.M., Sha, A., Ye, T., Li, Y. Effects of pre-curing treatment and chemical accelerators on Portland cement mortars at low temperature (5 °C). Construction and Building Materials. 2020. 240. 117893. DOI: 10.1016/j.conbuildmat.2019.117893
13. Zhou, Y., Fall, M. Investigation on rheological properties of cemented pastefill with chloride-bearing antifreeze additives in sub-zero environments. Cold Regions Science and Technology. 2022. 196. 103506. DOI: 10.1016/j.coldregions.2022.103506
14. Gholami, S., Hu, J., Kim, Y.R., Mamirov, M. Performance of Portland Cement-Based Rapid-Patching Materials with Different Cement and Accelerator Types, and Cement Contents Transportation Research Record. 2019. 2673(11). Pp. 172–184. DOI: 10.1177/0361198119852330
15. [1dd, N.T., Suraneni, P., Weiss, W.J. Hydration of cement pastes containing accelerator at various temperatures: Application to high early strength pavement patching. Advances in Civil Engineering Materials. 2017. 6. DOI: 10.1520/ACEM20160079
16. Zhou, Q.W. Analysis of low temperature strength and drying shrinkage characteristics of cement stabilized macadam. Bulletin of the Chinese Ceramic Society. 2016. 3. Pp. 948–952.
17. Hosseinzadeh, N., Suraneni, P. Synergistic effects of air content and supplementary cementitious materials in reducing damage caused by calcium oxychloride formation in concrete. Cement and Concrete Composites. 2021. 122. 104170. DOI: 10.1016/j.cemconcomp.2021.104170
18. Xie, N., Dang, Y., Shi, X. New insights into how MgCl2 deteriorates Portland cement concrete. Cement and Concrete Research. 2019. 120. Pp. 244–255. DOI: 10.1016/j.cemconres.2019.03.026
19. Kiyanets, A. The Negative Temperature Impact on Hardening of Magnesia Composites. Materials Science Forum. 2016. 843. Pp. 91–95. DOI: 10.4028/www.scientific.net/MSF.843.91
20. Demirboğa, R., Karagöl, F. Polat, Ri., Kaygusuz, M.A. The effects of urea on strength gaining of fresh concrete under the cold weather conditions. Construction and Building Materials. 2014. 64. Pp. 114-120. DOI: 10.1016/j.conbuildmat.2014.04.008
21. Çullu, M., Arslan, M. The effects of chemical attacks on physical and mechanical properties of concrete produced under cold weather conditions. Construction and Building Materials. 2014. 57. Pp. 53–60. DOI: 10.1016/j.conbuildmat.2014.01.072
22. Reddy, P.N. Effect of sodium nitrite and potassium carbonate on Cold Weather Concrete. LAP LAMBERT Academic Publishing, 2019.
23. Zhou, Y., Fall, M., Haruna, S.Flow ability of cemented paste backfill with chloride-free antifreeze additives in sub-zero environments. Cement and Concrete Composites. 2022. 126. 104359. DOI: 10.1016/j.cemconcomp.2021.104359
24. Skripkiūnas, G., Kičaitė, A., Justnes, H., Pundienė, I. Effect of calcium nitrate on the properties of portland– limestone cement-based concrete cured at low temperature. Materials. 2021. 14. 1611. DOI: 10.3390/ma14071611
25. Alzaza, A., Ohenoja, K., Langås, I., Arntsen, B., Poikelispää, M., Illikainen, M. Low-temperature (−10 °C) curing of Portland cement paste – Synergetic effects of chloride-free antifreeze admixture, C–S–H seeds, and room-temperature pre-curing. Cement and Concrete Composites. 2022. 125. 104319. DOI: 10.1016/j.cemconcomp.2021.104319
26. Zhang, G., Yang, Y., Yang, H., Li, H. Calcium sulphoaluminate cement used as mineral accelerator to improve the property of Portland cement at sub-zero temperature. Cement and Concrete Composites. 2020. 106. 103452. DOI: 10.1016/j.cemconcomp.2019.103452
27. Li, G., Zhang, J., Song, Z., Shi, C., Zhang, A. Improvement of workability and early strength of calcium sulphoaluminate cement at various temperature by chemical admixtures. Construction and Building Materials, 160, 427–439. DOI: 10.1016/j.conbuildmat.2017.11.076
28. Huang, G., Pudasainee, D., Gupta, R. Liu, W.V. (2019) Hydration reaction and strength development of calcium sulfoaluminate cement-based mortar cured at cold temperatures, Construction and Building Materials. 2018. 224. Pp. 493–503. DOI: 10.1016/j.conbuildmat.2019.07.085
29. Pizon, J., Lazniewska-Piekarczyk, B. Microstructure of High C3A portland slag cement pastes, modified with accelerating admixtures for concrete. IOP Conference Series: Materials Science and Engineering, IOP Publishing. 2019. 603. 032089. DOI: 10.1088/1757-899X/603/3/032089
30. Pizoń, J., Miera, P., Łaźniewska-Piekarczyk, B. Influence of Hardening Accelerating Admixtures on Properties of Cement with Ground Granulated Blast Furnace Slag. Procedia Engineering. 2016. 161. Pp. 1070–1075. DOI: 10.1016/j.proeng.2016.08.850
31. Pizoń, J. Long-term Compressive Strength of Mortars Modified with Hardening Accelerating Admixtures. Procedia Engineering. 2017. 195. Pp. 205–211. DOI: 10.1016/j.proeng.2017.04.545
32. Gushchin, S., Drozd, A. The effect of sodium formate on concrete hardening at low temperatures. Problems of Modern Concrete and Reinforced Concrete. 2014. 6. Pp. 68–75. (rus)
33. Kondakov, D.F., Frolova, E.A., Kudryashova, O.S., Danilov, V.P. Deicing reagents based on Sodium Chloride, Calcium Chloride, and Sodium Formate. Theoretical Foundations of Chemical Engineering. 2021. 55. Pp. 971–974. DOI: 10.1134/S0040579521050080
34. Zhao, Y., Yu, H., Wang, W., Li, Y. Research on mix proportion design method of cement concrete for road mixed with antifreeze admixtures sealed in capsules. Key Engineering Materials. 2020. 861. Pp. 429–437. DOI: 10.4028/www.scientific.net/KEM.861.429
35. Karagol, F., Demirboga, R., Khushefati, W.H. Behavior of fresh and hardened concretes with antifreeze admixtures in deep-freeze low temperatures and exterior winter conditions. Construction and Building Materials. 2015. 76. Pp. 388–395. DOI: 10.1016/j.conbuildmat.2014.12.011
36. Svintsov, A.P., Galishnikova, V. V., Stashevskaya, N. Dataset on the effect of nano-modified additives of concrete mixes technological properties for winter concreting. Data in Brief. 2020. 31. 105756. DOI: 10.1016/j.dib.2020.105756
37. Tene, O. Mixture of substances, applicable, in particular, as an additive for concrete mixture: Patent of the Russian Federation 2433096 No. 2009134179/03; publ. 10.11.11, n.d.

38. Maksimova, I.N. Influence of chemical additive and reduced initial temperature of structure formation and hardening on parameters of structural strength of cement composites. Vestnik MGSU. 2019. 14. Pp. 442–449. DOI: 10.22227/1997-0935.2019.4.442-449
39. Tarakanov, O.V., Erofeev, V.T., Belyakova, E.A. Rational Design of Effective Antifreeze Additives for Mortars and Concretes. IOP Conference Series: Materials Science and Engineering, IOP Publishing. 2021. 1079. 062022. DOI: 10.1088/1757-899x/1079/6/062022
40. Vdovin, E.A., Stroganov, V.F. Optimization of complex frost-resisting additives in line with operational requirements towards freezing temperature in road dressing constructions. IOP Conference Series: Materials Science and Engineering, IOP Publishing. 2020. 832. 012034. DOI: 10.1088/1757-899X/832/1/012034
41. Pizoń, J., Łaźniewska-Piekarczyk, B. Microstructure of CEM II/B-S Pastes Modified with Set Accelerating Admixtures. Materials. 2021. 14(21). 6300. DOI: 10.3390/ma14216300
42. Liu, J., Ji, X., Luo, Q., Xue, J., Ma, M. Improvement of early age properties of Portland cement by ternary hardening-accelerating admixture. Magazine of Concrete Research. 2019. 73. Pp. 1–29. DOI: 10.1680/jmacr.19.00148
43. Wang, L., Shen, A., Lyu, Z., Guo, Y., He, Z., Mou, G., Wei, Z. Rapid regeneration cement-stabilized macadam: Preparation, mechanical properties, and dry shrinkage performance. Construction and Building Materials. 2022. 341. DOI: 127901.10.1016/j.conbuildmat.2022.127901

Information about authors:

Evgenii Vdovin, *PhD in Technical Sciences*
ORCID: https://orcid.org/0000-0002-0649-4342
E-mail: vdovin007@mail.ru

Victor Stroganov, *Doctor of Technical Sciences*
ORCID: https://orcid.org/0000-0001-9680-6698
E-mail: svf08@mail.ru

Received 10.01.2023. Approved after reviewing 04.04.2023. Accepted 04.04.2023.

Magazine of Civil Engineering. 2023. 120(4). Article No. 12008

Magazine of Civil Engineering

ISSN 2712-8172

journal homepage: http://engstroy.spbstu.ru/

Research article

UDC 627.52

DOI: 10.34910/MCE.120.8

Sedimentation simulation of the Temryuk seaport approach channel

I.G. Kantardgi [1], ***I.O. Leont'yev*** [2], ***A.V. Kuprin*** [1]

[1] *Moscow State University of Civil Engineering (National Research University), Moscow, Russian Federation*

[2] *Shirshov Institute of Oceanology, Russian Academy of Sciences, Moscow, Russian Federation*

rtyter55@gmail.com

Keywords: longshore sediment transport, erosion, drift, accumulation, protective measures, mathematical model

Abstract. The sedimentation of the approach channel and the water area of Temryuk port is an important problem that has recently attracted the attention of researchers and engineers. The object of the study is the influence of the extension of the east and west breakwaters of the port. An analytical method of forecasting lithodynamic processes for various extensions of protective breakwaters was used. To verify the results, an analysis of space images of the coastal zone was applied. The volumes of sedimentation of the sea part of the Temryuk port approach channel were determined; recommendations for the extension of breakwaters were given. The sedimentary layer in the Temryuk Bay has two demarcated zones, one dominated by silty material, and the other, coastal, by fine-grained sand. Therefore, to determine the total alongshore sediment flow, the movement of muddy and sand flows was determined separately. The west breakwater retains only a small part of the sand transported to the canal; the east breakwater also has an insufficient length. The majority of the sand passing in the west and east directions falls into the canal. After the extension of the east breakwater by 100 m, the sedimentation of sand will be due mainly to its arrival from the west side, and thus the maximum thickness of the sediment layer will be about 2 m. The extension of the east breakwater by 200 m does not lead to a significant improvement compared to the extension option of 100 m, therefore, to reduce the sedimentation, it is necessary to extend the west breakwater by 100 m as well. After the extension of the west breakwater, the flow of sand into the channel from the west side will be significantly reduced. Thus, after the lengthening of both breakwaters, the volume of sedimentation of the channel with sand will decrease from 55 to 15 thousand cubic meters per year. The main contribution to the sedimentation will continue to be made not by sandy, but by silty material.

Citation: Kantardgi, I.G., Leont'yev, I.O., Kuprin, A.V. Sedimentation simulation of the Temryuk seaport approach channel. Magazine of Civil Engineering. 2023. 120(4). Article no. 12008. DOI: 10.34910/MCE.120.8

1. Introduction

Construction of protective structures at seaports is a classical way to protect the approach channel and water area from sedimentation and penetrating waves. However, in practice, the effectiveness of breakwaters as a protection against sedimentation decreases with the time of port operation. Sedimentation in the area of the unprotected approach channel approaches catastrophic levels. It is expressed in more rapid reduction of depths in the fairway at the port gates, as compared to the remote parts of the channel at sea. The most exposed to this type of sedimentation are port approach channels located on the shallow sandy shores of the Black, Azov and Baltic Seas with a developed longshore sediment flow.

Enclosing west and east breakwaters are located in the port of Temryuk, Krasnodar region, Temryuk district, Temryuk Bay of the Azov Sea (Fig. 1). The approach channel of Temryuk seaport was built in 1910 for navigational safety of vessel passage.

Figure 1. Location of the investigated breakwaters of Temryuk port, Russia (breakwaters are highlighted in red).

A serious problem of Temryuk port geographical location is its proximity to the mouth of the Kuban River. Solid flow of the Kuban River determines morphodynamic changes in the coastal zone, including a significant sedimentation of the approach channel of Temryuk port by sand and silt deposits.

Observations and experimental studies in a number of ports [1, 2] revealed the sedimentation characteristics of approach channels protected by barrier structures. The construction of breakwaters divides the coastal zone into two regions with a different dynamic activity of waves, currents and sediment transport. As a result of the interruption of longshore sediment flow, large volumes of bottom sediments rapidly accumulate at the root of the windward mole (Fig. 1). This form of filling the incoming angle with sediment, followed by downstream erosion of the section of coast behind the leeward breakwater, is most relevant to port construction.

Previous work on the subject was analysed in the preparation of this paper. Papers [3–6] provide material on the modelling of longshore sediment transport. Information on the comparison of different approaches to the determination of longshore sediment transport rates is given in [7]. The papers [8, 9] discuss new models for predicting shoreline changes: a model based on the dynamic coupling of a high-resolution one-dimensional cross-shore model to a two-dimensional area model for calculating the total longshore sedimentation rate; a model based on machine learning techniques. A new method for verification of beach dynamics predictions was developed in [10].

One of the goals of this work is to estimate the possible volumes of sediment accumulation in the approach channel to the port of Temryuk, considering the general lithodynamic situation in the adjacent area. We are talking about the marine part of the channel, where the main factors of sedimentation are waves and associated currents that generate longshore sedimentations, which deliver the material to the channel bed.

The second goal of the work is to develop recommendations for extending the breakwaters enclosing of the coastal part of the channel on the east and west sides. The extension of the breakwater should reduce the sedimentation of the channel. However, the considerable cost of the structure imposes restrictions on the choice of its optimal length.

The mentioned problems are investigated in the present work on the basis of mathematical modelling of coastal lithodynamic processes [11–18].

At present, all-Russian and departmental normative documents on the design of approach channels [19] do not contain recommendations for determining the volume of catastrophic sediment deposition and methods for preventing it. Existing software complexes for determining the volume of approach channel sedimentation have certain drawbacks.

The existing normative base for design of sea approach channels is outdated and requires updating. A number of recommendations of all-Russian and departmental normative documents do not meet the requirements of modern design practice. They are developed on the models, which do not correspond to the modern level of knowledge about hydrolytodynamics of the coastal zone. The norms of design of sea approach channels do not contain recommendations, in which the initial data would include the parameters of engineering geology and coastal hydrolytodynamics. The sedimentation reserves are set depending on the dimensions of the design vessel. The phenomenon of sedimentation is accounted for by an empirical coefficient. In the process of designing, incorrect decisions lead to unjustifiably high volumes of repair dredging, and, consequently, to significant financial costs. In this connection, investigation of the process of sedimentation of the approach channels and the ways of its prevention is an actual problem.

Analysis of baseline information confirms high, constant sedimentation of the approach channel, which leads to the need for regular repair clearing of the channel and the port water area. Thus, according to FSUE Rosmorport, the volume of repair dredging was 129406.2 m^3 in 2020 and 120102.4 m^3 in 2021.

At the same time, sedimentation ability of the approach channel varies significantly along its length. According to the passport of approach channel, its sedimentation varies from 10 cm per year, to 100 cm and more per quarter.

Maximum sedimentation occurs in the head part of the east breakwater, both in the direction to the sea part of the channel and to the port part of the channel.

Simultaneously with sedimentation of the channel, the incoming angle for the east breakwater is filling up with shoreline advance into the sea. The rate of shore advance near the breakwater during the first year after its construction is about 50 m. The process of shore advancement from the inlet corner of the east breakwater directly affects the sedimentation of the approach channel, since after the shore reaches the head of the breakwater, the sediment will be transported by the longshore current directly into the channel.

According to survey data, the sedimentation of the approach channel occurs by storms from the east and west directions, the main sediment flow occurs from the east direction.

The main objectives of the work are:

1) Study of lithodynamic regime of the area under consideration in natural (modern) conditions.

2) Forecast of sedimentation of the approach channel of the seaport for several proposed variants of the east and west breakwater extension and selection of the extension option that provides an acceptable level of sedimentation.

2. Methods

An important feature of the sediment layer on the bottom in the studied area of the Azov coast, Russia (Temryuk Bay) is the existence of two rather clearly delineated zones, one of which (at depths greater than 3 m) is dominated by silty material, while the other, coastal (at depths less than 3 m) is dominated by fine-grained sand. This leads to the need to model separately the flows of sandy and muddy sediments when determining the total longshore flow. It should be noted that existing methods focus mainly on sandy sediments. In order to obtain estimates with respect to silt transport, it was necessary to develop a special calculation methodology.

2.1. Sandy sediment

The methodology for calculations concerning sandy sediments is outlined, for example, in [17, 20–26]. The basic formula for determining the local longshore sand discharge q under the action of waves and the accompanying current, expressed in m^{3}m^{-1}h^{-1}:

$$q=\mu\left[\frac{9\pi}{8}\frac{\varepsilon_b}{\tan\alpha_g}\frac{D_f}{u_m}+\frac{\varepsilon_s}{w_g}\left(4D_f+B\right)\right]V_b. \tag{1}$$

Here $\mu=3600\Big/\left[g\left(\rho_g-\rho\right)\left(1-\sigma\right)\right]$ is the coefficient, which agrees dimensions, g is acceleration of gravity, ρ and ρ_g are densities of water and solid particles, σ and α_g are porosity and angle of natural slope of ground, ε_b and ε_s are efficiency coefficients of transport of bedload and suspended sediments (0.1 and 0.02 respectively), u_m is amplitude of orbital wave velocity near the bottom, $D_f=\dfrac{2}{3\pi}\rho f_w u_m^3$ is energy dissipation rate due to bottom friction, f_w is coefficient of bottom friction for waves, w_g is sedimentation rate of solid particles (hydraulic coarseness), B value accounts for additional energy dissipation in the bottom layer due to turbulence penetration from surface layer at wave collapse, V_b is bottom velocity of longshore current. The latter is related to the depth-averaged current velocity $\bar{V}$ as $V_b = \bar{V} \big/ \left[\ln\left(h/z_a \right) - 1 \right]$, where h is depth and z_a is the apparent roughness of the bottom for the current. The value $\bar{V}$ is calculated using the equations of hydrodynamics, and Snell's law of refraction and the energy balance equation are used to calculate refraction, transformation, and wave energy dissipation.

2.2. Slimy sediments

Unlike sand, physical properties of silty sediments change in time and depend on dynamic conditions. Thus, to set in motion a layer of silt formed relatively recently (days, weeks), a flow velocity of about 0.2 m*s^{-1} is sufficient, and to move the sediment particles that have been at rest for a long time (months, years) a speed of about 1 m*s^{-1} is required. It is also known that under the influence of waves the threshold of touching for silty soils is much lower, since periodic pressure changes in the pores lead to weakening of particles adhesion. According to the data given by Van Rijn [27] the wave action on low compacted clayey soil starts the movement of the material at bottom tangential stress τ_m > 0.2 N*m^{-2}. Even relatively small waves can create an appreciable flow of muddy material.

In contrast to the sandy bottom, the current above the silt layer acts in a smooth regime, the roughness parameter is characterized by a value of less than 1 mm. Accordingly, the friction coefficient is significantly reduced.

Considering the fact that the sludge is mainly transported in suspension, its flow rate q', based on formula (1), can be expressed as

$$q' = 4\mu\alpha_w D_f V_b, \quad \alpha_w = \frac{\varepsilon_s}{w_g} \tag{2}$$

(B is neglected, assuming that the muddy sediments lie outside the collapse zone). The main problem is the estimation of the parameter α_w. In the case of sand, the efficiency factor ε_s is estimated to be 0.02, the settling velocity w_g for fine sand is of the order of 10^{-2} m*s^{-1}, and the value of α_w is close to unity. For silt, due to the bonding forces between particles, the value of ε_s should probably be lower than for sand. However, the solids deposition rate w_g is also significantly lower here. The order of magnitude of α_w for silty soil can only be estimated from experimental data.

Let us express flow q' in units of dry mass (in kg m^{-1}s^{-1}), rewrite formula (2) in terms of bottom tangential stress τ_m and pass from flow to depth average suspended solids concentration C (kg/m^3), connected with flow as $C = \dfrac{q'}{hV_b}$. Keeping in mind that in wave flow $D_f = \dfrac{4}{3\pi}\tau_m u_m$, where $\tau_m = \dfrac{1}{2}\rho f_w u_m^2$, we obtain from (2)

$$\begin{gathered} q' = \frac{16}{3\pi}\frac{\rho_g}{\left(\rho_g - \rho\right)}\alpha_w \tau_m u_m V_b, \\ C = \frac{16}{3\pi}\frac{\rho_g}{\left(\rho_g - \rho\right)}\frac{\tau_m u_m}{gh}\alpha_w \cong 3.4\frac{\tau_m u_m}{gh}\alpha_w, \end{gathered} \tag{3}$$

where the numerical coefficient in the last ratio corresponds to the typical value of the density of mud particles ρ_g = 2×10^3 kg/m^3.

To estimate the value of α_w, the data on suspended sediment concentration obtained in [28] can be used. The measurements were made both in a wave basin and in full-scale conditions (in the coastal zone of the Yellow Sea). The observation conditions and obtained estimates of α_w values are shown in

Table 1. The depths h, significant heights H_s and corresponding wave periods T_s, as well as the values of concentration C are shown here.

In the calculations it was assumed that under smooth bottom conditions the coefficient of friction is close to the values of f_w = 0.01. The obtained values of α_w have quite a large scatter, but in general of the same order. In the first approximation it is possible to accept the averaged estimation α_w = 2.8, on which further calculations of sediment flow using formula (2) will be based.

Table 1. Measurement conditions of sludge suspended solids concentration in laboratory and marine conditions [20] and calculated estimates of parameter α_w.

h, m	H_s, m	T_s, s	C, kg/m^3	α_w, s m^{-1}
Wave Pool				
0.1	0.075	1.2	0.5	1.8
0.1	0.050	2.2	0.2	2.5
0.1	0.035	1.2	0.05	1.7
Marine conditions				
5	2	8	0.65	2.4
5	1.5	8	0.55	4.8

2.3. The amount of accumulation in the channel

Some of the sediment passes over the channel by transit. Therefore, it is necessary to estimate how much of the material falls to the bottom and contributes to the sedimentation. In this case, the well-known Galvin dependence is used for this purpose [29]:

$$Ac = q\left[1 - \left(\frac{h}{h_c}\right)^2\right], \tag{4}$$

where Ac is the local rate of sediment accumulation in the channel (per meter of length), q is the longshore flow rate of sediment in front of the channel, h is the natural depth, h_c is the depth in the channel. The deeper the channel is relative to the natural depth, the more sediment it absorbs.

3. Results and Discussion

The bathymetric basis for modelling is a navigation map of scale 1:10000, as well as survey data in the vicinity of the channel. The isobath plan in the Temryuk port area is shown in Fig. 2. The general direction of the coastline in the area under consideration is close to the west-east direction.

As mentioned above, at depths less than 3 m the bottom is covered by a layer of fine sand with shell fragments averaging 0.15 mm, while deeper than 3 m there is silt. The bottom within the sandy layer has a slope of about 0.01, and more narrowly the slopes decrease to values of 0.002–0.005.

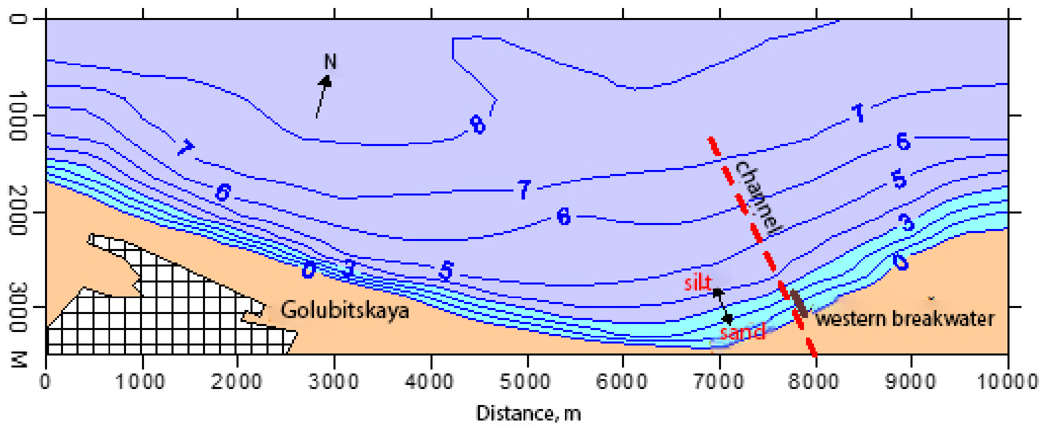

Figure 2. Bottom bathymetry in the channel vicinity.

The position of the existing structures at the mouth of the channel is reflected in Fig. 2. The east breakwater currently terminates at a depth of 1 m and thus allows sandy sediments to flow into the channel at depths of 1 to 3 m. The depth at the end of the west breakwater is only about 0.5 m, and the longshore flow of sediment created by the waves of the west channels is almost unimpeded into the channel.

The length of the offshore part of the channel from the beginning in the open sea to the head of the east breakwater is 2,700 m. The channel floor width varies from 95 to 100 m. The design depth in the channel varies from 6.4 to 6.9 m. The deepest part is before the end of the east breakwater. During calculations, the depth of the channel was assumed to be 6.9 m.

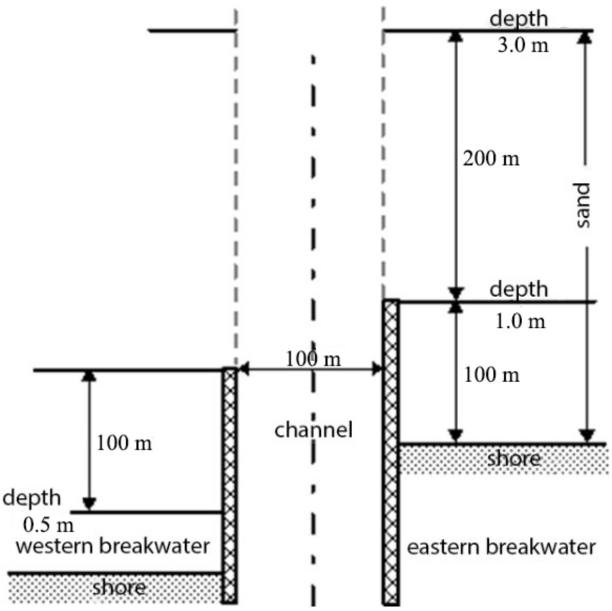

Figure 3. Diagram of the shoreline at the mouth of the channel.

The wave pattern in the Temryuk coastal area is characterized by the predominance of the NE direction. The wave mode is shown in Table 1, based on data from the Russian Maritime Register of Shipping [30].

Table 2. Annual duration of waves of different strengths for the main directions.

H_S, m	T_S, s	t_w, h			
		W Θ = 85°	NW Θ = 40°	N Θ = –5°	NE Θ = –50°
0.6	3.6	429	473	394	929
1.0	4.2	184	158	131	464
1.3	4.7	53	35	26	166
1.8	5.0	8.8	6.1	3.5	44
2.1	6.0				7.0

Here is the total annual duration of waves (t_w) of different strength for the main wave directions (H_s and T_s are the significant height and corresponding period of waves in the open sea, Θ are the angles of approach of waves relative to the coastal normal).

3.1. Modelling of longshore sediment flows

The calculated distributions of the volumes of sand and silt moving over the profile of the coastal slope during the year are shown in Fig. 4. Separately, the westward and eastward flows created by the eastward and westward waves, respectively, are shown. As can be seen, the resultant flows are directed westward. The sandy sediment flow peaks closer to the water's edge at 1–2 m depths, while the silt flow peaks near the upper boundary of its distribution. The maximum values of sand fluxes in the near-river zone reach 200–400 cubic meters per meter of profile length per year. The peaks of flows to the west and to the east are shifted relative to each other due to the unequal position of the coastline on both sides of the channel (Fig. 3).

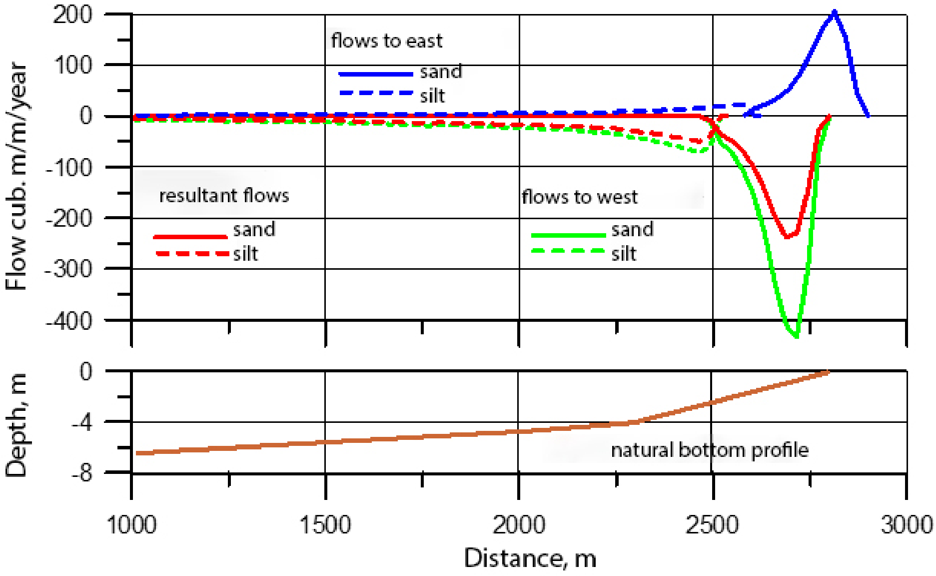

Figure 4. Distribution of longshore sediment fluxes along the profile of the coastal slope.

At depths greater than 3 m, only muddy sediment moves (at a peak of about 75 $m^3m^{-1}yr^{-1}$). Although the silt flows subside with increasing depth, the movement of material can be traced throughout the channel.

An idea of the integral material flows is given in Table 3. About 40,000 cubic meters of sand and silt move in the east direction per year, and about 100,000 cubic meters in the west direction. The resulting flow is westward and is about 60 thousand cubic meters per year, and the contributions of sand and silt are comparable.

Table 3. Integral longshore sediment flows (thousand cubic meters per year).

Flow	Sand	Silt
On east	27.2	9.4
On west	–58.8	–37.8
Totally	–31.6	–28.4

3.2. Channel sedimentation under existing conditions

The results of calculations of specific sediment accumulation (per meter of channel length) are shown in the upper graph of Fig. 5. The accumulation of sand is characterized by two peaks. The smallest and closest peak is associated with the westward rumb waves (209 m^3m^{-1} $year^{-1}$). The second and largest peak (440 m^3m^{-1} $year^{-1}$) is due to the eastward waves. It is displaced towards the sea, as part of the flow is blocked near the coast by the east breakwater. As for the silt, it is deposited mainly at depths of 3 to 5 m (in the peak up to 75 m^3m^{-1} $year^{-1}$ at 3 m depth).

Specific channel sedimentation is also presented as Table 4. The distance between pickets is 100 m, they are counted from the end of the east breakwater towards the sea. Picket №-1 is located at the distance between the west and east breakwaters (Fig. 3).

Table 4. Accumulation of sediment in the channel at the existing conditions.

No range	Accum., m^3m^{-1} $year^{-1}$	No range	Accum., m^3m^{-1} $year^{-1}$	No range	Accum., m^3m^{-1} $year^{-1}$
-1	209	9	10	19	0.2
0	440	10	9.0	20	0.0
1	140	11	7.1	21	0.0
2	75	12	5.6	22	0.0
3	50	13	4.4	23	0.0
4	33	14	3.3	24	0.0
5	24	15	2.6	25	0.0
6	19	16	1.9	26	0.0
7	15	17	1.2	27	0.0
8	13	18	0.7		

The middle graph of Fig. 5 shows the distribution of conditional thickness of sediment layer Δh along the length of the channel (quotient of specific accumulation volume divided by the width of the channel). At depths less than 3 m, the thickness of sand sediment layer can reach 4 m per year. Maximum silt layer up to 0.7–0.8 m per year is observed at a depth of about 3 m (near the conventional boundary between sand and silt). With the distance from the shore the thickness of accumulation layer decreases and at the depth of more than 5 m the value of Δh becomes less than 0.2 m.

Integral indices of channel sedimentationing and accumulation near moles are shown in Table 5. Total volume of channel sedimentationing is estimated as 78 thousand m^3/year, 70 % of which is caused by sand.

The west breakwater retains only a small part of the sand transported to the channel (3 thousand m^3/year). The east breakwater, apparently, also has insufficient length and retains only 24 thousand m^3/year. Most of the sand passing in the west and east directions enters the channel (55 thousand m^3/year).

Table 5. Accumulation at the breakwaters and in the channel (thousand cubic meters per year) at the existing breakwaters.

Material	W breakwater	E breakwater	Channel
Sand	3.2	24.3	55.1
Silt	-	-	23.1

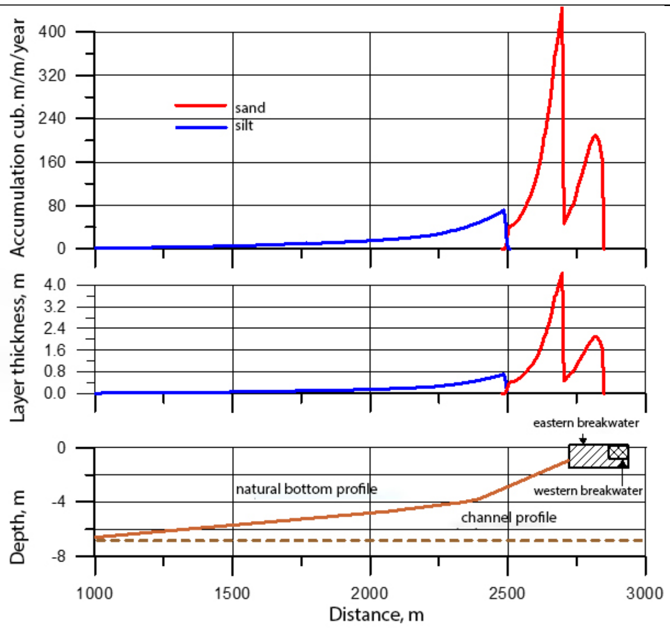

Figure 5. Distribution of the volume of sedimentation and thickness of sediment in the channel along the profile of the bank slope.

It should be noted that a certain part of sand can move along the breakwater and eventually end up in the channel as well. This is evidenced by the results of modelling of storm bottom deformations in the area of the channel mouth under NE storm conditions (Fig. 6). As can be seen, an accumulative sand body is formed near the head of the breakwater, which can be later moved into the channel. Thus, the local sedimentation here may exceed the values given above.

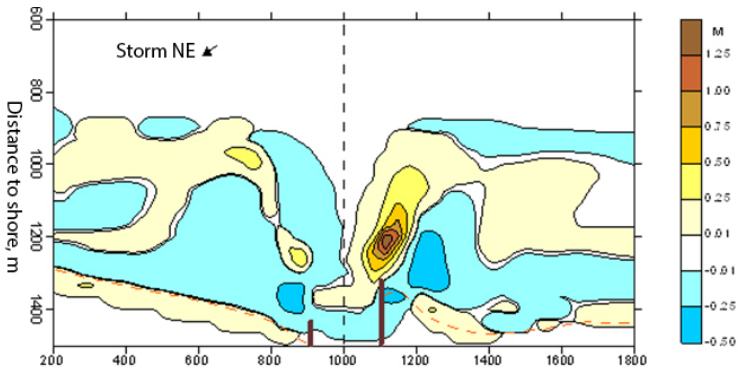

Figure 6. Storm deformation in the area of the channel mouth during the NE storm. Accumulation is highlighted in yellow and brown.

3.3. Options for extending the east breakwater

Based on the results obtained and the planned service life of the structures (class III – 50 years), two options for extending the east breakwater are considered.

Variant 1 assumes extension by 100 m. In this case, after 25 years, the situation with sedimentation will be approximately the same as it is at present. Namely, the presently existing section of the breakwater will be reached by the extending coastline. And about 100 m of the breakwater will provide protection.

Variant 2 assumes an extension of 200 m from the present position. In this case, the entire sandbar will be blocked. The sedimentationing will decrease and reach the present values only in 50 years.

Let's return to consideration of variant 1. If the breakwater is extended by 100 m, its length with respect to the current position of the shore will be 200 m, and the depth at the head will be about 2 m (Fig. 3).

The results of calculations of sedimentationing in variant 1 are shown in Fig. 7.

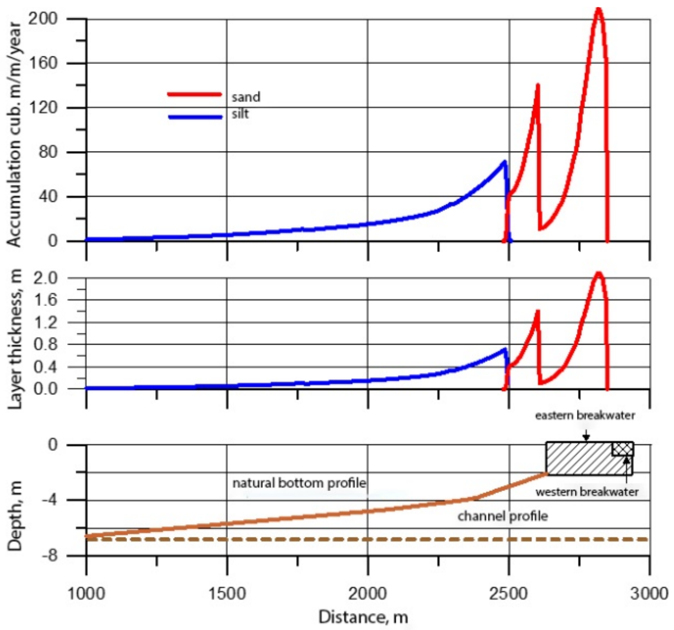

Figure 7 - Distribution of the channel skid volumes after extending the east breakwater by 100 m (variant 1).

As can be seen, the inflow of sand into the channel from the east side is markedly reduced (at a peak of 140 vs. 440 m^3m^{-1} $year^{-1}$ under the current position). The sand accumulation is now caused mainly by its inflow from the west side. The volume of silty sedimentation from the east side does not change.

The specific sedimentation of the channel in variant 1 is shown in Table 6, and the integral indices of sediment load and accumulation near the breakwaters are shown in Table 7. The east breakwater now retains twice as much sand. In total, about 30 thousand m^3 of sand per year enters the channel, which is almost twice less than under the current situation (Table 5).

Table 6. Accumulation of sediment in the channel, variant 1.

No range	Accum., m^3m^{-1} $year^{-1}$	No range	Accum., m^3m^{-1} $year^{-1}$	No range	Accum., m^3m^{-1} $year^{-1}$
–1	209	9	10	19	0.2
0	43	10	9.0	20	0.0
1	140	11	7.1	21	0.0
2	75	12	5.6	22	0.0
3	50	13	4.4	23	0.0
4	33	14	3.3	24	0.0
5	24	15	2.6	25	0.0
6	19	16	1.9	26	0.0
7	15	17	1.2	27	0.0
8	13	18	0.7		

Table 7. Accumulation at the breakwaters and in the channel (thousand cubic meters per year), variant 1.

Material	W breakwater	E breakwater	Channel
Sand	3.2	50.3	30.2
Silt	-	-	23.1

The catching capacity of the east breakwater will gradually decrease over time, due to shoreline advance, which was noted in [19].

Variant 2. After extending the breakwater by 200 m, its length relative to the current position of the shore will be 300 m, and the depth at the head will be about 3 m (Fig. 3).

The results of calculations of sedimentationing in variant 2 are shown in Fig. 8. The enclosing breakwater now completely cuts off the inflow of sand on the east side. However, the sand sedimentation on the west side remains the same (more than 200 m^3m^{-1} $year^{-1}$, sediment thickness 2 m/year). The volume of sediment sedimentation is also unchanged.

Specific sedimentation of the channel in variant 2 is shown in Table 8, and the integral indices of sedimentation and accumulation near the breakwaters are characterized in Table 9.

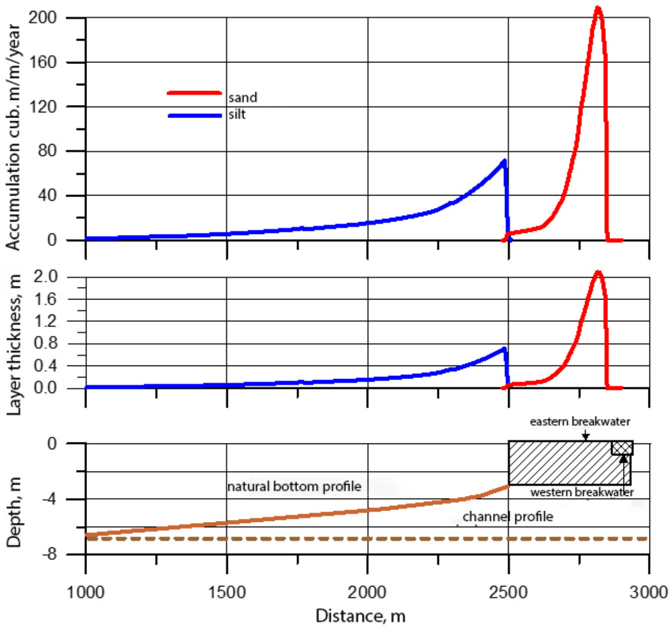

Figure 8. Distribution of channel skid volumes after extending the east breakwater by 200 m (variant 2).

Table 8. Accumulation of sediment in the channel, variant 2.

No range	Accum., m^3m^{-1} $year^{-1}$	No range	Accum., m^3m^{-1} $year^{-1}$	No range	Accum., m^3m^{-1} $year^{-1}$
-1	209	9	10	19	0.2
0	43	10	9.0	20	0.0
1	10	11	7.1	21	0.0
2	75	12	5.6	22	0.0
3	50	13	4.4	23	0.0
4	33	14	3.3	24	0.0
5	24	15	2.6	25	0.0
6	19	16	1.9	26	0.0
7	15	17	1.2	27	0.0
8	13	18	0.7		

Table 9. Accumulation at the breakwaters and in the channel (thousand cubic meters per year), variant 2.

Material	W breakwater	E breakwater	Channel
Sand	3.2	58.8	22.8
Silt	-	-	23.1

As can be seen, the sedimentation of sand in the channel is now a little less than 23 thousand cubic meters per year, which is only 7 thousand cubic meters less than in option 1. Consequently, Option 2 (extension of the breakwater by 200 m) does not result in a significant improvement over Option 1 (extension by 100 m). A more noticeable reduction in sedimentation can most likely be achieved by extending the west breakwater by the same 100 m.

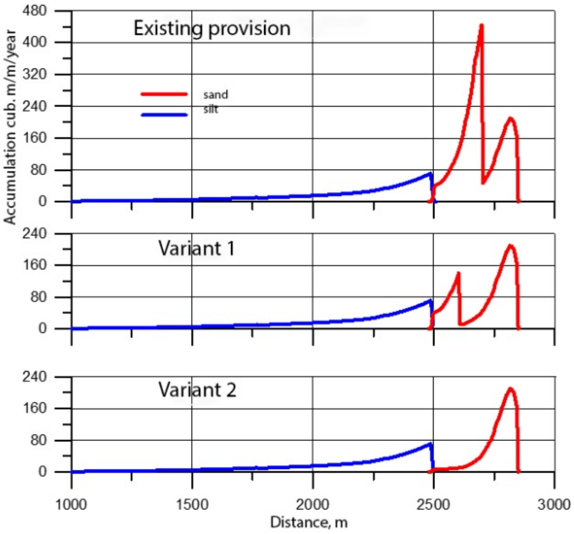

Figure 9. Distribution of channel skid volumes at different lengths of the east breakwater.

For the convenience of comparison, the channel sedimentation for different variants of the east breakwater is shown in Fig. 9. Variant 2, as compared to variant 1, removes the second peak of sand sedimentation on the east side, which is almost half the size of the sand sedimentation on the west side.

3.4. Channel sedimentation after extending the west breakwater

The distribution of the sedimentation after the extension of the west breakwater by 100 m is shown in Fig. 10. It is assumed that the east breakwater has already been extended by the same distance. The inflow of sand into the channel from the west side is now significantly less than before (at peak about 100 vs. 200 $m^3 m^{-1}$ $year^{-1}$ under the current position).

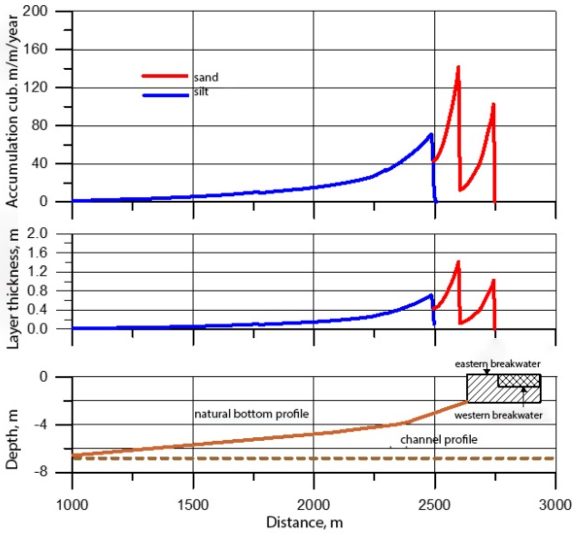

Figure 10. Distribution of the volume of the channel sedimentation after extending the west breakwater by 100 m (it is assumed that the east breakwater has already been extended by 100 m).

The specific sedimentation of the channel after extending the west breakwater is shown in Table 10, and the integral indices of sedimentation and accumulation at the breakwaters are characterized in Table 11. The west breakwater now retains 6 times more sand than before. In total, less than 15 thousand m^3 of sand per year enters the channel, which is half as much as before the west breakwater extending (Table 5).

Table 10. Accumulation of sediment in the channel after extending the west breakwater.

No range	Accum., m^3m^{-1} $year^{-1}$	No range	Accum., m^3m^{-1} $year^{-1}$	No range	Accum., m^3m^{-1} $year^{-1}$
-1	102	9	10	19	0.2
0	43	10	9.0	20	0.0
1	140	11	7.1	21	0.0
2	75	12	5.6	22	0.0
3	50	13	4.4	23	0.0
4	33	14	3.3	24	0.0
5	24	15	2.6	25	0.0
6	19	16	1.9	26	0.0
7	15	17	1.2	27	0.0
8	13	18	0.7		

Table 11. Accumulation at the breakwaters and in the channel (thousand cubic meters per year) after the extension of the west breakwater.

Material	W breakwater	E breakwater	Channel
Sand	19.9	50.3	14.6
Silt	-	-	23.1

Thus, after extending the breakwaters, the volume of sedimentation of the channel will decrease from 55 to 15 thousand cubic meters per year. As a result, the main contribution to the sedimentation will be made not by sand, but by silty material. It should be emphasized that the planned measures for extending the breakwaters have no effect on the volume of silty sediment accumulation, which spreads beyond the 3-meter isobath.

Distribution of sedimentation volumes at the existing position, at extension of the east breakwater only, as well as at extension of both breakwaters are compared in Fig. 11. Obviously, the latter option is the most preferable in terms of sedimentation reduction.

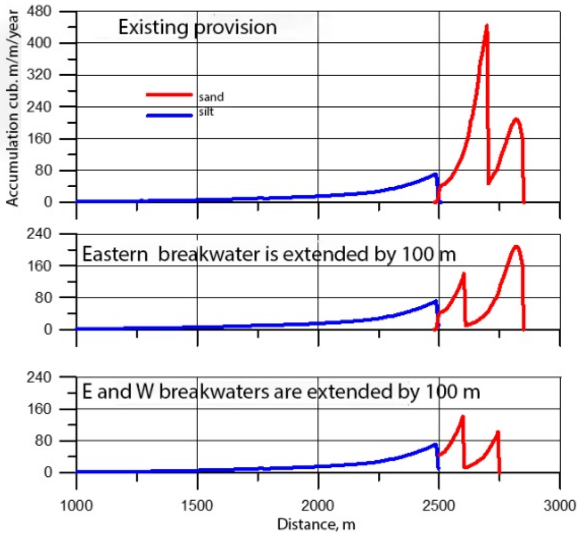

Figure 11. Comparison of the distributions of channel sedimentation volumes for different phases of breakwater extension.

3.5. Shoreline dynamics in the vicinity of the east breakwater

In order to solve the problem of the breakwater extension, it is first necessary to trace the dynamics of the shoreline in the vicinity of the structure and assess its possible future changes. The fact is that due to the accumulation of sand in front of the breakwater, the shore gradually grows. If we compare the present position of the shoreline with the one marked on the sea maps of the 1980s, it turns out to be shifted towards the sea by about a hundred meters.

Figure 12. Shoreline changes in the area of the channel mouth from 2006 to 2019 based on the analysis of satellite images.

The coastal advance is most clearly demonstrated by satellite images taken at intervals of several years. Fig. 12 shows the changes in the shore position near the east breakwater for the period from 2006 to 2019 (the results were obtained at MGSU). The linear scale in this case can be a channel width of 100 m. The figure shows that over 13 years, the coastline has shifted toward the sea by about 40–50 m, i.e., the rate of advancement is close to 3–4 m/year.

3.6. Shore dynamics to the west of the channel

The dynamics of the shoreline area adjacent to the channel on the west side can be judged based on information obtained by analyzing satellite images taken over the past decades. The results of the shoreline changes analysis provided by MGSU are shown in Fig. 13.

First of all, it should be noted that there are no significant changes in the area in question. The shoreline fluctuates from year to year with an amplitude of about 10 m. However, its average position remains generally stable. The tendency to erosion is not detected. It is rather possible to speak about some accretion of the shore. For example, between 2003 and 2020, the west breakwater shore has moved out at a distance of about 10 m. I.e., the average advance rate over 17 years was about 0.6 m/year.

Figure 13. Shoreline changes to the west of the approach channel.

Thus, over the next 50 years, the shoreline at the west breakwater may be extended by about 30 m. However, this is unlikely to noticeably affect the protective function of the structure, the length of which, considering the planned extension, should be about 150 m.

Although there is no coastal retreat in the area considered, it is possible that there may be downstream erosion due to interruption of sediment flow after the extension of the breakwater. It should, however, be considered that the flow is also interrupted in the present position, with the bulk of it accumulating in the channel. After the reconstruction of the breakwaters, most of the material will be retained not in the channel, but near the structures, i.e. there will be a redistribution of accumulation volumes, but the total volume of sediment deficit downstream will not change significantly. Consequently, we can expect shoreline changes to the west of the channel to continue to be insignificant.

4. Conclusions

The results of the study can be summarised as follows:

1) The sedimentation of the approach channel is determined separately for the area of predominantly sandy and the area of predominantly muddy sediments. The technique allows you to explore various scenarios of mole extension and determine the best option. The results are verified by the data of space images.

2) At present, the existing protective structures of Temryuk seaport contain a relatively small part of sand sedimentation moving along the shore: 3 thousand m^3/year for the west breakwater and 24 thousand m^3/year for the east one. The total volume of sand sedimentation into the channel reaches 50 000 m^3/year. Maximum specific sedimentation exceeds 400 $m^3m^{-1}year^{-1}$ (at the head of the east breakwater).

3) Due to the accumulation of sand in front of the east breakwater, the coastline is gradually advancing into the sea and, based on the obtained estimations, will reach the head of the existing breakwater in 25 years. In this connection, two variants of the east breakwater extension are considered: variant 1 – by 100 m, variant 2 – by 200 m.

4) If the east breakwater is extended by 100 m, the sedimentation of the channel will almost halve (from 55 to 30 thousand m^3/year). Maximum specific accumulation will decrease to 200 $m^3m^{-1}year^{-1}$.

5) If the east breakwater is extended by 200 m, the sedimentation will decrease insignificantly in comparison with the variant of extended by 100 m (from 30 to 23 thousand m^3/year), though the structure will be able to fulfil its protective function twice as long (approximately 100 years).

6) If the west breakwater is lengthened by 100 m, the sedimentation will become two times less, and the volume of sand accumulation in the channel will not exceed 15 thousand m^3/year. The maximum specific accumulation will decrease to 140 $m^3m^{-1}year^{-1}$. For a radical reduction of the channel's sanding, it is advisable to extend not only the eastern, but also the west breakwater.

7) According to the available data, the bank to the west of the channel is generally stable and will not undergo significant changes after the breakwater reconstruction. At the same time, the shoreline may be extended by about 30 m over a 50-year period at the west breakwater, which, however, will not lead to any noticeable deterioration of the protective properties of the structure.

References

1. Szmytkiewicz, M., Biegowski, J.X., Kaczmarek, L.M., Okrój, T., Ostrowski, R.X., Pruszak, Z., Różyńsky, G., Skaja, M. Coastline changes nearby harbour structures: comparative analysis of one-line models versus field data. Coastal Engineering. 2000. 40 (2). Pp. 119–139. DOI: 10.1016/S0378-3839(00)00008-9
2. El-Asmar, H.M., White, K. Changes in coastal sediment transport processes due to construction of New Damietta Harbour, Nile Delta, Egypt. Coastal Engineering. 2002. 46(2). Pp. 127–138. DOI: 10.1016/S0378-3839(02)00068-6
3. Zarifsanayei, A.R., Antolínez, J.A.A., Etemad-Shahidi, A., Cartwright, N., Strauss, D. A multi-model ensemble to investigate uncertainty in the estimation of wave-driven longshore sediment transport patterns along a non-straight coastline. Coastal Engineering. 2022. 173. Pp. 104080. DOI: 10.1016/j.coastaleng.2022.104080
4. Bergillos, R.J., Masselink, G., Ortega-Sánchez, M. Coupling cross-shore and longshore sediment transport to model storm response along a mixed sand-gravel coast under varying wave directions. Coastal Engineering. 2017. 129. Pp. 93–104. DOI: 10.1016/j.coastaleng.2017.09.009
5. Kuriyama, Y., Sakamoto, H. Cross-shore distribution of long-term average longshore sediment transport rate on a sandy beach exposed to waves with various directionalities. Coastal Engineering. 2014. 86. Pp. 27–35. DOI: 10.1016/j.coastaleng.2014.01.009
6. Sheela Nair, L., Sundar, V., Kurian, N.P. Longshore Sediment Transport along the Coast of Kerala in Southwest India. Procedia Engineering. 2015. 116 (1). Pp. 40–46. DOI: 10.1016/j.proeng.2015.08.262
7. Samaras, A.G., Koutitas, C.G. Comparison of three longshore sediment transport rate formulae in shoreline evolution modeling near stream mouths. Ocean Engineering. 2014. 92. Pp. 255–266. DOI: 10.1016/j.oceaneng.2014.10.005
8. Zhang, W., Deng, J., Harff, J., Schneider, R., Dudzinska-Nowak, J. A coupled modeling scheme for longshore sediment transport of wave-dominated coasts — A case study from the southern Baltic Sea. Coastal Engineering. 2013. 72. Pp. 39–55. DOI: 10.1016/j.coastaleng.2012.09.003
9. Goldstein, E.B., Coco, G., Plant, N.G. A review of machine learning applications to coastal sediment transport and morphodynamics. Earth-Science Reviews. 2019. 194. Pp. 97–108. DOI: 10.1016/j.earscirev.2019.04.022
10. Bosboom, J., Mol, M., Reniers, A.J.H.M., Stive, M.J.F., de Valk, C.F. Optimal sediment transport for morphodynamic model validation. Coastal Engineering. 2020. 158. Pp. 103662. DOI: 10.1016/j.coastaleng.2020.103662
11. Haas, K.A., Hanes, D.M. Process-based modeling of total longshore sediment transport. Journal of Coastal Research. 2004. 20(3). Pp. 853–861.

12. Bailard, J.A. An energetics total load sediment transport model for a plane sloping beach. Journal of Geophysical Research. 1981. 86 (C11). Pp. 10938. DOI: 10.1029/JC086iC11p10938
13. Bayram, A., Larson, M., Hanson, H. A new formula for the total longshore sediment transport rate. Coastal Engineering. 2007. 54 (9). Pp. 700–710. DOI: 10.1016/j.coastaleng.2007.04.001
14. Hanson, H., Larson, M., Kraus, N.C. Calculation of beach change under interacting cross-shore and longshore processes. Coastal Engineering. 2010. 57 (6). Pp. 610–619. DOI: 10.1016/j.coastaleng.2010.02.002
15. Hanson, H. Genesis: a generalized shoreline change numerical model. Journal of Coastal Research. 1989. 5(1). Pp. 1–27.
16. Bowen, A.J. Simple models of nearshore sedimentation; beach profiles and longshore bars. Geol. Survey of Canada. 1980. Pp. 1–11. DOI: 10.4095/102213
17. Leont'yev, I.O. Izmeneniya kontura berega, vyzvannyye poperechnym sooruzheniyem v beregovoy zone morya [Changes in shoreline contour due to cross-shore structure in the Sea Coastal Zone]. Geomorphology RAS. 2018. (3). Pp. 32–39. DOI: 10.7868/S0435428118030033
18. Eelsalu, M., Parnell, K.E., Soomere, T. Sandy beach evolution in the low-energy microtidal Baltic Sea: Attribution of changes to hydrometeorological forcing. Geomorphology. 2022. 414. Pp. 108383. DOI: 10.1016/j.geomorph.2022.108383
19. RD.31.31.47-88. Normy proyektirovaniya morskikh kanalov [Design Standards for Maritime Canals]. USSR Minmorflot 114, Moscow, 1988.
20. Leont'yev, I.O. Coastal dynamics: waves, currents, sediment transport. Moscow, GEOS, 2001. 272 p.
21. Hadla, G., Anshakov, A.S., Kantarzhi, I.G. The Role of Currents and Waves in the Movement of Sediments in the Vicinity of Coastal Hydraulic Structures. Power Technology and Engineering. 2021. 54 (6). Pp. 841–847. DOI: 10.1007/s10749-021-01297-0
22. Kantarzhi, I., Leont'yev, I., Hadla, G. Modeling of Lithodynamic Processes in the Area of a Large Navigation Channel. APAC 2019. Singapore, Springer Singapore, 2020. Pp. 441–447. DOI: 10.1007/978-981-15-0291-0_61
23. Van Wellen, E., Chadwick, A.J., Mason, T. A review and assessment of longshore sediment transport equations for coarse-grained beaches. Coastal Engineering. 2000. 40 (3). Pp. 243–275. DOI: 10.1016/S0378-3839(00)00031-4
24. Capobianco, M., Larson, M., Nicholls R.J., Kraus, N.C. Depth of closure: a contribution to the reconcillation of theory, practice and evidence. Int. Conf. Coastal Dynamics'97. Plymouth, 1997. Pp. 506–515.
25. Gladish, V.A., Logvina, E.A., Nesterov, A.V., Kubishkin, N.V. Intensity of the lithodynamical processes in the sea navigation channel Sabetta. Eng. Stud. 2017. No. 4. Pp. 36–45.
26. Van Wellen, E., Chadwick, A.J., Bird, P.A.D., Bray, M., Lee, M., Morfett, J.C. Coastal sediment transport on shingle beaches. Proceedings of Coastal Dynamics'97, American Society of Civil Engineers, 1997. Pp. 38–47.
27. Van Rijn L. Principles of sediment transport in rivers, estuaries and coastal seas. Aqua Publ. Amsterdam, 1993.
28. Rodriguez, H.N., Mehta, A.J. Longshore transport of fine-grained sediment. Continental Shelf Research. 2000. 20 (12–13). Pp. 1419–1432. DOI: 10.1016/S0278-4343(00)00030-3
29. Ghosh, L.K., Prasad, N., Joshi, V.B., Kunte, S.S. A study on siltation in access channel to a port. Coastal Engineering. 2001. 43 (1). Pp. 59–74. DOI: 10.1016/S0378-3839(01)00006-0
30. Rossiyskiy morskoy registr sudokhodstva. Spravochnyye dannyye po rezhimu vetra i volneniya Baltiyskogo, Severnogo, Chernogo, Azovskogo i Sredizemnogo morey [Russian Maritime Register of Shipping. Reference data on wind and wave regimes in the Baltic, North, Black, Azov and Mediterranean Seas]. St. Petersburg: Gidrometeoizdat, 2006. 452.

Information about authors:

Izmail Kantardgi, *Doctor of Technical Sciences*
E-mail: kantardgi@yandex.ru

Igor Leont'yev, *Doctor of Geography*
ORCID: https://orcid.org/0000-0002-5010-6239
E-mail: igor.leontiev@gmail.com

Alexander Kuprin,
ORCID: https://orcid.org/0000-0002-4186-2753
E-mail: rtyter55@gmail.com

Received 05.02.2023. Approved after reviewing 07.04.2023. Accepted 07.04.2023.

Magazine of Civil Engineering

ISSN 2712-8172

journal homepage: http://engstroy.spbstu.ru/

Research article

UDC 624.139.22

DOI: 10.34910/MCE.120.9

Regression models of irregular vertical displacement of a roadway cross section caused by frost heaving

V.S. Churilin ✉ **,** ***O.V. Matvienko, V.N. Efimenko, S.V. Efimenko***

Tomsk State University of Architecture and Building, Tomsk, Russian Federation

✉ *lex-16-2008@mail.ru*

Keywords: frost heaving, air-freezing, thermal resistance of pavement, pavement displacement, regression model

Abstract. Subgrade clay is subjected to frost heaving under the effect of cold air and adequate soil moisture. The existing prediction models for frost heaving have a number of drawbacks: they are complicated for practical use and unable to evaluate irregular vertical displacements. Winter monitoring of 14 road sections was performed to evaluate irregular vertical displacement of pavement surface cross section under the action of frost heaving. The obtained data on vertical displacement of points were processed using mathematical statistics methods, and predictive regression models were built for vertical displacement of pavement during winter season. Stable relations were defined between displacement of points on the broken line (center-line of a road) and the factors including air-freezing index, thermal resistance of pavement, impact of subsurface water on frost heave, the pressure of pavement on the subgrade surface. Adequacy of the built models was checked using the results of displacement of points on the pavement surface within test sections. The first check concerned comparison of the values of modeling of the average displacement of points on the broken line caused by frost heaving, where mean absolute error was up to 20 %. For the case of close occurrence of subsurface water, the model prediction of the average displacement of points on the broken line showed significant difference from the actually recorded values. The second check concerned the displacement of points on the pavement in relation to displacement of points on the broken line, with the mean absolute value of up to 13 %.

Funding: FEMN-2022-0003 of the Ministry of Science and Higher Education of the Russian Federation

Acknowledgments: The authors thank the anonymous reviewers, whose comments helped to improve the quality of this paper. The authors would like to acknowledge Shannon Fiecke, Benjamin Worrell, and Sandy McCully the Department of transportation Minnesota for the information provided. My thanks are due to our Italian colleague Lucia Tsantilis for her help.

Citation: Churilin, V.S., Matvienko, O.V., Efimenko, V.N., Efimenko, S.V. Regression models of irregular vertical displacement of a roadway cross section caused by frost heaving. Magazine of Civil Engineering. 2023. 120(4). Article no. 12009. DOI: 10.34910/MCE.120.9

1. Introduction

Phase change of water in clay soil in cold climate regions (according to the climate classification by Köppen-Geiger [1]) causes significant pavement defects and increase of repair costs [2–4]. When subgrade soil freezes, the water in it starts migrating and transits from liquid to solid state, thus leading to displacement of pavement surface, or frost heaving. The study performed by Taber [5] highlights that the main reason of frost heaving is ice segregation in the subgrade soil caused by mass transfer (of water) to the cooling region. In 1929, Taber performed an experiment with freezing soil samples saturated with benzene (the latter contracts as it freezes) which enabled him to conclude that volume expansion of pore water while freezing in soil is not related to the main mechanism of frost heaving. S. Taber's vision of the reasons of mass transfer to the cooling region has been improved in the research by Beskow [6] and other studies. In 1937, Tsytovich [7] formulated the concept of moisture redistribution, which found scientific consensus.

Today, studies on physical causes of ice segregation, influencing factors and their combination, as well as their impacts on engineering structures are still ongoing [8, 9]. Fig. 1 shows the development of research on frost heaving of soil. The qualitative parameter of publications shows an annual growth, which demonstrates the relevance of the topic of soil frost heaving and its effect on engineering structures.

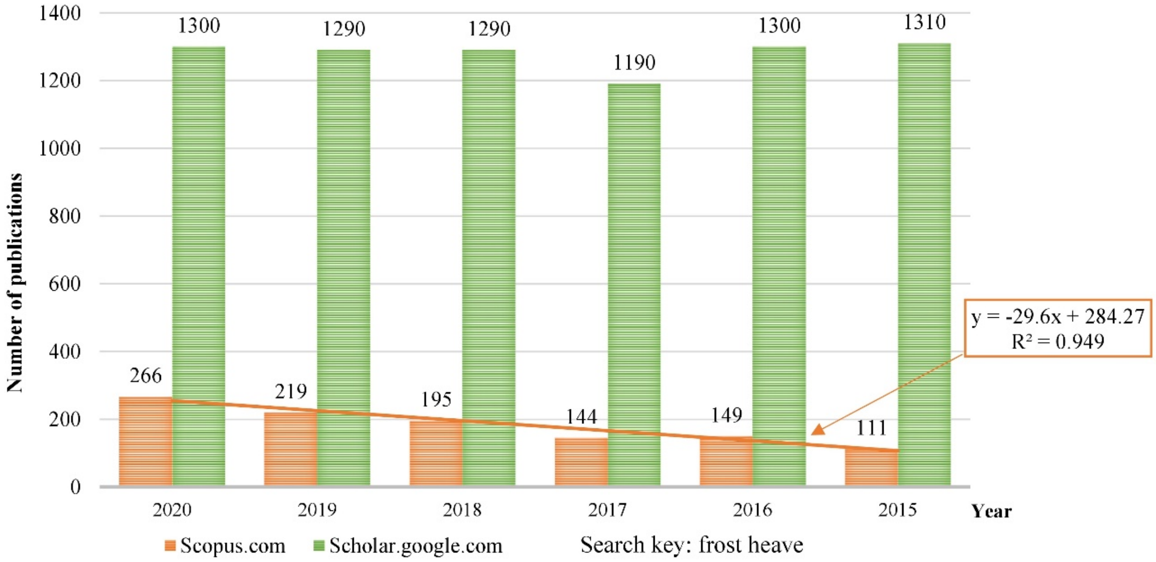

Figure 1. Variation of the number of publications on frost heaving (based on scopus.com and scholar.google.com data as of January 2021).

Studies on physical mechanisms, chemical and thermodynamic processes in frozen subgrade soil are the basis for building predictive models of frost heaving of soil.

A comprehensive description of predictive model building and development forsoil frost heaving is provided in the review carried out by Black [10]. Other studies that are worth to mention include research works that consider heat transfer through isotopic medium [11, 12] and the secondary frost heaving theory developed in 1985 by O'Neill and Miller [13]. These studies made a considerable contribution to the understanding and prediction of frost heaving of soil. Recent investigations suggest the adoption of both traditional and innovative approaches that can be used to model the frost heaving process [14–17].

The study performed by Jing et al. in 2021 [18] is worth noting for providing a prediction of longitudinal strains occurring in the railway subgrade under the action of frost heave by using the Artificial Intelligence (AI) technology, namely Artificial Neural Network (ANN) and Long-Short Term Memory (LSTM). The frost heave prediction made for a 10-day period with the use of the LSTM model of a single-layer neural network revealed good agreement between the modeling and full-scale experiment results. Eighty percent of the data obtained during the monitoring were used for training of the neural network, while twenty percent were applied in the network testing. The LSTM model was tested using the full-scale monitoring results obtained for the railway sections and used for its training. This may not be representative of the frost heave pattern on other railway sections taking into account variation of railway subgrade freezing conditions. The prediction of frost heave for the entire period is necessary for the model to be applicable for practical use. This aspect implies that a high computing capacity is needed.

Despite the actual achievements in frost heaving prediction, difficulties were found in performing practical comparison between the above-mentioned models and their applications. The problem of irregular vertical displacements of the pavement surface caused by frost heaving cannot be easily solved by using most of mathematical models. Complex specialized equipment and highly trained professionals are required to obtain soil parameters used for modeling.

The goal of this study is the development of a regression model for predicting irregular vertical displacement of pavements in crosswise direction under the action of frost heaving. The model will serve as an available solution for road engineers. The factors selected for the regression analysis take into consideration not only the relevance for the frost heaving phenomenon but also the availability of data for road engineers.

2. Materials and Methods

Monitoring of the pavement surface displacement during winter season was performed for model building purposes. Studies of soil conditions were carried out for the road network in the area in question (geolocation data of the monitored sections are provided in the paper appendix). The area is characterized by excessive moisture and deep seasonal freezing. The frost depth from the clean surface of subgrade soil in the studied area by early spring is approximately 200 to 220 cm, and in certain years it reaches 260 cm. Vast areas covered with swamps and forest have significant impact on the moisture content in soil and affect mass transfer in subgrade soils of roadways in the area under study [19]. Soil samples were taken along the curb of the roadway from the sections selected for monitoring (Fig. 2) to be tested in the laboratory. Trial holes were designed on the selected sections in order to specify structural solutions.

Figure 2. Location of sections for monitoring of pavement displacement in the area under study.

Table 1 presents the overview of laboratory test results for soils from the sections of operating roadways selected for monitoring.

Table 1. The results of laboratory tests of soil samples.

Number of section	Classification of soil according to Unified Soil Classification System [20]	Particle density, g/cm^3 (kN/m^3) [21]	Natural moisture content, % [21]	Plastic limit [22]	Liquid limit [22]	Plasticity index [22]	Liquidity index [23]
1	Lean clay	2.74 (26.87)	18.93	18	30	12	stiff
2	Lean clay	2.64 (25.89)	21.76	21	37	16	stiff
3	Lean clay	2.71 (26.58)	19.64	19	27	8	stiff
4	Lean clay	2.68 (26.28)	17.93	23	38	15	very stiff
5	Lean clay	2.77 (27.16)	18.95	22	37	15	stiff
6	Lean clay	2.72 (26.67)	21.38	24	32	8	very stiff
7	Lean clay	2.72 (26.67)	20.28	19	31	12	stiff
8	Lean clay	2.60 (25.50)	22.35	20	33	13	stiff
9	Lean clay	2.68 (26.28)	25.00	22	30	8	firm-stiff
10	Lean clay	2.78 (27.26)	19.80	18	35	17	stiff
11	Lean clay	2.66 (26.09)	22.19	20	32	12	stiff
12	Lean clay	2.75 (26.97)	15.96	17	31	14	very stiff
13	Lean clay	2.54 (24.91)	23.00	28	40	12	very stiff
14	Lean clay	2.65 (25.99)	24.40	18	32	14	firm-stiff

Subgrade soils of the roadway sections selected for monitoring of pavement displacement belong to lean clay [20]. The values of plastic limit vary between 17 and 28, while the values of liquid limit belong to the range from 27 to 40 (Table 1). Soil samples taken from the road sections were subjected to hydrometer grain size analysis. Fig. 3 illustrates the final grain-size distributions.

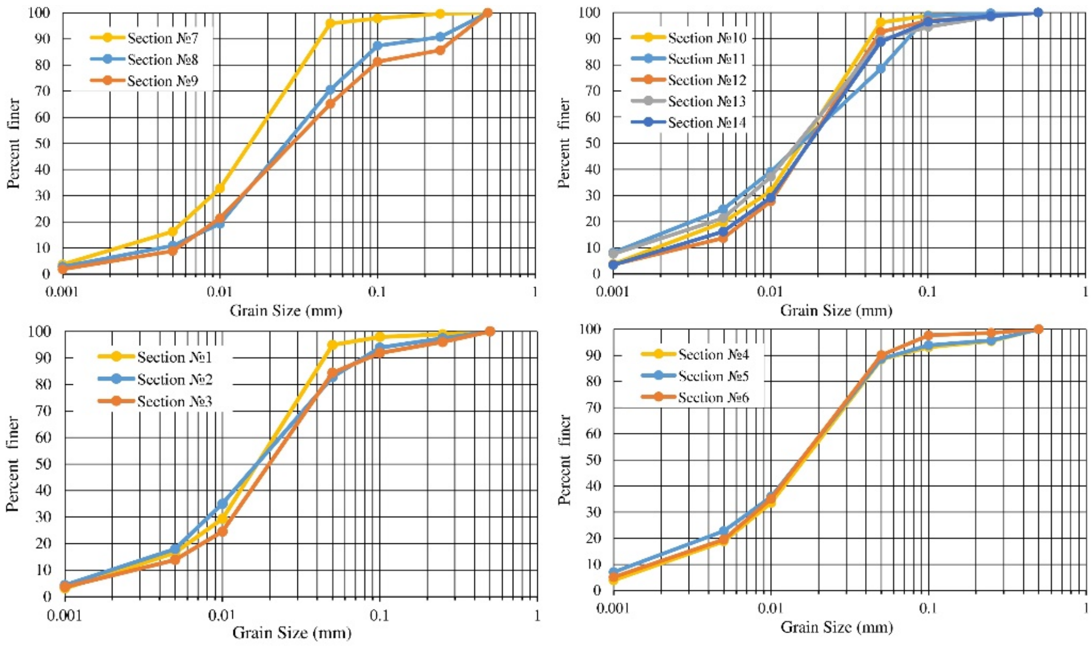

Figure 3. Grain-size distributions for the tested soils.

Normally, soils that belong to the same class and have similar grain-size composition show similar heaving properties in the same testing conditions. This observation is confirmed by the outcomes of laboratory tests performed to define the relative frost heave. The results of these tests are presented in Table 2. In laboratory conditions, relative frost heave was defined with freely supplied water in two freeze-thaw cycles at a temperature of –6 °C in the freezing chamber. The soil sample was 15.5 cm high and 10 cm in diameter [24].

Table 2. The results of laboratory tests of relative frost heave.

No. of section	Bulk density, g/cm^3	Relative frost heave
1	2.10	0.0407
2	2.11	0.0409
3	2.11	0.0403
4	2.13	0.0415
5	2.10	0.0388
6	2.14	0.0416
7	2.05	0.0389
8	2.11	0.0402
9	2.10	0.0406
10	2.10	0.0403
11	2.03	0.0389
12	2.12	0.0386
13	2.04	0.0388
14	2.10	0.0405

Note: the table contains average values out of the testing campaign. The campaign consisted of two laboratory tests of the same type of soil sampled from the subgrade of the corresponding section for pavement displacement monitoring.

The test results obtained for relative frost heave vary around the average value of 0.0400 within ±4 %. Besides, one should note the impact of the content of exchangeable cations containing ions of Ca^{2+}, Mg^{2+} and Na^{+} in montmorillonite, kaolinite and illite minerals that affect the heaving properties of clay soil. In the area under study, the total content of exchangeable cations of Ca^{2+}, Mg^{2+} in soil is ≈ 5.2 times higher than that of Na^{+} [25]. Darrow and Ross [26] estimated the impact of exchangeable cations of Ca^{2+}, Mg^{2+}, Na^{+}, K^{+} on segregation of ice lenses when cooling down the soil monolith from the Source Clay Repository (Purdue University, West Lafayette, IN) and non-uniform soil from the Copper River Basin. It is found that the soils containing illite-smectite show no variation in their heaving properties as affected by Ca^{2+} and Na^{+} cations.

For the purpose of monitoring of irregular pavement surface displacement on the selected 15 m long sections the points were fixed with impact anchors and marked. The scheme of points' location was taken from the study [27] and is presented in Fig. 4. Due to reducing the cross section from 3 to 1.5 m the number of points per section was increased from 42 to 77. Leveling of the pavement had been performed in summer before freezing of the road structure and till the end of winter season, when stable positive temperatures were set.

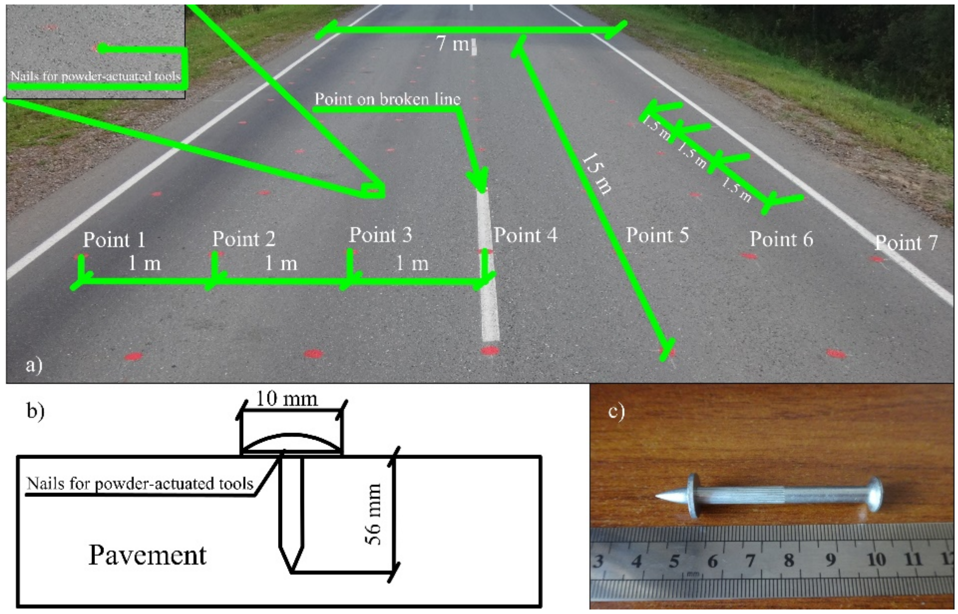

Figure 4. a) Scheme of points' location in the sections for monitoring of pavement surface displacement. b) Layout of the nail location in the pavement. c) Visual representation of the nail.

To ensure stability of marking when soil freezing and heaving occur, permanent reference markers were installed, in relation to which the points in the monitored section were leveled (Fig. 5). The permanent reference markers were covered with plastic caps to avoid moisture.

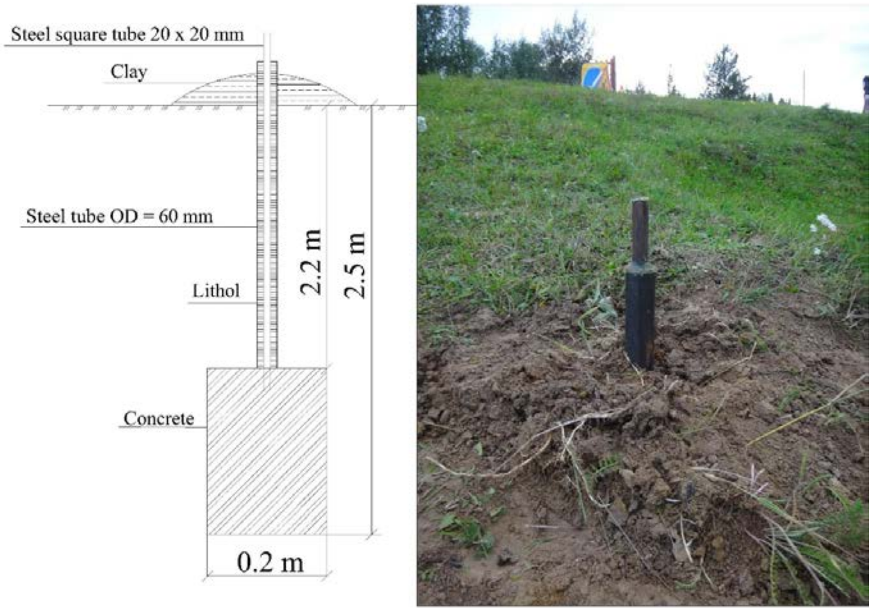

Figure 5. Permanent reference marker.

The results of surface irregular displacements analyzed in this study were obtained for 2017–2019 winter seasons. For instance, the average monthly air temperature during the winter season 2017–2018 for the sections No. 4 – 6 (south of the monitored region) was –10. 3 °C, while for the sections No. 13 – 14 (north of the monitored region) it was around –12.7 °C.

In many practical problems linear regression with a single regressor provides incomplete information on the independent variable [28, 29]. Frost heaving is affected by an array of factors, thus for building a prediction for an average roadway cross section is it preferable to use a multiple nonlinear regression model with a combination of factors. On the first stage, a nonlinear regression analysis of the vertical displacement of pavement surface points on the broken line shall be performed for the selected road sections. A database with the parameters and values under study was created using Statistica software (Fig. 6). This model includes parameters available for engineers and serves as a rather quick solution with a satisfactory accuracy of result. The analyzed database can be found in the appendix to the paper in the “Table1” tab. Average variation of point displacements is found as the mean value for 7 points on the pavement within 1 section (Fig. 4).

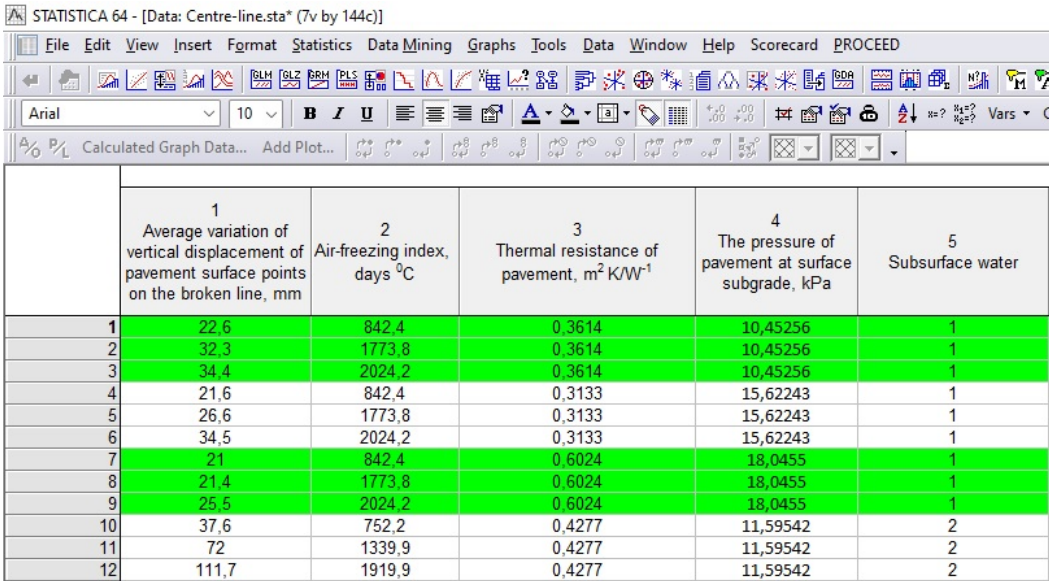

	1 Average variation of vertical displacement of pavement surface points on the broken line, mm	2 Air-freezing index, days °C	3 Thermal resistance of pavement, m² K/W⁻¹	4 The pressure of pavement at surface subgrade, kPa	5 Subsurface water
1	22,6	842,4	0,3614	10,45256	1
2	32,3	1773,8	0,3614	10,45256	1
3	34,4	2024,2	0,3614	10,45256	1
4	21,6	842,4	0,3133	15,62243	1
5	26,6	1773,8	0,3133	15,62243	1
6	34,5	2024,2	0,3133	15,62243	1
7	21	842,4	0,6024	18,0455	1
8	21,4	1773,8	0,6024	18,0455	1
9	25,5	2024,2	0,6024	18,0455	1
10	37,6	752,2	0,4277	11,59542	2
11	72	1339,9	0,4277	11,59542	2
12	111,7	1919,9	0,4277	11,59542	2

Figure 6. Statistica workspace with data for the parameters under study.

Air-freezing index (FI) is defined by the formula below [30]:

$$FI = \sum_{i=1}^{n} \overline{T}_i, \tag{1}$$

where $\overline{T}_i$ is average daily air temperature, °C.

Thermal resistance of pavement $(R_{\max})$ is calculated using the following formula [31]:

$$R_{\max} = \sum_{i=1}^{n} \frac{z_i}{\lambda_i}, \tag{2}$$

where z_i is layer thickness, λ_i is thermal conductivity of pavement layer.

The pressure of pavement on the subgrade surface (P) is defined by the formula below:

$$P = \frac{\sum_{i=1}^{n} m_i g}{S}, \tag{3}$$

where m_i is mass of the i^{th} structural layer of pavement, kg; g is gravitational acceleration, m/s²; S is area of the subgrade surface subjected to pressure of pavement, m².

The impact of subsurface water is represented by a nominal scale. Value 2 in column 4 (Fig. 6) indicates that capillary rise of subsurface water has the effect on the value of frost heaving, while value 1 indicates zero effect.

The impact of subsurface water on frost heaving is evaluated based on its possible capillary rise to the freezing front [32]:

$$h_c = \frac{C}{e \cdot D_{10}}, \tag{4}$$

where C is constant (0.1 to 0.5 cm^2), e is void ratio, D_{10} is soil particle size, 10 percent finer passing (cm).

To predict the average variation of vertical displacement of pavement surface points on the broken line, 3 nonlinear regression models were built. The process of such model generation is given below.

A standard form of a multiple nonlinear regression model [28] is as follows:

$$E\left(Y \middle| x_1,\ x_2,\ \ldots,\ x_k\right) = \alpha_0 + \beta_1 x_1 + \beta_2 x_2 + \beta_3 x_3, \tag{5}$$

where Y is average variation of vertical displacement of pavement surface points on the broken line, α_0 is intercept, x_1 is air-freezing index, x_2 is thermal resistance of pavement, x_3 is subsurface water.

The average variation of vertical displacement of pavement surface points on the broken line is a dependent variable. The matrix elements are found by using the values of the studied parameters (air-freezing index, thermal resistance of pavement, subsurface water) in the formulas 6 – 8 [28]:

$$\begin{gathered} B_1 a_{11} + B_2 a_{12} + \ldots + B_k a_{1k} = a_{1Y}, \\ B_1 a_{21} + B_2 a_{22} + \ldots + B_k a_{2k} = a_{2Y}, \end{gathered} \tag{6}$$

$$\begin{gathered} B_1 a_{k1} + B_2 a_{k2} + \ldots + B_k a_{kk} = a_{kY}, \\ a_{jj'} = \sum_j \left(x_{ij} - \bar{x}_i\right)\left(x_{j'j} - \bar{x}_{j'}\right) = a_{j'j}. \end{gathered} \tag{7}$$

$$a_{jY} = \sum_j \left(x_{ij} - \bar{x}_i\right)\left(Y_j - \bar{Y}\right). \tag{8}$$

3. Results and Discussion

Calculation of formulas 6–8 is performed automatically with Statistica software for defining the matrix elements. Estimates obtained by using the least squares method for $\alpha_0,\ \beta_1,\ \beta_2,\ \beta_3,$ as well as the model parameters are presented in Table 3.

Table 3. Regression summary for the dependent variable.

	Standardized coefficients, β^*	Standard error of β^*	Partial regression coefficients, β	Standard error of β	t (52)	p-value
intercept			–0.00057	0.612979	–0.00093	0.99
x_1	0.375560	0.068740	1.06749	0.195386	5.46348	0.0000
x_2	–0.163756	0.069773	–3.70842	1.580082	–2.34698	0.0228
x_3	0.740057	0.069768	2.66608	0.251343	10.60733	0.0000

In Table 3, student's t-test for intercept is smaller than the threshold value based on the p-value that is bigger than 0.05. Hence, the hypothesis that the intercept is insignificant is accepted, and in the model it equals to zero. In Table 4, the model parameters are given for intercept = 0.

Table 4. Regression summary for the dependent variable (intercept = 0).

	Standardized coefficients, β^*	**Standard error of β^***	**Partial regression coefficients, β**	**Standard error of β**	**t (52)**	**p-value**
x_1	0.900947	0.018198	1.06731	0.021558	49.50866	0.0000
x_2	–0.032963	0.013861	–3.70854	1.559512	–2.37801	0.0210
x_3	0.156328	0.014546	2.66606	0.248071	10.74716	0.0000

In Table 4, the p-value is smaller than 0.05, and the hypothesis of significance of the factors in the model is accepted. Next, the normal probability plot of residuals is built (Fig. 7).

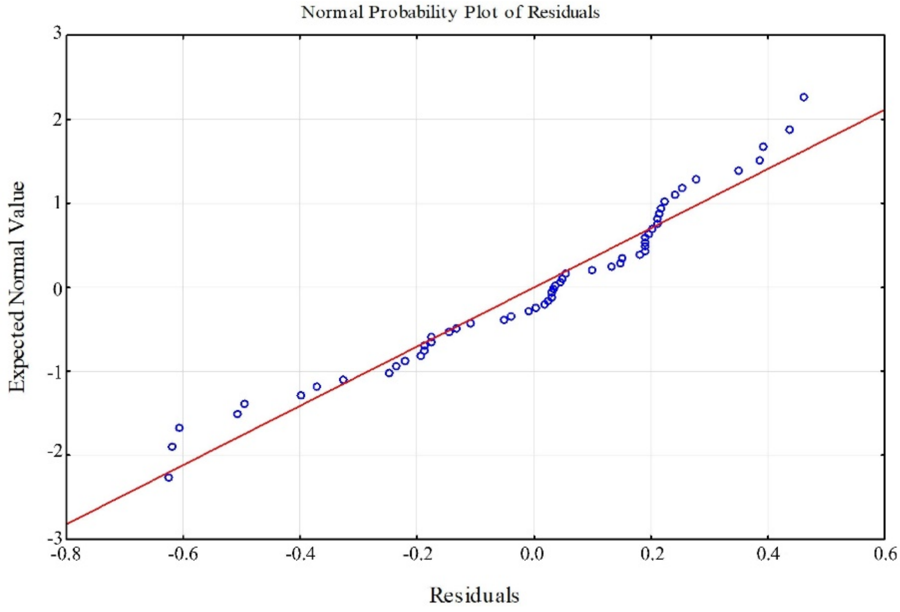

Figure 7. Normal probability plot of residuals.

On the plot (Fig. 7), no systematic deviations of actual observation data from the theoretical normal line are observed. Therefore, regression residuals follow the normal distribution. It should be defined whether there is a dependence of regression residuals on the predicted values (Fig. 8).

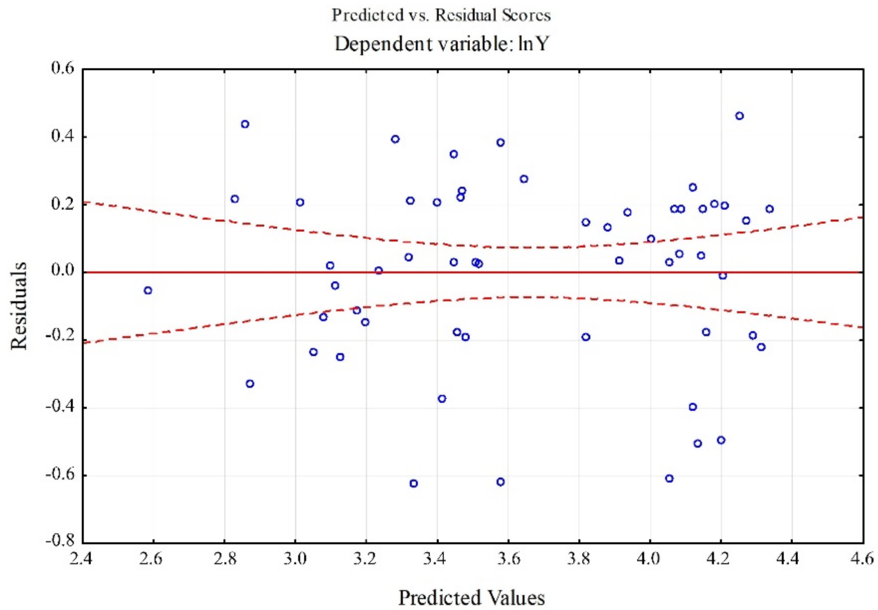

Figure 8. Plot of predicted vs. residual scores (0.95 conf. int.).

In the plot (Fig. 8), the dots are located chaotically, which means that the regression residuals are independent on the predicted values. Having fulfilled the condition of applicability of the obtained model [29], a comparison of dispersion caused by the difference between the groups with that caused by intra-class variance is presented in the following (Table 5).

Table 5. Analysis of variance.

Effect	Sums of squares	df	Mean squares	F	p-value
Regress.	760.3003	3	253.4334	3325.382	0.00
Residual	4.0392	53	0.0761		
Total	764.3395				

As seen from Table 5, the significance level for the regression model is smaller than 0.05, which indicates that the model is acceptable, and the average displacement of points on the broken line caused by frost heaving can be calculated as follows:

$$Y = \exp\left(1.06731 \cdot \log\left(FI\right) - 3.70854 \cdot R_{\max}^{5} + 2.66606 \cdot \log\left(SW\right)\right), \quad (9)$$

where Y is average variation of vertical displacement of pavement surface points on the broken line, mm; FI is air-freezing index, days °C; $R_{\max}$ is thermal resistance of pavement, m^2 K/W^{-1}; SW is the impact of subsurface water on frost heaving (2 – affects, 1 – does not affect).

As a result of statistical analysis of the data, two additional models of average variation of vertical displacement of pavement surface points on the broken line are built:

$$Y^1 = 10^{\left(1.209602 + 0.167 \cdot 10^{-3} \cdot (FI) - 0.60945 \cdot 10^{-7} \cdot P^5 + 0.496961 \cdot \ln(SW)\right)}, \quad (10)$$

where Y^1 is average variation of vertical displacement of pavement surface points on the broken line, mm; FI is air-freezing index, days °C; P is the pressure of pavement on the subgrade surface, kPa; SW is the impact of subsurface water on frost heaving (2 – affects, 1 – does not affect).

$$Y^2 = -99.8766 \cdot 40.5205 \log\left(FI\right) + 114.8265 \cdot \left(SW\right), \quad (11)$$

where Y^2 is average variation of vertical displacement of pavement surface points on the broken line, mm; FI is air-freezing index, days °C; SW is the impact of subsurface water on frost heaving (2 – affects, 1 – does not affect).

The obtained models were checked for adequacy with the use of the results of vertical displacement of pavement surface points during the winter season 2019–2020. The monitoring results for these (test) roadway sections were not included when building the above models. The test sections' parameters and geolocations are given in the "Table 3 (test)" tab of the appendix to the paper.

Fig. 9 illustrates the results of comparison between the prediction for models $\left(Y,\ Y^1,\ Y^2\right)$ and the 2019–2020 monitoring data. The detailed performance metrics for these prediction models are given in Table 6.

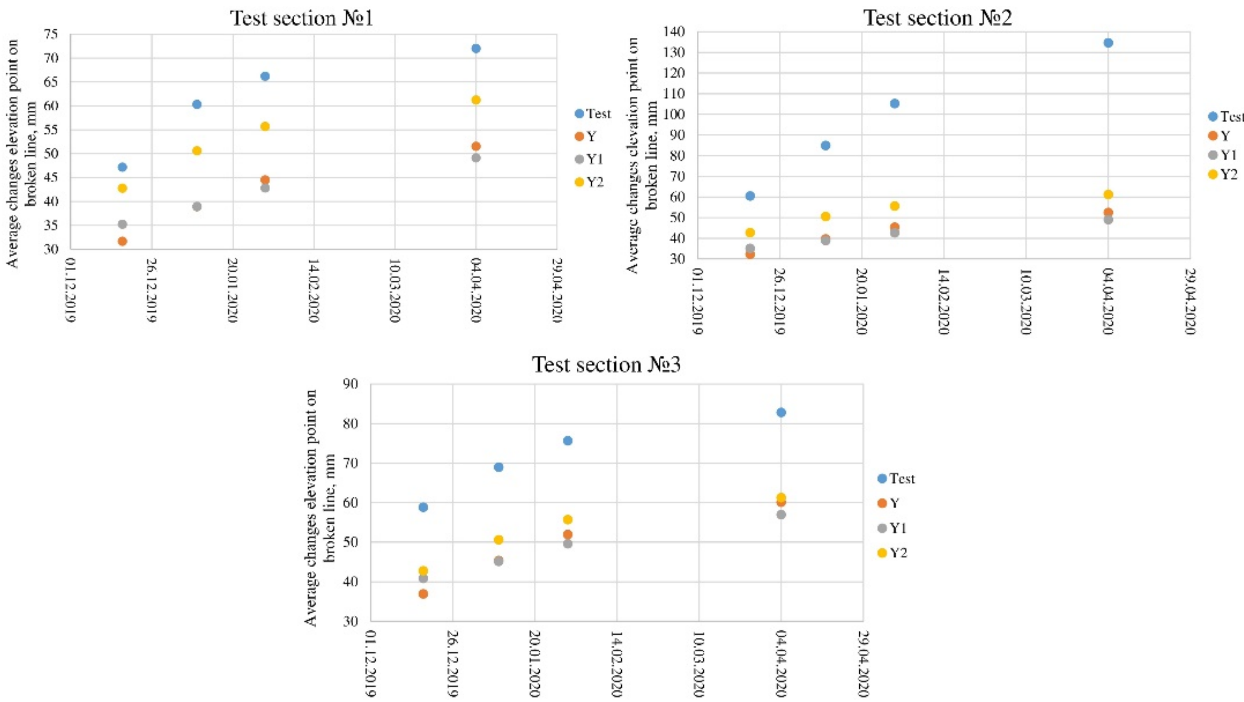

Figure 9. Results of comparison between the prediction and the monitoring data for test roadway sections.

Table 6. Performance metrics for the models of average variation of vertical displacement of pavement surface points on the broken line.

Models	Test section No. 1		Test section No. 2		Test section No. 3	
	MAE	RMSE	MAE	RMSE	MAE	RMSE
Y	19.768	19.923	53.870	57.391	23.002	23.014
Y^1	19.883	20.417	54.903	59.190	43.785	23.647
Y^2	8.835	9.202	43.785	48.344	18.992	19.101

Fig. 9 demonstrates the advantage of Y^2 alternative model. The prediction of time series of average variation of vertical displacement of pavement surface points on the broken line was performed for 3 test sections (Table 6) for which the measured data on pavement vertical displacement were obtained. MAE and RMSE are calculated as follows:

$$MAE = \frac{\left|\left(y_i - y_p\right)\right|}{n}, \quad (12)$$

$$RMSE = \sqrt{\frac{\sum\left(y_i - y_p\right)}{n}}, \quad (13)$$

where y_i is actual value; y_p is predicted value; n is number of observations.

In the meantime, MAE and $RMSE$ metrics of Y^2 model in all cases are found to be lower than those of the models Y and Y^1. Reduction of model factors had a positive effect. However, all three models showed unsatisfactory results for the test section No. 2. This can be explained either by an insufficient amount of monitoring data for the sections with close subsurface water occurrence, or by the fact that SW factor had its strong impact on the regression model coefficient calculation. It may be worth splitting the SW factor for close occurrence of subsurface water into levels as it approaches the pavement bottom, which is highlighted in the studies by Dahu [30] and Wang [31]. The value of subsurface water occurrence level for the test section No. 2 was the closest to the pavement bottom and was approximately equal to 180 cm. The general trend line of displacement of test section points coincides with the predicted model values with some error.

Based on the average vertical displacement of pavement surface points on the broken line caused by frost heaving let us define the relation of displacement of other points of the roadway cross section (points 1 – 6, Fig. 4). For that purpose, a database of the studied parameters was created (Fig. 10).

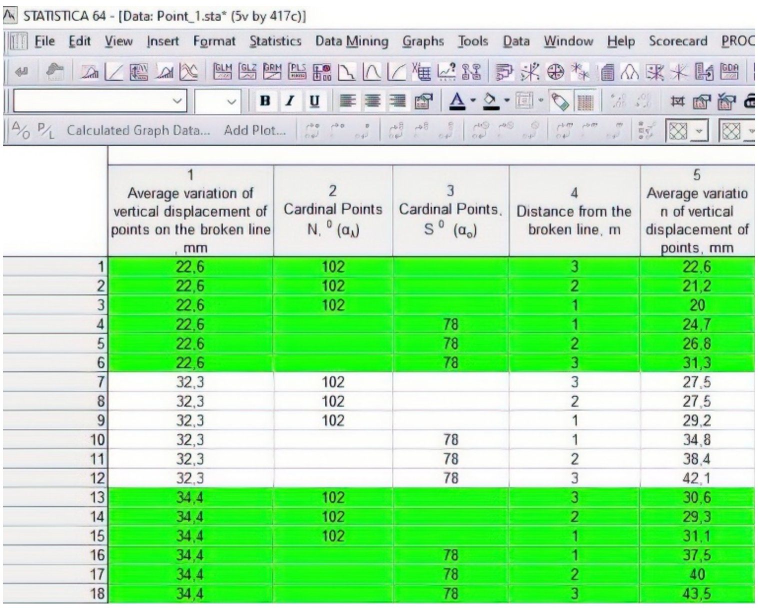

	1 Average variation of vertical displacement of points on the broken line, mm	2 Cardinal Points N, ⁰ (αN)	3 Cardinal Points, S ⁰ (αS)	4 Distance from the broken line, m	5 Average variation of vertical displacement of points, mm
1	22,6	102		3	22,6
2	22,6	102		2	21,2
3	22,6	102		1	20
4	22,6		78	1	24,7
5	22,6		78	2	26,8
6	22,6		78	3	31,3
7	32,3	102		3	27,5
8	32,3	102		2	27,5
9	32,3	102		1	29,2
10	32,3		78	1	34,8
11	32,3		78	2	38,4
12	32,3		78	3	42,1
13	34,4	102		3	30,6
14	34,4	102		2	29,3
15	34,4	102		1	31,1
16	34,4		78	1	37,5
17	34,4		78	2	40
18	34,4		78	3	43,5

Figure 10. Statistica workspace with the data for the parameters under study (for points 1 – 6, Fig. 4).

Right and left sides of the roadway cross section are defined in the direction of travel from West to East. Angles α_l and α_r are measured in degrees clockwise between the North direction and the centerline of the road for the left side of the roadway cross section, and counterclockwise between the South direction and the centerline of the road for the right side. The scheme of setting cardinal points for the Northern Hemisphere is given in Fig. 11.

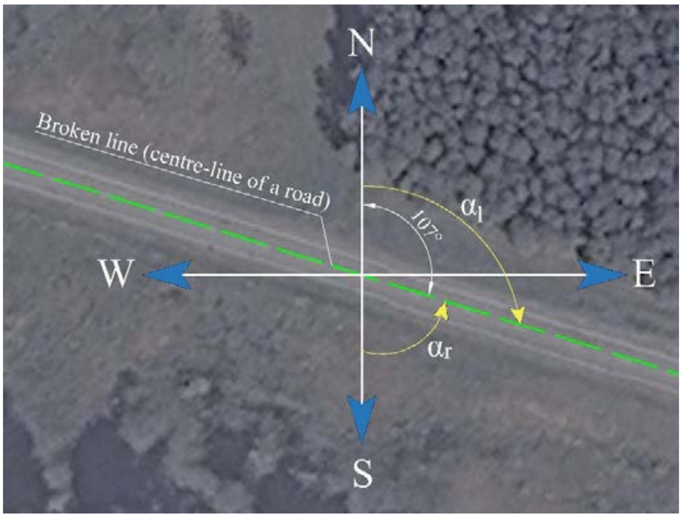

Figure 11. The scheme of setting cardinal points for the Northern Hemisphere.

The model parameters of the points displacement caused by frost heaving are given in Table 7 – for the left roadway cross section, and in Table 8 – for the right roadway cross section.

Table 7. Regression summary for the dependent variable (left roadway cross section).

	Standardized coefficients, β^*	**Standard error of β^***	**Partial regression coefficients, β**	**Standard error of β**	***t* (164)**	**p-value**
intercept			–3.73374	1.194798	–3.12500	0.002103
Y	0.973793	0.014314	1.00698	0.014801	68.03256	0.000000
Distance from the broken line	0.061105	0.014165	1.80357	0.418091	4.31383	0.000028
Cardinal point, α_l	0.046246	0.014314	0.00016	0.000049	3.23091	0.001491

Table 8. Regression summary for the dependent variable (right roadway cross section).

	Standardized coefficients, β^*	**Standard error of β^***	**Partial regression coefficients, β**	**Standard error of β**	***t* (164)**	**p-value**
Y	1.276508	0.033510	89.874	2.35930	38.09377	0.000000
Distance from the broken line	–0.299438	0.034991	–483.060	56.44889	–8.55747	0.000000
Cardinal point, α_r	–0.129914	0.027476	–0.043	0.00920	–4.72830	0.000005

In Table 7 and Table 8, the p-value is smaller than 0.05, which supports the hypothesis of significance of factors in the model of roadway cross section points displacement under the action of frost heaving. When performing statistical analysis of the model of points displacement for the right roadway cross section, the parameter of intercept was assumed equal to zero. Table 8 presents the results with intercept = 0.

The results of the analysis of variance (ANOVA) for the displacement model for the left and right roadway cross sections are given in Table 9 and Table 10, respectively.

Table 9. Analysis of variance (left roadway cross section).

Effect	**Sums of squares**	***df***	**Mean squares**	***F***	**p-value**
Regress.	94362.62	3	31454.21	1606.644	0.00
Residual	3210.72	164	19.58		
Total	97573.34				

Table 10. Analysis of variance (right roadway cross section).

Effect	Sums of squares	*df*	Mean squares	*F*	p-value
Regress.	1.921838E+09	3	640612566	891.9153	0.00
Residual	1.185102E+08	166	718244		
Total	2.040348E+09				

In Table 9 and Table 10, the F-test for the models of vertical displacement of pavement surface points is higher than the table values for 0.05 significance level considering the p-value parameter. Therefore, the hypothesis of factor significance is accepted and the vertical displacement of roadway cross section points can be calculated as follows:

$$Y_1 = -3.73374 + 1.00698 \cdot Y + 1.80357 \cdot 1 + 0.00016 \cdot CP^2, \tag{14}$$

$$Y_r = \sqrt{89.874 \cdot Y - 483.060 \cdot 1 - 0.043 \cdot CP^2}, \tag{15}$$

where Y_l, Y_r are average variations of displacement of points (left and right sides of the roadway cross section), mm; Y is average variation of displacement of points on the broken line, mm; l is distance from the broken line, m; CP is cardinal points, deg.

Fig. 12 presents the comparison of results for the (Y_l, Y_r) model prediction and the 2019–2020 monitoring data. The dataset for the adequacy check for the regression model is given in the appendix to the paper in the "Table 3 (test)" tab. Detailed performance metrics for these prediction models for the test set are compiled in Table 11.

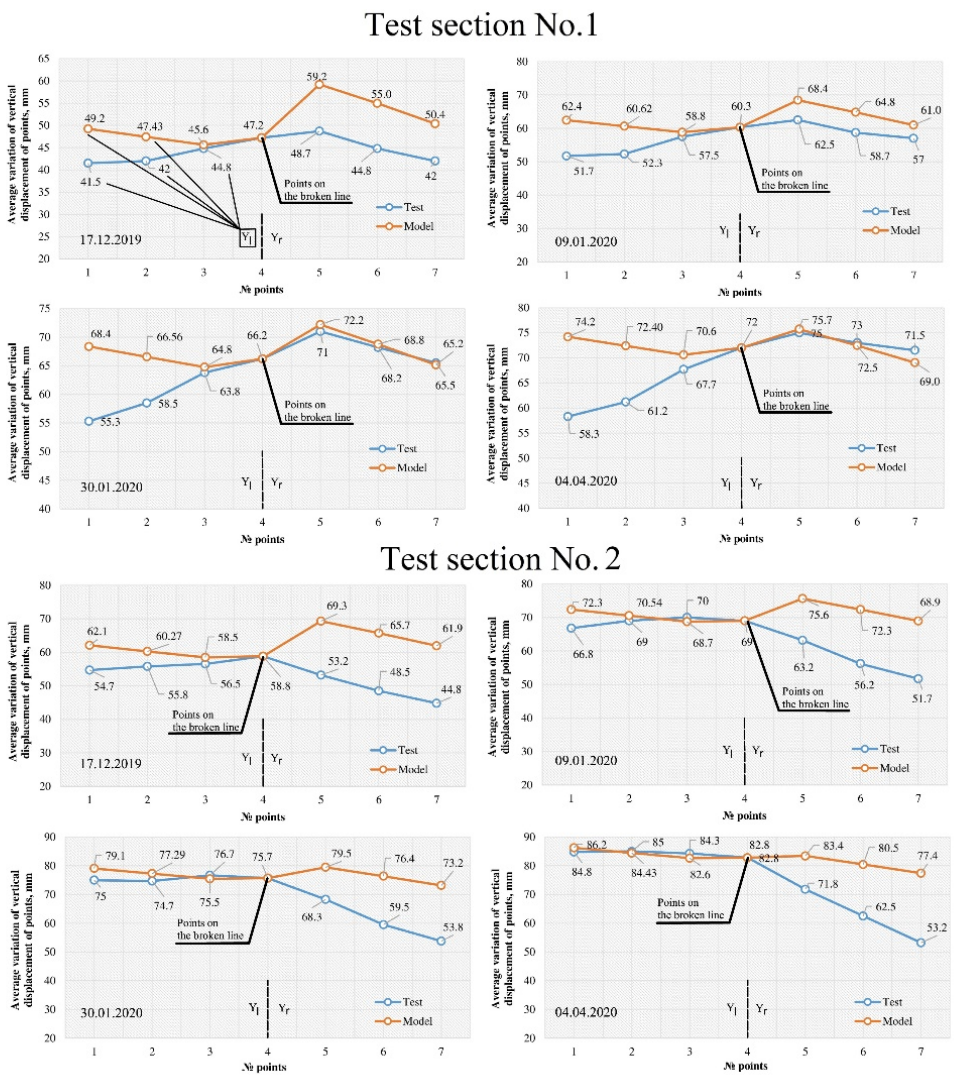

Figure 12. Comparison of the results for the (Y_l, Y_r) model prediction and the monitoring data for test sections (point №4 is located on the broken line).

Table 11. Performance metrics for the models $(Y_l,\ Y_r)$**.**

Models	**Test sections No. 1, 3**	
	MAE	RMSE
Y_l	5.007	5.591
Y_l	Predicted Y	The residual
	43.2	–1.7
	41.3	0.7
	39.3	5.5
	57.4	–5.7
	55.5	–3.2
	53.5	4.0
	63.8	–8.5
	61.9	–3.4
	59.9	3.9
	70.1	–11.8
	68.2	–7.0
	66.2	1.5
	57.0	–2.3
	55.1	0.7
	53.2	3.3
	68.1	–1.3
	66.2	2.8
	64.2	5.8
	75.4	–0.4
	73.4	1.3
	71.5	5.2
	83.1	1.7
	81.1	3.9
	79.2	5.1
	MAE	RMSE
Y_r	10.345	12.533
Y_r	Predicted Y	The residual
	43.2	–1.7
	41.3	0.7
	39.3	5.5
	57.4	–5.7
	55.5	–3.2
	53.5	4.0
	63.8	–8.5
	61.9	–3.4
	59.9	3.9
	70.1	–11.8
	68.2	–7.0
	66.2	1.5
	57.0	–2.3
	55.1	0.7
	53.2	3.3
	68.1	–1.3
	66.2	2.8
	64.2	5.8
	75.4	–0.4
	73.4	1.3
	71.5	5.2
	83.1	1.7
	81.1	3.9
	79.2	5.1

In Fig. 12, the displacement prediction for points 1–3 is carried out by the Y_l model, and the Y_r model is used for points 5 – 7. Point 4 denotes the point on the broken line, and the value of its displacement was set based on the monitoring data. According to Fig. 12, for the test section No. 1 the predicted values for the left part of the pavement surface cross section are higher than those obtained in the process of monitoring. The same pattern is observed for the right part of the pavement cross section of the test section No. 3. This part and the left part of the section No. 1 are located in the embankment and have approximately the same moisture conditions. Also, it shall be taken into account that the right part of the cross section of the test section No. 1 is located in the open cutting. The left part of the test section No. 3 has additional inflow of moisture from the swampy side. Consequently, the models $\left(Y_l,\ Y_r\right)$ fit well for predicting mean displacement of pavement surface points in crosswise direction with moisture inflow. Table 11 demonstrates good convergence of the models $\left(Y_l,\ Y_r\right)$. To increase their efficiency it is suggested to differentiate between the moisture conditions of the roadway cross section (whether there is a moisture inflow to the freezing front). The left and the right parts of the roadway cross section may differ with respect to the conditions of moisture inflow to the freezing front. This shall be noted when designing roads on rough terrain.

After performing calculations of the equation 11 first, and then of the equations 14–15, the values of average vertical displacement of the roadway cross section under the action of frost heaving can be obtained. The risk of defects that may occur on the road pavement under irregular vertical displacement, the values of which were obtained after calculation of equations 11, 14–15, can be evaluated using the [32] mathematical model or specified software based on the final element method (FEM).

4. Conclusions

The models of irregular vertical displacement of pavement surface points, which were based on a thorough mathematical analysis, were found to be able to design an average pavement cross section of 15 m. When evaluating performance of the regression model of displacement of points on the broken line, an increase in the model accuracy was observed with a reduction of the number of factors. The best-performing RMSE value of the regression model $\left(Y^2\right)$ for prediction of mean displacement of points on the broken line was around 30 % when averaged over the test sections. The regression model of displacement of points on the broken line has satisfactory accuracy and requires further monitoring for its calibration. It is worth noting that the displacement trend for the three regression models $\left(Y,\ Y^1,\ Y^2\right)$ quite accurately accounts for the variation of displacement of pavement surface points in time with varying factors. In order to refine the prediction of mean displacements of pavement surface on the broken line caused by frost heave, the SW factor might be transformed from the nominal scale to the ordinal one. The SW factor has a significant impact on the prediction of irregular displacement of pavement surface points. Thus, when making a prediction of mean displacements of the pavement surface, one should refer to the least favorable conditions for the road section in question. The factors of the model of pavement displacement caused by frost heaving can be easily calculated by design engineers without additional complex and expensive tests. Good convergence was demonstrated by the models $\left(Y_l,\ Y_r\right)$ of mean irregular displacements of pavement surface points in crosswise direction for the sections where moisture migration to the freezing front is observed. The consideration of the angle of the roadway position relative to the North and South for predicting mean displacement of pavement surface points had a positive impact. Regression models of mean pavement displacements can be applied for evaluating frost resistance of pavement with asphalt concrete layers. This approach enables consideration of the solution to the issue of subgrade frost heave from top to bottom. Having defined the value of pavement surface points displacement one can assume what amount of ice the roadway subgrade clay contains. The model is applicable to evaluate evenness of road pavement affected by frost heave.

The model is based on empirical results, which can limit its applicability for different pavement freezing conditions. Another limitation of the model is a pavement width of 8 meters. To make predictions for wider sections, similar research is required to calibrate the model. The suggested model is not applicable for predicting average irregular vertical displacements occurring in sand-clay soils, where freezing and heaving processes differ from those in clay soils.

5. Data Availability

Some or all data, models, or code that support the findings of this study are available from the corresponding author upon reasonable request.

Churilin, V.S. 2021. "Data of irregular vertical displacement of a roadway cross section caused by frost heaving" Harvard Dataverse Accessed September 14, 2021. https://doi.org/10.7910/DVN/DBZ92O

References

1. Kottek, M., Grieser, J., Beck, C., Rudolf, B., Rubel, F. World Map of Köppen-Geiger Climate Classification updated. Meteorologische Zeitschrift. 2006. 15. Pp. 259–263. DOI: 10.1127/0941-2948/2006/0130
2. Jin, H., Wei, Z., Wang, S., Yu, Q., Lu, L., Wu, Q., Ji, Y. Assessment of frozen-ground conditions for engineering geology along the Qinghai–Tibet highway and railway, China. Engineering Geology. 2008. DOI: 10.1016/j.enggeo.2008.04.001
3. Dagli, D. Laboratory investigations of frost action mechanisms in soils. Diss. Luleå Tekniska Universitet, 2017.
4. Ivanov, K.S. Granulated foam-glass ceramics for ground protection against freezing. Magazine of Civil Engineering. 2018. 79(3). Pp. 95–102. DOI: 10.18720/MCE.79.10
5. Taber, S. The mechanics of frost heaving. The Journal of Geology. 1930. 38(4). Pp. 307–317. DOI: 10.1086/623720
6. Beskow, G. Soil freezing and frost heaving, with special application to roads and railroads. Swedish Geological Society, Series C (375). (translated by J.O. Osterberg). Historical Perspectives in Frost Heave Research. 1935. Pp. 41–157 CRREL. Special Report. Pp. 91–23.
7. Tsytovich, N. Osnovaniya i fundamenty na merzlykh gruntakh [Bases and foundations on frozen soil]. National Academy of Sciences, National Research Council, 1958. 168 p. (rus)
8. Feng, R., Wu, L., Wang, B. Numerical Simulation for Temperature Field and Salt Heave Influential Depth Estimation in Sulfate Saline Soil Highway Foundations. International Journal of Geomechanics. 2020. 20(10). DOI: 10.1061/(ASCE)GM.1943-5622.0001843
9. Zhang, X., Zhai, E., Wu, Y., Sun, D., Lu, Y. Theoretical and Numerical Analyses on Hydro–Thermal–Salt–Mechanical Interaction of Unsaturated Salinized Soil Subjected to Typical Unidirectional Freezing Process. International Journal of Geomechanics. 2021. 21(7). DOI: 10.1061/(ASCE)GM.1943-5622.0002036
10. Black, P.B., Hardenberg, M.J. Historical Perspectives in Frost Heave Research The Early Works of S. Taber and G. Beskow. Hanover. New Hampshire: U.S. Army Corps of Engineers Cold Regions Research & Engineering Laboratory, 1991. 167 p.
11. Puzakov, N. Vodno-teplovoy rezhim gruntovogo pokrytiya avtomobil'nykh dorog [Water and heat regime of road subgrade]. Moscow: Avtotransizdat, 1958. 168 p. (rus)
12. Penner, E. The importance of freezing rate in frost action in soils. Proceedings of the American Society for Testing and Materials. 1960. 60. Pp. 1151–1165.
13. O'Neill, K., Miller, R.D. Explorations of a rigid ice model of frost heave. Water Resour. Res. 1985. 21(3). Pp. 281–296. DOI: 10.1029/WR021i003p00281
14. Liu, Z., Yu, X. Coupled thermo-hydro-mechanical model for porous materials under frost action: theory and implementation. Acta Geotechnica. 2011. DOI: 10.1007/s11440-011-0135-6
15. Hao, Z., Shunji, K., Fujun, N., Anyuan, L. Three-dimensional frost heave evaluation based on practical Takashi's equation. Cold Regions Science and Technology. 2015. 118. Pp. 30–37. DOI: 10.1016/j.coldregions.2015.06.010
16. Teng, J., Liu, J., Zhang, S., Sheng, D. Modelling frost heave in unsaturated coarse-grained soils. Acta Geotechnica. 2020. 15. Pp. 3307–3320. DOI: 10.1007/s11440-020-00956-2
17. Huang, S., Lu, Z., Ye, Z., Xin, Z. An elastoplastic model of frost deformation for the porous rock under freeze-thaw. Engineering Geology. 2020. 278. 105820. DOI: 10.1016/j.enggeo.2020.105820
18. Jing, C., Anyuan. L., Chunyan, B., Yanhua, D., Minghao, L., Zhanju, L., Fujun, N., Tianxiang, Z. A deep learning forecasting method for frost heave deformation of high-speed railway subgrade. Cold Regions Science and Technology. 2021. 185. 103265. DOI: 10.1016/j.coldregions.2021.103265
19. Efimenko, V.N., Efimenko, S.V., Teltaev, B.B., Sukhorukov, A.V. On the need for differentiated account of properties of the geocomplex of territories in pavements design. News of the Academy of sciences of the Republic of Kazakhstan Satbayev University. Series of Geology and Technical Sciences. 2020. 2(440). Pp. 72–80. DOI: 10.32014/2020.2518-170X.33
20. ASTM D 2487 – 17 Standard Practice for Classification of Soils for Engineering Purposes (Unified Soil Classification System).
21. Interstate Standard GOST 5180 – 2015 Soils. Laboratory methods for determination of physical characteristics. 2016. 19 p.
22. ISO/TS 17892 – 12:2018 Geotechnical investigation and testing – Laboratory testing of soil – Part 12: Determination of liquid and plastic limits.
23. ISO 14688-2:2017 Geotechnical investigation and testing – Identification and classification of soil – Part 2: Principles for a classification.
24. GOST 28622 – 2012 Soils. Laboratory method for determination of frost-heave degree.
25. Efimenko, V.N., Vilisov, V.P., 1983. "Analiz prichin razrusheniya nezhyostkih dorozhnyh odezhd v usloviyah Zapadnoj Sibiri [Analysis of destruction of non-rigid pavements in West Siberia]." Racional'nye metody stroitel'stva i ehkspluatacii avtomobil'nyh dorog v usloviyah Sibiri. Tomsk. TSU Publ. Pp. 41–45. (rus)
26. Darrow, M.M., Ross, M.L. Visualizing cation treatment effects on frozen clay soils through µCT scanning. Cold Regions Science and Technology. 2020. 175. 103085. DOI: 10.1016/j.coldregions.2020.103085
27. Preferansova, L.A., Troitskaya, M.N., Bel'kovskij, S.V. Proektirovanie gruntovyh osnovanij usovershenstvovannyh pokrytij s uchjotom ih raboty v zimnih uslovijah [Design of soil bases for improved coatings, taking into account their work in winter conditions]. 1953. 113 p. (rus)
28. Johnson, N.L., Leone, F.C. Statistics and experimental design in engineering and the physical sciences. New York: Wiley, 1964. 534 p.

29. StatSoft, Inc. Electronic Statistics Textbook. Tulsa, OK: StatSoft. 2011. [Online] URL: http://www.statsoft.com/textbook (reference date: 06.11.2022)
30. Calculation Methods for Determination of Depths of Freeze and Thaw Soils – Emergency Construction. Department of the Air Force. Manual AFM 88-40. Chapter 46. Washington, D.C.
31. Stenberg, L. Design of frost protection in roads. Linköping: Statens Väg- och Trafikinstitut., VTI notat V 223. 1993.
32. Oman, M.S., Neil G.L., Braun, I. Designing base and subbase to resist environmental effects on pavements. No. MN/RC 2018-06. Minnesota. Dept. of Transportation. Research Services & Library. 2018.
33. Dahu, R., Jinbang, Z., Guoyu, L., Jun, Z., Teruyuki, S. Field experimental study of the characteristics of heat and water transfer during frost heaving. Cold Regions Science and Technology. 2019. 168. 102892. DOI: 10.1016/j.coldregions.2019.102892
34. Wang, T., Liu, Y., Wang, J., Wang, D. Assessment of spatial variability of hydraulic conductivity of seasonally frozen ground in Northeast China. Engineering Geology. 2020. 274. 105741. DOI: 10.1016/j.enggeo.2020.105741
35. Churilin, V., Efimenko, S., Matvienko, O., Bazuev, V. Simulation of stresses in asphalt-concrete pavement with frost heaving. MATEC Web of Conferences. 2018. 216. 01011. DOI: 10.1051/matecconf/201821601011

Information about authors:

Vladimir Churilin, *PhD in Technical Sciences*
ORCID: https://orcid.org/0000-0002-8898-4766
E-mail: lex-16-2008@mail.ru

Oleg Matvienko, *Doctor of Physical and Mathematical Sciences*
E-mail: matvolegv@mail.ru

Vladimir Efimenko, *Doctor of Technical Sciences*
E-mail: svefimenko80@gmail.com

Sergei Efimenko, *Doctor of Technical Sciences*
E-mail: svefimenko_80@mail.ru

Received 06.11.2022. Approved after reviewing 09.01.2023. Accepted 15.01.2023.

Magazine of Civil Engineering

ISSN 2712-8172

journal homepage: http://engstroy.spbstu.ru/

Research article

UDC 539.3

DOI: 10.34910/MCE.120.10

Parametric oscillations of a viscous-elastic orthotropic shell of variable thickness

***D.A. Khodzhaev*[1] ✉ *R.A. Abdikarimov*[2], *M. Amabili*[3], *B.A. Normuminov*[1]**

[1] *Tashkent Institute of Irrigation and Agricultural Mechanization Engineers National Research University, Tashkent, Uzbekistan*
[2] *Tashkent Institute of Architecture and Civil Engineering, Tashkent, Uzbekistan*
[3] *McGill University, Montreal, Canada*

✉ *dhodjaev@mail.ru*

Keywords: thin walled shell, viscoelasticity, composite materials, variable thickness, nonlinear vibrations, dynamic stability, Galerkin method, numerical method

Abstract. A solution to the problem of parametric oscillations of a viscous-elastic orthotropic shallow shell of variable thickness is presented. Dynamic loading acts along one side of the shell in the form of a periodic load. Unlike linear problems, the nonlinear problem under consideration could not be solved by applying analytical methods; therefore, approximate methods were used. The mathematical model of the problem is built within the Kirchhoff-Love theory. In this case, tangential inertial forces and geometric non-linearity are taken into account. Deflection and displacements approximation is performed using the Galerkin method in higher order approximations, which allows reducing the problem solution to a system of nonlinear integro-differential equations (IDE) with variable coefficients. The weakly singular Koltunov-Rzhanitsyn kernel with three rheological parameters is used as the relaxation kernel; it describes the viscous-elastic properties of the shallow shell. A numerical method based on the use of quadrature formulas is used to obtain a resolving system of equations for the problem. To obtain numerical results, a computer software was compiled in the Delphi environment for a computational algorithm of the problem solution. The effects of viscous-elastic, orthotropic, nonlinear properties of the shell material, thickness variability, and other physical, mechanical, and geometrical parameters on the dynamic strength of a shallow shell are studied.

Citation: Khodzhaev, D.A., Abdikarimov, R.A., Amabili, M., Normuminov, B.A. Parametric vibrations of a viscoelastic orthotropic shell of variable thickness. Magazine of Civil Engineering. 2023. 120(4). Article no. 12010. DOI: 10.34910/MCE.120.10

1. Introduction

The problem of parametric oscillations of elastic and viscous-elastic thin-wall structures (plates and shells of variable thickness) is one of the most relevant problems in the mechanics of a deformable rigid body. The solution to such problems is of great importance for the modern aerospace industry, rocket technology, and mechanical engineering. Structural elements (plates and shells of variable thickness) can be found in many engineering and building structures, in aviation and motor transport, and in various units.

The first studies devoted to the problem of parametric oscillations of plates and shells of constant thickness, within the framework of the theory of thin plates, include the research work by V.V. Bolotin [1]. To solve problems, he used methods based on the variational approach.

There are a great number of articles in the literature devoted mainly to the dynamic stability and parametric oscillations of elastic thin-wall structures (plates, panels, and shells) under the impact of periodic load.

An analysis of the study of oscillation problems of shells made of various materials, conducted in the period from 2003 to 2013, can be found in [2], [3]. It also contains a review of publications related to parametric oscillations.

Analytical and numerical solutions for different types of structures (plates and shells) were considered in [4].

In [5], the dynamic stability of truncated-conical shells under dynamic axial load was studied. To solve the problem, described by a differential equation of the Mathieu-Hill type, the Galerkin method was used.

Reference [6] is devoted to the dynamic stability of a linearly elastic thin rectangular plate subjected to a bi-axial time-varying load. The differential equation of plate motion was solved using the finite difference method (FDM). To identify domains of dynamic stability, the Mathieu-Hill equation was derived.

The dynamic stability of a viscous-elastic rectangular plate subjected to constant and variable loads in the plane of the plate was considered in [7]. The equation of motion is described by an integro-differential equation with respect to an unknown time function. The effect of the viscous-elastic characteristics of material on the dynamic instability zone was shown.

Reference [8] considers the dynamic instability of laminated non-homogeneous orthotropic truncated-conical shells under periodic axial loading. The problem was reduced to solving the Mathieu equation. Bolotin's method was used to evaluate the behavior of the shell for various parameters.

The dynamic instability of layered composite panels of variable stiffness under non-uniform periodic excitation was studied in [9]. The Ritz method was used to obtain the resolving system of equations for the problem. The domains of dynamic instability were constructed by the Bolotin method.

In [10], the behavior of a footbridge under rhythmic loading was studied. The footbridge was considered a shell of variable thickness. The problem was solved by the FEM. The influence of different mass distributions along the footbridge on its dynamic behavior was analyzed.

In [11], the dynamic stability of a cylindrical shell with linear variable thickness was considered under axial forces and pulsed external pressure. The Bubnov–Galerkin method was used to solve the problem. A resolving system of equations for the problem was derived in the form of an infinite system of homogeneous algebraic equations.

In [12], the dynamic instability of toroidal shells was studied. The Galerkin method was used to obtain a semi-analytical solution to the problem. The results obtained were compared with the ones available in the literature. The effect of various geometric and mechanical parameters on the dynamic instability of shells was studied.

A study of the nonlinear dynamic stability of a cylindrical shell of variable thickness is given in [13]. The equation of motion was derived based on the classical theory of shells in a geometric non-linear formulation. The solution to the equation was obtained by the fourth-order Runge-Kutta method and the Galerkin method. The effect of the characteristics of material and geometrical parameters on the dynamic behavior of a shell was investigated.

In [14], the impact behavior of an elastic spherical shell under step pressure was considered. Initial geometric imperfections were introduced.

The study in [15] concerns the analysis of the nonlinear dynamic behavior and stability of heterogeneous axisymmetric shells of variable thickness. The equation of motion was constructed based on the Kirchhoff–Love hypothesis. The Ritz method was used.

In [16], the dynamic behavior of a three-layer (sandwich) conical shell under the action of a periodic load was studied. At that, various boundary conditions were considered. The problem was reduced to solving an equation of the Mathieu-Hill type, the solution of which was obtained by the Bolotin method. The results obtained were compared with the results obtained by other authors.

The behavior of a sandwich plate under periodic load was considered in [17]. Using the constructed mathematical model of the problem, the effect of various geometric and mechanical parameters of a plate on its dynamic behavior was studied.

The study in [18] is devoted to the dynamic instability of a cylindrical shell made of a thin-walled composite material. The ABAQUS program was used. The influence of the parameters of periodic loading and initial geometric imperfections on the dynamic behavior of the shell was investigated.

In [19], the dynamic stability of sandwich panels under periodic load was considered. The solution to the problem was obtained by reducing the obtained equation of motion to an equation of the Mathieu type and applying the Bolotin method. The effect of different geometric and mechanical parameters of panels on their dynamic behavior was studied.

Reference [20] is devoted to the study of the dynamic stability of cylindrical composite shells under the action of a pulsed loading. The FEM was used with the ABAQUS program. The impact of different parameters on the dynamic behavior of the shell was shown.

In [21], an annular plate under external harmonic excitation was studied. Resolving equations were derived based on the non-linear von Karman theory. New mechanical effects were observed.

A brief analysis of the available scientific publications showed that there are almost no studies of nonlinear oscillations and dynamic stability of thin-wall structures (viscous-elastic plates and shells of variable thickness) [22]–[24]. In the article below, nonlinear parametric oscillations of viscous-elastic shallow shells of variable thickness are numerically studied.

The object of the research is various viscous-elastic thin-wall constructions of variable thickness.

The purpose of the study is to develop effective methods, algorithms and a computer program to evaluate the dynamic behavior of thin-wall constructions, taking into account the viscoelasticity of the material properties and variable thickness.

The following problems were solved to achieve this goal:

– to obtain resolving systems of nonlinear integro-differential equations with singular kernels of viscous-elastic thin-wall constructions of variable thickness under the impact of periodical loads;
– to develop an effective approach to numerical solution, computational algorithm and software products for evaluating the strength of viscous-elastic thin-wall constructions of variable thickness under periodical influences.

2. Methods

A rectangular viscous-elastic shallow shell of variable thickness $h(x,y)$ is considered with an account fort the geometric nonlinearity based on the Kirchhoff-Love hypotheses. Let the shell be dynamically loaded along side a by a periodic load $P(t)=P_0+P_1\cos(\Theta t)$, $P_0,P_1=const,\Theta$ - is the frequency of external periodic load (Fig.1). A coordinate lines x and y of the curvilinear orthogonal coordinate frame is directed along the lines of principal curvatures, and the z-axis - along the internal normal of the middle surface.

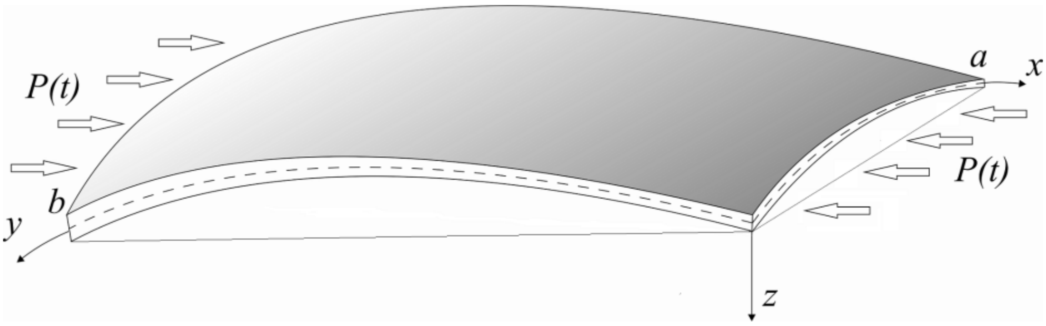

Figure 1. Shallow shell of variable thickness.

The system of equations of motion in the framework of the chosen theory has the following form [25]

$$\frac{\partial N_x}{\partial x}+\frac{\partial N_{xy}}{\partial y}+p_x-\rho h\frac{\partial^2 u}{\partial t^2}=0,\quad \frac{\partial N_{xy}}{\partial x}+\frac{\partial N_y}{\partial y}+p_y-\rho h\frac{\partial^2 v}{\partial t^2}=0,$$

$$\frac{\partial^2 M_x}{\partial x^2}+\frac{\partial^2 M_y}{\partial y^2}+2\frac{\partial^2 H}{\partial x\partial y}+k_xN_x+k_yN_y+\frac{\partial}{\partial x}\left(N_x\frac{\partial w}{\partial x}+N_{xy}\frac{\partial w}{\partial y}\right)+ \tag{1}$$

$$+\frac{\partial}{\partial y}\left(N_{xy}\frac{\partial w}{\partial x}+N_y\frac{\partial w}{\partial y}\right)+P(t)\frac{\partial^2 w}{\partial x^2}+q-\rho h\frac{\partial^2 w}{\partial t^2}=0,$$

where $k_x = 1/R_1$ and $k_y = 1/R_2$ are the principal curvatures (R_1 and R_2 are the principal radii of curvature) of the shell along the x and y axes, respectively; p_x, p_y and q - external static loads applied to the shell element in directions x, y and z.

The system of equations (1) is supplemented by the corresponding boundary conditions [25], which will be used in the solution to the problems:

1. All edges are simply supported:

at $x = 0, a: u = 0, v = 0, w = 0, M_x = 0$; at $y = 0, b: u = 0, v = 0, w = 0, M_y = 0$.

2. All edges are fixed:

at $x = 0, a: u = 0, v = 0, w = 0, \dfrac{\partial w}{\partial x} = 0$; at $y = 0, b: u = 0, v = 0, w = 0, \dfrac{\partial w}{\partial y} = 0$.

3. Two opposite edges are simply supported, the other two edges are fixed:

at $x = 0, a: u = 0, v = 0, w = 0, \dfrac{\partial w}{\partial x} = 0$; at $y = 0, b: u = 0, v = 0, w = 0, M_y = 0$.

The initial conditions at *t*=0 are as follows:

$$u(x,y,0) = u_0(x,y),\ \dot{u}(x,y,0) = \dot{u}_0(x,y),\ v(x,y,0) = v_0(x,y),\ \dot{v}(x,y,0) = \dot{v}_0(x,y),$$
$$w(x,y,0) = w_0(x,y),\ \dot{w}(x,y,0) = \dot{w}_0(x,y).$$

Here, $u_0(x,y)$, $v_0(x,y)$, $w_0(x,y)$, $\dot{u}_0(x,y)$, $\dot{v}_0(x,y)$ and $\dot{w}_0(x,y)$ are given functions.

The components of the vector of forces $\{N\} = (N_x, N_y, N_{xy})$ and moments $\{M\} = (M_x, M_y, M_{xy})$ for symmetric structure shells in matrix form can be written as:

$$\{N\} = \{N_x; N_y; N_{xy}\}^T = [C]\cdot\{\varepsilon\},\ \ \{M\} = \{M_x; M_y; M_{xy}\}^T = [D]\cdot\{\chi\}, \tag{2}$$

here

$$\{\varepsilon\} = (\varepsilon_x,\quad \varepsilon_y,\quad \varepsilon_{xy})^T,\ \ \{\chi\} = (\chi_x,\quad \chi_y,\quad \chi_{xy})^T,$$

$$\varepsilon_x = \frac{\partial u}{\partial x} - k_x w + \frac{1}{2}\left(\frac{\partial w}{\partial x}\right)^2, \varepsilon_y = \frac{\partial v}{\partial y} - k_y w + \frac{1}{2}\left(\frac{\partial w}{\partial y}\right)^2, \varepsilon_{xy} = \frac{\partial u}{\partial x} + \frac{\partial v}{\partial y} + \frac{\partial w}{\partial x}\frac{\partial w}{\partial y}, \tag{3}$$

$$\chi_x = -\frac{\partial^2 w}{\partial x^2}, \chi_y = -\frac{\partial^2 w}{\partial y^2}, \chi_{xy} = -\frac{\partial^2 w}{\partial x \partial y}.$$

Stiffness matrices $[C]$ and $[\mathrm{D}]$ have the following form:

$$C = \begin{pmatrix} C_{11} & C_{12} & C_{16} \\ C_{12} & C_{22} & C_{26} \\ C_{16} & C_{26} & C_{66} \end{pmatrix}, \quad \mathrm{D} = \begin{pmatrix} D_{11} & D_{12} & D_{16} \\ D_{12} & D_{22} & D_{26} \\ D_{16} & D_{26} & D_{66} \end{pmatrix}, \tag{4}$$

where the coefficients of the stiffness matrix C_{ij}, D_{ij} $(ij = 11,22,12,16,26,66)$, depending on the mechanical characteristics of the material and coefficient m are determined as follows:

$$C_{ij} = \int_{-\frac{h(x,y)}{2}}^{\frac{h(x,y)}{2}} B_{ij}\left(1 - \Gamma_{ij}^*\right)dz, \quad D_{ij} = \int_{-\frac{h(x,y)}{2}}^{\frac{h(x,y)}{2}} B_{ij}\left(1 - \Gamma_{ij}^*\right)z^2 dz,\ (i,j = 1,2,6),\ \ m = \int_{-\frac{h(x,y)}{2}}^{\frac{h(x,y)}{2}} \rho dz. \tag{5}$$

Here B_{ij} are the stiffness coefficients [26], Γ^*, Γ_{ij}^* – are the integral operators with relaxation kernels $\Gamma(t)$ and $\Gamma_{ij}(t)$, respectively:

$$\Gamma^*\varphi = \int_0^t \Gamma(t-\tau)\varphi(\tau)d\tau,\ \ \Gamma_{ij}^*\varphi = \int_0^t \Gamma_{ij}(t-\tau)\varphi(\tau)d\tau,\ \ i, j = 1{,}2\,.$$

In operator form, the system of equations of motion (1) is written as:

$$L_{11}u + L_{12}v + L_{13}w = -L_{14}w - p_x + \rho h\frac{\partial^2 u}{\partial t^2},\ \ L_{21}u + L_{22}v + L_{23}w = -L_{24}w - p_y + \rho h\frac{\partial^2 v}{\partial t^2},$$

$$L_{31}u + L_{32}v + L_{33}w = -L_{34}w - q - P(t)\frac{\partial^2 w}{\partial x^2} + \rho h\frac{\partial^2 w}{\partial t^2}. \qquad (6)$$

Here u, v and w - are the components of displacement vector $\{U\}$ in the directions of the Ox, Oy, and Oz axes, respectively.

$$L_{11} = C_{11}\frac{\partial^2}{\partial x^2} + 2C_{16}\frac{\partial^2}{\partial x\partial y} + C_{66}\frac{\partial^2}{\partial y^2},\ \ L_{12} = L_{21} = C_{16}\frac{\partial^2}{\partial x^2} + (C_{12}+C_{66})\frac{\partial^2}{\partial x\partial y} + C_{26}\frac{\partial^2}{\partial y^2},$$

$$L_{13} = -L_{31} = -\left((k_1C_{11} + k_2C_{12})\frac{\partial}{\partial x} + (k_1C_{16} + k_2C_{26})\frac{\partial}{\partial y}\right),$$

$$L_{22} = C_{66}\frac{\partial^2}{\partial x^2} + 2C_{26}\frac{\partial^2}{\partial x\partial y} + C_{22}\frac{\partial^2}{\partial y^2},$$

$$L_{23} = L_{32} = \left((k_1C_{16} + k_2C_{26})\frac{\partial}{\partial x} + (k_1C_{12} + k_2C_{22})\frac{\partial}{\partial y}\right),$$

$$L_{22} = C_{66}\frac{\partial^2}{\partial x^2} + 2C_{26}\frac{\partial^2}{\partial x\partial y} + C_{22}\frac{\partial^2}{\partial y^2},$$

$$L_{33} = D_{11}\frac{\partial^4}{\partial x^4} + 2(\mathrm{D}_{12} + 2D_{66})\frac{\partial^4}{\partial x^2\partial y^2} + 4D_{16}\frac{\partial^4}{\partial x^3\partial y} + 4D_{26}\frac{\partial^4}{\partial x\partial y^3} + D_{22}\frac{\partial^4}{\partial y^4} -$$
$$-\left(C_{11}k_x^2 + 2C_{12}k_xk_y + C_{22}k_y^2\right),$$

$$L_{14}(u,v,w,C_{ij}) = \frac{\partial}{\partial x}\left[\frac{1}{2}C_{11}\left(\frac{\partial w}{\partial x}\right)^2 + \frac{1}{2}C_{12}\left(\frac{\partial w}{\partial y}\right)^2 + C_{16}\frac{\partial w}{\partial x}\frac{\partial w}{\partial y}\right] +$$

$$+\frac{\partial}{\partial y}\left[\frac{1}{2}C_{16}\left(\frac{\partial w}{\partial x}\right)^2 + \frac{1}{2}C_{26}\left(\frac{\partial w}{\partial y}\right)^2 + C_{66}\frac{\partial w}{\partial x}\frac{\partial w}{\partial y}\right] + \qquad (7)$$

$$+\left[\frac{\partial u}{\partial x} - k_xw + \frac{1}{2}\left(\frac{\partial w}{\partial x}\right)^2\right]\left(\frac{\partial C_{11}}{\partial x} + \frac{\partial C_{16}}{\partial y}\right) + \left[\frac{\partial v}{\partial y} - k_yw + \frac{1}{2}\left(\frac{\partial w}{\partial y}\right)^2\right]\left(\frac{\partial C_{12}}{\partial x} + \frac{\partial C_{16}}{\partial y}\right) +$$

$$+\left(\frac{\partial u}{\partial y} + \frac{\partial v}{\partial x} + \frac{\partial w}{\partial x}\frac{\partial w}{\partial y}\right)\left(\frac{\partial C_{16}}{\partial x} + \frac{\partial C_{66}}{\partial y}\right),$$

$$L_{24}(u,v,w,C_{ij})=\frac{\partial}{\partial x}\left[\frac{1}{2}C_{16}\left(\frac{\partial w}{\partial x}\right)^2+\frac{1}{2}C_{26}\left(\frac{\partial w}{\partial y}\right)^2+C_{66}\frac{\partial w}{\partial x}\frac{\partial w}{\partial y}\right]+$$

$$+\frac{\partial}{\partial y}\left[\frac{1}{2}C_{12}\left(\frac{\partial w}{\partial x}\right)^2+\frac{1}{2}C_{22}\left(\frac{\partial w}{\partial y}\right)^2+C_{26}\frac{\partial w}{\partial x}\frac{\partial w}{\partial y}\right]+$$

$$+\left[\frac{\partial u}{\partial x}-k_x w+\frac{1}{2}\left(\frac{\partial w}{\partial x}\right)^2\right]\left(\frac{\partial C_{12}}{\partial y}+\frac{\partial C_{16}}{\partial x}\right)+\left[\frac{\partial v}{\partial y}-k_y w+\frac{1}{2}\left(\frac{\partial w}{\partial y}\right)^2\right]\left(\frac{\partial C_{22}}{\partial y}+\frac{\partial C_{26}}{\partial x}\right)+$$

$$+\left(\frac{\partial u}{\partial y}+\frac{\partial v}{\partial x}+\frac{\partial w}{\partial x}\frac{\partial w}{\partial y}\right)\left(\frac{\partial C_{26}}{\partial y}+\frac{\partial C_{66}}{\partial x}\right),$$

$$L_{34}(u,v,w,C_{ij},D_{ij})=2\frac{\partial^3 w}{\partial x^3}\left(\frac{\partial D_{11}}{\partial x}+\frac{\partial D_{16}}{\partial y}\right)+2\frac{\partial^3 w}{\partial x\partial y^2}\left(\frac{\partial D_{12}}{\partial x}+3\frac{\partial D_{26}}{\partial y}+2\frac{\partial D_{66}}{\partial x}\right)+$$

$$+2\frac{\partial^3 w}{\partial x^2\partial y}\left(\frac{\partial D_{12}}{\partial y}+3\frac{\partial D_{16}}{\partial x}+2\frac{\partial D_{66}}{\partial y}\right)+2\frac{\partial^3 w}{\partial y^3}\left(\frac{\partial D_{22}}{\partial y}+\frac{\partial D_{26}}{\partial x}\right)+$$

$$+\frac{\partial^2 w}{\partial x^2}\left(\frac{\partial^2 D_{11}}{\partial x^2}+\frac{\partial^2 D_{12}}{\partial y^2}+2\frac{\partial^2 D_{16}}{\partial x\partial y}\right)+\frac{\partial^2 w}{\partial y^2}\left(\frac{\partial^2 D_{12}}{\partial x^2}+\frac{\partial^2 D_{22}}{\partial y^2}+2\frac{\partial^2 D_{26}}{\partial x\partial y}\right)+$$

$$+2\frac{\partial^2 w}{\partial x\partial y}\left(\frac{\partial^2 D_{16}}{\partial x^2}+\frac{\partial^2 D_{26}}{\partial y^2}+2\frac{\partial^2 D_{66}}{\partial x\partial y}\right)+\frac{1}{2}\left(\frac{\partial w}{\partial x}\right)^2\left(k_x C_{11}+k_y C_{12}\right)+$$

$$+\frac{1}{2}\left(\frac{\partial w}{\partial y}\right)^2\left(k_x C_{12}+k_y C_{22}\right)+\frac{\partial w}{\partial x}\frac{\partial w}{\partial y}\left(k_x C_{16}+k_y C_{26}\right)+$$

$$+\frac{\partial^2 w}{\partial x^2}\left\{C_{11}\left[\frac{\partial u}{\partial x}-k_x w+\frac{1}{2}\left(\frac{\partial w}{\partial x}\right)^2\right]+C_{12}\left[\frac{\partial v}{\partial y}-k_y w+\frac{1}{2}\left(\frac{\partial w}{\partial y}\right)^2\right]+C_{16}\left(\frac{\partial u}{\partial y}+\frac{\partial v}{\partial x}+\frac{\partial w}{\partial x}\frac{\partial w}{\partial y}\right)\right\}+$$

$$+2\frac{\partial^2 w}{\partial x\partial y}\left\{C_{16}\left[\frac{\partial u}{\partial x}-k_x w+\frac{1}{2}\left(\frac{\partial w}{\partial x}\right)^2\right]+C_{26}\left[\frac{\partial v}{\partial y}-k_y w+\frac{1}{2}\left(\frac{\partial w}{\partial y}\right)^2\right]+C_{66}\left(\frac{\partial u}{\partial y}+\frac{\partial v}{\partial x}+\frac{\partial w}{\partial x}\frac{\partial w}{\partial y}\right)\right\}+$$

$$+\frac{\partial^2 w}{\partial y^2}\left\{C_{12}\left[\frac{\partial u}{\partial x}-k_x w+\frac{1}{2}\left(\frac{\partial w}{\partial x}\right)^2\right]+C_{22}\left[\frac{\partial v}{\partial y}-k_y w+\frac{1}{2}\left(\frac{\partial w}{\partial y}\right)^2\right]+C_{26}\left(\frac{\partial u}{\partial y}+\frac{\partial v}{\partial x}+\frac{\partial w}{\partial x}\frac{\partial w}{\partial y}\right)\right\}+$$

$$+\frac{\partial w}{\partial x}\left[L_{11}(u)+L_{12}(v)+L_{13}(w)+L_{14}(w)\right]+\frac{\partial w}{\partial y}\left[L_{21}(u)+L_{22}(v)+L_{23}(w)+L_{24}(w)\right].$$

If the shell under consideration has orthotropic properties, then the coefficients are $C_{16}=C_{26}=0$ and $D_{16}=D_{26}=0$. In relationships (2), the stiffness matrices have the following form:

$$C=\begin{pmatrix} C_{11} & C_{12} & 0 \\ C_{12} & C_{22} & 0 \\ 0 & 0 & C_{66} \end{pmatrix},\qquad \mathrm{D}=\begin{pmatrix} D_{11} & D_{12} & 0 \\ D_{12} & D_{22} & 0 \\ 0 & 0 & D_{66} \end{pmatrix}, \tag{8}$$

Here, coefficients C_{ij} and D_{ij} $(ij=11,12,22,66)$ are expressed in terms of elastic constants E_1, E_2, G_{12}, μ_1, μ_2 as follows:

$$C_{11}=hB_{11}\left(1-\mathit{\Gamma}_{11}^*\right)=\frac{hE_1\left(1-\mathit{\Gamma}_{11}^*\right)}{1-\mu_1\mu_2},\ C_{22}=hB_{22}\left(1-\mathit{\Gamma}_{22}^*\right)=\frac{hE_2\left(1-\mathit{\Gamma}_{22}^*\right)}{1-\mu_1\mu_2},$$

$$C_{12}=B_{12}\left(1-\mathit{\Gamma}_{12}^*\right)h=\frac{\mu_2E_1\left(1-\mathit{\Gamma}_{12}^*\right)h}{1-\mu_1\mu_2},\ C_{66}=B_{66}\left(1-\mathit{\Gamma}_{66}^*\right)h=hG_{12}\left(1-\mathit{\Gamma}_{66}^*\right),$$

$$D_{11}=B_{11}\left(1-\mathit{\Gamma}_{11}^*\right)h^3=\frac{E_1\left(1-\mathit{\Gamma}_{11}^*\right)h^3}{12(1-\mu_1\mu_2)},\ D_{22}=B_{22}\left(1-\mathit{\Gamma}_{22}^*\right)h^3=\frac{E_2\left(1-\mathit{\Gamma}_{22}^*\right)h^3}{12(1-\mu_1\mu_2)},$$

$$D_{12}=B_{12}\left(1-\mathit{\Gamma}_{12}^*\right)h^3=\frac{\mu_2E_1\left(1-\mathit{\Gamma}_{12}^*\right)h^3}{12(1-\mu_1\mu_2)},\ C_{66}=B_{66}\left(1-\mathit{\Gamma}_{66}^*\right)h^3\,\frac{G_{12}}{12}h^3. \tag{9}$$

Here $E_1,E_2-$are the moduli of elasticity in the direction of the x and y axes; G_{12} is the shear modulus; $\mu_1,\mu_2-$are the Poisson's ratios.

If the shell has isotropic properties ($E_1=E_2,\mu_1=\mu_2$), then the elements of the stiffness matrix take a simpler form with two elastic constants E (modulus of elasticity) and μ (Poisson's ratio):

$$C_{11}=C_{22}=B\left(1-\mathit{\Gamma}^*\right)h=\frac{E\left(1-\mathit{\Gamma}^*\right)h}{1-\mu^2},\ C_{12}=\mu B\left(1-\mathit{\Gamma}^*\right)h=\frac{\mu Eh}{1-\mu^2},$$

$$C_{66}=\frac{(1-\mu)}{2}B\left(1-\mathit{\Gamma}^*\right)h=\frac{E\left(1-\mathit{\Gamma}^*\right)h}{2(1+\mu)},\ D_{11}=D_{22}=B\left(1-\mathit{\Gamma}^*\right)\frac{h^3}{12}=\frac{E\left(1-\mathit{\Gamma}^*\right)h^3}{12(1-\mu^2)},$$

$$D_{12}=\mu B\left(1-\mathit{\Gamma}^*\right)\frac{h^3}{12}=\frac{\mu E\left(1-\mathit{\Gamma}^*\right)h^3}{12(1-\mu^2)},\ D_{66}=\frac{1-\mu}{2}B\left(1-\mathit{\Gamma}^*\right)\frac{h^3}{12}=\frac{E\left(1-\mathit{\Gamma}^*\right)h^3}{24(1+\mu)}. \tag{10}$$

By introducing into equation (6) the following dimensionless quantities

$$\bar{u}=\frac{u}{h_0};\ \bar{v}=\frac{v}{h_0};\ \bar{w}=\frac{w}{h_0};\ \bar{x}=\frac{x}{a};\ \bar{y}=\frac{y}{b};\ \bar{t}=\omega t;\ \bar{h}=\frac{h}{h_0};\ \lambda=\frac{a}{b};\ \delta=\frac{b}{h_0};\ \bar{k}_x=\frac{a^2}{h_0R_1};$$

$$\bar{k}_y=\frac{b^2}{h_0R_2};\ \bar{q}=\frac{q}{\sqrt{E_1E_2}}\left(\frac{b}{h_0}\right)^4;\ \overline{p_x}=\frac{p_x}{\sqrt{E_1E_2}};\ \overline{p_y}=\frac{p_y}{\sqrt{E_1E_2}};\ \bar{\Theta}=\frac{\Theta}{\omega};\ \delta_0=\frac{P_0}{P_{cr}};\ \delta_1=\frac{P_1}{P_{cr}}$$

and taking into account relationship (9) for orthotropic shells and keeping the previous notation, we obtain a dimensionless system of nonlinear integro-differential equations for problems of parametric oscillations of a viscous-elastic orthotropic shallow shell of variable thickness. Here, operators L_{ij} take the following form:

$$L_{11}(u)=h\Delta\left(1-\Gamma_{11}^*\right)\frac{\partial^2u}{\partial x^2}+\lambda^2h(1-\mu_1\mu_2)g\left(1-\Gamma_{11}^*\right)\frac{\partial^2u}{\partial y^2}+\frac{\partial h}{\partial x}\Delta\left(1-\Gamma_{11}^*\right)\frac{\partial u}{\partial x}+$$

$$+\lambda^2\frac{\partial h}{\partial y}(1-\mu_1\mu_2)g\left(1-\Gamma^*\right)\frac{\partial u}{\partial y},$$

$$L_{12}(v)=\lambda h\left[\mu_2\Delta\left(1-\Gamma_{12}^*\right)+(1-\mu_1\mu_2)g\left(1-\Gamma^*\right)\right]\frac{\partial^2 v}{\partial x\partial y}+\lambda\frac{\partial h}{\partial x}\mu_2\Delta\left(1-\Gamma_{12}^*\right)\frac{\partial v}{\partial y}+$$

$$\lambda\frac{\partial h}{\partial y}(1-\mu_1\mu_2)g\left(1-\Gamma^*\right)\frac{\partial v}{\partial x},$$

$$L_{13}(w)=h\left[\frac{k_x\Delta}{\lambda\delta}\left(1-\Gamma_{11}^*\right)+\frac{\lambda k_y}{\delta}\mu_2\Delta\left(1-\Gamma_{12}^*\right)\right]\frac{\partial w}{\partial x}-\frac{\partial h}{\partial x}\left[\left[\frac{k_x\Delta}{\lambda\delta}\left(1-\Gamma_{11}^*\right)+\frac{\lambda k_y\mu_2\Delta}{\delta}\left(1-\Gamma_{12}^*\right)w\right],\right.$$

$$L_{14}(w)=\frac{h\Delta}{\lambda\delta}\left(1-\Gamma_{11}^*\right)\frac{\partial w}{\partial x}\frac{\partial^2 w}{\partial x^2}\frac{\lambda h}{\delta}\left[\mu_2\Delta\left(1-\Gamma_{12}^*\right)+(1-\mu_1\mu_2)g\left(1-\Gamma^*\right)\right]\frac{\partial w}{\partial y}\frac{\partial^2 w}{\partial x\partial y}+$$

$$+(1-\mu_1\mu_2)\frac{\lambda gh}{\delta}\left(1-\Gamma^*\right)\frac{\partial w}{\partial x}\frac{\partial^2 w}{\partial y^2}+\frac{\partial h}{\partial x}\left[\frac{\Delta}{2\lambda\delta}\left(1-\Gamma_{11}^*\right)\left(\frac{\partial w}{\partial x}\right)^2+\right.$$

$$\left.+\frac{\lambda\mu_2\Delta}{2\delta}\left(1-\Gamma_{12}^*\right)\left(\frac{\partial w}{\partial y}\right)^2\right]+\frac{\partial h}{\partial y}(1-\mu_1\mu_2)\frac{\lambda g}{\delta}\left(1-\Gamma^*\right)\frac{\partial w}{\partial x}\frac{\partial w}{\partial y},$$

$$L_{21}(u)=\frac{h}{\lambda}\left[\frac{\mu_1}{\Delta}\left(1-\Gamma_{21}^*\right)+(1-\mu_1\mu_2)g\left(1-\Gamma^*\right)\right]\frac{\partial^2 u}{\partial x\partial y}+$$

$$+(1-\mu_1\mu_2)\frac{g}{\lambda}\frac{\partial h}{\partial x}\left(1-\Gamma^*\right)\frac{\partial u}{\partial y}+\frac{\mu_1}{\lambda\Delta}\frac{\partial h}{\partial y}\left(1-\Gamma_{21}^*\right)\frac{\partial u}{\partial x},$$

$$L_{22}(м)=\frac{h}{\Delta}\left(1-\Gamma_{22}^*\right)\left(\frac{\partial^2 v}{\partial y^2}\right)+(1-\mu_1\mu_2)\frac{gh}{\lambda^2}\left(1-\Gamma^*\right)\frac{\partial^2 v}{\partial x^2}+$$

$$+(1-\mu_1\mu_2)\frac{g}{\lambda^2}\frac{\partial h}{\partial x}\left(1-\Gamma^*\right)\frac{\partial v}{\partial x}+\frac{1}{\Delta}\frac{\partial h}{\partial y}\left(1-\Gamma_{22}^*\right)\frac{\partial v}{\partial y},$$

$$L_{23}(w)=h\left[\frac{k_x}{\lambda^2\delta}\frac{\mu_1}{\Delta}\left(1-\Gamma_{21}^*\right)+\frac{k_y}{\delta\Delta}\left(1-\Gamma_{22}^*\right)\right]\frac{\partial w}{\partial y}+\frac{\partial h}{\partial y}\left[\frac{k_y}{\delta\Delta}\left(1-\Gamma_{22}^*\right)+\frac{k_x}{\lambda^2\delta}\frac{\mu_1}{\Delta}\left(1-\Gamma_{21}^*\right)w\right],$$

$$L_{24}(w)=h\left\{\frac{1}{\delta\Delta}\left(1-\Gamma_{22}^*\right)\frac{\partial w}{\partial y}\frac{\partial^2 w}{\partial y^2}+\left[\frac{\mu_1}{\Delta}\left(1-\Gamma_{21}^*\right)+(1-\mu_1\mu_2)\frac{g}{\lambda^2\delta}\left(1-\Gamma^*\right)\right]\frac{\partial w}{\partial x}\frac{\partial^2 w}{\partial x\partial y}+\right.$$

$$\left.+(1-\mu_1\mu_2)\frac{g}{\lambda^2\delta}\left(1-\Gamma^*\right)\frac{\partial w}{\partial y}\frac{\partial^2 w}{\partial x^2}\right\}+\frac{\partial h}{\partial x}(1-\mu_1\mu_2)\frac{g}{\lambda^2\delta}\left(1-\Gamma^*\right)\frac{\partial w}{\partial x}\frac{\partial w}{\partial y}+$$

$$+\frac{\partial h}{\partial y}\left[\frac{1}{2\delta\Delta}\left(1-\Gamma_{22}^*\right)\left(\frac{\partial w}{\partial y}\right)^2+\frac{\mu_1}{2\lambda^2\delta\Delta}\left(1-\Gamma_{21}^*\right)\left(\frac{\partial w}{\partial x}\right)^2\right],$$

$$L_{31}(u)=-12h\left\{\left[\lambda\delta\Delta k_x\left(1-\Gamma_{11}^*\right)+\frac{\lambda^3\delta\mu_1 k_y}{\Delta}\left(1-\Gamma_{21}^*\right)\right]\frac{\partial u}{\partial x}+\right.$$

$$+\frac{\partial h}{\partial x}\lambda\delta\Delta\left(1-\Gamma_{11}^{*}\right)\frac{\partial u}{\partial x}+\frac{\partial h}{\partial y}(1-\mu_1\mu_2)\lambda^3\delta g\left(1-\Gamma^{*}\right)\frac{\partial u}{\partial y}+$$

$$+\frac{\partial h}{\partial x}(1-\mu_1\mu_2)\lambda^3\delta g\left(1-\Gamma^{*}\right)\frac{\partial u}{\partial y}+\frac{\partial h}{\partial y}\frac{\mu_1\lambda^3\delta}{\Delta}\left(1-\Gamma_{21}^{*}\right)\frac{\partial u}{\partial x},$$

$$L_{32}(v)=\left[\lambda^2\delta\mu_2\Delta k_x\left(1-\Gamma_{12}^{*}\right)+\frac{\lambda^4\delta k_y}{\Delta}\left(1-\Gamma_{22}^{*}\right)\right]\frac{\partial v}{\partial y}-$$

$$+\frac{\partial h}{\partial x}\mu_2\lambda^2\delta\Delta\left(1-\Gamma_{12}^{*}\right)\frac{\partial v}{\partial y}+\frac{\partial h}{\partial y}(1-\mu_1\mu_2)\lambda^2\delta g\left(1-\Gamma^{*}\right)\frac{\partial v}{\partial x}+$$

$$+\frac{\partial h}{\partial x}(1-\mu_1\mu_2)\lambda^2\delta g\left(1-\Gamma^{*}\right)\frac{\partial v}{\partial x}+\frac{\partial h}{\partial y}\frac{\lambda^4\delta}{\Delta}\left(1-\Gamma_{22}^{*}\right)\frac{\partial v}{\partial y},$$

$$L_{33}(w)=h^3\left\{\Delta\left(1-\Gamma_{11}^{*}\right)\frac{\partial^4 w}{\partial x^4}+\left[4(1-\mu_1\mu_2)g\left(1-\Gamma^{*}\right)+\mu_2\Delta\left(1-\Gamma_{12}^{*}\right)+\frac{\mu_1}{\Delta}\left(1-\Gamma_{21}^{*}\right)\right]\lambda^2\frac{\partial^4 w}{\partial x^2\partial y^2}+\right.$$

$$\left.+\frac{\lambda^4}{\Delta}\left(1-\Gamma_{22}^{*}\right)\frac{\partial^4 w}{\partial y^4}\right\}+3\left[2h\left(\frac{\partial h}{\partial x}\right)^2+h^2\frac{\partial^2 h}{\partial x^2}\right]\left[\Delta\left(1-\Gamma_{11}^{*}\right)\frac{\partial^2 w}{\partial x^2}+\lambda^2\mu_2\Delta\left(1-\Gamma_{12}^{*}\right)\frac{\partial^2 w}{\partial y^2}\right]+$$

$$+6h^2\frac{\partial h}{\partial x}\left\{\Delta\left(1-\Gamma_{11}^{*}\right)\frac{\partial^3 w}{\partial x^3}+\left[\mu_2\Delta\left(1-\Gamma_{12}^{*}\right)+2(1-\mu_1\mu_2)g\left(1-\Gamma^{*}\right)\right]\lambda^2\frac{\partial^3 w}{\partial x\partial y^2}\right\}+$$

$$+6h^2\frac{\partial h}{\partial y}\left\{\frac{1}{\Delta}\left(1-\Gamma_{22}^{*}\right)\lambda^4\frac{\partial^3 w}{\partial y^3}+\left[\frac{\mu_1}{\Delta}\left(1-\Gamma_{21}^{*}\right)+2(1-\mu_1\mu_2)g\left(1-\Gamma^{*}\right)\right]\lambda^2\frac{\partial^3 w}{\partial x^2\partial y}\right\}+$$

$$+3\left[2h\left(\frac{\partial h}{\partial y}\right)^2+h^2\frac{\partial^2 h}{\partial y^2}\right]\left[\frac{1}{\Delta}\left(1-\Gamma_{22}^{*}\right)\lambda^4\frac{\partial^2 w}{\partial y^2}+\frac{\mu_1}{\Delta}\left(1-\Gamma_{21}^{*}\right)\lambda^2\frac{\partial^2 w}{\partial x^2}\right]+$$

$$+12\left[2h\frac{\partial h}{\partial x}\frac{\partial h}{\partial y}+h^2\frac{\partial^2 h}{\partial x\partial y}\right](1-\mu_1\mu_2)g\left(1-\Gamma^{*}\right)\lambda^2\frac{\partial^2 w}{\partial x\partial y}-$$

$$-12h\left\{\Delta k_x^2\left(1-\Gamma_{11}^{*}\right)+\lambda^2k_xk_y\left[\mu_2\Delta\left(1-\Gamma_{12}^{*}\right)+\frac{\mu_1}{\Delta}\left(1-\Gamma_{21}^{*}\right)\right]+\frac{\lambda^4k_y^2}{\Delta}\left(1-\Gamma_{22}^{*}\right)\right\}w-$$

$$-\frac{\partial h}{\partial x}\left[k_x\Delta\left(1-\Gamma_{11}^{*}\right)+\lambda^2k_y\mu_2\Delta\left(1-\Gamma_{12}^{*}\right)\right]w+\frac{\partial h}{\partial y}\left[\frac{\lambda^4k_y}{\Delta}\left(1-\Gamma_{22}^{*}\right)+\frac{\lambda^2\mu_1k_x}{\Delta}\left(1-\Gamma_{21}^{*}\right)\right]w,$$

$$L_{34}(u,v,w)=\frac{1}{2}\left[k_x\Delta\left(1-\Gamma_{11}^{*}\right)+\frac{\lambda^2\mu_1k_y}{\Delta}\left(1-\Gamma_{21}^{*}\right)\right]\left(\frac{\partial w}{\partial x}\right)^2+$$

$$
\begin{aligned}
&+\frac{1}{2}\Big[\lambda^2 k_x \mu_2 \Delta\big(1-\Gamma_{12}^*\big)+\frac{\lambda^4 k_y}{\Delta}\big(1-\Gamma_{22}^*\big)\Big]\Big(\frac{\partial w}{\partial y}\Big)^2\Big\}-\\
&-12\frac{\partial w}{\partial x}\Big\{h\Big\{\Delta\big(1-\Gamma_{11}^*\big)\Big(\lambda\delta\frac{\partial^2 u}{\partial x^2}+\frac{\partial w}{\partial x}\frac{\partial^2 w}{\partial x^2}\Big)-\big[k_x\Delta\big(1-\Gamma_{11}^*\big)+\lambda^2\mu_2\Delta k_y\big(1-\Gamma_{12}^*\big)\big]\frac{\partial w}{\partial x}+\\
&+\big[\mu_2\Delta\big(1-\Gamma_{12}^*\big)+(1-\mu_1\mu_2)g\big(1-\Gamma^*\big)\big]\Big(\lambda^2\delta\frac{\partial^2 v}{\partial x\partial y}+\lambda^2\frac{\partial w}{\partial y}\frac{\partial^2 w}{\partial x\partial y}\Big)+\\
&+(1-\mu_1\mu_2)g\big(1-\Gamma^*\big)\Big(\lambda^3\delta\frac{\partial^2 u}{\partial y^2}+\lambda^2\frac{\partial w}{\partial x}\frac{\partial^2 w}{\partial y^2}\Big)\Big\}-\\
&-12\frac{\partial^2 w}{\partial x^2}h\Big\{\Delta\big(1-\Gamma_{11}^*\big)\Big[\lambda\delta\frac{\partial u}{\partial x}+\frac{1}{2}\Big(\frac{\partial w}{\partial x}\Big)^2\Big]+\mu_2\Delta\big(1-\Gamma_{12}^*\big)\Big[\lambda^2\delta\frac{\partial v}{\partial y}+\frac{\lambda^2}{2}\Big(\frac{\partial w}{\partial y}\Big)^2\Big]-\\
&-\big[k_x\Delta\big(1-\Gamma_{11}^*\big)+\lambda^2 k_y\mu_2\Delta\big(1-\Gamma_{12}^*\big)\big]w\Big\}-12\frac{\partial w}{\partial y}\Big\{h\Big\{\frac{1}{\Delta}\big(1-\Gamma_{22}^*\big)\Big(\lambda^4\delta\frac{\partial^2 v}{\partial y^2}+\lambda^4\frac{\partial w}{\partial y}\frac{\partial^2 w}{\partial y^2}\Big)-\\
&-\Big[\frac{\lambda^2\mu_1 k_x}{\Delta}\big(1-\Gamma_{21}^*\big)+\frac{\lambda^4 k_y}{\Delta}\big(1-\Gamma_{22}^*\big)\Big]\frac{\partial w}{\partial y}+\Big[\frac{\mu_1}{\Delta}\big(1-\Gamma_{21}^*\big)+(1-\mu_1\mu_2)g\big(1-\Gamma^*\big)\Big]\times\\
&\times\Big(\lambda^3\delta\frac{\partial^2 u}{\partial x\partial y}+\lambda^2\frac{\partial w}{\partial x}\frac{\partial^2 w}{\partial x\partial y}\Big)+(1-\mu_1\mu_2)g\big(1-\Gamma^*\big)\Big(\lambda^2\delta\frac{\partial^2 v}{\partial x^2}+\lambda^2\frac{\partial w}{\partial y}\frac{\partial^2 w}{\partial x^2}\Big)\Big\}+\\
&-12\frac{\partial^2 w}{\partial y^2}h\Big\{\frac{\mu_1}{\Delta}\big(1-\Gamma_{21}^*\big)\Big[\lambda^3\delta\frac{\partial u}{\partial x}+\frac{\lambda^2}{2}\Big(\frac{\partial w}{\partial x}\Big)^2\Big]+\\
&+\frac{1}{\Delta}\big(1-\Gamma_{22}^*\big)\Big[\lambda^4\delta\frac{\partial v}{\partial y}+\frac{\lambda^4}{2}\Big(\frac{\partial w}{\partial y}\Big)^2\Big]-\Big[\frac{\lambda^2\mu_1 k_x}{\Delta}\big(1-\Gamma_{21}^*\big)+\frac{\lambda^4 k_y}{\Delta}\big(1-\Gamma_{22}^*\big)\Big]w\Big\}-\\
&-24\frac{\partial^2 w}{\partial x\partial y}h(1-\mu_1\mu_2)g\big(1-\Gamma^*\big)\Big(\lambda^3\delta\frac{\partial u}{\partial y}+\lambda^2\delta\frac{\partial v}{\partial x}+\lambda^2\frac{\partial w}{\partial x}\frac{\partial w}{\partial y}\Big)+\\
&+\frac{\partial h}{\partial x}\Big\{\Delta\big(1-\Gamma_{11}^*\big)\Big[\frac{1}{2}\Big(\frac{\partial w}{\partial x}\Big)^2\Big]+\mu_2\Delta\big(1-\Gamma_{12}^*\big)\Big[\frac{\lambda^2}{2}\Big(\frac{\partial w}{\partial y}\Big)^2\Big]\Big\}+\\
&+\Big(\frac{\partial h}{\partial x}+\frac{\partial h}{\partial y}\Big)(1-\mu_1\mu_2)\lambda^2 g\big(1-\Gamma^*\big)\frac{\partial w}{\partial x}\frac{\partial w}{\partial y}+\frac{\partial h}{\partial y}\Big\{\frac{1}{\Delta}\big(1-\Gamma_{22}^*\big)\Big[\frac{\lambda^4}{2}\Big(\frac{\partial w}{\partial y}\Big)^2\Big]+\frac{\mu_1}{\Delta}\big(1-\Gamma_{21}^*\big)\Big[\frac{\lambda^2}{2}\Big(\frac{\partial w}{\partial x}\Big)^2\Big]
\end{aligned}
\tag{11}
$$

,

here $P_{cr}=\dfrac{\pi^2}{3(1-\mu_1\mu_2)}\sqrt{E_1E_2}\left(\dfrac{h_0}{b}\right)^2$ is the static critical load; $\omega=\sqrt{\pi^2\sqrt{E_1E_2}\,h_0^2P_{cr}^*/(\rho b^4)}$ is the frequency of the fundamental tone of oscillations; $P_{cr}^{*}=\frac{P_{cr}}{\sqrt{E_1E_2}(b/h_0)^2}=\frac{\pi^2}{3(1-\mu_1\mu_2)}$; $\Delta=\sqrt{E_1/E_2}$

.

The system of equations (6), (11) with the corresponding boundary and initial conditions describes the motion of a viscous-elastic orthotropic shallow shell of variable thickness under a periodic load $P(t)=P_0+P_1\cos(\Theta t)$.

In calculations, the singular Koltunov-Rzhanitsin kernels [27] are used as relaxation kernels:

$$\Gamma(t)=Ae^{-\beta t}t^{\alpha-1},(0<\alpha<1),\ \Gamma_{ij}(\mathrm{t})=A_{ij}e^{-\beta_{ij}t}t^{\alpha_{ij}-1},\left(0<\alpha_{ij}<1\right) \tag{12}$$

Let the shell thickness change following the law $h(x)=\frac{1}{2}h_0(1+\alpha^* x)$, i.e., it leads to a linear increase in the shell thickness (Fig.2).

Here, α^* is the parameter characterizing the thickness variability; h_0 is the shell thickness corresponding to $\alpha^*=0$.

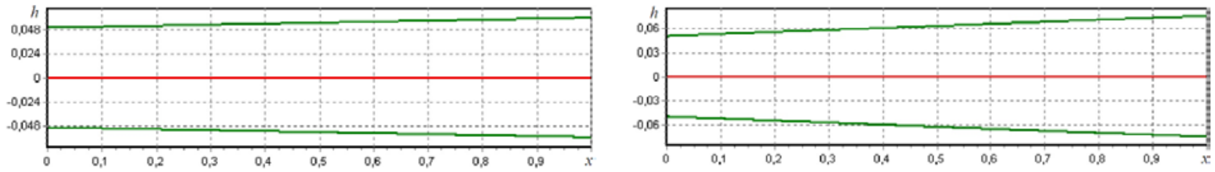

a) **b)**

Figure 2. Change in the shell thickness depending on the value of parameter α^*:

a) $\alpha^*=0.2$**; b)** $\alpha^*=0.5$

The solution to the obtained IDE system that satisfies the boundary conditions of the problem is sought with respect to the displacements *u* and *v*, and the deflection *w* in the form

$$u(x,y,t)=\sum_{n=1}^{N}\sum_{m=1}^{M}u_{nm}(t)\phi_{nm}(x,y),\ \ v(x,y,t)=\sum_{n=1}^{N}\sum_{m=1}^{M}v_{nm}(t)\varphi_{nm}(x,y),$$

$$w(x,y,t)=\sum_{n=1}^{N}\sum_{m=1}^{M}w_{nm}(t)\psi_{nm}(x,y), \tag{13}$$

where $u_{nm}=u_{nm}(t)$, $v_{nm}=v_{nm}(t)$, $w_{nm}=w_{nm}(t)$ - unknown functions of time; $\phi_{nm}(x,y)$, $\varphi_{nm}(x,y)$, $\psi_{nm}(x,y)$, $n=1,2,...,N$; $m=1,2,...,M$ - coordinate functions that satisfy the given boundary conditions of the problem.

Substituting (13) into the system of equations (6), (11) and performing the Bubnov-Galerkin procedure, we obtain the following system of basic resolving nonlinear IDEs:

$$\sum_{n=1}^{N}\sum_{m=1}^{M}a_{klnm}\ddot{u}_{nm}-\eta_1\Bigg\{\sum_{n=1}^{N}\sum_{m=1}^{M}\Big\{\Big[\left(1-\Gamma_{11}^{*}\right)d_{1klnm}+\left(1-\Gamma^{*}\right)d_{2klnm}\Big]u_{nm}+$$

$$+\Big[\left(1-\Gamma_{12}^{*}\right)d_{3klnm}+\left(1-\Gamma^{*}\right)d_{4klnm}\Big]v_{nm}+\Big[\left(1-\Gamma_{11}^{*}\right)d_{5klnm}+\left(1-\Gamma_{12}^{*}\right)d_{6klnm}\Big]w_{nm}\Big\}+$$

$$+\sum_{n,i=1}^{N}\sum_{m,j=1}^{M}\Big[\left(1-\Gamma_{11}^{*}\right)d_{7klnmij}+\left(1-\Gamma_{12}^{*}\right)d_{8klnmij}+\left(1-\Gamma^{*}\right)d_{9klnmij}\Big]\left(w_{nm}w_{ij}-w_{0nm}w_{0ij}\right)\Bigg\}=0,$$

$$\sum_{n=1}^{N}\sum_{m=1}^{M} b_{klnm}\ddot{v}_{nm} - \eta_2\left\{\sum_{n=1}^{N}\sum_{m=1}^{M}\left\{\left[\left(1-\Gamma_{21}^{*}\right)e_{1klnm} + \left(1-\Gamma^{*}\right)e_{2klnm}\right]u_{nm} + \right.\right.$$

$$\left.+\left[\left(1-\Gamma_{22}^{*}\right)e_{3klnm} + \left(1-\Gamma^{*}\right)e_{4klnm}\right]v_{nm} + \left[\left(1-\Gamma_{21}^{*}\right)e_{5klnm} + \left(1-\Gamma_{22}^{*}\right)e_{6klnm}\right]w_{nm}\right\}+ \tag{14}$$

$$\left.+\sum_{n,i=1}^{N}\sum_{m,j=1}^{M}\left[\left(1-\Gamma_{22}^{*}\right)e_{7klnmij} + \left(1-\Gamma_{21}^{*}\right)e_{8klnmij} + \left(1-\Gamma^{*}\right)e_{9klnmij}\right]\left(w_{nm}w_{ij} - w_{0nm}w_{0ij}\right)\right\} = 0,$$

$$\sum_{n=1}^{N}\sum_{m=1}^{M} c_{klnm}\ddot{w}_{nm} + \eta_3\sum_{n=1}^{N}\sum_{m=1}^{M} p_{klnm}^{2}\left(1-2\mu_{klnm}\cos\Theta t\right)w_{nm} -$$

$$-\eta_3\left\{\sum_{n=1}^{N}\sum_{m=1}^{M}\left\{\left[\left(1-\Gamma_{11}^{*}\right)f_{1klnm} + \left(1-\Gamma_{21}^{*}\right)f_{2klnm}\right]u_{nm} + \left[\left(1-\Gamma_{12}^{*}\right)f_{3klnm} + \left(1-\Gamma_{22}^{*}\right)f_{4klnm}\right]v_{nm} + \right.\right.$$

$$\left.+\left[\Gamma_{11}^{*}f_{5klnm} + \Gamma_{12}^{*}f_{6klnm} + \Gamma_{22}^{*}f_{7klnm} + \Gamma_{21}^{*}f_{8klnm} + \Gamma^{*}f_{9klnm}\right]w_{0nm}\right\} -$$

$$-\eta_3\left\{\sum_{n,i=1}^{N}\sum_{m,j=1}^{M} w_{nm}\left\{\left[\left(1-\Gamma_{11}^{*}\right)\xi_{1klnmij} + \left(1-\Gamma_{21}^{*}\right)\xi_{2klnmij} + \left(1-\Gamma^{*}\right)\xi_{3klnmij}\right]u_{ij} + \right.\right.$$

$$\left.+\left[\left(1-\Gamma_{22}^{*}\right)\xi_{4klnmij} + \left(1-\Gamma_{12}^{*}\right)\xi_{5klnmij} + \left(1-\Gamma^{*}\right)\xi_{6klnmij}\right]v_{ij}\right\}+$$

$$+\left[\left(1-\Gamma_{11}^{*}\right)\xi_{7klnmij} + \left(1-\Gamma_{12}^{*}\right)\xi_{8klnmij} + \left(1-\Gamma_{22}^{*}\right)\xi_{9klnmij} + \left(1-\Gamma_{21}^{*}\right)\xi_{10klnmij}\right]\left(w_{ij} - w_{0ij}\right)\Big\}+$$

$$+\sum_{n,i=1}^{N}\sum_{m,j=1}^{M}\left(\left(1-\Gamma_{11}^{*}\right)g_{1klnmijrs} + \left(1-\Gamma_{12}^{*}\right)g_{2klnmijrs} + \left(1-\Gamma_{21}^{*}\right)g_{3klnmijrs} + \left(1-\Gamma_{22}^{*}\right)g_{4klnmijrs}\right)\left(w_{nm}w_{ij} - w_{0nm}w_{0ij}\right)+$$

$$+\sum_{n,i,r=1}^{N}\sum_{m,j,s=1}^{M} w_{nm}\left(\left(1-\Gamma_{11}^{*}\right)g_{5klnmijrs} + \left(1-\Gamma_{12}^{*}\right)g_{6klnmijrs} + \left(1-\Gamma_{22}^{*}\right)g_{7klnmijrs} + \right.$$

$$\left.\left.+\left(1-\Gamma_{21}^{*}\right)g_{8klnmijrs} + \left(1-\Gamma^{*}\right)g_{9klnmijrs}\right\}\left(w_{ij}w_{rs} - w_{0ij}w_{0rs}\right)\right\} = 12\eta_3\left(1-\mu_1\mu_2\right)\lambda^4 q_{kl},$$

$$u_{nm}(0) = u_{0nm},\ \dot{u}_{nm}(0) = \dot{u}_{0nm},\ v_{nm}(0) = v_{0nm},\ \dot{v}_{nm}(0) = \dot{v}_{0nm},$$

$$w_{nm}(0) = w_{0nm},\ \dot{w}_{nm}(0) = \dot{w}_{0nm},\ k = 1,2,\ldots,N;\ l = 1,2,\ldots,M,$$

where the constant coefficients included in this system are related to coordinate functions and their derivatives and have the following form:

$$a_{klnm} = \int_0^1\int_0^1 h\phi_{nm}\phi_{kl}\,dxdy;$$

$$d_{1klnm} = \int_0^1\int_0^1 \Delta\left(h\phi''_{nm,xx} + h'_x\phi'_{nm,x}\right)\phi_{kl}\,dxdy;$$

$$d_{2klnm} = \int_0^1\int_0^1 \left(1-\mu_1\mu_2\right)g\lambda^2\left(h\phi''_{nm,yy} + h'_y\phi'_{nm,y}\right)\phi_{kl}\,dxdy;$$

$$d_{3klnm} = \int_0^1\int_0^1 \mu_2 \Delta\lambda \left(h\varphi''_{nm,xy} + h'_x \varphi'_{nm,y}\right)\phi_{kl}\, dxdy;$$

$$d_{4klnm} = \int_0^1\int_0^1 (1-\mu_1\mu_2) g\lambda \left(h\varphi''_{nm,xy} + h'_y \varphi'_{nm,x}\right)\phi_{kl}\, dxdy;$$

$$d_{5klnm} = -\int_0^1\int_0^1 \frac{\Delta k_x}{\lambda\delta}\left(h\psi'_{nm,x} + h'_x \psi_{nm}\right)\phi_{kl}\, dxdy;$$

$$d_{6klnm} = -\int_0^1\int_0^1 \frac{\Delta k_y \mu_2 \lambda}{\delta}\left(h\psi'_{nm,x} + h'_x \psi_{nm}\right)\phi_{kl}\, dxdy;$$

$$d_{7klnmij} = \int_0^1\int_0^1 \frac{\Delta}{\lambda\delta}\left(h\psi'_{nm,x}\psi''_{ij,xx} + \frac{1}{2}h'_x \psi'_{nm,x}\psi'_{ij,x}\right)\phi_{kl}\, dxdy;$$

$$d_{8klnmij} = \int_0^1\int_0^1 \frac{\mu_2\Delta\lambda}{\delta}\left(h\psi'_{nm,y}\psi''_{ij,xy} + \frac{1}{2}h'_x \psi'_{nm,y}\psi'_{ij,y}\right)\phi_{kl}\, dxdy;$$

$$d_{9klnmij} = \int_0^1\int_0^1 (1-\mu_1\mu_2) g \frac{\lambda}{\delta}\left(h\psi'_{nm,y}\psi''_{ij,xy} + h\psi'_{nm,x}\psi''_{ij,yy} + h'_y \psi'_{nm,x}\psi'_{ij,y}\right)\phi_{kl}\, dxdy;$$

$$b_{klnm} = \int_0^1\int_0^1 h\varphi_{nm}\varphi_{kl}\, dxdy;$$

$$e_{1klnm} = \int_0^1\int_0^1 \frac{\mu_1}{\Delta\lambda}\left(h\phi''_{nm,xy} + h'_y \phi'_{nm,x}\right)\varphi_{kl}\, dxdy;$$

$$e_{2klnm} = \int_0^1\int_0^1 \frac{(1-\mu_1\mu_2)g}{\lambda}\left(h\phi''_{nm,xy} + h'_x \phi'_{nm,y}\right)\varphi_{kl}\, dxdy;$$

$$e_{3klnm} = \int_0^1\int_0^1 \frac{1}{\Delta}\left(h\varphi''_{nm,yy} + h'_y \varphi'_{nm,y}\right)\varphi_{kl}\, dxdy;$$

$$e_{4klnm} = \int_0^1\int_0^1 \frac{(1-\mu_1\mu_2)g}{\lambda^2}\left(h\varphi''_{nm,xx} + h'_x \varphi'_{nm,x}\right)\varphi_{kl}\, dxdy;$$

$$e_{5klnm} = -\int_0^1\int_0^1 \frac{k_x\mu_1}{\lambda^2\delta\Delta}\left(h\psi'_{nm,y} + h'_y \psi_{nm}\right)\varphi_{kl}\, dxdy; \quad e_{6klnm} = -\int_0^1\int_0^1 \frac{k_y}{\delta\Delta}\left(h\psi'_{nm,y} + h'_y \psi_{nm}\right)\varphi_{kl}\, dxdy;$$

$$e_{7klnmij} = \int_0^1\int_0^1 \frac{1}{\delta\Delta}\left(h\psi'_{nm,y}\psi''_{ij,yy} + \frac{1}{2}h'_y \psi'_{nm,y}\psi'_{ij,y}\right)\varphi_{kl}\, dxdy;$$

$$e_{8klnmij} = \int_0^1\int_0^1 \frac{\mu_1}{\lambda^2\delta\Delta}\left(h\psi'_{nm,x}\psi''_{ij,xy} + \frac{1}{2}h'_y \psi'_{nm,x}\psi'_{ij,x}\right)\varphi_{kl}\, dxdy;$$

$$e_{9klnmij} = \int_0^1\int_0^1 \frac{(1-\mu_1\mu_2)g}{\lambda^2\delta}\left(h\psi'_{nm,x}\psi''_{ij,xy} + h\psi'_{nm,y}\psi''_{ij,xx} + h'_x \psi'_{nm,x}\psi'_{ij,y}\right)\varphi_{kl}\, dxdy;$$

$$c_{klnm} = \int_0^1\int_0^1 h\psi_{nm}\psi_{kl}\, dxdy;$$

$$f_{1klnm} = -12\int_0^1\int_0^1 \lambda\delta\Delta k_x h\phi'_{nm,x}\psi_{kl}dxdy; \quad f_{2klnm} = -12\int_0^1\int_0^1 \frac{\lambda^3\delta\mu_1 k_y}{\Delta} h\phi'_{nm,x}\psi_{kl}dxdy;$$

$$f_{3klnm} = -12\int_0^1\int_0^1 \lambda^2\delta\mu_2\Delta k_x h\varphi'_{nm,y}\psi_{kl}dxdy; \quad f_{4klnm} = -12\int_0^1\int_0^1 \frac{\lambda^4\delta k_y}{\Delta} h\varphi'_{nm,y}\psi_{kl}dxdy;$$

$$f_{5klnm} = \int_0^1\int_0^1 \Delta\left(h^3\psi^{IV}_{nm,xxxx} + 3\left[2h(h'_x)^2 + h^2h''_{xx}\right]\psi''_{nm,xx} + 6h^2h'_x\psi'''_{nm,xxx} + 12k_x^2h\psi_{nm}\right)\psi_{kl}dxdy;$$

$$f_{6klnm} = \int_0^1\int_0^1 \mu_2\Delta\lambda^2\left(h^3\psi^{IV}_{nm,xxyy} + 3\left[2h(h'_x)^2 + h^2h''_{xx}\right]\psi''_{nm,yy} + 6h^2h'_x\psi'''_{nm,xyy} + 12k_xk_yh\psi_{nm}\right)\psi_{kl}dxdy;$$

$$f_{7klnm} = \int_0^1\int_0^1 \frac{\lambda^4}{\Delta}\left(h^3\psi^{IV}_{nm,yyyy} + 6h^2h'_y\psi'''_{nm,yyy} + 3\left[2h(h'_y)^2 + h^2h''_{yy}\right]\psi''_{nm,yy} + 12k_y^2h\psi_{nm}\right)\psi_{kl}dxdy;$$

$$f_{8klnm} = \int_0^1\int_0^1 \frac{\mu_1\lambda^2}{\Delta}\left(h^3\psi^{IV}_{nm,xxyy} + 6h^2h'_y\psi'''_{nm,xxy} + 3\left[2h(h'_y)^2 + h^2h''_{yy}\right]\psi''_{nm,xx} + 12k_xk_yh\psi_{nm}\right)\psi_{kl}dxdy;$$

$$f_{9klnm} = \int_0^1\int_0^1 (1-\mu_1\mu_2)g\lambda^2\left(4h^3\psi^{IV}_{nm,xxyy} + 12h^2h'_x\psi'''_{nm,xyy} + 12h^2h'_y\psi'''_{nm,xxy} + \right.$$

$$\left. + 12\left[2hh'_xh'_y + h^2h''_{xy}\right]\psi''_{nm,xy}\right)\psi_{kl}dxdy;$$

$$\xi_{1klnmij} = 12\int_0^1\int_0^1 \lambda\delta\Delta\left(h\psi'_{nm,x}\phi''_{ij,xx} + h'_x\psi'_{nm,x}\phi'_{ij,x} + h\psi''_{nm,xx}\phi'_{ij,x}\right)\psi_{kl}dxdy;$$

$$\xi_{2klnmij} = 12\int_0^1\int_0^1 \frac{\mu_1\lambda^3\delta}{\Delta}\left(h\psi'_{nm,y}\phi''_{ij,xy} + h'_y\psi'_{nm,y}\phi'_{ij,x} + h\psi''_{nm,yy}\phi'_{ij,x}\right)\psi_{kl}dxdy;$$

$$\xi_{3klnmij} = 12\int_0^1\int_0^1 (1-\mu_1\mu_2)g\lambda^3\delta\left(h\psi'_{nm,x}\phi''_{ij,yy} + h'_y\psi'_{nm,y}\phi'_{ij,y} + h\psi'_{nm,y}\phi''_{ij,xy} + \right.$$

$$\left. + h'_x\psi'_{nm,y}\phi'_{ij,y} + 2h\psi''_{nm,xy}\phi'_{ij,y}\right)\psi_{kl}dxdy;$$

$$\xi_{4klnmij} = 12\int_0^1\int_0^1 \frac{\lambda^4\delta}{\Delta}\left(h\psi'_{nm,y}\varphi''_{ij,yy} + h'_y\psi'_{nm,y}\varphi'_{ij,y} + h\psi''_{nm,yy}\varphi'_{ij,y}\right)\psi_{kl}dxdy;$$

$$\xi_{5klnmij} = 12\int_0^1\int_0^1 \mu_2\lambda^2\delta\Delta\left(h\psi'_{nm,x}\varphi''_{ij,xy} + h'_x\psi'_{nm,x}\varphi'_{ij,y} + h\psi''_{nm,xx}\varphi'_{ij,y}\right)\psi_{kl}dxdy;$$

$$\xi_{6klnmij} = 12\int_0^1\int_0^1 (1-\mu_1\mu_2)g\lambda^2\delta\left(h\psi'_{nm,x}\varphi''_{ij,xy} + h'_y\psi'_{nm,x}\varphi'_{ij,x} + h\psi'_{nm,y}\varphi''_{ij,xx} + \right.$$

$$\left. + h'_x\psi'_{nm,y}\varphi'_{ij,x} + 2h\psi''_{nm,xy}\varphi'_{ij,x}\right)\psi_{kl}dxdy;$$

$$\xi_{7klnmij} = -12\int_0^1\int_0^1 k_x\Delta\left(h\psi'_{nm,x}\psi'_{ij,x} + h'_x\psi'_{nm,x}\psi_{ij} + h\psi''_{nm,xx}\psi_{ij}\right)\psi_{kl}dxdy;$$

$$\xi_{8klnmij} = -12\int_0^1\int_0^1 \lambda^2 \mu_2 k_y \Delta\left(h\psi'_{nm,x}\psi'_{ij,x} + h'_x\psi'_{nm,x}\psi_{ij} + h\psi''_{nm,xx}\psi_{ij}\right)\psi_{kl}dxdy;$$

$$\xi_{9klnmij} = -12\int_0^1\int_0^1 \frac{\lambda^4 k_y}{\Delta}\left(h\psi'_{nm,y}\psi'_{ij,y} + h'_y\psi'_{nm,y}\psi_{ij} + h\psi''_{nm,yy}\psi_{ij}\right)\psi_{kl}dxdy;$$

$$\xi_{10klnmij} = -12\int_0^1\int_0^1 \frac{\lambda^2 \mu_1 k_x}{\Delta}\left(h\psi'_{nm,y}\psi'_{ij,y} + h'_y\psi'_{nm,y}\psi_{ij} + h\psi''_{nm,yy}\psi_{ij}\right)\psi_{kl}dxdy;$$

$$g_{1klnmij} = 6\int_0^1\int_0^1 k_x \Delta h\psi'_{nm,x}\psi'_{ij,x}\psi_{kl}dxdy;\ g_{2klnmij} = 6\int_0^1\int_0^1 \lambda^2\mu_2 k_x \Delta h\psi'_{nm,y}\psi'_{ij,y}\psi_{kl}dxdy;$$

$$g_{3klnmij} = 6\int_0^1\int_0^1 \frac{\lambda^2\mu_1 k_y}{\Delta} h\psi'_{nm,x}\psi'_{ij,x}\psi_{kl}dxdy;\ g_{4klnmij} = 6\int_0^1\int_0^1 \frac{\lambda^4 k_y}{\Delta} h\psi'_{nm,y}\psi'_{ij,y}\psi_{kl}dxdy;$$

$$g_{5klnmijrs} = 12\int_0^1\int_0^1 \Delta\left(h\psi'_{nm,x}\psi'_{ij,x}\psi''_{rs,xx} + \frac{1}{2}h'_x\psi'_{nm,x}\psi'_{ij,x}\psi'_{rs,x} + \frac{1}{2}h\psi''_{nm,xx}\psi'_{ij,x}\psi'_{rs,x}\right)\psi_{kl}dxdy;$$

$$g_{6klnmijrs} = 12\int_0^1\int_0^1 \mu_2\Delta\lambda^2\left(h\psi'_{nm,x}\psi'_{ij,y}\psi''_{rs,xy} + \frac{1}{2}h'_x\psi'_{nm,x}\psi'_{ij,y}\psi'_{rs,y} + \frac{1}{2}h\psi''_{nm,xx}\psi'_{ij,y}\psi'_{rs,y}\right)\psi_{kl}dxdy;$$

$$g_{7klnmijrs} = 12\int_0^1\int_0^1 \frac{\lambda^4}{\Delta}\left(h\psi'_{nm,y}\psi'_{ij,y}\psi''_{rs,yy} + \frac{1}{2}h'_y\psi'_{nm,y}\psi'_{ij,y}\psi'_{rs,y} + \frac{1}{2}h\psi''_{nm,yy}\psi'_{ij,y}\psi'_{rs,y}\right)\psi_{kl}dxdy;$$

$$g_{8klnmijrs} = 12\int_0^1\int_0^1 \frac{\mu_1\lambda^2}{2\Delta}\left(2h\psi'_{nm,y}\psi'_{ij,x}\psi''_{rs,xy} + h'_y\psi'_{nm,y}\psi'_{ij,x}\psi'_{rs,x} + h\psi''_{nm,yy}\psi'_{ij,x}\psi'_{rs,x}\right)\psi_{kl}dxdy;$$

$$g_{9klnmijrs} = 12\int_0^1\int_0^1 (1-\mu_1\mu_2)g\lambda^2\left(h\psi'_{nm,x}\psi'_{ij,y}\psi''_{rs,xy} + h\psi'_{nm,x}\psi'_{ij,x}\psi''_{rs,yy} +\right.$$

$$+ h'_y\psi'_{nm,x}\psi'_{ij,x}\psi'_{rs,y} + h\psi'_{nm,y}\psi'_{ij,x}\psi''_{rs,xy} + h\psi'_{nm,y}\psi'_{ij,y}\psi''_{rs,xx} +$$

$$\left.+ h'_x\psi'_{nm,y}\psi'_{ij,x}\psi'_{rs,y} + 2h\psi''_{nm,xy}\psi'_{ij,x}\psi'_{rs,y}\right)\psi_{kl}dxdy;\ q_{kl} = q\int_0^1\int_0^1 \psi_{kl}dxdy;$$

$$p^2_{klnm} = f_{5klnm} + f_{6klnm} + f_{7klnm} + f_{8klnm} + f_{9klnm} - 4\pi^2\lambda^2 p^*_{klnm}\delta_0;\ \mu_{klnm} = \frac{2\pi^2\lambda^2 p^*_{klnm}}{p^2_{klnm}}\delta_1.$$

System (14) was integrated using a numerical method based on the use of quadrature formulas [28]. Assuming harmonic oscillations, system (14) in integral form is obtained by integrating it twice over time t:

$$\sum_{n=1}^{N}\sum_{m=1}^{M} a_{klnm}u_{nm} = \sum_{n=1}^{N}\sum_{m=1}^{M} a_{klnm}\left(u_{0nm} + \dot{u}_{0nm}t\right) + \eta_1\int_0^t\int_0^\tau\left\{\sum_{n=1}^{N}\sum_{m=1}^{M}\left\{\left[\left(1-\Gamma^*_{11}\right)d_{1klnm} + \left(1-\Gamma^*\right)d_{2klnm}\right]u_{nm} +\right.\right.$$

$$\left.+\left[\left(1-\Gamma^*_{12}\right)d_{3klnm} + \left(1-\Gamma^*\right)d_{4klnm}\right]v_{nm} + \left[\left(1-\Gamma^*_{11}\right)d_{5klnm} + \left(1-\Gamma^*_{12}\right)d_{6klnm}\right]w_{nm}\right\} +$$

$$\left.+\sum_{n,i=1}^{N}\sum_{m,j=1}^{M}\left[\left(1-\Gamma^*_{11}\right)d_{7klnmij} + \left(1-\Gamma^*_{12}\right)d_{8klnmij} + \left(1-\Gamma^*\right)d_{9klnmij}\right]\left(w_{nm}w_{ij} - w_{0nm}w_{0ij}\right)\right\}d\tau ds,$$

$$\sum_{n=1}^{N}\sum_{m=1}^{M} b_{klnm}v_{nm} = \sum_{n=1}^{N}\sum_{m=1}^{M} b_{klnm}\left(v_{0nm}+\dot{v}_{0nm}t\right)+\eta_2\int_0^t\int_0^\tau\left\{\sum_{n=1}^{N}\sum_{m=1}^{M}\left\{\left[\left(1-\Gamma_{21}^*\right)e_{1klnm}+\left(1-\Gamma^*\right)e_{2klnm}\right]u_{nm}+\right.\right.$$

$$+\left[\left(1-\Gamma_{22}^*\right)e_{3klnm}+\left(1-\Gamma^*\right)e_{4klnm}\right]v_{nm}+\left[\left(1-\Gamma_{21}^*\right)e_{5klnm}+\left(1-\Gamma_{22}^*\right)e_{6klnm}\right]w_{nm}\Big\}+ \tag{15}$$

$$\left.+\sum_{n,i=1}^{N}\sum_{m,j=1}^{M}\left[\left(1-\Gamma_{22}^*\right)e_{7klnmij}+\left(1-\Gamma_{21}^*\right)e_{8klnmij}+\left(1-\Gamma^*\right)e_{9klnmij}\right]\left(w_{nm}w_{ij}-w_{0nm}w_{0ij}\right)\right\}d\tau ds,$$

$$\sum_{n=1}^{N}\sum_{m=1}^{M} c_{klnm}w_{nm} = \sum_{n=1}^{N}\sum_{m=1}^{M} c_{klnm}\left(w_{0nm}+\dot{w}_{0nm}t\right)-\eta_3\int_0^t\int_0^\tau\left\{\sum_{n=1}^{N}\sum_{m=1}^{M} p_{klnm}^2\left(1-2\mu_{klnm}\cos\Theta t\right)w_{nm}-\right.$$

$$-\sum_{n=1}^{N}\sum_{m=1}^{M}\left\{\left[\left(1-\Gamma_{11}^*\right)f_{1klnm}+\left(1-\Gamma_{21}^*\right)f_{2klnm}\right]u_{nm}+\left[\left(1-\Gamma_{12}^*\right)f_{3klnm}+\left(1-\Gamma_{22}^*\right)f_{4klnm}\right]v_{nm}+\right.$$

$$\left.+\left[\Gamma_{11}^* f_{5klnm}+\Gamma_{12}^* f_{6klnm}+\Gamma_{22}^* f_{7klnm}+\Gamma_{21}^* f_{8klnm}+\Gamma^* f_{9klnm}\right]w_{0nm}\right\}-$$

$$-\sum_{n,i=1}^{N}\sum_{m,j=1}^{M} w_{nm}\left\{\left[\left(1-\Gamma_{11}^*\right)\xi_{1klnmij}+\left(1-\Gamma_{21}^*\right)\xi_{2klnmij}+\left(1-\Gamma^*\right)\xi_{3klnmij}\right]u_{ij}+\right.$$

$$+\left[\left(1-\Gamma_{22}^*\right)\xi_{4klnmij}+\left(1-\Gamma_{12}^*\right)\xi_{5klnmij}+\left(1-\Gamma^*\right)\xi_{6klnmij}\right]v_{ij}+$$

$$\left.+\left[\left(1-\Gamma_{11}^*\right)\xi_{7klnmij}+\left(1-\Gamma_{12}^*\right)\xi_{8klnmij}+\left(1-\Gamma_{22}^*\right)\xi_{9klnmij}+\left(1-\Gamma_{21}^*\right)\xi_{10klnmij}\right]\left(w_{ij}-w_{0ij}\right)\right\}+$$

$$+\sum_{n,i=1}^{N}\sum_{m,j=1}^{M}\left\{\left(1-\Gamma_{11}^*\right)g_{1klnmijrs}+\left(1-\Gamma_{12}^*\right)g_{2klnmijrs}+\left(1-\Gamma_{21}^*\right)g_{3klnmijrs}+\left(1-\Gamma_{22}^*\right)g_{4klnmijrs}\right\}\left(w_{nm}w_{ij}-w_{0nm}w_{0ij}\right)+$$

$$+\sum_{n,i,r=1}^{N}\sum_{m,j,s=1}^{M} w_{nm}\left\{\left(1-\Gamma_{11}^*\right)g_{5klnmijrs}+\left(1-\Gamma_{12}^*\right)g_{6klnmijrs}+\left(1-\Gamma_{22}^*\right)g_{7klnmijrs}+\right.$$

$$\left.\left.+\left(1-\Gamma_{21}^*\right)g_{8klnmijrs}+\left(1-\Gamma^*\right)g_{9klnmijrs}\right\}\left(w_{ij}w_{rs}-w_{0ij}w_{0rs}\right)-12\eta_3\left(1-\mu_1\mu_2\right)\lambda^4 q_{kl}\right\}d\tau ds.$$

By the formula for replacing the double integral with a single integral the system (15) is given in the following form:

$$\sum_{n=1}^{N}\sum_{m=1}^{M} a_{klnm}u_{nm} = \sum_{n=1}^{N}\sum_{m=1}^{M} a_{klnm}\left(u_{0nm}+\dot{u}_{0nm}t\right)+\eta_1\int_0^t(t-\tau)\left\{\sum_{n=1}^{N}\sum_{m=1}^{M}\left\{\left[\left(1-\Gamma_{11}^*\right)d_{1klnm}+\left(1-\Gamma^*\right)d_{2klnm}\right]u_{nm}+\right.\right.$$

$$+\left[\left(1-\Gamma_{12}^*\right)d_{3klnm}+\left(1-\Gamma^*\right)d_{4klnm}\right]v_{nm}+\left[\left(1-\Gamma_{11}^*\right)d_{5klnm}+\left(1-\Gamma_{12}^*\right)d_{6klnm}\right]w_{nm}\Big\}+$$

$$\left.+\sum_{n,i=1}^{N}\sum_{m,j=1}^{M}\left[\left(1-\Gamma_{11}^*\right)d_{7klnmij}+\left(1-\Gamma_{12}^*\right)d_{8klnmij}+\left(1-\Gamma^*\right)d_{9klnmij}\right]\left(w_{nm}w_{ij}-w_{0nm}w_{0ij}\right)\right\}d\tau,$$

$$\sum_{n=1}^{N}\sum_{m=1}^{M} b_{klnm}v_{nm} = \sum_{n=1}^{N}\sum_{m=1}^{M} b_{klnm}\left(v_{0nm}+\dot{v}_{0nm}t\right)+\eta_2\int_0^t(t-\tau)\left\{\sum_{n=1}^{N}\sum_{m=1}^{M}\left\{\left[\left(1-\Gamma_{21}^*\right)e_{1klnm}+\left(1-\Gamma^*\right)e_{2klnm}\right]u_{nm}+\right.\right.$$

$$+\left[\left(1-\Gamma_{22}^*\right)e_{3klnm}+\left(1-\Gamma^*\right)e_{4klnm}\right]v_{nm}+\left[\left(1-\Gamma_{21}^*\right)e_{5klnm}+\left(1-\Gamma_{22}^*\right)e_{6klnm}\right]w_{nm}\Big\}+ \tag{16}$$

$$+\sum_{n,i=1}^{N}\sum_{m,j=1}^{M}\left[\left(1-\Gamma_{22}^{*}\right)e_{7klnmij}+\left(1-\Gamma_{21}^{*}\right)e_{8klnmij}+\left(1-\Gamma^{*}\right)e_{9klnmij}\right]\left(w_{nm}w_{ij}-w_{0nm}w_{0ij}\right)\Bigg\}d\tau,$$

$$\sum_{n=1}^{N}\sum_{m=1}^{M}c_{klnm}w_{nm}=\sum_{n=1}^{N}\sum_{m=1}^{M}c_{klnm}\left(w_{0nm}+\dot{w}_{0nm}t\right)-\eta_3\int_0^t(t-\tau)\Bigg\{\sum_{n=1}^{N}\sum_{m=1}^{M}p_{klnm}^{2}\left(1-2\mu_{klnm}\cos\Theta t\right)w_{nm}-$$

$$-\sum_{n=1}^{N}\sum_{m=1}^{M}\Bigg\{\left[\left(1-\Gamma_{11}^{*}\right)f_{1klnm}+\left(1-\Gamma_{21}^{*}\right)f_{2klnm}\right]u_{nm}+\left[\left(1-\Gamma_{12}^{*}\right)f_{3klnm}+\left(1-\Gamma_{22}^{*}\right)f_{4klnm}\right]v_{nm}+$$

$$+\left[\Gamma_{11}^{*}f_{5klnm}+\Gamma_{12}^{*}f_{6klnm}+\Gamma_{22}^{*}f_{7klnm}+\Gamma_{21}^{*}f_{8klnm}+\Gamma^{*}f_{9klnm}\right]w_{0nm}\Bigg\}-$$

$$-\sum_{n,i=1}^{N}\sum_{m,j=1}^{M}w_{nm}\Bigg\{\left[\left(1-\Gamma_{11}^{*}\right)\xi_{1klnmij}+\left(1-\Gamma_{21}^{*}\right)\xi_{2klnmij}+\left(1-\Gamma^{*}\right)\xi_{3klnmij}\right]u_{ij}+$$

$$+\left[\left(1-\Gamma_{22}^{*}\right)\xi_{4klnmij}+\left(1-\Gamma_{12}^{*}\right)\xi_{5klnmij}+\left(1-\Gamma^{*}\right)\xi_{6klnmij}\right]v_{ij}+$$

$$+\left[\left(1-\Gamma_{11}^{*}\right)\xi_{7klnmij}+\left(1-\Gamma_{12}^{*}\right)\xi_{8klnmij}+\left(1-\Gamma_{22}^{*}\right)\xi_{9klnmij}+\left(1-\Gamma_{21}^{*}\right)\xi_{10klnmij}\right]\left(w_{ij}-w_{0ij}\right)\Bigg\}+$$

$$+\sum_{n,i=1}^{N}\sum_{m,j=1}^{M}\Big\{\left(1-\Gamma_{11}^{*}\right)g_{1klnmijrs}+\left(1-\Gamma_{12}^{*}\right)g_{2klnmijrs}+\left(1-\Gamma_{21}^{*}\right)g_{3klnmijrs}+\left(1-\Gamma_{22}^{*}\right)g_{4klnmijrs}\Big\}\left(w_{nm}w_{ij}-w_{0nm}w_{0ij}\right)+$$

$$+\sum_{n,i,r=1}^{N}\sum_{m,j,s=1}^{M}w_{nm}\Big\{\left(1-\Gamma_{11}^{*}\right)g_{5klnmijrs}+\left(1-\Gamma_{12}^{*}\right)g_{6klnmijrs}+\left(1-\Gamma_{22}^{*}\right)g_{7klnmijrs}+$$

$$+\left(1-\Gamma_{21}^{*}\right)g_{8klnmijrs}+\left(1-\Gamma^{*}\right)g_{9klnmijrs}\Big\}\left(w_{ij}w_{rs}-w_{0ij}w_{0rs}\right)-12\eta_3\left(1-\mu_1\mu_2\right)\lambda^4 q_{kl}\Bigg\}d\tau,$$

$$u_{nm}(0)=u_{0nm},\ \dot{u}_{nm}(0)=\dot{u}_{0nm},\ v_{nm}(0)=v_{0nm},\ \dot{v}_{nm}(0)=\dot{v}_{0nm},$$

$$w_{nm}(0)=w_{0nm},\ \dot{w}_{nm}(0)=\dot{w}_{0nm},\ k=1,2,\ldots,N;\ \ l=1,2,\ldots,M.$$

Assuming that $t=t_i$, $t_i=i\Delta t, i=1,2,...$ (where Δt is the integration step) and replacing the integrals with quadrature trapezoidal formulas to calculate the unknowns $w_{inm}=w_{inm}(t_i)$, $u_{inm}=u_{inm}(t_i)$ and $v_{inm}=v_{inm}(t_i)$, a system of recurrent formulas is obtained.

Based on the developed algorithm, a program was compiled in the Delphi algorithmic language.

3. Results and Discussion

The results of calculations for various physical and geometric parameters are shown in graphs in Fig. 3–7. Numerical results are compared to the ones available in the literature.

The effect of orthotropic properties of the material on the behavior of a shell was studied (Fig. 3). As seen from the figure, an increase in parameter Δ that determines the degree of anisotropy (curve 1 - Δ=1; curve 2 - Δ=1.5; curve 3 - Δ=2.0) leads to an increase in the oscillation amplitude and a phase shift to the left.

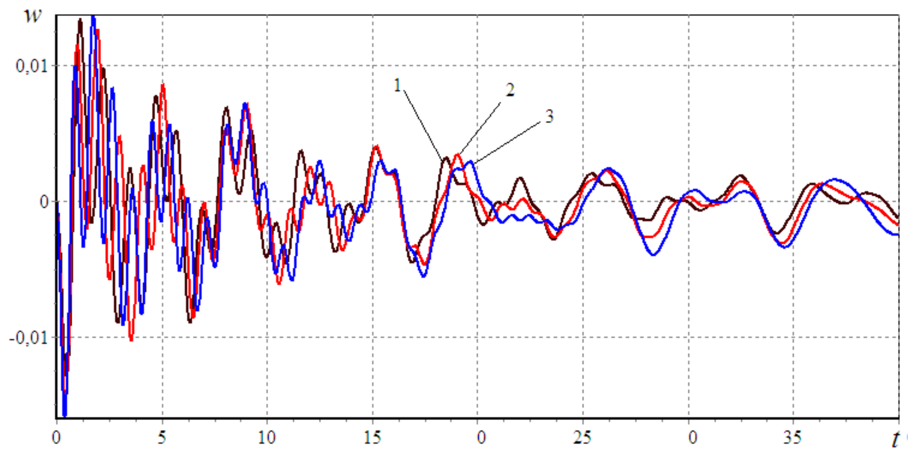

Figure 3. Dependence of the deflection vs time for

$$\lambda = 1; \delta = 25; k_x = 10; k_y = 10; q = 0; \ p_x = 0; \ p_y = 0; \alpha^* = 0.5; \Theta = 1.1;$$

$$A = A_{ij} = 0.05, \ i, \ j = 1{,}2;$$

Δ =1 (1); 1.5 (2); 2.0 (2)

Figure 4 shows the results obtained from different theories. Here, curve 1 corresponds to the case when the shell material is elastic, curve 2 - to the case when the viscosity of the material is taken into account in the direction of shear $\left(A = 0.05, \ A_{ij} = 0, \ i, \ j = 1{,}2\right)$, and curve 3 - to the case when the viscosity is taken into account in all directions $\left(A = A_{ij} = 0.05, \ i, \ j = 1{,}2\right)$.

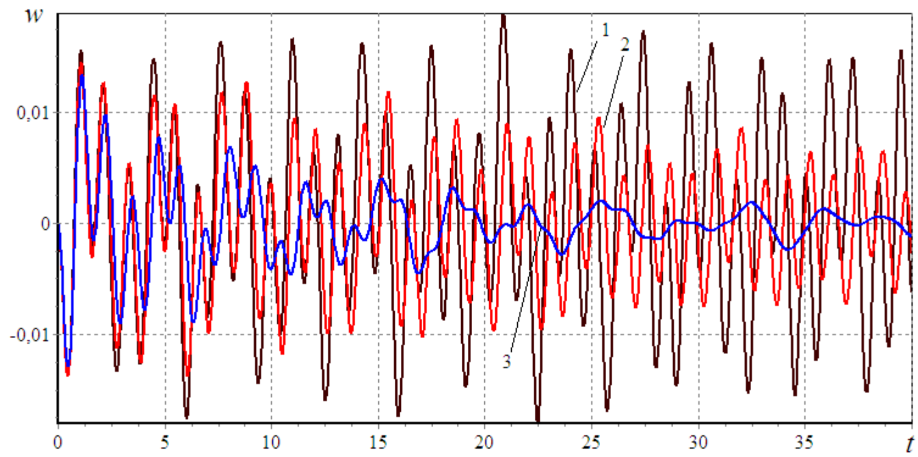

Figure 4. Dependence of the deflection vs time for

$$\lambda = 1; \ \delta = 25; \ k_x = 10; \ k_y = 10; \ q = 0; \ p_x = 0; \ p_y = 0; \ \alpha^* = 0.5; \ \Theta = 1.1; \ \Delta = 1$$

The results obtained confirm that viscous-elastic properties of the material should be considered not only in the shear direction but also in other directions.

The influence of the shell thickness on its behavior is studied. Figure 5 shows the results obtained for various values of the thickness change parameter α^*. It can be seen that with an increase in this parameter, the oscillation amplitude increases. In particular, the results obtained for a shallow shell of constant thickness ($\alpha^* = 0$) coincide with the results obtained in [29].

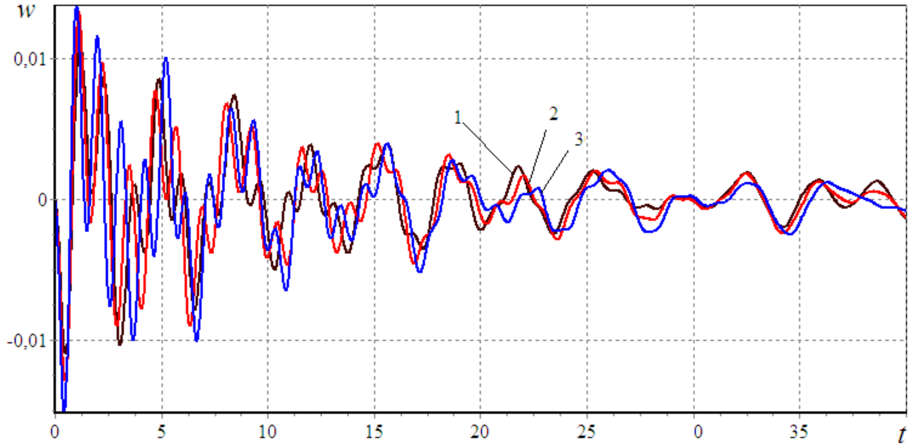

Fig.5. Dependence of the deflection vs time for

$$\lambda = 1; \delta = 25; k_x = 10; k_y = 10; q = 0; p_x = 0; p_y = 0; \Theta = 1.1;$$
$$A = A_{ij} = 0.05, i, j = 1,2; \Delta = 1$$
α^*=0 (1); 0.5 (2); 0.8 (3)

Figure 6 shows the results obtained for various values of the curvature parameter k_x. An increase in this parameter leads to an increase in the amplitude of oscillations.

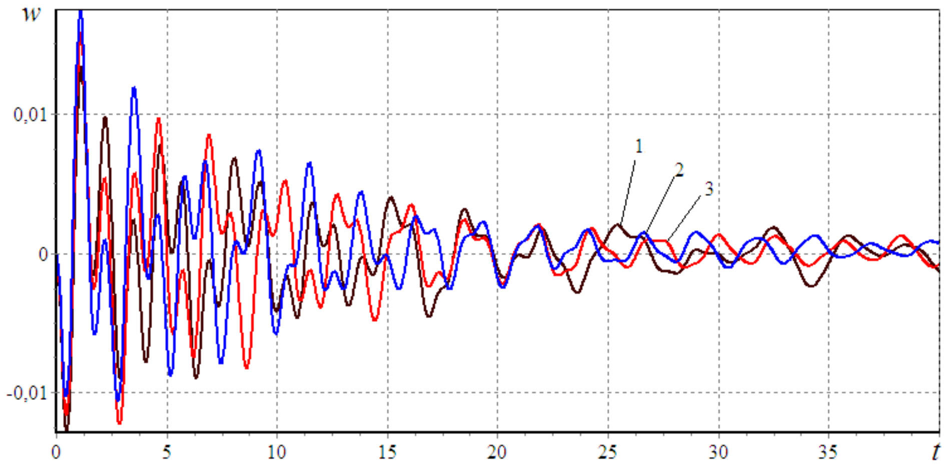

Figure 6. Dependence of the deflection vs time for

$$\lambda = 1; \delta = 25; k_y = 10; q = 0; p_x = 0; p_y = 0; \alpha^* = 0.5; \Theta = 1.1;$$
$$A = A_{ij} = 0.05, i, j = 1,2; \Delta = 1$$
k_x=10 (1); 15 (2); 20 (3)

Figure 7 shows the results obtained for various values of the frequency of the external periodic load Θ. An increase in this parameter leads to an increase in the amplitude of oscillations.

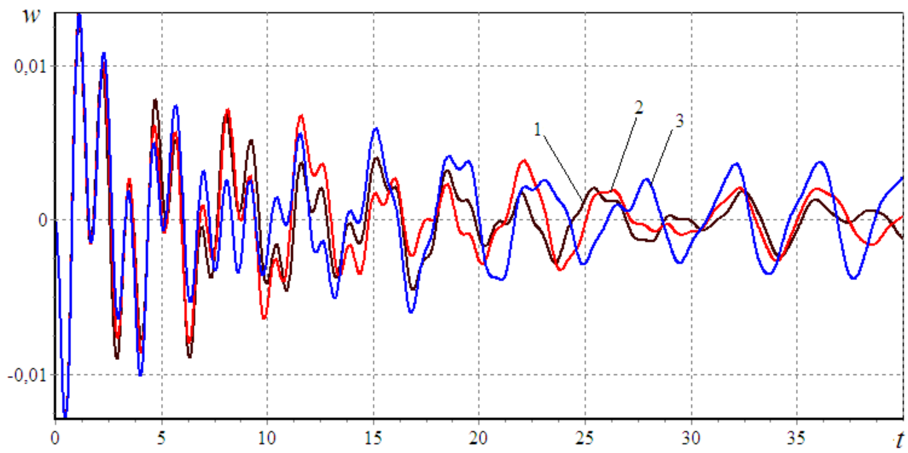

Figure 7. Dependence of the deflection vs time for

$$\lambda = 1;\ \delta = 25;\ k_x = 10;\ k_y = 10;\ q = 0;\ p_x = 0;\ p_y = 0;\ \alpha^* = 0.5;$$

$$A = A_{ij} = 0.05,\ i, j = 1,2;\ \Delta = 1$$

Θ =1.1 (1); 1.3 (2); 1.5 (3)

4. Conclusion

A mathematical model, method, and computer program were developed to estimate parametric oscillations of a viscous-elastic orthotropic shallow shell of variable thickness, taking into account geometric nonlinearity under periodic loads.

The dynamic stability of a viscous-elastic orthotropic shallow shell of variable thickness was described by a nonlinear system of IDEs.

The application of Galerkin method with the discretization of spatial variables at each time point reduces the problem of dynamic stability of a viscous-elastic orthotropic shallow shell of variable thickness to solving a non-decaying system of ordinary nonlinear IDEs with weakly singular kernels with variable coefficients.

The impact on the amplitude-time characteristics and the SSS of a change in the physical-mechanical and geometric parameters of the shell material was estimated.

The method proposed in this article can be used for various types of thin-wall structures (plates, panels, and shells of variable thickness).

References

1. Bolotin, V. V. Dynamic Stability of Structures. Nonlinear Stability of Structures: Theory and Computational Techniques. Vienna, Springer Vienna, 1995. Pp. 3–72.
2. Alijani, F., Amabili, M. Non-linear vibrations of shells: A literature review from 2003 to 2013. International Journal of Non-Linear Mechanics. 2014. 58. Pp. 233–257. DOI: 10.1016/j.ijnonlinmec.2013.09.012
3. Amabili, M. Nonlinear vibrations and stability of shells and plates. New York, USA, Cambridge University Press, 2008. 374 p. ISBN:978-0521883290.
4. Radwańska, M., Stankiewicz, A., Wosatko, A. Plate and Shell Structures: Selected Analytical and Finite Element Solutions. John Wiley & Sons, 2017. 424 p. ISBN:9781118934548.
5. H., S.A., Zihni, Z., P., A.B., David, H., Ferruh, T., Hakan, E. The dynamic instability of FG orthotropic conical shells within the SDT. Steel and Composite Structures. 2017. 25(5). Pp. 581–591. DOI: 10.12989/SCS.2017.25.5.581
6. Talimian, A., Beda, P. Dynamic Stability of a Thin Plate Subjected to Bi-Axial Edged Loads. Acta Polytechnica Hungarica. 2018. 15(2). Pp. 125–139. DOI: 10.12700/aph.15.1.2018.2.7
7. Kosheleva, E. Plate stability under periodic load action, material of which obeys hereditary law of viscoelasticity. Proceedings of the 2018 7th International Conference on Energy, Environment and Sustainable Development (ICEESD 2018). 2018. Pp. 568–572. DOI: 10.2991/iceesd-18.2018.103
8. Sofiyev, A.H. Influences of shear deformations and material gradient on the linear parametric instability of laminated orthotropic conical shells. Composite Structures. 2019. 225. Pp. 111156. DOI: 10.1016/j.compstruct.2019.111156
9. Dey, T., Jansen, E., Kumar, R., Rolfes, R. Instability characteristics of variable stiffness laminated composite curved panels under non-uniform periodic excitation. Thin-Walled Structures. 2022. 171. Pp. 108735. DOI: 10.1016/j.tws.2021.108735
10. Becerra, H.C., Silva, A.R. Parametric study using a curved shell finite element to dynamic analysis of footbridge under rhythmic loading. Structures. 2021. 34. Pp. 135–148. DOI: 10.1016/j.istruc.2021.07.057
11. Bakulin, V.N., Nedbai, A.Y. Dynamic Stability of a Composite Cylindrical Shell with Linear-Variable Thickness under Pulsed External Pressure. Journal of Engineering Physics and Thermophysics. 2021. 94(2). Pp. 525–533. DOI: 10.1007/s10891-021-02324-7

12. Shahmohammadi, M.A., Mirfatah, S.M., Salehipour, H., Azhari, F., Civalek, Ö. Dynamic stability of hybrid fiber/nanocomposite-reinforced toroidal shells subjected to the periodic axial and pressure loadings. Mechanics of Advanced Materials and Structures. 2022. Pp. 1–17. DOI: 10.1080/15376494.2022.2037172
13. Phu, K. Van, Bich, D.H., Doan, L.X. Nonlinear Dynamic Stability of Variable Thickness FGM Cylindrical Shells Subjected to Mechanical Load. Modern Mechanics and Applications. 2022. Pp. 506–521.
14. Sieber, J., Hutchinson, J.W., Thompson, J.M.T. Nonlinear dynamics of spherical shells buckling under step pressure. Proceedings of the Royal Society A: Mathematical, Physical and Engineering Sciences. 2019. 475(2223). Pp. 20180884. DOI:10.1098/rspa.2018.0884
15. Krysko, A. V, Awrejcewicz, J., Mitskevich, S.A., Zhigalov, M. V, Krysko, V.A. Nonlinear dynamics of heterogeneous shells. Part 2. Chaotic dynamics of variable thickness shells. International Journal of Non-Linear Mechanics. 2021. 129. Pp. 103660. DOI: 10.1016/j.ijnonlinmec.2020.103660
16. Fu, T., Wu, X., Xiao, Z., Chen, Z. Study on dynamic instability characteristics of functionally graded material sandwich conical shells with arbitrary boundary conditions. Mechanical Systems and Signal Processing. 2021. 151. Pp. 107438. DOI: 10.1016/j.ymssp.2020.107438
17. Safaei, B. Frequency-dependent damped vibrations of multifunctional foam plates sandwiched and integrated by composite faces. The European Physical Journal Plus. 2021. 136(6). Pp. 646. DOI: 10.1140/epjp/s13360-021-01632-4
18. Zaczynska, M., Abramovich, H., Bisagni, C. Parametric studies on the dynamic buckling phenomenon of a composite cylindrical shell under impulsive axial compression. Journal of Sound and Vibration. 2020. 482. Pp. 115462. DOI: 10.1016/j.jsv.2020.115462
19. Chen, C.-S., Wang, H., Yeh, C.-C., Chen, W.-R. Dynamic Instability Response of Soft Core Sandwich Plates Based on Higher-Order Plate Theory. International Journal of Structural Stability and Dynamics. 2021. 21(09). Pp. 2150118. DOI: 10.1142/S0219455421501182
20. Lin, G., Li, F., Zhang, Q., Chen, P., Sun, W., Saikov, I., Shcherbakov, V., Alymov, M. Dynamic instability of fiber composite cylindrical shell with metal liner subjected to internal pulse loading. Composite Structures. 2022. 280. Pp. 114906. DOI: 10.1016/j.compstruct.2021.114906
21. Ma, L., Liu, X., Moradi, Z. On the chaotic behavior of graphene-reinforced annular systems under harmonic excitation. Engineering with Computers. 2022. 38(3). Pp. 2583–2607. DOI: 10.1007/s00366-020-01210-9
22. Normuminov, B., Abdikarimov, R., Mirsaidov, M., Khodzhaev, D., Mirzaev, B. Parametric vibrations of viscoelastic orthotropic cylindrical panels of variable thickness. {IOP} Conference Series: Materials Science and Engineering. 2020. 869. Pp. 52034. DOI: 10.1088/1757-899x/869/5/052034
23. Khodzhaev, D.A., Abdikarimov, R.A., Mirsaidov, M.M. Dynamics of a physically nonlinear viscoelastic cylindrical shell with a concentrated mass. Magazine of Civil Engineering. 2019. 91(7). Pp. 39–48. DOI: 10.18720/MCE.91.4
24. Abdikarimov, R., Amabili, M., Vatin, N.I., Khodzhaev, D. Dynamic Stability of Orthotropic Viscoelastic Rectangular Plate of an Arbitrarily Varying Thickness. Applied Sciences. 2021. 11(13). DOI: 10.3390/app11136029
25. Reddy, J.N. Theory and analysis of elastic plates and shells. 2nd Editio . CRC Press, 2007. 547 p. ISBN:9780849384158.
26. Ambartsumyan, S.A. Theory Of Anisotropic Plates: Strength, Stability, & Vibrations. CRC Press, 1991. 360 p.
27. Mal'tsev, L.E. The analytical determination of the Rzhanitsyn-Koltunov nucleus. Mechanics of Composite Materials. 1979. 15(1). Pp. 131–133.
28. Abdikarimov, R.A., Khodzhaev, D.A. Computer modeling of tasks in dynamics of viscoelastic thinwalled elements in structures of variable thickness. Magazine of Civil Engineering. 2014. 49(5). Pp. 83–94. DOI: 10.5862/MCE.49.9
29. Harvan, J., Psorty, M. Stability analysis of a shallow shell. Procedia Engineering. 2017. 190. Pp. 148–153. DOI: 10.1016/j.proeng.2017.05.320

Information about authors:

Dadakhan Khodzhaev, *PhD in Physics and Mathematics*
ORCID: https://orcid.org/0000-0001-5526-8723
E-mail: dhodjaev@mail.ru

Rustamkhan Abdikarimov*, Doctor of Physics and Mathematics*
ORCID: https://orcid.org/0000-0001-8114-1187
E-mail: rabdikarimov@mail.ru

Marco Amabili, *PhD*
ORCID: https://orcid.org/0000-0001-9340-4474
E-mail: marco.amabili@mcgill.ca

Bakhodir Normuminov,
ORCID: https://orcid.org/0000-0002-5018-3533
E-mail: normuminovb_77@inbox.ru

Received 11.10.2022. Approved after reviewing 20.03.2023. Accepted 23.03.2023.